

IMMISCIBLE FOAM FOR ENHANCING OIL RECOVERY

Mohammad Simjoo

IMMISCIBLE FOAM FOR ENHANCING OIL RECOVERY

Proefschrift

ter verkrijging van de graad van doctor
aan de Technische Universiteit Delft,
op gezag van de Rector Magnificus prof. ir. K.C.A.M. Luyben,
voorzitter van het College voor Promoties,
in het openbaar te verdedigen op woensdag 26 september 2012 om 10:00 uur

door

Mohammad SIMJOO

Master of Science in Petroleum Engineering, Petroleum University of Technology, Ahwaz, Iran

geboren te Bandar Anzali, Iran

Dit proefschrift is goedgekeurd door de promotor:

Prof. dr. P. L. J. Zitha

Samenstelling promotiecommissie:

Rector Magnificus,	voorzitter
Prof. dr. P. L. J. Zitha	Technische Universiteit Delft, promotor
Prof. dr. H. Bertin	Universiteit van Bordeaux, Frankrijk
Prof. dr. J. Bruining	Technische Universiteit Delft
Prof. dr. J. D. Jansen	Technische Universiteit Delft
Prof. dr. S. J. Picken	Technische Universiteit Delft
Prof. dr. W. R. Rossen	Technische Universiteit Delft
Dr. A. Andrianov	Shell Global Solutions International

The work described in this thesis was performed in the section of Petroleum Engineering, Department of Geoscience and Engineering, Delft University of Technology, the Netherlands. This research was financially supported by Iran Ministry of Science, Research, and Technology and by Shell Global Solutions International.

Copyright © 2012 by Mohammad Simjoo

Cover design by Mohammad Chahardowli

Picture by Mohammad Simjoo (CT images of foam propagation in a surfactant-saturated core)

Printed by Wöhrmann Print Service B.V., Zutphen, the Netherlands

ISBN: 978-94-6203-153-1

In the name of the Lord, Life-Creating,

The Wise One, Speech-Creating with the Tongue (Saadi, 1184-1283)

To

Whom all waiting for him

To

My family

and the memory of my friends: Saeed and Mousa

Contents

Chapter 1: Introduction	1
1.1 World oil supply and demand	1
1.2 Prospects of EOR techniques	2
1.3 EOR: definition and mechanisms	3
1.4 Gas flooding EOR	4
1.5 Foam EOR	5
1.6 Objectives of the thesis	7
1.7 Outline of the thesis	7
Chapter 2: Bulk Foam Stability in the Absence and Presence of Oil	11
2.1 Introduction	12
2.2 Experimental description	15
2.2.1 Materials and methods	15
2.2.2 Experimental set-up	15
2.3 Results and discussion	17
2.3.1 Surfactant screening	17
2.3.1.1 Foam decay	18
2.3.1.2 Entering, spreading and bridging coefficient and lamella number	21
2.3.2 AOS foam stability	22
2.3.2.1 Baseline foaming	22
2.3.2.1.1 Foam development and decay in the absence of oil	22
2.3.2.1.2 Foam development and decay in the presence of oil	24
2.3.2.2 Effect of surfactant concentration	25
2.3.2.3 Effect of oil type	28
2.3.3 Foam-oil interaction mechanism	30
2.4 Conclusions	31
Chapter 3: Dynamics of Foam Flow in Porous Media in the Absence of Oil	33
3.1 Introduction	34
3.2 Experimental description	36
3.2.1 Materials	36
3.2.2 Core sample and core-holder	36
3.2.3 Experimental set-up	37
3.2.4 CT imaging settings	38
3.2.5 Experimental procedure	38
3.3 Results and discussion	40
3.3.1 Baseline foam dynamics	40

3.3.1.1 CT scan images	40
3.3.1.2 Saturation profiles	41
3.3.1.3 Mobility reduction factor	43
3.3.1.4 Dynamic capillary desaturation curve	44
3.3.2 Effect of surfactant concentration	46
3.3.2.1 Multiple cores experiments	46
3.3.2.2 Single core experiments	48
3.3.2.3 MRF and water saturation	49
3.3.3 Effect of flow velocity	51
3.4 General discussion	54
3.5 Conclusions	56
Chapter 4: Foam Mobility Transition in Porous Media	57
4.1 Introduction	58
4.2 Experimental description	59
4.2.1 Materials	59
4.2.2 Set-up and CT imaging settings	59
4.2.3 Experimental procedure	61
4.3 Results and discussion	62
4.3.1 Long core foam flow	62
4.3.2 Foam mobility transition	65
4.3.3 Mechanistic description of foam mobility transition	67
4.3.4 Dependence of yield stress on saturation	72
4.4 Conclusions	75
Chapter 5: Modeling of Transient Foam Flow using Stochastic Bubble Population Model	77
5.1 Introduction	78
5.2 Model formulation	79
5.3 Constitutive relations	80
5.4 Numerical simulation	81
5.5 Method of solution	82
5.6 Results and discussion	84
5.6.1 Sensitivity to the grid size and time step	84
5.6.2 Transient foam flow: base case	86
5.6.3 Influence of the physical parameters	88
5.6.3.1 Effect of maximum bubble density	88
5.6.3.2 Effect of bubble generation coefficient	89
5.6.4 Comparison of SBP model and experiments	91

5.6.5 Comparison of SBP model with other foam models	92
5.7 Conclusion	94
Chapter 6: Effects of Oil on Foam Generation and Propagation in Porous Media	95
6.1 Introduction	96
6.2 Experimental description	97
6.2.1 Materials	97
6.2.2 Core sample and core-holder	97
6.2.3 Experimental set-up	98
6.2.4 CT scanner	98
6.2.5 Experimental procedure	100
6.3 Results and discussion	101
6.3.1 Primary drainage and imbibition	101
6.3.1.1 CT scan images	101
6.3.1.2 Saturation profiles	101
6.3.1.3 Pressure drop profiles	103
6.3.2 Gas flooding	105
6.3.3 Foam flooding	106
6.3.3.1 CT scan images	106
6.3.3.2 Saturation profiles	108
6.3.3.3 Foam mobility reduction factor	111
6.3.3.4 Incremental oil recovery by foam	112
6.3.4 Foam EOR mechanism	114
6.4 Conclusions	119
Chapter 7: Further Investigation of Oil Recovery by Immiscible Foam	121
7.1 Introduction	122
7.2 Experimental description	123
7.2.1 Materials	123
7.2.2 Core sample and core-holder	123
7.2.3 Experimental set-up	124
7.2.4 CT scanner	124
7.2.5 Experimental procedure	126
7.3 Results and discussion	128
7.3.1 Primary drainage and imbibition	128
7.3.1.1 CT scan images	128
7.3.1.2 Saturation profiles	130
7.3.2 Gas flooding	131
7.3.3 Foam flooding	133

7.3.3.1 Effect of surfactant concentration	133
7.3.3.2 Effect of surfactant pre-flush	135
7.3.3.3 Effect of injection direction	137
7.3.3.4 Effect of core length	139
7.4 General discussion	143
7.5 Conclusions	146
Chapter 8: Summary and Conclusions	149
References	153
Synopsis van het proefschrift	163
چکیده پایان نامه	169
Acknowledgments	173
Scientific Contribution	175
About the Author	177

Chapter 1

INTRODUCTION

1.1 World oil supply and demand

After a decline of energy consumption in 2009 due to the global economic recession, energy demand experienced significant growth in 2010. World primary energy consumption, including oil, natural gas, coal, hydroelectricity, nuclear and renewable energies, grew by 5.6% due to the economic recovery in 2010 (BP statistical review of world energy, 2011). This has been the largest increase since 1973. Oil and gas are the world's leading energy resources, accounting for 58% of the global energy demand, Fig. 1.1. According to the International Energy Agency (IEA) daily global oil production reached 89 million barrels per day (MMBD) in February 2011. However, OPEC expects that this number will grow to 109.7 MMBD by 2035 mainly due to the increasing energy demand of developing countries (World oil outlook, 2011).

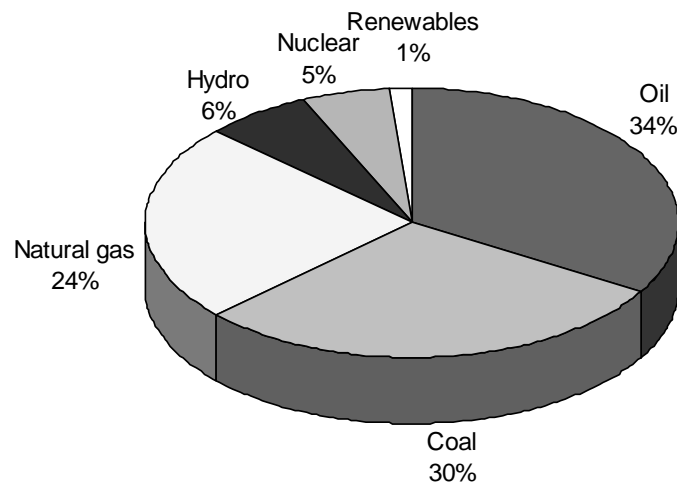


Fig. 1.1: World primary energy consumption in 2010 (BP statistical review of world energy, 2011).

Today, a main concern is that the global growth of the oil demand is starting to outpace the world's oil production. In 2010, the rate of growth of the oil demand was 3.1%, which is higher than the increase in the global oil production by 2.2% (BP statistical review of world energy,

2011). These figures cause concern how we can meet the world's oil demand in the coming years. The official reports state that most of the thirty giant oil fields, accounting for half of the world's oil reserves, are becoming mature and are experiencing a decline in oil production (Babadagli, 2007; Höök et al., 2009). It is estimated that the reserves in sandstone and carbonate fields have respectively around 20 and 80 years of production time left at the current production rates (Montaron, 2008). Moreover, the probability of new oil discoveries to replace the produced reserves has gotten smaller in the last decades (Blaskovich, 2000; Alvarado and Manrique, 2010). The discovery rate of the giant oil fields peaked in the late 1960s and early 1970s, but declined remarkably afterwards (Ivanhoe, 1997). Most likely, new large oil fields will be discovered in deep offshore or in difficult-to-produce or environmentally sensitive areas (e.g., in the Arctic), which eventually will lead to new oil barrels becoming more expensive. These facts have put an emphasis on identifying realistic solutions to meet future world energy demands. Applying enhanced oil recovery (EOR) techniques in the existing fields is indeed a key step to sustain the oil production level.

1.2 Prospects of EOR techniques

Worldwide, oil recovery from the existing fields is on average only one-third of the oil initially in place (OIIP), leaving a large target for application of EOR techniques (Lake, 1989; Green and Willhite, 1998). IEA estimates that EOR techniques could help to unlock 300 billion barrels of oil (IEA, 2005). According to the worldwide EOR surveys of the Oil and Gas Journal (2007) an increase of 1% in the efficiency of global oil recovery could expand conventional oil reserves by 88 billion barrels. EOR techniques are becoming more feasible mainly due to scientific and technological progress as well as increasing interest of governments to boost their oil production because of higher oil prices.

The volume of oil produced by EOR techniques increased considerably from 0.6 MMBD in 1982 to 2.5 MMBD in 2006 (Sandrea and Sandrea, 2007). Most of the world's EOR projects (about 90%) are preformed in four countries: the US (193 projects), Venezuela (49 projects), Canada (39 projects), and China (39 projects) (Moritis, 2010). In the Middle East (ME), the EOR projects have also received attention over the past decade (Al-Mutairi and Kokal, 2011). Currently, there are 11 EOR projects in the ME either on a pilot or a commercial scale. Most of the EOR projects have been performed in Oman where it is expected that EOR contributes one-third of Oman's total oil production by 2016 (Al-Mutairi and Kokal, 2011). Currently, there are 300 active EOR projects worldwide, accounting for about 4% of the daily global oil production (Moritis, 2010). IEA predicts that EOR contribution will grow to about 20% (ca. 25 million barrels per day) by 2030 (Petroleum Economist Magazine, 2010).

1.3 EOR: definition and mechanisms

The production life cycle of a typical oil field is characterized by three main stages: production build-up, plateau production, and production declining. Fig. 1.2 shows a schematic of these three stages. After initial discovery, the oil production rate usually increases in several steps during the field development period, and eventually reaches a plateau. Later the oil field enters the declining production stage, which ends in abandonment once the economical limit is reached. A common practice to improve oil production beyond this natural decline is pressure maintenance, either by expanding the gas cap or aquifer, followed by (or simultaneously) water flooding. However, as these methods approach their own economic limit of operation, a huge amount of initial oil (roughly two-third of oil initially in place) is left in the reservoir. EOR methods are applied to extend the production life cycle of the oil fields and thus to increase the profitable recovery of the remaining oil.

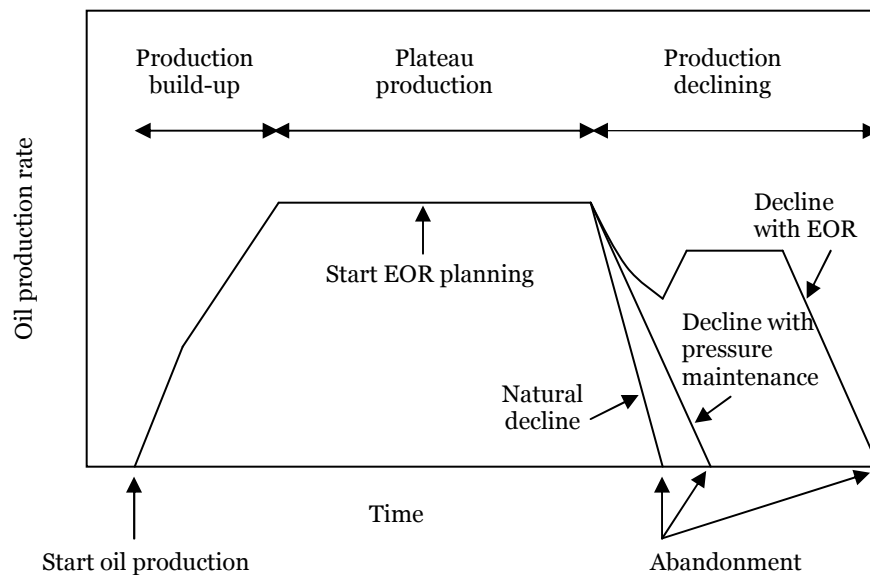


Fig. 1.2: Production life time of a typical oil field (Ali and Thomas, 2000).

EOR is typically defined as oil recovery by the injection of materials not normally present in the reservoir (Lake, 1989). The focus of the process is on the rock-oil-injectant system and on the interplay of capillary and viscous forces. The goal of any EOR process is to mobilize remaining oil. This is achieved by enhancing oil displacement and volumetric sweep efficiencies. Oil displacement efficiency is improved by reducing oil viscosity or by reducing capillary forces or interfacial tension. Volumetric sweep efficiency is improved by developing a more favorable mobility ratio between injectant and oil remaining in the reservoir.

1.4 Gas flooding EOR

One of the most accepted and widely used methods for EOR is gas flooding (Orr, 2007). Fig. 1.3 shows that in 2010 the contribution of gas flooding to the World's EOR oil production was 39%. This is the injection of hydrocarbon (mixture of methane to propane) or non-hydrocarbon (carbon dioxide, nitrogen, flue gas, and even hydrogen sulfide) components into oil reservoirs that have been typically waterflooded to residual oil. The basic mechanism to increase oil recovery by gas flooding is a better microscopic sweep efficiency compared to water flooding, leading to a further reduction in residual oil saturation by gas (Lake, 1989). The mechanisms of enhancing oil recovery by gas flooding are viscosity reduction and swelling of oil phase as well as lowering of interfacial tension between oil and the displacing phase. Gas EOR methods are commonly divided into miscible floods in which the injected gas eventually forms a single phase with oil, and immiscible floods in which only part of the injected gas dissolves in oil. Higher pressure and injection of CO₂ or light hydrocarbons into oil reservoirs containing light components favor miscibility. However, miscibility is hard to achieve with the injection of N₂ or reservoirs with heavy components.

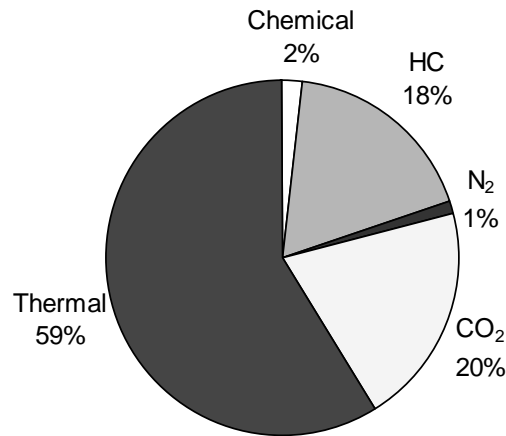


Fig. 1.3: Worldwide EOR oil production in 2010: Contribution of gas EOR methods is 39% (Oil and Gas Journal, 2010).

A major problem associated with any gas EOR process is the adverse mobility ratio (Koval, 1963; Wellington and Vinegar, 1988; Rao, 2001; Farajzadeh et al., 2010). The gas-drive fluids exhibit a very low viscosity compared to water and to crude oil at the reservoir conditions. For instance the viscosity of CO₂ at 2000 psi and 100 °F is about 0.066 cP, which is at least one order of magnitude less than the viscosity of conventional reservoir oils. This low viscosity means that the mobility of the injected gas, which is defined as the ratio of gas effective permeability to its viscosity, is much higher than that of the displaced oil. Because of this unfavorable mobility ratio the displacement front is subject to instability when the injected gas displaces the oil from a reservoir. Instability leads to the growth of gas fingers through the oil, eventually reaching the

production well, and causing premature gas breakthrough. This results in an increase in the costs of the handling of the injected gas as the gas production/recycling volumes increases (Krause et al., 1992). In heterogeneous reservoirs the situation is even worse since highly mobile gas-drive fluids channel selectively through highly permeable streaks rather than efficiently displacing oil (Waggoner et al., 1992; Chang et al., 1993). Another disadvantage of the gas EOR process is the low density of the gas-drive fluids compared to water and oil. This leads to gas segregating at the top of the reservoir and overriding the oil-bearing layers (Rossen and Shen, 2007; Rossen et al., 2010). The above mentioned challenges contribute to a poor volumetric sweep efficiency during the gas EOR process, leading to a large amount of oil remaining untouched.

A common practice to control gas mobility and improve sweep efficiency is water-alternating-gas (WAG) injection (Caudle and Dyes, 1959; Righi et al., 2004). However, field tests and simulation studies (Holm, 1987; Christensen et al., 2001; Andrianov et al., 2011) revealed that WAG provides only a modest mobility control: eventually gravity segregation and viscous instabilities recur, leading to a weak vertical sweep efficiency. Foaming of the injected gas is a potential solution to mitigate the above mentioned challenges in gas EOR processes and also in WAG (Bond and Holbrook, 1958; Fried, 1961; Kovsky and Radke, 1994; Rossen, 1996; Du et al., 2007; Farajzadeh et al., 2009). Foam can drastically reduce the mobility of the gas phase by increasing gas effective viscosity and trapping a large gas fraction inside the porous medium (Bernard and Holm, 1965; Hirasaki and Lawson, 1985). The latter effect leads to gas relative permeability greatly diminishes by blocking some of the gas-flow paths.

1.5 Foam EOR

Foam in porous media is a dispersion of gas in a liquid phase such that the liquid (containing surfactant) is continuous and at least some part of the gas phase is made discontinuous by thin liquid films called lamellae (Hirasaki, 1989). Foam films are stabilized by surfactants adsorbed at the gas-liquid interface (Farajzadeh et al., 2008). When foam films are created in the porous medium, the flow of gas is substantially hindered. The injected gas can sweep reservoir pores that would not be reached in the absence of foam leading to better sweep efficiency (Rossen, 1996; Farajzadeh et al., 2012). Three main methods have been used to generate foam in porous media: gas-surfactant co-injection, surfactant-alternating-gas (SAG) injection, and dissolving surfactant in the injected gas (e.g., supercritical CO₂) (Friedmann and Jensen, 1986; Rossen and Gauglitz, 1990; Chou, 1991; Farajzadeh et al., 2009; Le et al., 2008; Xing et al., 2010).

The application of foam for mobility control was first proposed by Bond and Holbrook (1958). Thereafter, many experimental and modeling studies have been devoted to understand the mechanisms underlying foam mobility control. This has been followed by many successful field

applications where foam has been mainly applied as diverting and mobility-reducing agents, for instance in East Vacuum field in the US (Hirasaki, 1989; Patzek and Koinis, 1990; Hoefner et al., 1995; Patzek, 1996), Oseberg and Snorre fields in the North Sea (Aarra et al., 1996; Skauge et al., 2002). In these applications gas mobility is lowered by a greater factor in the high permeable layers compared to the low permeable ones. The lowered gas mobility diverts at least part of the displacing fluid into the other parts of the reservoir that are less-permeable and have not been swept before. This leads to improvement in both vertical and areal sweep efficiency, and thus to additional oil recovery from the unswept regions.

Until recently, abundant experimental and modeling studies have been devoted to describe the behavior of foam in the absence of oil, but comparatively few studies of foam in the presence of oil have been done. There are still important and unsolved questions regarding the stability of foam and its propagation in the reservoirs containing oil. Available evidence resulting from the bulk foam studies and full-field simulation suggests that the presence of oil can significantly affect the success of foam-flood performance (Low et al., 1992; Wasan et al., 1994, Namdar Zanganeh et al., 2011). In fact, to develop a practical foam process for a given field application where residual oil saturation may vary from zero to 50%, any effect of oil on the behavior of foam generation, propagation, and destruction is an important issue. Notwithstanding the primary importance of oil on foam stability, the existing data in the literature show a controversy about the ability of foam to generate and propagate when oil is present in porous media. While several studies argued that the presence of oil could be detrimental on foam stability (Minssieux, 1974; Jensen and Friedmann, 1987; Svorstøl et al., 1996; Arnaudov et al., 2001; Hadjiiski et al., 2001; Farajzadeh et al., 2012), others supported that relatively stable foam could be formed in the presence of oil (Schramm et al., 1993; Mannhardt et al., 1998; Aarra et al., 2002; Vikingstad and Aarra, 2009; Emadi et al., 2011). It was found that oil saturation must be below a critical value before gas mobility is reduced by foam (Jensen and Friedmann, 1987; Svorstøl et al., 1996; Mannhardt and Svorstøl, 1999), but this has not been supported by other studies where the possibility of generating foam even at relatively high oil saturation was observed (Ali et al., 1985; Farajzadeh et al., 2010; Andrianov et al., 2012). In some studies the type of oil was found not to be crucial for foam generation and propagation; instead the type of surfactant exhibited large effects (Jensen and Friedmann, 1987). This is not in line with other bulk and porous media studies where foaming behavior was found to depend on the combination of surfactant and oil types (Nikolov et al., 1986; Raterman, 1989; Vikingstad et al., 2006).

1.6 Objectives of the thesis

The overall objective of this research is to achieve a better understanding of foam-oil interaction by performing systematic bulk and porous media studies. In fact, the main premise of this thesis is whether immiscible foam can be an EOR method to recover tertiary oil. More specifically, the objectives of this thesis are as follows:

- Identifying surfactants to generate stable foam in the presence of model oils, and examining the effects of surfactant concentration and oil types on the foamability and stability of the bulk foam.
- Investigating the dynamics of foam flow in natural sandstones in the absence of oil, and describing the effects of surfactant concentration and injection velocity on foam mobility and foam propagation.
- Demonstrating that foam undergoes a transition from a weak to a strong state at a characteristic gas saturation and proposing a rheological model to describe foam mobility transition.
- Describing the transient foam flow in an oil-free porous medium using the stochastic bubble population model.
- Studying the behavior of foam flow in the presence of water-flood residual oil and providing the appropriate criteria for generation and propagation of a stable foam.
- Assessing the feasibility of the foam EOR concept as a recovery (not only diverting and blocking) agent and providing the mechanisms by which foam recovers tertiary oil.

1.7 Outline of the thesis

This thesis is based on a number of articles published by the author, describing results in the research area of foam EOR. The thesis consists of eight chapters, starting with Chapter 1 as the introduction.

Chapter 2 deals with a systematic study to investigate foam-oil interaction in bulk. The foaming properties of a selected set of commercially available surfactants used in petroleum industry are investigated. Bulk foam is generated by sparging nitrogen at fixed flow rates through the surfactant solution. Effects of surfactant concentration and oil types on the foam longevity are investigated by measuring foam volume and liquid fraction in the foam. These data are taken to explain the dominating destruction mechanisms during foam generation and decay in the absence and presence of alkane-type oils. The results of this chapter will serve as a basis for studying the surfactants used to do the core-flood experiments.

Chapter 3 investigates the mechanism of foam mobility reduction in natural sandstones porous media in the absence of oil. The C₁₄₋₁₆ alpha olefin sulfonate (AOS) surfactant is used to stabilize

nitrogen foam. Foam is generated by co-injection of gas and surfactant solution at fixed foam quality of 91% at a back-pressure of 20 bar and ambient temperature. X-ray CT scan images are taken during foam propagation to map fluid saturations over time. Effects of surfactant concentration and injection velocity are examined in detail as these are key parameters for controlling foam strength and foam propagation under field conditions. We also show that the existence of a hysteresis in foam mobility when surfactant concentration and injection velocity vary through an increasing-decreasing cycle. We provide a mechanistic description to explain the observed effects along with some remarks about foam propagation over typical inter-well distances.

Chapter 4 demonstrates a relation between foam mobility and gas saturation for foam flow in porous media in the absence of oil. We show that foam undergoes a transition from a weak to a strong state at a certain critical gas saturation, leading to a substantial reduction in foam mobility and water saturation. This finding is verified for foams generated at different surfactant concentrations and core lengths. We describe foam mobility transition in the light of foam rheology where foam is treated as a power-law fluid with a yield stress term. Our analyses provide evidence that foam mobility transition is due to the surge of yield stress above the critical gas saturation. A functional relationship between yield stress and gas saturation is proposed for foam flow in porous media.

Chapter 5 presents a numerical analysis of the transient foam flow, the forward movement of foam until breakthrough time, by using the stochastic bubble population (SBP) model. We describe the SBP foam model in a series of non-linear partial differential equations in saturation, pressure and bubble density. These equations are solved using the IMPES method. We show that the SBP foam model represents the main feature of the transient foam flow by comparing the saturation and pressure data obtained numerically with those obtained from the experiment reported in Chapter 4.

Chapter 6 shows a systematic study of N_2 foam in natural sandstone porous media subject to water flooding. Foam is generated in-situ by co-injection of gas and surfactant solution at different surfactant concentrations. We focus on the concentration effect because it is one of the main physical parameters that directly affects the stability of foam films in the presence of oil. We demonstrate that stable foam can be obtained in the presence of water-flood residual oil for sufficiently high surfactant concentrations. CT scan analyses prove that foam is potentially an efficient EOR method. We show the presence of two oil production regimes for incremental oil recovery by foam-flood EOR.

Chapter 7 presents a further practical insight into the performance of foam EOR by investigating the effects of the following parameters: presence and absence of surfactant pre-flush, injection direction (gravity stable/unstable condition), and core length. We show that foam with surfactant pre-flush provides a better mobility control in the presence of oil. We demonstrate that how gravity stable foam injection in a surfactant pre-flushed core improves the efficiency of gas utilization by reducing the volume of gas required per unit volume of oil produced.

Chapter 8 summarizes the main conclusions of this thesis.

Chapter 2

BULK FOAM STABILITY IN THE ABSENCE AND PRESENCE OF OIL *

Abstract

A systematic laboratory study of foamability and foam stability is reported. Foam was generated by sparging nitrogen gas at a fixed flow rate through the surfactant solution in the absence and presence of alkane-type oils. We first examined the foaming properties of a selected set of commercial surfactants used in the petroleum industry (Dowfax 8390, C₁₂₋₁₅ Enordet, Petrostep SB, and C₁₄₋₁₆ AOS). It was found that C₁₄₋₁₆ AOS exhibits the best foam stability in the presence of oil. Then we characterized the foaming behavior of AOS by varying surfactant concentration and oil types. We measured precisely the evolution of the foam volume and the amount of liquid fraction in the foam. AOS surfactant exhibited a good foamability in the presence of alkanes with different carbon chains. The generated foam decayed in three main stages: first a small and rapid decay in foam volume occurred at early times, followed by a stabilized foam volume extended for a certain period, and then a second decay by which foam volume decreased continuously over a relatively long time to reach its final volume. From the liquid fraction in the foam it was found that the first decay was dominated by gravity drainage, while bubble coalescence played a main role during the second decay. Presence of oil led to AOS foam entering the second decay at an earlier time. The oil destabilizing effect was more pronounced for alkanes with a shorter carbon chain. Foam stability and liquid fraction in the foam increased with surfactant concentration. The obtained results for foam stability in the presence of oil were discussed in terms of the classical entering/spreading coefficient, oil solubilization effect and stability of pseudoemulsion film.

* Submitted to *Colloids and Surfaces A: Physicochemical and Engineering Aspects* (2012).

2.1 Introduction

Foam has been widely used in oil and gas recovery operations as a mobility control and profile correction agent. A brief list of foam applications includes hydraulic fracturing (Blauer and Kohlhaas, 1974), gas blocking (Hanssen and Dalland, 1994), acid diversion during matrix stimulation (Kibodeaux et al., 1994; Behenna, 1995), clean-up of contaminated subsoil (Hirasaki, et al., 1997), and enhanced oil recovery (Li et al., 2008; Guo et al., 2011; Simjoo et al., 2012). The idea of using foam is marked by the drastic lowering of gas mobility, which is essential to improve volumetric sweep efficiency, for instance, during gas flooding of oil reservoirs (Patzek, 1988; Kovscek and Radke, 1994; Schramm and Wassmuth, 1994; Rossen, 1996).

A major concern about the application of foam in oil reservoirs is the stability of foam in the presence of oil. To be effective in achieving good mobility control, it is crucial that foam remains stable when it comes in contact with oil (Ali et al., 1985; Jensen and Friedmann, 1987; Mannhardt et al., 1998; Farajzadeh et al., 2012). The available experimental data both in bulk and porous media present varied results in terms of foam-oil interaction. Some studies report that the generated foam is destabilized by the oil phase (Minssieux, 1974; Schramm and Novosad, 1992; Garrett, 1993; Denkov, 2004). It was suggested that foam stability depends on the composition of the oil phase so that the presence of light components is detrimental to foam stability (Kuhlman, 1990; Schramm et al., 1993). Aveyard et al. (1993) reported that low molecular weight oil dispersed in the surfactant solution reduces the longevity of foam films. Nevertheless, other studies argued that stable foams can be effectively generated in the presence of oil by selecting appropriate foaming agents. Mannhardt et al. (1998) observed that the addition of fluorinated surfactant to different types of hydrocarbon surfactants increases foam tolerance to oil. Nikolov et al. (1986) found that foam stability is enhanced by increasing the hydrophobic chain length of the hydrocarbon surfactants. Suffridge et al. (1989) reported a series of foam flow experiments where foam was generated effectively in porous media and exhibited a higher stability in the presence of oil with a higher molecular weight. This observation has been supported by performing foam column experiments (Vikingstad et al., 2005 and 2006; Andrianov et al., 2012). In this chapter, we present a systematic bulk foam study where the effect of the surfactant and oil type has been examined separately on foamability and foam stability.

The underlying foam stability mechanism in the presence of oil has been mainly discussed in terms of aqueous film thinning due to entry of oil drop (Garrett, 1993), oil spreading on the gas-water interface (Lau and O'Brien, 1988), occurrence of an unstable bridge across the foam film (Garrett, 1980), and stability of pseudoemulsion film (Koczo et al, 1992; Nikolov et al., 1986), which is a thin aqueous film separating the approaching oil drop and gas-water interface. In order

to describe foam stability in the presence of oil we use entering (E), spreading (S) and bridging (B) coefficients. They are defined as follows:

$$E = \sigma_{gw} + \sigma_{ow} - \sigma_{og} \quad (2.1)$$

$$S = \sigma_{gw} - \sigma_{ow} - \sigma_{og} \quad (2.2)$$

$$B = \sigma_{gw}^2 + \sigma_{ow}^2 - \sigma_{og}^2 \quad (2.3)$$

where σ_{gw} is surface tension between gas and water, σ_{ow} is interfacial tension between oil and water, and σ_{og} is surface tension between oil and gas. The ability of oil drop to enter the gas-water interface is a necessary condition to rupture foam lamellae (Robinson and Woods, 1948). If entry condition is favorable (i.e., E is positive) and oil drop is able to exhibit a spreading behavior (i.e., S is positive), the gas-water interface is expected to expand. This expansion results in a thinning of the foam film and eventually the film ruptures (Harkins, 1941). If the spreading condition does not occur (i.e., S is negative) and instead oil drop forms a lens at the gas-water interface, foam film may rupture once oil drop enters both surfaces of the lamella (Garrett, 1980). Under this condition oil drop spans the film by making an unstable bridge (i.e., B is positive). Table 2.1 gives a summary of the foam stability prediction by the sign of the E , S and B coefficients.

Table 2.1: Foam stability prediction by the sign of the E , S and B coefficients.

		E							
		-	+						
S	-	Stable foam	<table border="1"> <thead> <tr> <th colspan="2">B</th> </tr> <tr> <th>-</th> <th>+</th> </tr> </thead> <tbody> <tr> <td>Stable foam</td> <td>Unstable foam</td> </tr> </tbody> </table>	B		-	+	Stable foam	Unstable foam
	B								
-	+								
Stable foam	Unstable foam								
+	Stable foam	Unstable foam							

Note that the above coefficients only determine whether the occurrence of oil entering and spreading is thermodynamically feasible for a specific oil-surfactant system. These coefficients cannot describe the rate at which oil entering and spreading occurs. It is possible that the entering coefficient is positive, but the foam remains rather stable due to the slow rate of oil entering in the interface (Aveyard et al., 1994). According to Koczko et al. (1992) the rate of oil entering depends on the thinning rate of the pseudoemulsion film. They observed a non-entering oil behavior for the system of surfactant-oil used, although both of the entering and spreading coefficients were positive. As the pseudoemulsion film is stable, oil droplets are unable to enter the lamella surface, and thus foam remains stable with oil. However, if the pseudoemulsion film is ruptured, oil

droplets enter the gas-water interface, and foam may breakdown by spreading or bridging processes (Nikolov et al., 1986; Aveyard et al., 1993).

The relation between oil-tolerant foam and stable pseudoemulsion film was also reported for foam flow in porous media. Nikolov et al. (1986) reported that oil droplets are unable to enter gas-water interface provided that a stable pseudoemulsion film is present. Raterman (1989) found that foam destabilization by oil in porous media is primarily dictated by the stability of pseudoemulsion film. The film stability was found to be strongly dependent on the oil-surfactant combination. Manlowe and Radke (1990), by doing a series of visual studies in micro-model, found that rupture of foam lamellae is induced by the collapse of the pseudoemulsion films.

Schramm and Novosad (1990 and 1992) proposed another mechanism for foam stability in terms of oil emulsification and imbibition in the foam structure. The main step of this mechanism is to form small oil droplets by emulsification, which allows oil droplets to move inside the foam structure. A dimensionless parameter, called lamella number (L), was proposed to describe foam stability. It was defined as a ratio of capillary pressure at Plateau borders to the pressure difference across the oil-water interface:

$$L = \frac{\Delta P_c}{\Delta P_R} = \frac{r_o}{r_p} \frac{\sigma_{gw}}{\sigma_{ow}} \quad (2.4)$$

where r_o is the radius of oil drop, and r_p is the radius of the Plateau border. Schramm and Novosad (1990 and 1992) found that the radius ratio was constant ($r_o/r_p = 0.15 \pm 0.01$) for all foams investigated. They defined three types of foam depending on the value of the lamella number (L): type *A* foam for $L < 1$, type *B* foam for $1 < L < 7$, and type *C* foam for $L > 7$. Table 2.2 presents a summary of the foam stability prediction by the lamella number theory.

Table 2.2: Foam stability prediction by the lamella number theory.

Type of foam	Foam stability to oil	<i>E</i>	<i>S</i>
<i>A</i>	Quite stable foam	negative	negative
<i>B</i>	Moderately stable foam	positive	negative
<i>C</i>	Quite unstable foam	positive	positive

The objective of this chapter is to gain better insight into the foam-oil interaction. First, foamability and foam stability in the absence and presence of alkane-type oils are investigated for a selected set of commercial surfactants used in the petroleum industry. Then the effects of surfactant concentration (0.1, 0.5 and 1.0 wt%) and oil type (n-C₆, n-C₁₀, and n-C₁₆) on the foam longevity are examined by performing well-controlled foam column experiments. This chapter proceeds with materials and methods. Next, the results of foam column experiments are

presented. Then foam-oil interaction is discussed in terms of classical entering/spreading coefficient, oil solubilization effect and stability of pseudoemulsion film. Then the main conclusions of this study are drawn.

2.2 Experimental description

2.2.1 Materials and methods

A total of four commercial surfactants were used to do the experiments: C₁₄₋₁₆ AOS (C₁₄₋₁₆ alpha olefin sulfonate, Stepan), Petrostep SB (cocoamido propyl hydroxysultaine, Stepan), Dowfax 8390 (alkyldiphenyloxide disulfonate, DOW), and Enordet (C₁₂₋₁₅ alcohol-7EO-sulfonate, Shell). They will be referred as AOS, SB, Dow, and Enordet. All surfactants were used as received without further treatment. The surfactant solution was prepared using brine containing 0.5 M sodium chloride (NaCl, Merck) in de-ionized water (pH=6.8±0.1). The surfactant concentrations are based on the active content and are well above the critical micelle concentration (c.m.c.). Nitrogen gas with a purity of 99.98% was used to generate foam. Three model oils were used to investigate the effect of oil on foam stability: normal hexane (n-C₆, Sigma-Aldrich), normal decane (n-C₁₀, Sigma-Aldrich), and normal hexadecane (n-C₁₆, Sigma-Aldrich). For some of the experiments 50 ppm of red dye (oil red O, Sigma-Aldrich) was added to the oil phase to visualize the oil droplets in the foam column. Preliminary tests, including surface tension measurement and foam column, were done to ensure no influence of the dye on the foaming behavior.

2.2.2 Experimental set-up

The foaming properties of the surfactant solutions were studied by using two set-ups providing visual observation and measurement of foam volume. The first set-up (Fig. 2.1) consisted of a conventional glass column with a length of 55.0 cm and inner diameter of 4.0 cm, fitted with a porous glass frit (Robu) placed at the base of the column. To provide nitrogen at a constant flow rate the gas supply equipped with a pressure regulator (KHP Series, Swagelok) was connected to the base of the column by using a mass flow meter (Sierra). Foam was generated by sparging gas at a flow rate of 20±1 cm³/min through the surfactant solution via the porous glass frit. The static foam stability was investigated by recording the height of foam above the liquid phase as a function of time.

The second set-up (Fig. 2.2) was the Foamscan instrument (IT Concept, France). It was used to characterize the foaming properties of the selected surfactant obtained from the screening study. Foam was generated by sparging nitrogen gas through a porous glass frit in a fixed amount of surfactant solution (50±1 cm³) and at a fixed gas flow rate of 16±1 cm³/min. The gas flow stopped automatically when foam volume reached a preset value of 150 cm³. Foam volume during generation and decay stages was determined by a CCD camera. The amount of liquid volume in

the foam was measured by conductivity measurements at the different heights of the foam column. A pair of electrodes at the bottom of the column was used to measure the amount of liquid, which was not present in the foam.

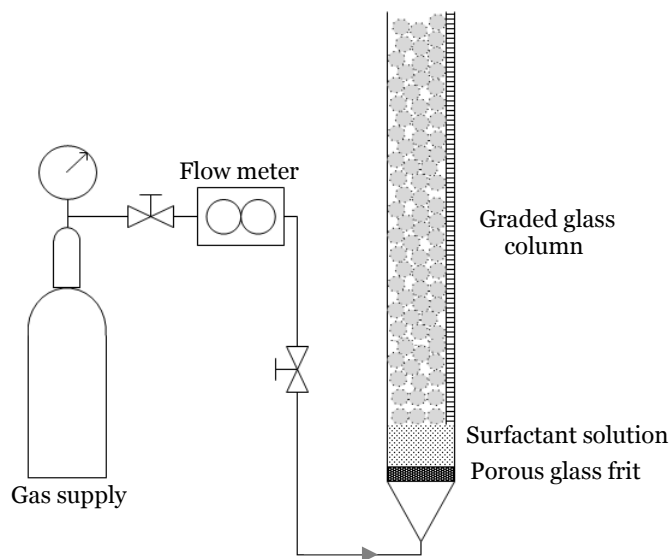


Fig. 2.1: Schematic of the foam column set-up used for surfactant screening study. Foam was generated by sparging gas through the surfactant solution via the porous glass frit.

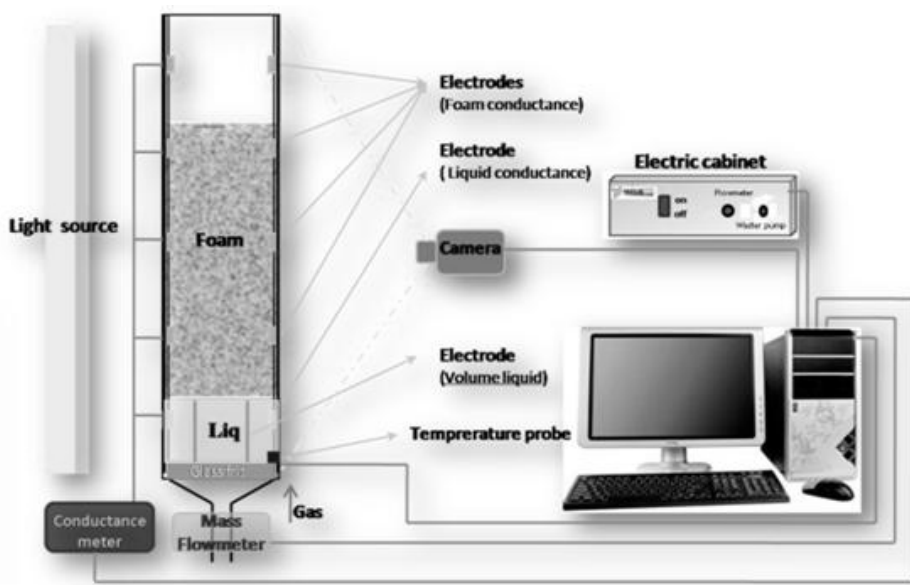


Fig. 2.2: Schematic of Foamscan set-up. Foam volume was determined by the camera. The amount of liquid volume in the foam was obtained from the conductivity data.

We measured the following parameters in the Foamscan set-up: foam volume generated during gas sparging (foamability part), decay of foam volume after gas sparging (foam stability part) and also the amount of liquid volume in the foam structure. The foamability of the surfactant

solutions was described by the foam capacity (FC) and foam maximum density (MD) coefficients. The FC coefficient is the ratio of foam volume at the end of gas sparging to the total gas volume injected. When the generated foam is stable, the FC coefficient is higher than unity. When the generated foam is not stable during the foaming process, the FC coefficient is less than unity, meaning that part of the injected gas has not been retained in the foam column. The MD coefficient was used to characterize the liquid retention in the generated foam and defined as a ratio of the liquid fraction in the foam to the final foam volume.

For the foam column experiments in the presence of oil, 5.0 vol% of oil was introduced into the surfactant solution before gas sparging. The amount of oil was calculated as a volume fraction of the surfactant solution. All foam tests were performed at least twice under the ambient temperature (21 ± 1 °C) and atmospheric pressure.

The surface and interfacial tensions were measured by a KSV Sigma tensiometer using the DuNouy ring method. The gas above oil and water was air. To measure the interfacial tension the oil phase and surfactant solutions were not pre-equilibrated with each other. The measurements were conducted for a sufficiently long time to obtain a constant value. All the measurements were performed at ambient temperature (21 ± 1 °C) and atmospheric pressure.

2.3 Results and discussion

2.3.1 Surfactant screening

Fig. 2.3 shows the half decay time ($t_{1/2}$) of foam columns generated using the four selected surfactants in the absence and presence of n-hexadecane. The $t_{1/2}$ refers to a time at which the height of the foam column reaches half of the initial value. It correlates with the foam stability such that a longer $t_{1/2}$ corresponds to more stable foam. Since foam was generated in a similar way for all experiments, difference in the foam stability depends essentially on the type of surfactant used, and also on the absence or presence of oil. In the absence of oil, the SB surfactant exhibited the most stable foam with a $t_{1/2}$ longer than 600 minutes. The foam column generated by Dow surfactant obtained the least stable foam with a very short $t_{1/2}$ of only about 15 minutes. The surfactants can be ranked in terms of their $t_{1/2}$ as follows: SB > AOS > Enordet > Dow. In the presence of oil, the half decay times are systematically lower than in the absence of oil for all the surfactants. This indicates that the oil phase, at the volume fraction used, diminishes the stability of the foam columns. However, the effect of oil on foam stability depends strongly on the surfactant-type. The SB foam, the most stable in the absence of oil, was largely influenced by the oil phase: its $t_{1/2}$ in presence of oil is 20 times smaller than that in absence of oil. This shows that very stable foam in the absence of oil does not necessarily imply an equally stable foam in the presence of oil. Once again Dow surfactant exhibited the least stable foam with a very short $t_{1/2}$,

which hardly exceeds 10 minutes. Among the surfactants used, AOS foam was the most stable one in the presence of oil: $t_{1/2}$ of AOS foam decreased by a factor of four compared to that in the absence of oil.

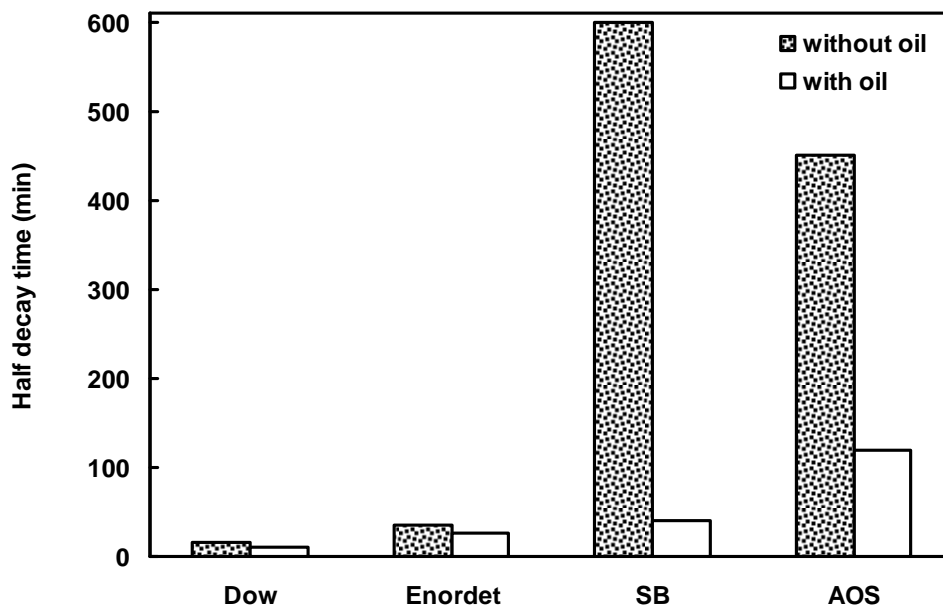


Fig. 2.3: Half decay time for different surfactants in the absence and presence of oil. Surfactant concentration was fixed at 0.5 wt%. The oil phase was n-hexadecane at 5.0 vol%.

2.3.1.1 Foam decay

In order to inspect how surfactant type and presence of oil influence foam stability, foam decay was monitored by imaging foam columns at different times. These images provide insight about the foam texture when the foam column enters the decay regime. Below we present the images for the foams stabilized by AOS and Dow surfactants, which are respectively the most and the least stable foam in the presence of n-hexadecane.

Fig. 2.4 shows snapshots of the foam columns generated by 0.5 wt% AOS and Dow surfactants in the absence of n-hexadecane. For AOS foam (left image) after gas sparging was terminated, the foam column persisted for a long time as noticed by a long $t_{1/2}$ in Fig. 2.3. AOS foam was characterized by fine bubbles and a fairly uniform bubble size distribution. However, the snapshot of Dow foam (right image) clearly reveals a different foam texture. Soon after the end of gas sparging, the foam column entered the decay regime. The texture of Dow foam was characterized by a broad bubble size distribution and with larger bubble sizes. By comparing AOS and Dow images one can infer that bubble coalescence was more significant for Dow foam, resulting in much faster collapse of the foam column. This is consistent with a very short $t_{1/2}$ for Dow foam in Fig. 2.3.

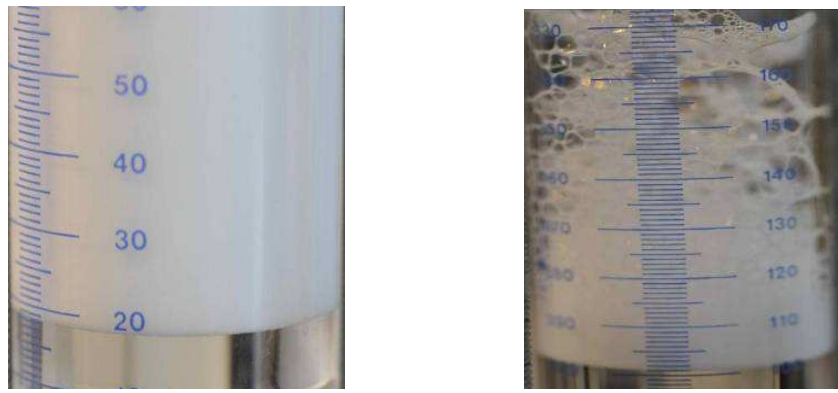


Fig. 2.4: Foam column stabilized by AOS (left) and Dow (right) surfactants in the absence of oil.

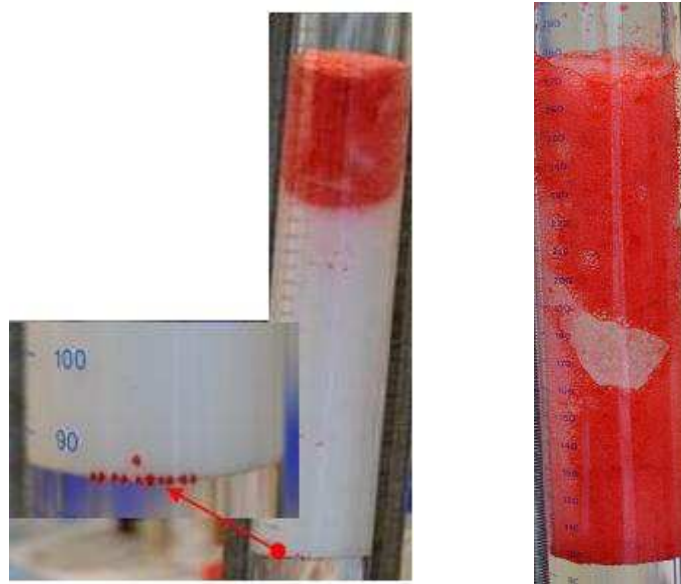


Fig. 2.5: Foam column stabilized by AOS surfactant in the presence of n-hexadecane. The oil phase was colored red. The left image was taken at the early time of the foam decay and the right one was taken at the later time.

Fig. 2.5 shows two snapshots taken at the early (left image) and later time (right image) of the decay of AOS foam in the presence of n-hexadecane. The oil phase was colored red. AOS surfactant created stable foam, carrying almost all the initial oil upward, and leading to a fairly uniform oil distribution in the top of the column (left image, Fig. 2.5). At the early time after stopping gas sparging, the texture of AOS foam was characterized by a rather narrow bubble size distribution. The initial height of the foam column remained unchanged until the column entered the decay regime. The decay of AOS foam was followed by coalescing bubbles at the apex of the column leading to a local change in the foam texture. The latter effect manifests itself by a wider bubble size distribution. This hints at a higher coalescence rate at the upper part of the column. However, the coalescence rate was not such that AOS foam would collapse completely, as the

foam column persisted for a long time (see the $t_{1/2}$ of AOS foam in presence of oil, Fig. 2.3). The resulting change in the foam texture led to redistribution of oil in the foam column. The redistribution itself may cause local accumulation of the oil phase, thereby leading to different coalescence rates at different parts of the foam column. This can be seen in the right image of Fig. 2.5 where a non-uniform oil distribution induced a local catastrophic coalescence in the middle of the column. It results in very large bubbles, and eventually a foam pattern with large gaps in its middle.

Fig. 2.6 shows the foam column generated by Dow surfactant in the presence of n-hexadecane. The generated foam was not as efficient as AOS foam to transport the oil phase. Dow foam carried only about half of the initial oil. The carried oil phase was in the form of oil droplets and spread in the different parts of the column. Soon after generating foam, the oil droplets performed like nuclei from which the foam structure collapsed. The poor stability of Dow foam in the presence of n-hexadecane is consistent with a short half decay time of about 10 minutes (see Fig. 2.3).

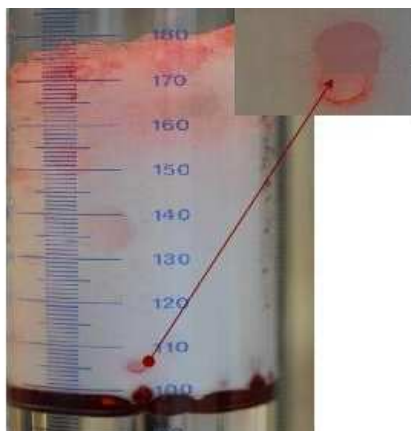


Fig. 2.6: Foam column stabilized by Dow surfactant in the presence of n-hexadecane.



Fig. 2.7: Distribution of n-hexadecane (red parts) inside AOS foam structure.

The different decay behavior of AOS and Dow foams is also reflected in the amount of oil drained from the foam during decay. As the foam column enters the decay regime, the oil phase was drained out of the foam structure and formed an excess oil layer between the aqueous phase and foam column. The amount of excess oil collected from Dow foam was higher compared to that from AOS foam at which most of the initial oil stayed within the foam structure. The amount of excess oil collected from AOS foam was about $12 \pm 2\%$ of the initial oil volume when the column reached the half decay time. Fig. 2.7 shows that how the oil phase with red color is distributed inside the AOS foam structure. The oil phase is mostly accumulated in the Plateau borders. This oil accumulation indicates that AOS foam films were strong enough to allow oil droplets to migrate from foam films toward the Plateau borders.

2.3.1.2 Entering, spreading and bridging coefficient and lamella number

In this section we examine the effect of surfactant type on the foam-oil interaction by calculating entering E , spreading S , and bridging B coefficients as well as lamella number L as given in Table 2.3. Note that these analyses provide insight about foam stability in the presence of oil, and not about the foamability of the surfactants. All of the coefficients depend on the interfacial and surface tension, and thus care should be taken for the accurate measurement of these quantities. As shown in Table 2.3, all the surfactants exhibit a positive E coefficient, indicating favorable conditions for n-hexadecane to enter the gas-water interface. Thus the foam stability depends on the magnitude and sign of the spreading S and bridging B coefficients. Among the surfactants used, Dow provides the largest positive S and B coefficients. This indicates that Dow foam should be unstable in the presence of n-hexadecane, in very good agreement with the observed decay behavior in Figs. 2.3 and 2.6.

Table 2.3: Entering, Spreading, and Bridging coefficients and Lamella number for different surfactants in the presence of n-hexadecane. Surfactant concentration was fixed at 0.5 wt%.

Surfactant	E (mN/m)	S (mN/m)	B (mN/m) ²	L (-)
Dow	24.7	2.5	1026.3	0.5
Enordet	0.2	-1.0	-20.6	6.5
SB	11.0	0.2	356.2	0.9
AOS	3.2	0.2	98.7	2.9

Among the surfactants used, Enordet exhibits a negative value for both of the S and B coefficients. Thus from the theory it follows that oil spreading does not occur along the gas-water interface and Enordet foam films are expected to be stable. However, the theory prediction is not in line with the observed results of the foam column, which shows that stability of Enordet foam is significantly reduced due to the presence of n-hexadecane (see the corresponding $t_{1/2}$ in Fig. 2.3).

For SB and AOS both of the S and B coefficients are positive. The S coefficient of these surfactants is slightly positive, but the magnitude of the B coefficient for SB is more than twice that for AOS. Thus it can be inferred that AOS foam is more stable than SB foam, in a good agreement with the measured $t_{1/2}$ in Fig. 2.3.

Foam stability can be examined further by comparing the value of lamella number. Dow and SB surfactants exhibit a lamella number less than unity, which corresponds to type A foam. According to Table 2.2, type A foam is a very stable foam in the presence of oil with a negative E coefficient. However, this is not in line with the calculated E and S coefficients in Table 2.3, and also not with the observed foam stability in Fig. 2.3, particularly for Dow, which was rather sensitive to the oil phase. For Enordet and AOS surfactants lamella number predicts type B foam, which is characterized by a moderate stability to oil and with a positive E and negative S coefficients. For Enordet, this prediction is consistent with the calculated E and S coefficients. However, it is not in agreement with the observed low foam stability (see Fig. 2.3). For AOS, however, if one would discount a negative S coefficient in the definition of type B foam with a slightly positive value ($S_{AOS} = 0.2$), AOS foam stability can be correlated with the predicted lamella number.

2.3.2 AOS foam stability

In accordance with the surfactant screening study AOS foam exhibited the largest oil-tolerance. Thus in the following section we will focus on this surfactant, and investigate its foaming behavior in detail by varying surfactant concentrations and using different alkane-type oils. First, we will examine the AOS foaming behavior at 0.5 wt% in the absence and presence of n-hexadecane as prototypical experiments. Then the stability of AOS foam will be addressed for different concentrations and oil types.

2.3.2.1 Baseline foaming

2.3.2.1.1 Foam development and decay in the absence of oil

Fig. 2.8 shows the variation of foam volume as a function of time for 0.5 wt% AOS in the absence of oil. During gas sparging AOS foam grows linearly with time, indicating a stable build-up of foam volume. This is inferred from a straight line in the foam volume profile as shown in the inset in Fig. 2.8. Thus AOS foam evolution is expected not to be influenced by the destruction processes such as gravity drainage, coalescence, and Ostwald ripening during foaming stage (Weaire and Hutzler, 1999). After gas sparging is finished, AOS foam enters the decay regime. Foam decay is characterized first by a small and rapid reduction in foam volume followed by a fairly long persistency time during which foam volume remains fairly constant. This pseudo-plateau foam

volume is followed by a second decay regime by which foam volume decreases continuously over a long period, and eventually reaches a finite value of $60 \pm 1 \text{ cm}^3$ after 460 minutes.

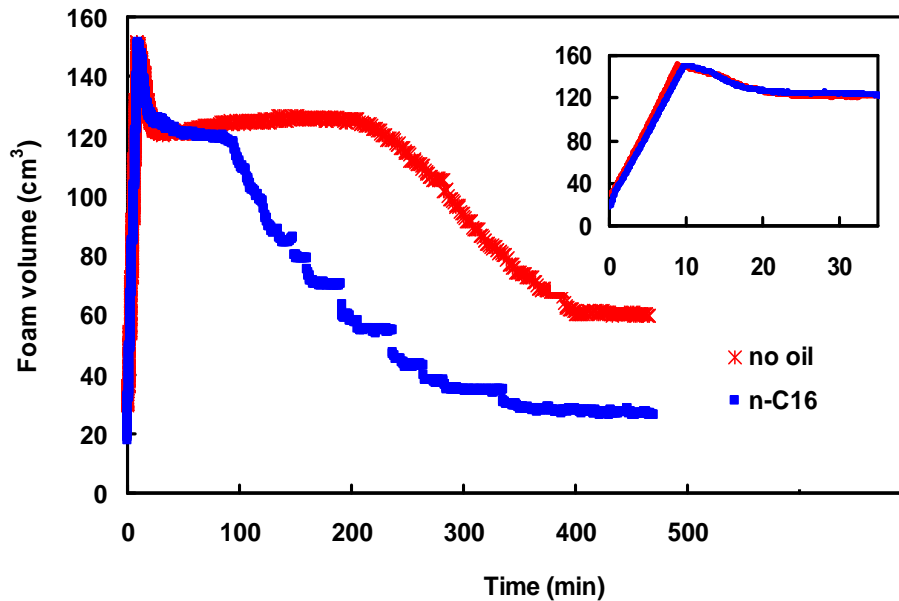


Fig. 2.8: Foam volume as a function of time for 0.5 wt% AOS foam in the absence and presence of n-hexadecane.

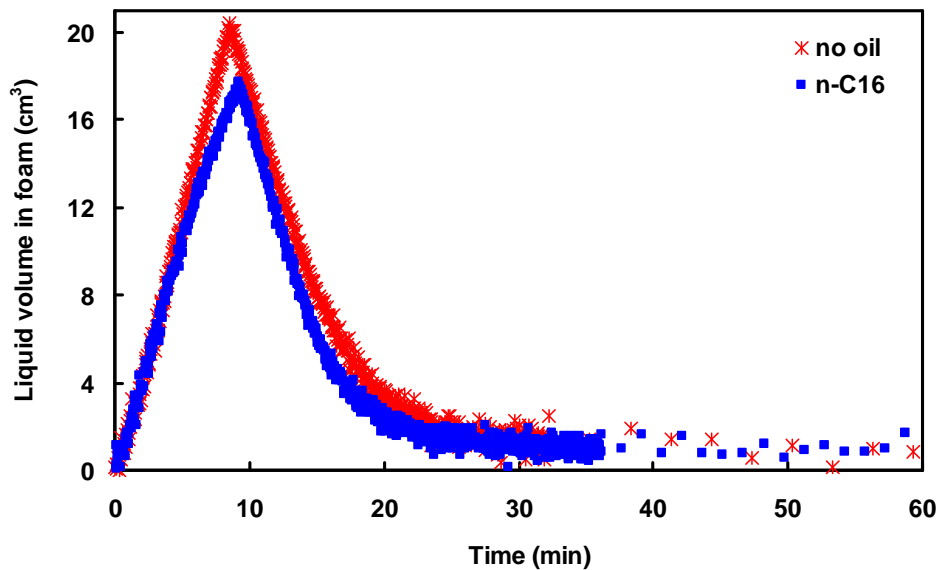


Fig. 2.9: Liquid volume in the foam as a function of time for 0.5 wt% AOS foam in the absence and presence of n-hexadecane.

To gain further insight into the dominating destruction mechanisms during foam development and decay, the overall liquid volume in the foam, V_l , was measured. The V_l profile is shown in Fig. 2.9 for AOS foam in the absence of oil. The foaming part is described by a monotonic increase in the V_l profile, confirming a stable foam development. However, as soon as gas sparging stops, the

V_l starts decreasing. The decreasing trend is characterized by a steep reduction in the V_l over the early time followed by a practically stabilized value for the rest of the measurement. Comparing V_l profile with foam volume (inset in Fig. 2.8) over the early time after stopping gas sparging shows that the rate of liquid drainage in the foam is consistent with the rate of foam decay. This reveals that gravity drainage is a dominating destruction mechanism during the initial foam decay. A close examination of the V_l profile shows that about 93 ± 2 % of the initial liquid has been drained out of the foam structure after 30 minutes. Beyond this time, the remaining liquid obtains a small finite value at around 1.0 ± 0.2 cm³. The rate of liquid drainage, which corresponds to the slope of the V_l profile, also becomes practically zero after 30 minutes. These observations hint that gravity drainage cannot play a dominating role to destruct the foam column beyond 30 minutes. This is also in line with the evolution of foam volume in Fig. 2.8 where after the initial decay the foam volume approaches a constant value of 125 ± 1 cm³. Thus one can infer that for the long time when the foam column enters the second decay regime, the foam destruction mechanism cannot be described by gravity drainage, but has to be related to bubble coalescence and Ostwald ripening. The latter mechanism plays a significant role in foam destruction if the generated foam exhibits a broad bubble size distribution, which means that the generated foam is inhomogeneous (Kabalnov and Shchukinb, 1992; Weaire and Hutzler, 1999; Tcholakova et al., 2011). However, visual inspection during gas bubbling emerging from the porous glass frit revealed a fairly uniform bubble size distribution, and most likely lower contribution of Ostwald ripening for the foam destruction.

2.3.2.1.2 Foam development and decay in the presence of oil

The effect of oil on the AOS foam volume is shown in Fig. 2.8. The corresponding foaming part is similar to what has been observed for the foam in the absence of oil. However, for AOS foam in the presence of oil there is a slight delay to reach the preset volume. This could already be an indication that oil favors foam decay. Fig. 2.8 also shows that the behavior of the foam decay in the presence oil is qualitatively similar to that in the absence of oil, but differs in several details. Similarly to the case of no oil, after the first decay regime the foam volume levels off to a plateau. However, the persistency time of this plateau is significantly shorter in the presence of oil: 198 minutes for the foam without oil compared to 73 minutes for the foam with oil. This indicates that AOS foam in the presence of oil enters the second decay much earlier. Fig. 2.8 also shows that the residual foam volume, i.e. the remaining foam volume at the end of the second decay regime, depends on the presence of oil. Without oil the residual foam volume is 60 ± 1 cm³, while in the presence of oil it hardly exceeds 30 ± 1 cm³.

To examine the destruction mechanisms on AOS foam when oil is present, we plotted the V_l as a function of time (Fig. 2.9). Let us first consider the foaming part. The V_l increases monotonically in a way similar to the foam in the absence of oil. However, for the foam with oil, the slope of the V_l profile decreases slightly near the end of gas sparging. The maximum value of V_l is also shifted to a higher sparging time. This is consistent with a longer time needed to create the preset foam volume in the presence of oil as already shown in the inset of Fig. 2.8. As AOS foam enters the decay regime, first the V_l decreases significantly with a slope of $1.8 \pm 0.1 \text{ cm}^3/\text{min}$ so that after 20 minutes more than $88 \pm 2\%$ of the initial liquid is drained out of the foam structure. Then the decreasing trend continues with a much slower rate at which after 30 minutes the V_l reduces only by $6 \pm 2\%$. Beyond this time, the V_l approaches a practically constant value of $0.8 \pm 0.2 \text{ cm}^3$. These results show that during the initial foam decay gravity drainage is a dominating foam destruction mechanism. This is supported by a rapid reduction in the foam volume by $17 \pm 1\%$ of the preset value after 30 minutes as shown in the inset of Fig. 2.8. However, beyond this time the amount of liquid drainage is not that much to influence the foam decay. Thus, gravity drainage is not a dominating mechanism and instead bubble coalescence becomes important to affect foam volume at the later times (second foam decay regime). As shown in Fig. 2.8, for the second decay regime presence of oil promotes a higher bubble coalescence rate, which in turn causes a quicker and also further reduction in foam volume. This is in line with a smaller half decay time for AOS foam with oil (155 minutes) compared to that without oil (314 minutes). Larger bubble coalescence for foam in the presence of oil is also supported with the results of single foam film studies (Bergeron and Radke, 1995).

2.3.2.2 Effect of surfactant concentration

This section is concerned with the effect of surfactant concentration (0.1, 0.5, and 1.0 wt%) on the AOS foaming properties. Let us first examine the effect of surfactant concentration on AOS foamability using foam capacity (FC) and foam maximum density (MD) coefficients. Fig. 2.10 shows the FC coefficient as a function of AOS concentration in the absence and presence of n-hexadecane. For all generated foams the FC coefficient is higher than unity even for the foam stabilized by a low surfactant concentration of 0.1 wt%. The FC coefficient for foam in the presence of oil is systematically lower than that in the absence of oil. The difference in the FC coefficients can be attributed to the gas sparging time. As shown in the inset of Fig. 2.8, for the foam in the presence of oil a slightly longer sparging time is required to reach the preset volume. This implies injection of a larger volume of gas, and thus a smaller value of the FC coefficient. Recall that the FC coefficient was defined as a ratio of foam volume at the end of gas sparging, i.e. the preset foam volume, to total gas volume injected.

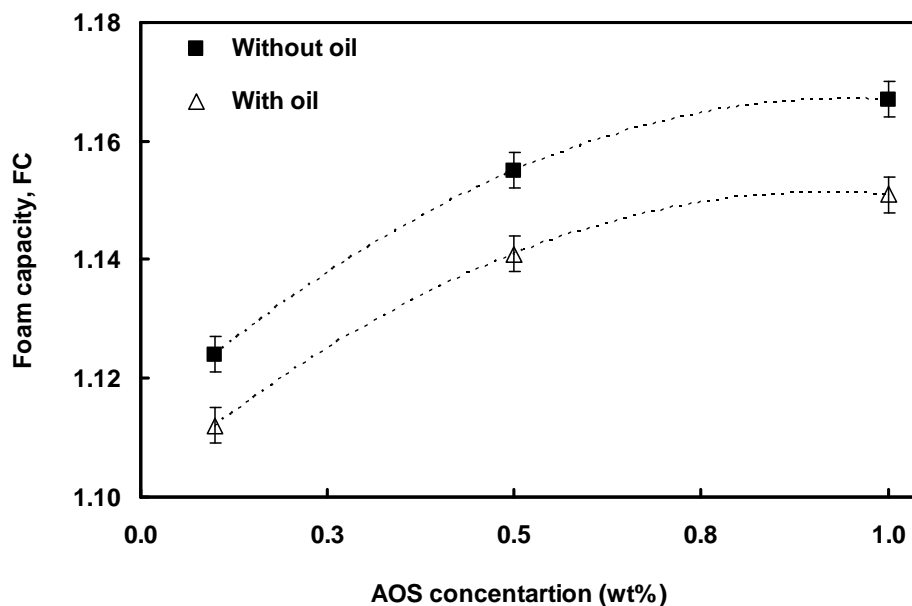


Fig. 2.10: Effect of AOS concentration on the foam capacity in the absence and presence of n-hexadecane.

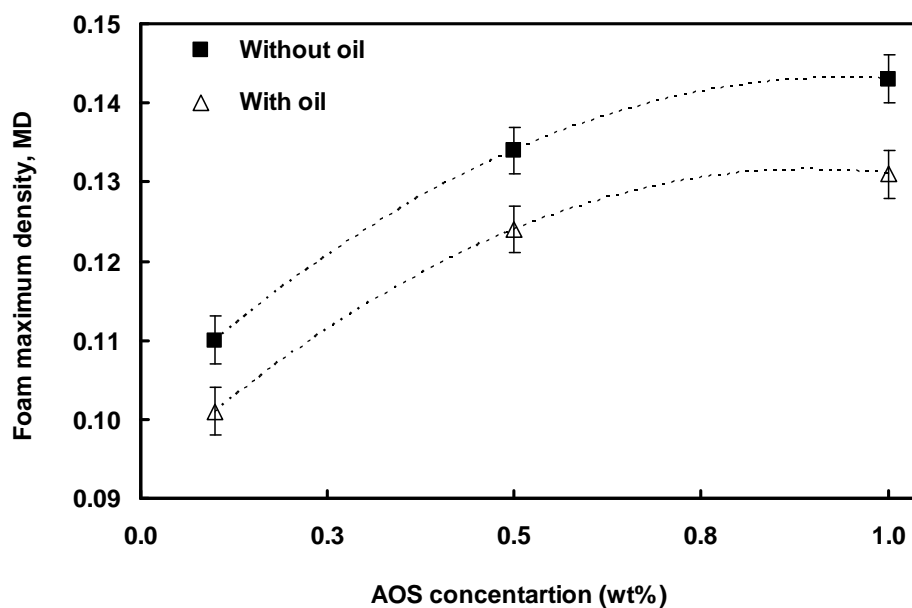


Fig. 2.11: Effect of AOS concentration on the foam maximum density in the absence and presence of n-hexadecane.

Fig. 2.11 shows the MD coefficient of freshly generated foams as a function of AOS concentration in the absence and presence of n-hexadecane. The MD coefficient increased with surfactant concentration: the effect is more pronounced as concentration increases from 0.1 to 0.5 wt%. The MD coefficient for the foam in the absence of oil is larger than that in the presence of oil. The variation of the MD coefficient with respect to surfactant concentration and presence of oil can be interpreted by considering the size of bubbles in the foam. As surfactant concentration increases,

the generated foam has finer texture, i.e., smaller and denser bubbles. This is in line with larger volumes of foam generated at higher surfactant concentration as shown by the FC coefficient in Fig. 2.10. Thus by increasing surfactant concentration more foam is generated and the amount of liquid volume in the foam increases. The above observations are supported by the previous studies (Koehler et al., 2000; Theander and Pugh, 2003, Saint-Jalmes et al., 2005; Sanchez & Patino, 2005; Marinova et al., 2009) which reported formation of foam with finer texture and increase in foam wetness with increasing surfactant concentration. A lower MD coefficient in the presence of oil can be attributed to the fact that part of surfactant molecules are adsorbed on the oil-water interface, and thus the amount of available surfactant for stabilizing foam may decrease (Aveyard et al, 1993). The reduction of surfactant leads to coarser bubble size, which, in turn, results in a lower liquid volume in the foam compared to the foam without oil (Fig. 2.11).

To examine the effect of surfactant concentration on the stability of AOS foam, we plotted half decay time, $t_{1/2}$, as shown in Fig. 2.12. In the absence of oil the $t_{1/2}$ is nearly the same ($t_{1/2} = 345 \pm 10$ min) for the three surfactant concentrations investigated. In the presence of oil the $t_{1/2}$ is systematically lower, and it increases with surfactant concentration. AOS foam with 0.1 wt% concentration exhibited the least stability, characterized by a reduction in the $t_{1/2}$ by a factor of three as compared to the foam with no oil. However, for the 0.5 and 1.0 wt% foams the $t_{1/2}$ was almost twice lower than the foams in the absence of oil. This indicates that the oil phase reduces foam longevity, but at different degrees, depending on the surfactant concentration.

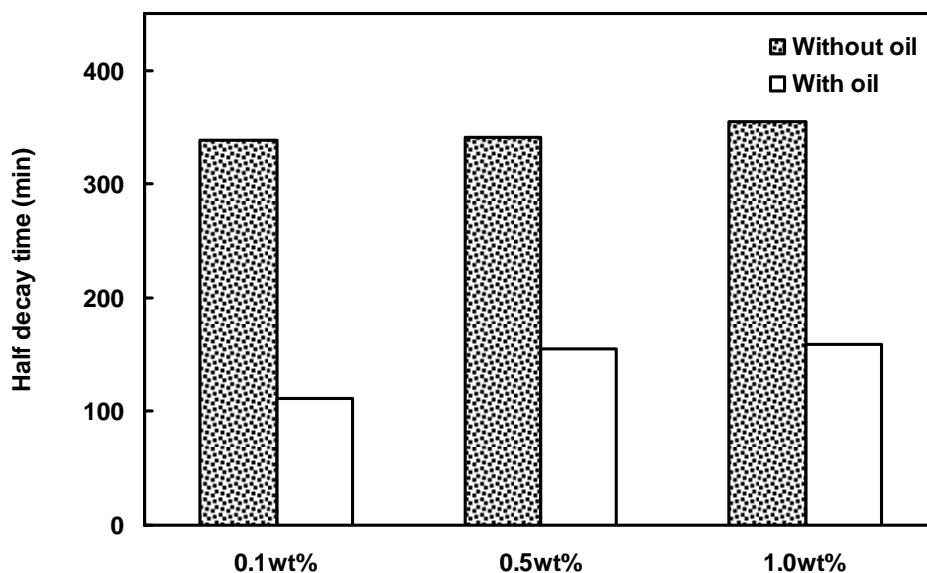


Fig. 2.12: Effect of AOS concentration on the foam half decay time in the absence and presence of n-hexadecane.

2.3.2.3 Effect of oil type

In this section we investigate AOS foaming properties in the presence of alkanes with different hydrocarbon chain lengths, namely n-C₆, n-C₁₀, and n-C₁₆. The surfactant concentration was fixed at 0.5 wt%. The inset in Fig. 2.13 shows that AOS foam volume grows linearly with time with the same slope for the oils investigated and reaches the preset volume in 9 ± 1 min. This behavior is qualitatively similar to that for AOS foam in the absence of oil in Fig. 2.8. Accordingly, the linear rise of foam volume indicates that foam decay processes are negligible during gas sparging.

The generated foams enter the decay regime soon after stopping gas sparging. The overall trend of the foam decay is rather similar for different oils, but it varies considerably in details depending on the type of oil used. First, foam volume diminishes steeply to a plateau slightly lower than the initial volume (125 ± 1 cm³). After a certain time, foam enters a second decay regime leading either to a finite volume or a complete foam breakdown (Fig. 2.13).

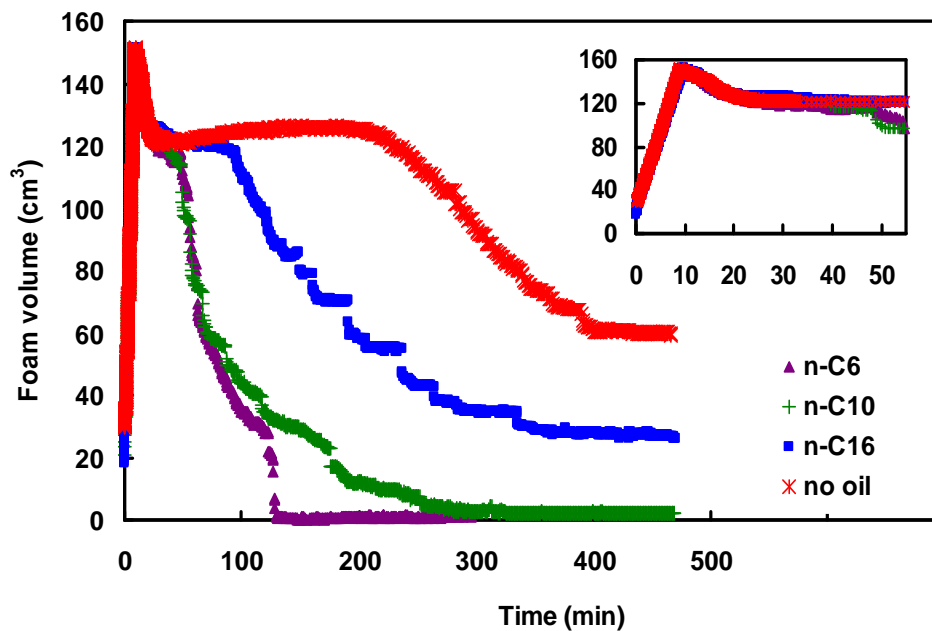


Fig. 2.13: Effect of oil type on the AOS foam volume. AOS concentration was fixed 0.5 wt%. The amount of oil introduced into the surfactant solution was 5.0 vol%.

A close look at Fig. 2.13 shows that the first foam decay is similar for the oil types investigated. However, the effect of oil type on foam stability is more evident after the initial decay. As shown in Fig. 2.14, the persistency time for AOS foam in the presence of n-C₆ and n-C₁₀ is three times smaller than that in the presence of n-C₁₆. Therefore, n-C₆ and n-C₁₀ cause to AOS foam enters sooner the second decay regime. The rate of the second decay is also oil-dependent: 1.5 cm³/min for n-C₆, 1.4 cm³/min for n-C₁₀ and 0.7 cm³/min for n-C₁₆. Accordingly, AOS foam in the presence of n-C₆ exhibits the least stability and the foam column is completely destroyed after 130 minutes

(Fig 2.13). However, for the other two oils, foam volume obtains a finite value after 130 minutes: 29 cm³ for n-C₁₀ and 79 cm³ for n-C₁₆.

To describe the dominating destruction mechanisms in the presence of different oils we rely on the liquid volume in the foam. Similar to Fig. 2.9, at the end of the first decay regime only a small amount of the liquid (less than 5.0±0.2%) remains in the foam for the oil types investigated. This once again reveals that the initial foam decay is caused mainly by gravity drainage. However, for the second foam decay the role of bubble coalescence is more important. As shown in Fig. 2.14, the type of oil influences the rate of bubble coalescence: the shorter the chain length of the alkane, the higher the coalescence rate, and consequently a smaller $t_{1/2}$. The $t_{1/2}$ of AOS foam in the presence of n-C₆ is three times smaller than that in the presence of n-C₁₆.

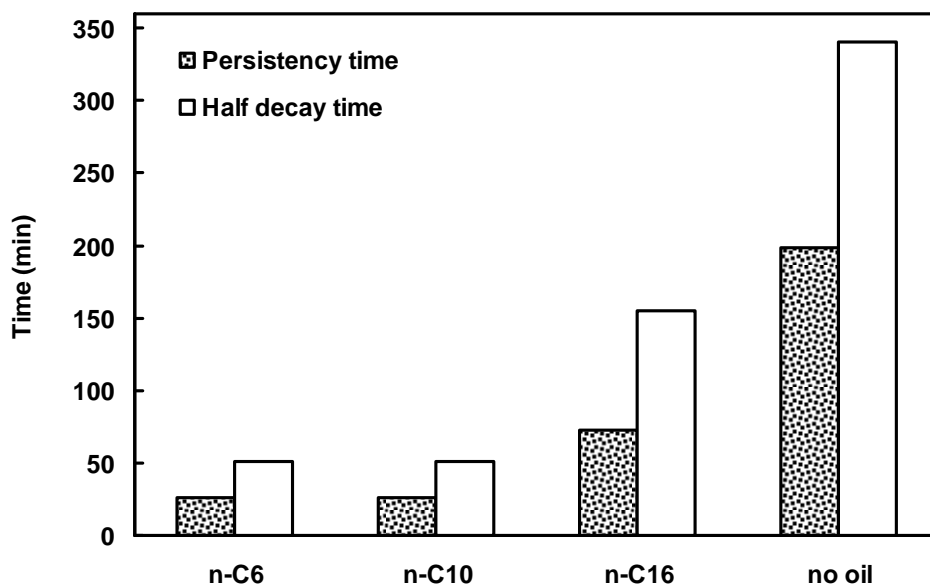


Fig. 2.14: Effect of oil type on the foam persistency and half decay time. Surfactant concentration was fixed at 0.5 wt%.

In order to further examine the interaction between AOS foam and different alkane-type oils, the entering E and spreading S coefficients were calculated. These data along with the bridging B coefficient and the lamella number (L) are presented in Table 2.4. Both of the E and S coefficients are positive for the alkanes investigated. This means that the oil phase is able to enter the foam films and then spread over the gas-water interface. The spreading coefficient is larger for the alkane with a shorter chain length, corresponding to a higher tendency of the oil phase to destabilize foam. This is further supported in the fact that the bridging coefficient increases as the alkane chain length decreases. AOS foam in the presence of n-C₆ exhibits the largest bridging coefficient, which is in line with a higher potential of n-C₆ to make an unstable bridge across the

foam films. The foam-oil interaction can also be interpreted in terms of the lamella number L . Type B foam (characterized by a positive E and negative S coefficients, see Table 2.2) was predicted for all the alkanes investigated. However, this prediction contradicts the results presented in Table 2.4, where the calculated S coefficient of all the alkanes is positive. Moreover, the lamella number theory cannot discriminate between a less stable foam with n-C₆ and a more stable foam with n-C₁₆, since this theory predicts a similar foam type (type B) for these oils.

Table 2.4: Entering, Spreading, and Bridging coefficients and Lamella number for 0.5 wt% AOS foam in the presence of different alkanes.

Oil	E (mN/m)	S (mN/m)	B (mN/m) ²	L (-)
n-C ₆	14.2	7.4	527.8	1.3
n-C ₁₀	8.8	2.2	302.9	1.3
n-C ₁₆	3.2	0.2	98.7	2.9

2.3.3 Foam-oil interaction mechanism

The low foam stability in the presence of alkanes with shorter chain length is in good agreement with previous studies (Suffridge et al., 1989; Aveyard et al., 1993; Vikingstad et al., 2005; Andrianov et al., 2012), despite the fact that foam was generated using different surfactants and under different experimental conditions. The destabilizing effect of short chain alkanes can be attributed to their higher tendency to solubilize in micelles. According to Lobo et al. (1989) and Koczko et al. (1992) presence of solubilized oil in micelles decreases the effective micellar volume by a reduction of repulsive forces between micelles. This inhibits the stratification phenomenon (a step-wise film thinning) in the foam films (Nikolov et al., 1986), thus leading to a faster foam destabilization. However, longer chain alkanes exhibit a lower tendency to solubilize in micelles due to the steric reasons (Ceglie et al., 1987-a and 1987-b). This is further supported by the observations of Vikingstad et al. (2005 and 2006) where they found that alkanes longer than n-C₁₀ are not solubilized in micelles and instead increase foam stability. The latter consequence can be attributed to a reduction in the film thinning rate due to the presence of long chain alkanes. This is supported by the foam film studies of Aveyard et al. (1993) where they obtained thicker foam lamellae by increasing the chain length of alkanes. Following Koczko et al. (1992) this effect is due to the accumulation of oil droplets in the Plateau borders, which slows down film thinning. These results are in line with our observations for 0.5 wt% AOS foam in the presence of n-C₁₆ in Fig. 2.7 where the oil droplets drain from the foam films and then accumulate in the Plateau borders. However, several studies (Nikolov et al., 1986; Wasan et al., 1994; Neethling et al., 2011) emphasized that before oil droplets are able to migrate towards the Plateau borders, the pseudoemulsion film should remain stable. Otherwise, oil droplets enter the gas-water interface,

leading to film rupture. It is found that the stability of pseudoemulsion film increases with surfactant concentration (Aronson et al., 1994; Bergeron and Radke, 1995). For concentrations above the c.m.c., a larger disjoining pressure is obtained in the foam films (Bergeron et al., 1993; Aveyard and Clint, 1996; Neethling et al., 2011). Also, the foam films undergo a stepwise layer-by-layer thinning process (Nikolov et al., 1986, Wasan et al., 1988; Bergeron and Radke, 1995). These concurrent effects slow down the thinning rate of the pseudoemulsion films, and thus lead to a more stable foam. These observations can be used to interpret the results in Fig. 2.12 where a longer half decay time for AOS foam is obtained at a higher concentration in the presence of n-C₁₆. Accordingly, one can infer that the increase of AOS concentration from 0.1 to 1.0 wt% is accompanied with a more stable pseudoemulsion film. This leads to a decrease in the film thinning rate and thus, at the macroscopic level, a more stable foam with a longer half decay time, which is obtained at a higher surfactant concentration.

2.4 Conclusions

A systematic study was performed to examine the bulk foaming characteristics of several commercial surfactants (Dowfax 8390, C₁₂₋₁₅ Enordet, Petrostep SB, and C₁₄₋₁₆ AOS). Foam was generated with these surfactants in the absence and presence of pure alkanes. The Petrostep SB surfactant provided the highest foam longevity in the absence of oil, while the AOS surfactant obtained the highest longevity in the presence of oil. These results showed no correlation between foam stability and surfactant type in the absence and presence of oil. The foaming behavior of AOS surfactant was further examined by using Foamscan instrument at different surfactant concentrations and oil types. The following conclusions have been drawn:

- AOS surfactant exhibited a good foamability in the presence of alkanes with different carbon chains. The corresponding foam volume increased linearly with time. This was further confirmed by a monotonic increase in the amount of liquid volume in the foam.
- The decay of AOS foam in the presence of oil was characterized by a small and rapid reduction in foam volume, followed by a stabilized value, and then a second decay by which the foam either obtained a finite volume or was completely broken down. From the amount of liquid volume in the foam it was found that the first decay was dominated by gravity drainage, while bubble coalescence was dominant during the second decay.
- The effect of oil type was more pronounced during the second foam decay. AOS foam in the presence of alkane with shorter carbon chain entered the second decay at an earlier time and exhibited the least foam stability. The rate of second decay was increased by decreasing the alkane chain length.

-
- Increase of surfactant concentration from 0.1 to 1.0 wt% enhanced foam stability considerably in the presence of oil. Both of the liquid volume in the foam and foam stability increased with surfactant concentration. The effect was more pronounced in the concentration range from 0.1 to 0.5 wt%.
 - AOS foam stability was influenced by the alkane chain length: the lower the chain length, the higher the tendency of alkane to destabilize foam.
 - Lower foam stability in the presence of short chain alkane was systematically described by the magnitude of the spreading and bridging coefficients, where the largest positive coefficients were obtained for a alkane with the shortest chain length (in our case n-C₆). Higher foam stability in the presence of long chain alkane (in our case n-C₁₆) was attributed to the accumulation of oil droplets in the Plateau borders, which is expected to slow down the rate of thinning of foam films.

Chapter 3

DYNAMICS OF FOAM FLOW IN POROUS MEDIA IN THE ABSENCE OF OIL*

Abstract

A detailed laboratory study of nitrogen foam propagation in natural sandstones in the absence of oil is reported. The goal of this study was to elucidate further the mechanisms of foam mobility control. The C₁₄₋₁₆ alpha olefin sulfonate (AOS) surfactant was selected to stabilize foam. X-ray CT scan images were taken during foam propagation to map water saturation over time. Effects of surfactant concentration and of total injection velocity were examined in detail as these are key parameters for controlling foam strength and foam propagation under field conditions. The experiments revealed that foam mobility decreases in two steps: (1) during initial forward foam propagation foam mobility diminishes by an order of magnitude, compared to water mobility and (2) during a secondary backward liquid desaturation it decreases further by one to two orders of magnitude for sufficiently high surfactant concentrations. The steady-state mobility reduction factor increases considerably with both surfactant concentration and total injection velocity. A hysteresis was observed for a cycle of increasing-decreasing surfactant concentration or total injection velocity. The observed effects could be interpreted mechanistically in terms of surfactant adsorption and foam rheology. Implications for field application of foam for immiscible and miscible gas EOR are discussed.

* Adapted from Simjoo et al. 'Novel insight into foam mobility control', revision submitted to SPE journal (2012).

3.1 Introduction

Foam is generally formed when gas is injected through a porous medium containing a foam-stabilizing surfactant. The gas breaks into bubbles that are stabilized by the surfactant in a liquid continuum (Holm, 1968; Schramm and Wassmuth, 1994). The occurrence of foam is discernible in the drastic lowering of gas mobility (Kovscek and Radke, 1994; Rossen, 1996; Zitha et al., 2006). Such mobility reduction is essential for improving the volumetric sweep efficiency during immiscible or miscible gas flooding of oil reservoirs. It has thus obvious potential benefits not only for enhanced oil recovery (EOR) (Patzek, 1996; Turta and Singhal, 1998; Yan et al., 2006; Farajzadeh et al., 2010) but also for near-wellbore applications such as acid diversion, gas-shutoff, and water-shutoff (Hanssen and Dalland, 1994; Kibodeaux et al., 1994; Behenna, 1995; Zhdanov et al., 1996). This study will focus on the effects of surfactant concentration and of total injection velocity on foam propagation and foam strength in the absence of oil: related studies of foam behavior in the presence of oil have been reported recently (Andrianov et al., 2012; Guo et al., 2011) and are the subject of Chapters 6 and 7. The emphasis on the surfactant concentration and injection velocity arises from two main reasons. Firstly, the surfactant concentration is one of the main physical parameters that can be used for switching foam on or off and for tuning foam strength to the requirements for a specific EOR field application. Secondly, the total injection velocity is a key parameter for controlling foam injection and propagation.

The mobility reduction by foam conceals the interplay of two distinct but intimately related effects. The first is the mobility reduction of the liquid phase and the second is the mobility reduction of the gaseous phase (Schramm and Wassmuth, 1994; Kovscek and Radke, 1994; Rossen, 1996). Bernard et al. (1965) showed that the relative permeability function for the aqueous phase during foam flow is identical to that during free (unfoamed) gas flow. Hence, since the liquid viscosity is constant, the reduction of the liquid mobility is simply due to the lowering of its relative permeability with increasing gas saturation. This has been largely confirmed by others (Sanchez et al., 1986; Friedmann et al., 1991; Vassenden et al., 1999). The lowering of gas mobility is much subtler and has been a subject of extensive research. Many authors (Bernard et al., 1965; Kovscek et al., 1997) distinguish two contributions to the foam mobility reduction: (a) the lowering of the foam relative permeability compared to the free gas and (b) the increase in the foam effective viscosity. Although separating relative permeability and viscosity effects experimentally remains an unresolved issue, the investigation of the two effects individually provided valuable insight on the foam behavior in porous media.

The concept of gas trapping plays a central role in the modeling of foam under dynamic and steady-state conditions (Bernard et al., 1965). To account for gas trapping, several authors scaled

gas relative permeability using an empirical factor (Falls et al., 1988; Friedmann et al., 1991); others included gas trapping effects into the residual gas saturation (Li et al., 2006). Foam relative permeability models, taking into account foam collapse near the limiting capillary pressure P_c^* (Khatib et al., 1988), were proposed to simplify fractional flow modeling of foam (Rossen and Zhou, 1995) where for convenience all the effects of foam were represented in the relative permeability function.

Foam viscosity was studied both theoretically and experimentally (Hirasaki and Lawson, 1985; Falls et al., 1989) using capillary tubes with either uniform or periodically varying cross-sections. The derived viscosity equations account for friction due to the sliding motion of the bubbles, drag on foam films, and surface tension gradient due to the periodic stretching-contracting of the foam films. They showed that foam viscosity grows proportionally to bubble density and decreases with the power of velocity, i.e., foam is shear-thinning. These predictions are supported by foam viscosity measurements in capillaries and glass-bead packs reported by the authors. However, data for foam flow in porous media suggesting that foam is shear-thickening are also available, as will be discussed below (see section 3.3.3).

The effect of surfactant concentration on foam strength can be ascribed to its role on the stability of foam films, i.e., to the balance between the (destabilizing) local capillary pressure and (stabilizing) disjoining pressure, of which P_c^* is a macroscopic manifestation. Several authors have shown that a minimum surfactant concentration is required for the existence of foam and that gas relative permeability decreases drastically as the surfactant concentration increases (Friedmann et al., 1991). The P_c^* rises when surfactant concentration increases from the c.m.c. to values several times the c.m.c. (Aronson et al., 1994) as does the disjoining pressure (Schulze-Schlarman et al., 2006). When the disjoining pressure is larger than the local capillary pressure, foam films are stable, foam coalescence rate drops (Exerowa and Kruglyakov, 1998) and foam becomes stronger.

Two flow regimes exist for foam flow in porous media (Osterloh and Jante, 1992): (a) in the low quality regime (low gas fractional flow), the apparent viscosity of foam increases with the gas rate and is practically independent of the liquid rate, whereas (b) in the high quality regime (high gas fractional flow), the apparent foam viscosity increases with the liquid rate. The transition between the two regimes occurs at a well defined critical foam quality, depending on rock and surfactant properties. The critical foam quality increases with surfactant concentration (Martinez, 1996; Alvarez and Rossen, 2001). Experimental studies using high quality nitrogen foam flow in sand-packs and Berea sandstone cores pre-saturated with surfactant solution showed that higher flow rates lead to finer and more uniform foam textures (Friedmann and Jansen, 1986).

The goal of this chapter is to gain further insight into the dependence of foam mobility on surfactant concentration and total injection velocity in natural sandstones, in the absence of oil. The foam flow is investigated in the range of a surfactant concentration from 0.1 to 1.5 wt%, which has been used for IOR/EOR projects. Besides, we are interested in a relatively small range of velocities from 1 to 10 ft/day corresponding to typical flow conditions in the field. Experiments were performed using Bentheimer sandstone core and nitrogen foam was stabilized by the C₁₄₋₁₆ AOS surfactant at the constant foam quality of 91% under 20 bar back-pressure and ambient temperature. This chapter proceeds with the experimental section. Next, the results are presented and discussed. Then the main conclusions of the study are drawn.

3.2 Experimental description

3.2.1 Materials

As already mentioned, the surfactant used to perform the experiments is the C₁₄₋₁₆ alpha olefin sulfonate (AOS, Stepan) with the molecular weight of 315 g/mole. It was provided as an aqueous solution containing 40.0 wt% active content and used as received without further treatment. The surfactant was diluted to the desired concentrations using 0.5 M sodium chloride (NaCl, Merck) brine, obtained by dissolving a required amount of the salt in de-ionized water. The critical micelle concentration of AOS surfactant in brine was 4×10^{-3} wt%. Nitrogen gas with a purity of 99.98% was used to conduct the experiments.

3.2.2 Core sample and core-holder

Bentheimer sandstone was used to perform the experiments. This quartzitic, quasi-homogeneous, and isotropic natural porous medium is often used as a model for reservoir rocks. The core samples were drilled from a cubical block of 40 cm by side and then sawn to the required dimensions using a water-cooled diamond saw. Next, the cores were dried in an oven at 60 °C for 48 hours. Then, they were encapsulated in a thin layer of low X-ray attenuation Araldite self-hardening glue to avoid possible bypassing along the side of the core. From the CT scans of the dry core it was estimated that the glue penetrates about 1.0 mm of the core sample. The effective diameter was taken into account for the calculation of the total pore volumes of the cores. After hardening, the glue was machined to ensure that the core fits precisely into the core-holder. The physical properties of the core samples are presented in Table 3.1.

The core-holder was made of polyether-ether-ketone (PEEK), a synthetic material combining good mechanical properties with low X-ray attenuation. It also transmits X-ray within a narrow energy window (refiltering the polyenergetic source X-rays), which appreciably minimizes the beam hardening artifact due to the polychromaticity of the X-ray beam. Several holes were drilled through the glue layer into the core surface along the core length for pressure measurements. The

pressure connectors were also made of PEEK to prevent interference of the pressure lines with the CT scanning.

Table 3.1: Physical properties of the cores used in the experiments.

Diameter (cm)	3.8 ± 0.1
Length (cm)	17.0 ± 0.1
Porosity (%)	21.0 ± 0.1
Pore volume (cm ³)	40.5 ± 0.5

3.2.3 Experimental set-up

The set-up used to conduct the core flow experiments is shown in Fig. 3.1. It consists of a core-holder in line with a double effect piston displacement pump (Pharmacia Biotech P-500) parallel with a gas mass flow controller (Bronkhorst) and on the other end a back pressure regulator and a collector for the produced fluids. The pump was used to inject the surfactant solution. Nitrogen gas was supplied by a 200 bar cylinder equipped with a pressure regulator (KHP Series, Swagelok) and connected to the core inlet through a mass-flow controller. Two differential pressure transducers were used to monitor the pressure drop over the core segments with increasing length from the core inlet (section 1: 4.3 ± 0.1 cm and section 2: 8.5 ± 0.1 cm). A third differential pressure transducer was used to record the overall pressure drop over the entire core (section 3: 17.0 ± 0.1 cm). A data acquisition system (National Instruments) was used to record pressure, liquid production and gas and liquid injection rates. The experiments were conducted at a back-pressure of 20 bar and ambient temperature (21 ± 1 °C).

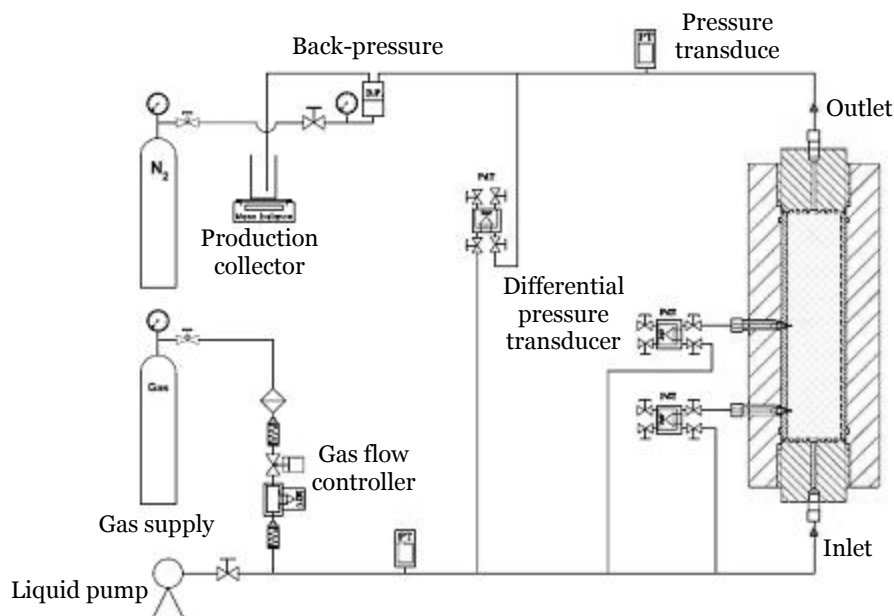


Fig. 3.1: Schematic of the experimental set-up used to perform the foam experiments. The core-holder was placed vertically on the CT scanner couch with its axis in the imaging plane of the gantry.

3.2.4 CT imaging settings

The CT scans were obtained using a third generation SAMATOM Volume Zoom Quad slice scanner. The core flow set-up was placed on the couch of the CT scanner and the core-holder was fixed vertically to the edge of the couch using polymethyl methacrylate (PMMA) stand, equally transparent to X-rays. The imaging settings used in the experiments are listed in Table 3.2. The X-ray tube of the CT scanner operated at a voltage of 140 kV and a current of 250 mA. The thickness of each CT slice was 1 mm and one series of scans included 8 slices. The sequential scan mode was used for the acquisition of the images. This method is slower than the helical mode but has a much lower noise-to-signal ratio. A typical slice image consists of 512×512 pixels with the pixel size of 0.3 mm×0.3 mm. Since the noise for CT images typically ranges from 3 to 20 Hounsfield units (*HU*), the accuracy in the measured fluid saturations is about ±2%.

Table 3.2: Setting of CT scan measurements.

Specification	Quantity
Tube voltage (kV)	140
Tube current (mA)	250
Slice thickness (mm)	01
Pixel size (mm×mm)	0.3×0.3
Image reconstruction kernel	B40 medium
Scan mode	Sequence

3.2.5 Experimental procedure

The basic sequence used to conduct core-flooding experiments is as follows. First air was removed from the core by flushing it with CO₂ at 5 bar injection pressure. Then the dry core was saturated by injecting brine while maintaining a back-pressure of 25 bar to dissolve any CO₂ present in the core and thus ensuring a complete saturation of the core with brine. The absolute permeability of the core sample was determined from the measured pressure drops of the single-phase water flow at different flow rates. Next, three pore volumes of the surfactant solution were injected into the core to satisfy its adsorption capacity. Then nitrogen and surfactant solution were injected simultaneously from the bottom of the core to generate foam in the porous medium varying either the surfactant concentration (0.1, 0.5, 1.0 and 1.5 wt%) or the total superficial velocity (1.15, 2.29, 4.58 and 9.16 ft/day). For all the experiments the foam quality was fixed at 91% at the indicated back pressure. Table 3.3 gives an overview of the foam flow experiments performed in this study.

The first part of this study was devoted to the effect of surfactant concentration. The experiments were done at the fixed injection velocity of 4.58 ft/day, using two approaches: (a) for each concentration a new core was used (multiple cores experiments) and (b) a single core was used for

an increasing-decreasing surfactant concentration cycle (single core experiments). The second part of the study was devoted to the effect of velocity. The surfactant concentration was fixed at 0.5 wt%. The experiments were done using a single core under an increasing-decreasing velocity cycle.

Table 3.3: Overview of the foam flow experiments performed in this study. Foam quality was equal to 91%.

Exp.	Core type (single/ separate)	Brine Permeability (Darcy)	Concentration (wt%)	Total flow rate (ft ³ /d)	Liquid velocity (ft/d)	Gas velocity (ft/d)
1	separate*	1.5±0.1	0.1	5.6×10 ⁻²	0.41	4.17
2	separate	2.7±0.1	0.5	5.6×10 ⁻²	0.41	4.17
3	separate	2.6±0.1	1.0	5.6×10 ⁻²	0.41	4.17
4			0.1			
5			0.5			
6			1.0			
7	single**	1.5±0.1	1.5	5.6×10 ⁻²	0.41	4.17
8			1.0			
9			0.5			
10			0.1			
11				1.4×10 ⁻²	0.11	1.04
12				2.8×10 ⁻²	0.21	2.08
13				5.6×10 ⁻²	0.41	4.17
14	single	2.3±0.1	0.5	11.2×10 ⁻²	0.83	8.33
15				5.6×10 ⁻²	0.41	4.17
16				2.8×10 ⁻²	0.21	2.08
17				1.4×10 ⁻²	0.11	1.04

* Separate means that foam flow at each concentration was studied in a new core. This approach is called multiple core experiments.

** Single means that concentration (or velocity) cycle was studied in a single core. This approach is called single core experiments.

The purpose of using a cycle of increasing-decreasing surfactant concentration or injection velocity was to reveal any hysteresis present during foam flow. The experiments started with the lowest surfactant concentration (or injection velocity) until the pressure drop reached a fairly stable value, indicating that the foam flow is at (or near) the steady-state condition. Then, the surfactant concentration (or injection velocity) was increased until it reached the highest value. Thereafter, the concentration (or injection velocity) decreased in a reverse way to the lowest value, decreasing concentration (velocity) branch.

At each stage of the experiments, CT scans of the core were made to determine the distribution of water saturation in the porous medium and reveal the propagation of foam front.

3.3 Results and discussion

The experiments were analyzed in terms of the CT images, the water saturation profiles obtained from these images and the reduction of foam mobility. Water saturations were obtained by averaging the CT scan images transversally, i.e., perpendicularly to the flow direction. In this work, the mobility reduction factor (MRF) is defined as a ratio of the measured sectional pressure drop for foam flow to the corresponding pressure drop for the flow of water at the same superficial velocity, u :

$$MRF = \frac{\Delta P_{foam}}{\Delta P_{water}} \Big|_u \quad (3.1)$$

In the following sections we will first elucidate the dynamics of foam flow for a specific surfactant concentration and injection velocity performed under the conditions listed in Table 3.3. Then the effects of surfactant concentration and injection velocity on foam mobility will be discussed.

3.3.1 Baseline foam dynamics

3.3.1.1 CT scan images

Fig. 3.2 shows the CT images for a prototypical foam development in the Bentheimer sandstone core previously saturated with surfactant solution (exp. 3 in Table 3.3). The experiment is taken as the reference case for this study. The number below each image represents the elapsed time expressed in the number of pore volumes injected. The red color indicates a core fully saturated with surfactant solution and the change from red to blue corresponds to decrease in water saturation. In the first injected pore volume, foam displaces the surfactant solution in a front-like manner, characteristic of the displacement of a less viscous fluid by a more viscous one. As a consequence, when foam front progresses, water saturation behind the front decreases. This is evident in the color change from red to yellowish blue. There is a small region near the inlet face with relatively high intensity of red color, indicating a higher water saturation compared to the rest of the core. This is the inlet effect and, most probably, due to the fact that gas has to travel a certain distance away from the injection face before foam has developed sufficiently to displace water (Nguyen et al., 2003; Farajzadeh et al., 2009; Zitha and Du, 2010; Ashoori et al., 2011-a). Ahead of the advancing foam front a transition region can be discerned where a fine fingering pattern is present. Foam breakthrough occurs at around 0.76 ± 0.02 PV. After the breakthrough, water saturation remains high for a certain time near the core outlet due to the capillary end effect (Huang and Honarpour, 1998; Apaydin and Kovscek, 2001). Thereafter, a backward desaturation

front propagates from the outlet to the inlet as indicated by the progressive darkening of the blue colored zone. The desaturation front becomes stationary at about 40 PV, indicating that the foam has practically reached the steady-state flow regime. A similar secondary desaturation was reported earlier by Nguyen et al. (2003) for foam stabilized with sodium dodecyl sulfate in Bentheimer and Berea cores, but no definite explanation on this phenomenon has been provided thus far. The authors argued that in their experiments the desaturation starts in the central part of the core and then becomes more visible after foam breakthrough. A slightly different picture emerges from our experiments: it appears that the secondary desaturation starts after foam breakthrough. The difference between the behavior observed by Nguyen et al. (2003) and the current results could be due to the difference in the total injection velocity and back-pressure used in the experiments. Nguyen et al. (2003) performed their experiments at a much higher total superficial velocity (17 ft/day *vs.* 4.58 ft/day) and much lower back-pressure (atmospheric pressure *vs.* 20 bar). Much lower backpressure in the work of Nguyen et al. (2003) might have resulted in a small gas expansion, which manifested itself in the desaturation observed before foam breakthrough.

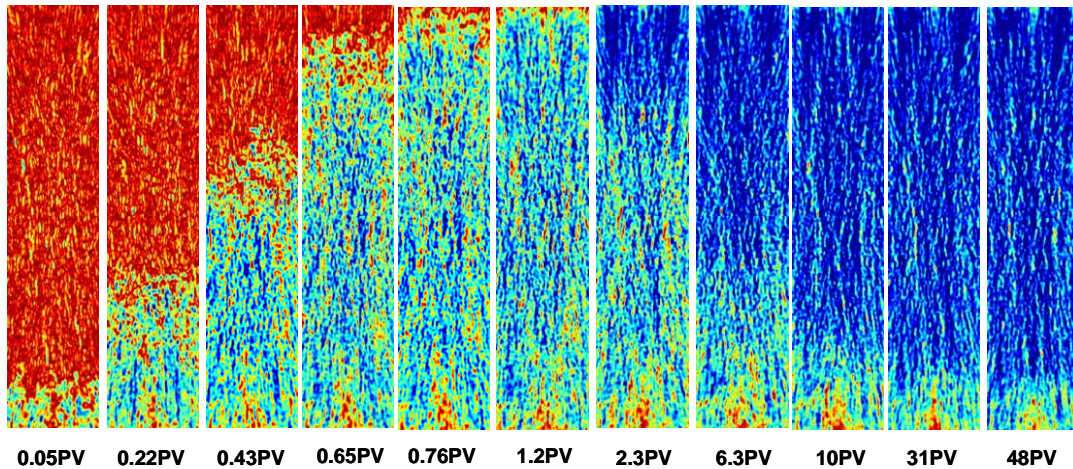


Fig. 3.2: CT images obtained during 1.0 wt% AOS foam flow (exp. 3 in Table 3.3). The blue and red colors stand for gas and water, respectively. First a forward foam front propagates throughout the core and breaks through slightly after 0.76 ± 0.02 PV. After foam breakthrough, a secondary desaturation front develops and propagates backward. The steady-state flow regime is obtained after 40 PV.

3.3.1.2 Saturation profiles

For further analysis of the foam flow we plotted water saturation profiles shown in Fig. 3.3 for different injected pore volumes. The water saturation S_w was obtained by the following equation:

$$S_w = \frac{HU_{foam} - HU_{dry}}{HU_{wet} - HU_{dry}} \quad (3.2)$$

Where HU_{foam} , HU_{dry} and HU_{wet} are the X-ray attenuation coefficients in Hounsfield units for foam flow, dry core and the surfactant solution saturated core, respectively.

The forward foam saturation profiles combine an upward-concave portion with a horizontal part. In the early times, for instance at 0.05 PV, the water saturation decreases slightly from 0.63 ± 0.02 to 0.59 ± 0.02 and then rises and reaches unity at 2.2 ± 0.1 cm. The remaining curves exhibit a slightly different trend. Let us, for example, focus on the curve corresponding to 0.44 PV. The water saturation decreases from about 0.50 ± 0.02 at the inlet to a minimum of nearly 0.35 ± 0.02 at the distance of 6.0 ± 0.1 cm from the core inlet. Then the saturation increases to unity over the next 6.0 ± 0.01 cm. The shape of the saturation profiles is reminiscent of the Buckley-Leverett flow, but includes effects of gas compressibility and capillary diffusion. Near the outlet a strong capillary-end effect is observed which persists up to about 1.2 PV. The capillary-end effect is consistent with the fact that the non-wetting phase (gas) displaces the wetting phase (surfactant solution), where the capillary pressure at the outlet tends to zero. As already noted on the CT images, a secondary backward desaturation front emerges beyond 1.2 PV, eliminating completely the capillary-end effect. The backward desaturation is characterized by a very low propagating rate. For example, at 5.0 PV water saturation increases slowly from about 0.11 ± 0.02 at the outlet region to about 0.35 ± 0.02 at 4.0 ± 0.1 cm from the core inlet. A long transition zone is observed from 11.0 ± 0.1 to 4.0 ± 0.1 cm.

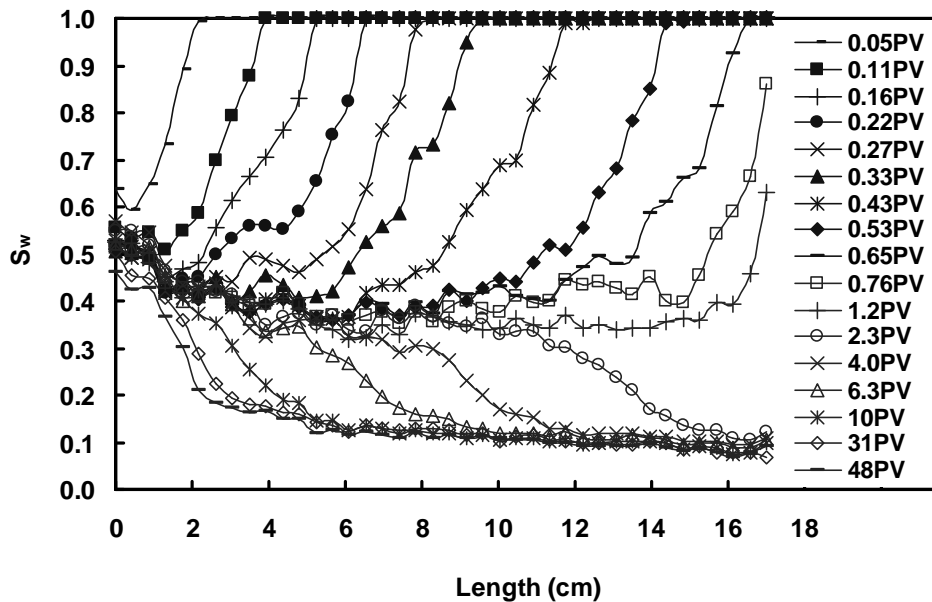


Fig. 3.3: Water saturation profiles obtained from the CT images shown in Fig. 3.2. During the forward foam flow an average water saturation of 0.35 ± 0.02 was established throughout the core, except in the inlet and outlet regions. As the secondary desaturation front develops, the end effect is completely eliminated and then the average water saturation of 0.11 ± 0.02 was established over the swept region.

The locus of the forward and backward foam fronts versus injected pore volumes is depicted in Fig. 3.4. The velocity, i.e. slope of the curve, of the forward front is practically constant and equal to 22.0 ± 0.1 cm/PV. However, the velocity of the backward desaturation front is much lower and decreases to almost zero as the front approaches the core inlet. This hints at rather different mechanisms for the forward foam development and for the backward desaturation front.

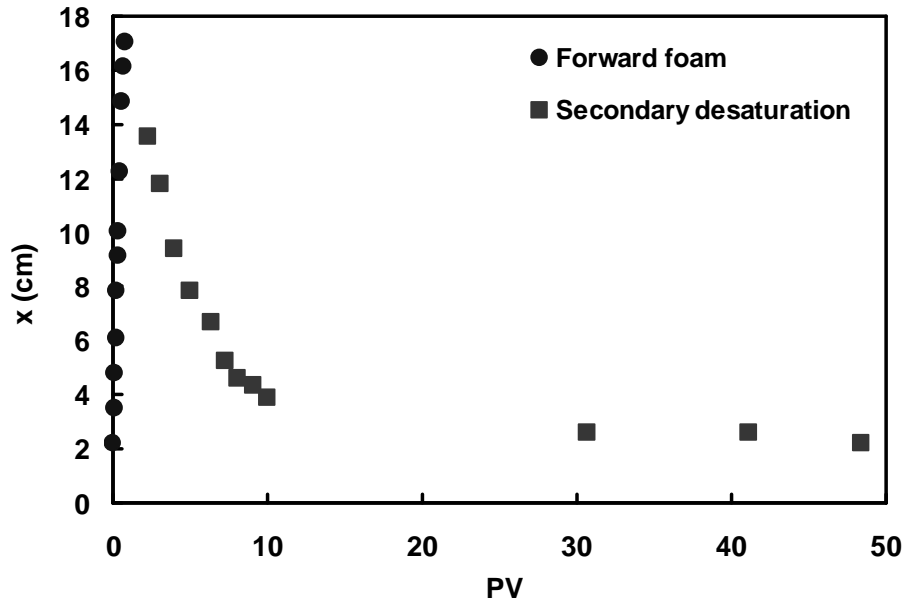


Fig. 3.4: Displacement of the locus of foam front during co-injection of 1.0 wt% AOS foam flow. The forward foam front travels with a velocity of 22.0 ± 0.1 cm/PV. The velocity of backward desaturation front is much lower and decreases to almost zero as the desaturation front approaches the inlet region.

3.3.1.3 Mobility reduction factor

Fig. 3.5 shows the mobility reduction factors (MRF) obtained during foam flow, for different core sections (section 1: 4.3 ± 0.1 cm, section 2: 8.5 ± 0.1 and section 3: 17.0 ± 0.1 cm). The inset in Fig. 3.5 shows MRF during the first 2.0 injected pore volumes. MRF in the first section near the inlet remains rather low over the duration of the experiment. In the other sections MRF increases first slowly and then more steeply. The sharp increase in the MRF slope corresponds to the onset of the secondary desaturation front, in good agreement with the CT images and water saturation profiles. For the total MRF (section 3) the slope in the first 1.5 PV is 0.2 PV^{-1} while it increases steeply to 1.6 PV^{-1} (eight times larger slope) during the next 10 PV. Beyond 12 PV the total MRF levels off to a plateau equal to 1400 ± 20 . This value coincides with the end of the secondary desaturation as can be seen from Figs. 3.2 and 3.3. To compare the magnitude of foam mobility along the core length, we examine the mobility reduction gradient (MRG), i.e. the ratio of the sectional MRF to the corresponding core section length. The MRG is 42, 68 and 84 cm^{-1} for three core sections after 40 PV at which the secondary front becomes practically stationary (see Fig.

3.2). The corresponding average water saturation at each section is 0.26 ± 0.02 , 0.20 ± 0.02 , and 0.15 ± 0.2 . It can therefore be concluded that foam strength increases with distance from the inlet so that the increase in MRG is accompanied by a decrease in water saturation. Below we interpret this effect based on the competition of viscous and capillary forces.

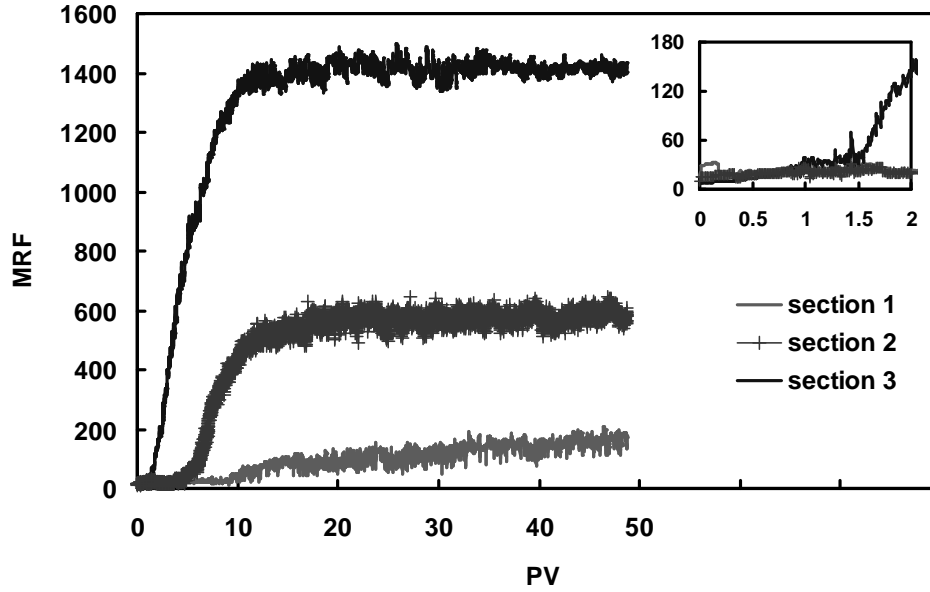


Fig. 3.5: Mobility reduction factor (MRF) obtained during 1.0 wt% AOS foam flow at different core sections with increasing length from the core inlet face (section 1: 4.3 ± 0.1 cm, section 2: 8.5 ± 0.1 cm and section 3: 17.0 ± 0.1 cm). A sharp increase in MRF occurs at nearly 1.5 PV coinciding with the start of the backward desaturation observed in Figs. 3.2 and 3.3.

3.3.1.4 Dynamic capillary desaturation curve

The above data are represented in terms of a desaturation curve in order to highlight the competition of viscous and capillary forces. Fig. 3.6 shows the water saturation as a function of the capillary number N_c for foam in the three core sections. The capillary number was used as defined in the literature (Jansen and Friedmann, 1987; Tanzil et al., 2002; Jeong, 2005):

$$N_c = \frac{u_f \mu_f}{\sigma_{fw}} \quad (3.3)$$

where μ_f is foam viscosity, u_f is superficial velocity of the foamed gas, and σ_{fw} is the surface tension between foamed gas and surfactant solution. Using Darcy's law foam viscosity satisfies:

$$\mu_f = \frac{kk_{rf}}{u_f} \frac{\Delta P}{L} \quad (3.4)$$

by substituting Eq. (3.4) in Eq. (3.3), the capillary number reads as follows:

$$N_c = \frac{kk_{rf} \Delta P}{\sigma_{fw} L} \quad (3.5)$$

where k is absolute permeability, k_{rf} is foam relative permeability, ΔP is pressure drop over the core segment, and L is length of the core segment. For simplicity, in Eq. (3.5) we assume that foam is a single-phase fluid such that $k_{rf} = 1$. Therefore, all quantities other than ΔP are constant, which implies that an increase in the capillary number amounts essentially to an increase of viscous forces. Since the trends are similar for the three core sections in Fig. 3.6, we will focus only on the one corresponding to the middle section, as highlighted by gray color with the length of 4.25 cm. First water saturation decreases from unity to 0.95 ± 0.02 as the capillary number increases from 2×10^{-7} to 6×10^{-7} . This initial jump in the capillary number is probably related to the entry capillary pressure for foam in the different core sections. Indeed, under the present experimental conditions the entry capillary pressure for gas was found to be nearly 59 ± 5 mbar: a value that is very close to the measured jump in pressure drop. Subsequently, water saturation drops sharply from 0.95 ± 0.02 to 0.40 ± 0.02 while the capillary number increases from 6×10^{-7} to 5×10^{-6} . This corresponds to the forward foam front propagation in the first injected pore volume. Finally, water saturation decreases steeply to about 0.11 ± 0.02 as the capillary number increases from 5×10^{-6} to 4×10^{-4} . This latter drop of water saturation is due to the propagation of the backward desaturation front.

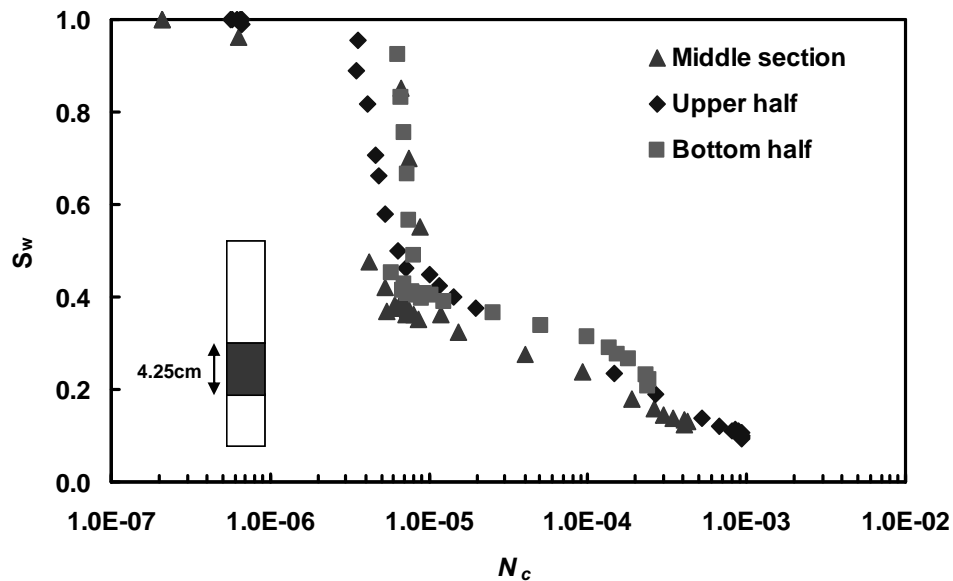


Fig. 3.6: Dynamic capillary desaturation curve for 1.0 wt% AOS foam flow at different core sections. The middle section was highlighted gray. Initially the capillary number N_c jumps by one order of magnitude corresponding to the entry capillary pressure for the core. A sharp reduction of water saturation occurs as N_c approaches 1.0×10^{-5} due to the propagation of the forward foam front. When the secondary front propagates, water saturation decreases steeply to 0.11 ± 0.02 as N_c increases by two orders of magnitude.

3.3.2 Effect of surfactant concentration

In this section the effect of surfactant concentration on the foam mobility is examined using multiple cores (i.e., using a fresh core for each surfactant concentration) and single core (increasing-decreasing the concentration in a single core). In all experiments, the gas and surfactant solution were co-injected at the fixed superficial velocity equal to 4.58 ft/d (see exp. 1 to 10 in Table 3.3).

3.3.2.1 Multiple cores experiments

The multiple cores experiments were performed using three AOS concentrations (0.1, 0.5 and 1.0 wt%). The initial foam propagation for 0.1 and 0.5 wt% is qualitatively similar to that for 1.0 wt% discussed above. Therefore, the corresponding CT scan images and saturation profiles will not be discussed further. The discussion will be limited to the dynamic and steady-state behaviors of the mobility reduction factor (MRF) and water saturation.

Fig. 3.7 shows MRF profiles obtained for three surfactant concentrations investigated. MRF for 0.1 wt% AOS foam remains rather low over 35 PV while for 0.5 wt% AOS foam MRF remains low only up to 5.0 PV and then increases steeply. The slope of MRF for 0.5 wt% AOS foam is three times smaller than that for 1.0 wt% AOS foam. The salient feature of the data presented is thus that the slope of MRF profiles versus the number of injected pore volumes increases significantly with surfactant concentration. At first sight, this seems inconsistent with the fact that based on the bulk experiments foam should have the same strength for all concentrations investigated. It was indeed observed from the bulk experiments that above the c.m.c. foam stability barely changed when the surfactant concentration was varied (Rosen and Solash, 1969; Vikingstad et al., 2006; also Fig. 2.10). It should be pointed out, nevertheless, that bulk experiments provide only information about foam stability and hardly anything about foam strength. Thus the discrepancy illustrates once more that while bulk foam experiments are rather useful for foam stability, they do not predict completely the exact behavior of foam flow in porous media.

Fig. 3.8 shows the average water saturation S_w for the entire core versus the capillary number N_c . For all surfactant concentrations, after an initial jump corresponding to the entry capillary pressure, N_c increases to 8×10^{-6} due to foam development while S_w diminishes to about 0.40 ± 0.02 . Reduction of S_w at a lower N_c for 0.1 wt% AOS foam compared to 0.5 and 1.0 wt% foams is most likely due to small differences in the permeability of the core samples, see exp. 1 to 3 in Table 3.3. The capillary number remains low for 0.1 wt% AOS foam consistent with the low apparent viscosity of the corresponding foam. While for 0.1 wt% AOS foam the overall water saturation remains constant, it decreases to 0.15 ± 0.02 for foam stabilized with 0.5 and 1.0 wt% AOS. At the same time the capillary number increases by two orders of magnitude. This supports

the idea that foam displaces fluids from porous media by ensuring that viscous forces are dominant over capillary forces. Other studies (Ranshoff and Radke, 1988; Tanzil et al., 2000) have argued that capillary forces drive the water saturation down leading to the reduction of the mobilities of foam and liquid. The former point of view has been adopted in this work as it appears more consistent with the fact that foaming increases gas apparent viscosity.

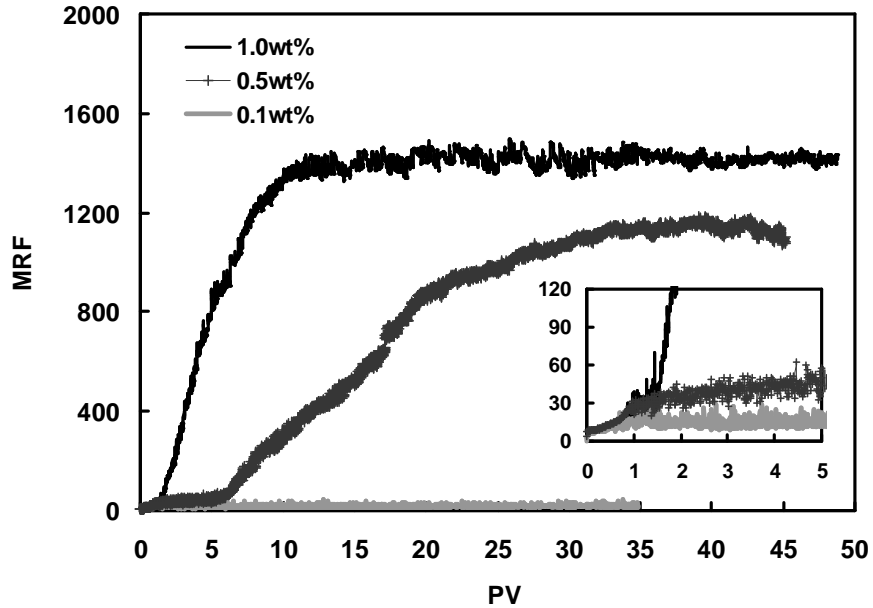


Fig. 3.7: Mobility reduction factor (MRF) during AOS foam flow at different surfactant concentrations (exp. 1 to 3 in Table 3.3). The slope of MRF profiles increases significantly with surfactant concentration.

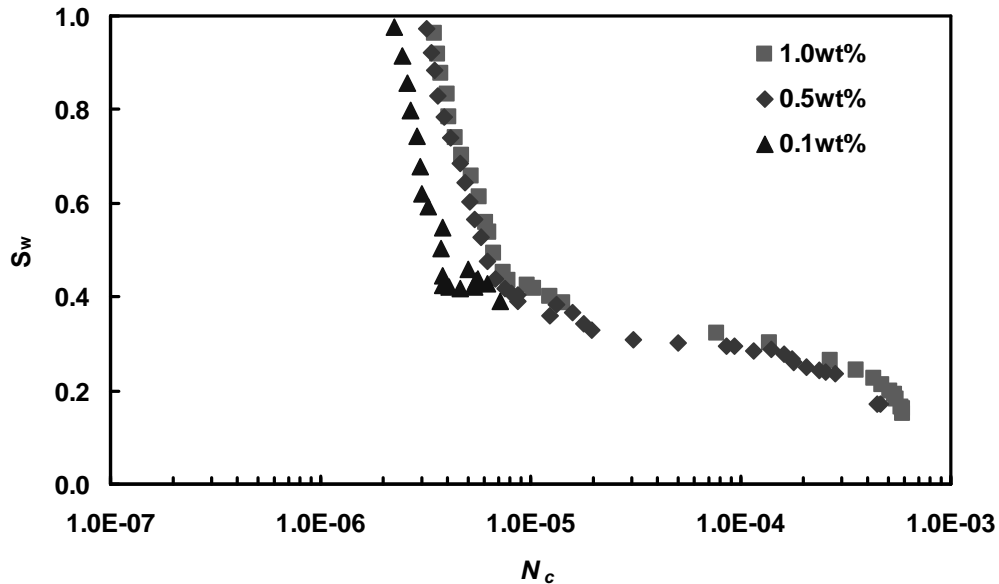


Fig. 3.8: Dynamic capillary desaturation curve for AOS foam flow at different surfactant concentrations. For all concentrations, first the overall water saturation diminishes sharply to 0.40 ± 0.02 due to the forward foam development. While for 0.1 wt% AOS foam the overall water saturation remains constant, it decreases to 0.15 ± 0.02 for 0.5 and 1.0 wt% AOS foams as the capillary number increases by two orders of magnitude.

3.3.2.2 Single core experiments

Fig. 3.9 shows the CT scan images obtained during foam flow in a single core with a cycle of increasing-decreasing surfactant concentration, ranging from 0.1, 0.5, 1.0, and 1.5 wt% (exp. 4 to 10, Table 3.3). Note that the reported pore volumes are separately injected volumes at each concentration. Foam was first generated in-situ at the lowest concentration and then the surfactant concentration was increased in steps to 1.5 wt%. Subsequently, the surfactant concentration was decreased to the lowest value, 0.1 wt%.

The transient foam flow for 0.1 wt% AOS foam is similar to that discussed above (Figs. 3.2 and 3.3) and will not be commented on further. We only note that the overall water saturation obtained after 35 PV is practically uniform and that is nearly equal to 0.40 ± 0.02 . It also does not show any sign of secondary desaturation. Upon increasing the surfactant concentration from 0.1 to 0.5 wt%, a secondary desaturation front (dark blue zone) emerges starting from the core outlet. From the intensity of the colors in the CT images, the front is characterized by a water saturation of about 0.40 ± 0.02 in the upstream part (the same as for foam flow at 0.1 wt%) and a much lower water saturation of 0.16 ± 0.02 towards the outlet. The speed of the desaturation front is quite low. The front does not move beyond 6.5 cm from the core outlet within the duration of the experiments. Intriguingly, increasing the AOS concentration from 0.5 to 1.0 wt% does not seem to have a significant effect on the saturation profiles. Even after injecting 77 PV, which corresponds to the injection of 7.0 PV of the aqueous surfactant solution, the front has moved only by 1-2 cm. When further increasing the surfactant concentration from 1.0 to 1.5 wt% we note a much faster desaturation wave as can be inferred from the position of the front in the CT images. Eventually the desaturation front breaks through the core and over time a uniform saturation of 0.11 ± 0.02 is established in the core. To our knowledge the above dependence of the desaturation front on the surfactant concentration has not been reported before in the literature.

The AOS foam flow continued while decreasing the surfactant concentration from 1.5 to 0.1 wt%. The CT images showed no discernable change in the color intensity upon decreasing AOS concentration from 1.5 to 0.5 wt%. The distribution of the water saturation in the foam-filled porous medium remains practically constant at about 0.11 ± 0.02 . However, as AOS concentration decreases further to 0.1 wt%, the color of the CT images changes from dark blue to green, due to a slight increase in the water saturation. More precisely, the water saturation increases slightly from 0.11 ± 0.02 to 0.15 ± 0.02 as AOS concentration decreases from 0.5 to 0.1 wt%. This is consistent with a gradual reduction of foam strength. Note that the 0.1 wt% AOS foam was injected for 26 PV, corresponding to 2.36 liquid PV.

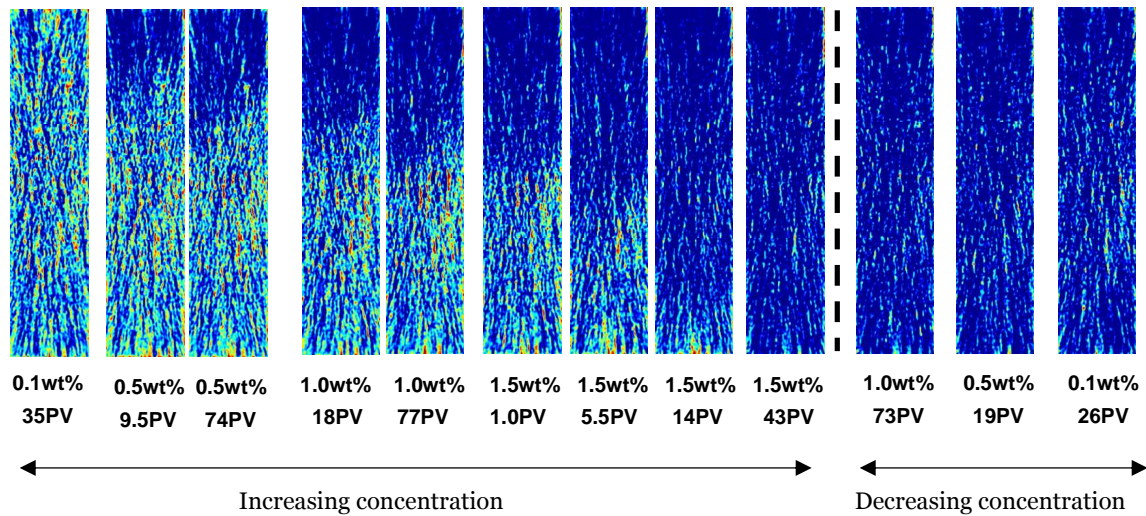


Fig. 3.9: CT images obtained during AOS foam flow for a cycle of increasing-decreasing surfactant concentration (exp. 4 to 10 in Table 3.3). First surfactant concentration increases in steps from 0.1 to 1.5 wt% and then it returns to 0.1 wt%. The speed of the backward desaturation front increases considerably with surfactant concentration. As surfactant concentration increases from 0.1 to 1.5 wt%, the overall water saturation decreases from 0.40 ± 0.02 to 0.11 ± 0.02 while in the reverse way there is a slight increase in the overall water saturation from 0.11 ± 0.02 to 0.15 ± 0.02 .

3.3.2.3 MRF and water saturation

In order to inspect the relation between water saturation and foam mobility in porous media when varying surfactant concentration, we examine now the behavior of MRF together with water saturation as a function of surfactant concentration. Fig. 3.10 presents such a relationship for the multiple cores and the single core experiments. MRF and water saturations were obtained over the total core length.

Focusing first on the multiple cores experiments (upper plot in Fig. 3.10), we note that MRF increases from 19 to 1400 as the surfactant concentration increases from 0.1 to 1.0 wt%. The largest relative increase occurs between 0.1 and 0.5 wt%. The corresponding end-point water saturations diminish from 0.39 ± 0.02 to 0.15 ± 0.02 . For the single core experiments we can make two observations from Fig. 3.10 (lower plot). Firstly, for the increasing concentration branch the largest relative increase in MRF occurs at the higher concentrations between 1.0 and 1.5 wt%, contrary to the multiple cores experiments. Secondly, for the decreasing concentration branch the values of MRF are systematically higher than those for the increasing branch, i.e. MRF exhibits a hysteresis. The MRF values for the decreasing branch are comparable to those of the multiple cores experiments. In the decreasing branch MRF diminishes to 300 ± 5 , while water saturation increases only slightly to 0.15 ± 0.02 , suggesting that the lowering in MRF is mainly due to foam coarsening.

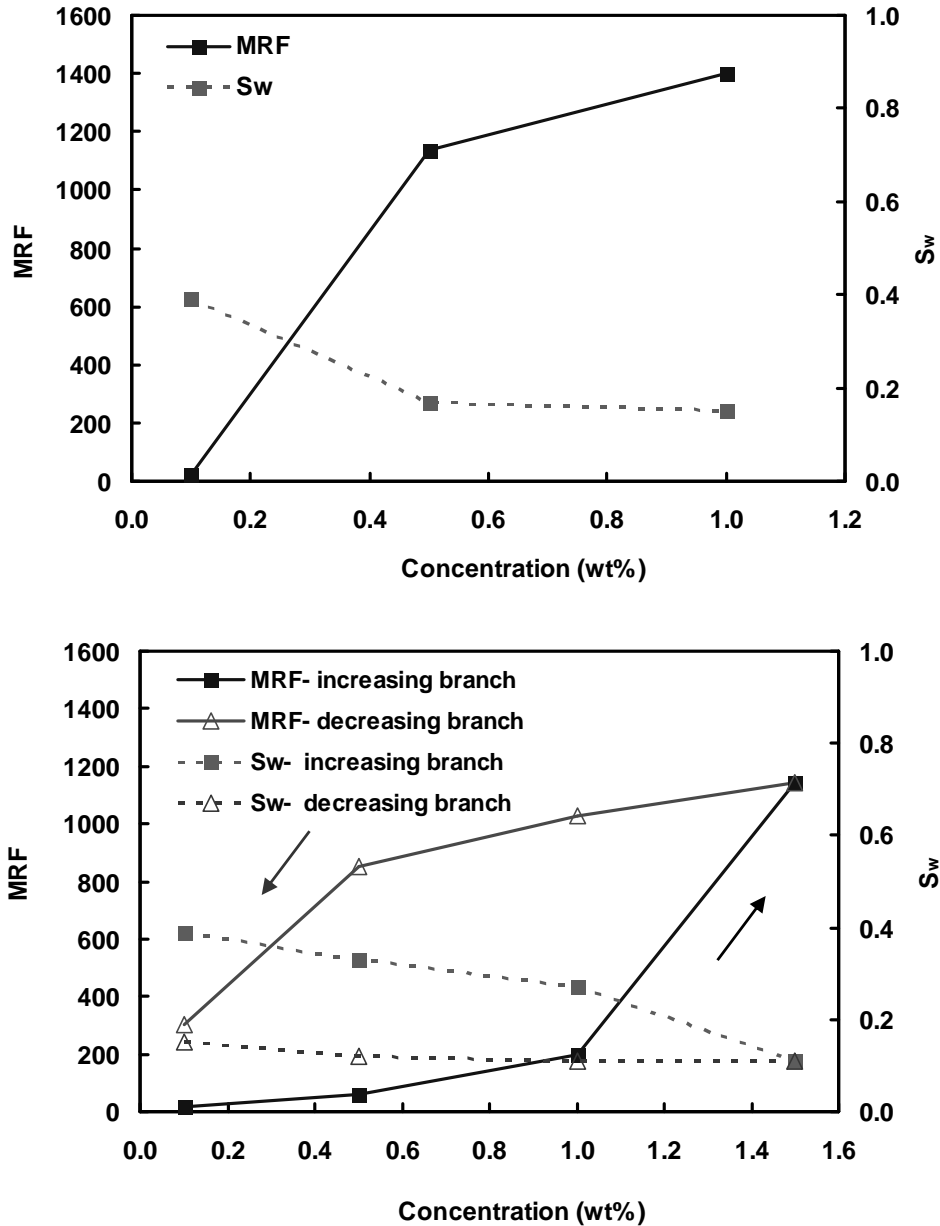


Fig. 3.10: Mobility reduction factor (MRF) and average water saturation (S_w) for AOS foam in the multiple cores (top) and single core experiments (bottom) as a function of surfactant concentrations. For the multiple cores experiments (exp. 1 to 3 in Table 3.3) MRF increases by two orders of magnitude as surfactant concentration increases from 0.1 to 1.0 wt%. For the single core experiments (exp. 4 to 10 in Table 3.3), MRF and S_w exhibit a hysteresis. The arrows show the direction of the surfactant change in the hysteresis plot.

The difference between the MRF data for the multiple cores experiments and the data relating to the increasing branch of the single core experiments is most likely due to a difference in the surfactant adsorption level on the rock surface. In the single core the surfactant adsorption is first satisfied at the lowest concentration and, thus, the corresponding surfactant adsorption level remains low. This can be easily inferred by recalling that surfactant adsorption satisfies the

Langmuir isotherm (Friedmann et al., 1991; Bonfillon et al., 1994; Lee and Heller, 1989). Accordingly, when foam flow continues at a higher surfactant concentration, the surfactant adsorption increases as well. Part of the injected surfactant is used to satisfy the adsorption and only a fraction is available to stabilize the foam. The adsorption is satisfied at a rather slow rate through the core, because of the low liquid injection rate (0.41 ft/day). This might be the reason why the secondary front emerging at 1.0 wt% (Fig. 3.9) of the single core experiments cannot propagate as fast as for the case shown in Fig. 3.2. By increasing the surfactant concentration to 1.5 wt%, however, the secondary desaturation front moves much faster towards the bottom of the core: after the injection of only 1.3 liquid PV, the secondary front moved over more than 80% of the core length. This supports the idea that surfactant adsorption is satisfied much faster than for the 0.5 and 1.0 wt% foams.

Now let us consider the hysteresis observed in the increasing-decreasing concentration cycle in the single core experiments. The hysteresis can be explained by surfactant adsorption/desorption kinetics. For the increasing branch if one would continue the foam flow of 0.5 and 1.0 wt% for much longer time in order to establish the corresponding adsorption equilibrium, the corresponding MRFs would increase further and the corresponding water saturations would diminish even more. The MRF and water saturation of the increasing branch would then follow the same trend as the multiple cores experiments. For the decreasing branch however, as concentration reduces from 1.5 to 0.5 wt%, MRF gradually decreases while the water saturation remains practically constant. The in-situ surfactant concentration through the core is most likely higher than the injected concentration, even after injection of 6.0 liquid PV of 1.0 wt% foam and about 3.0 liquid PV of 0.5 wt% foam. It is thus inferred the foam floods are not prolonged enough to reach the corresponding desorption equilibrium, which is known to be a slow process compared to the adsorption (Sanchez et al., 1986; Mannhardt and Svorstøl, 2001). As the surfactant concentration decreases further to the lowest tested value (0.1 wt%), a substantial reduction in MRF along with a slight increase in water saturation was observed. The adsorption level diminishes due to the decrease in surfactant concentration, but MRF is still one order of magnitude higher than that in the increasing branch. This indicates that the duration of 0.1 wt% foam flood is too short to allow desorption of the surfactant retained from the preceding foam floods at higher concentrations.

3.3.3 Effect of flow velocity

The effect of total injection velocity was studied in a single core by a cycle of increasing-decreasing velocities (exp. 11 to 17, Table 3.3). AOS concentration was fixed at 0.5 wt%. Fig. 3.11 shows the CT images obtained during foam flow for this velocity cycle. The foam flow behavior at 1.15 ft/day is

similar to that discussed before for the forward foam in Fig. 3.3: the corresponding water saturation after 8.0 PV is practically uniform over the core and is nearly equal to 0.45 ± 0.02 . Upon increasing the total velocity from 1.15 to 2.29 ft/day, a new backward foam front with a higher strength develops in the upper part of the core. The change in the foam strength is evident in the color shift from yellowish-green to dark blue. After 5.0 PV the strong foam propagates from the outlet face to around 5.0 ± 0.1 cm upstream where water saturation drops from 0.45 ± 0.02 to 0.19 ± 0.02 . This part is followed by a long transition zone extending from 12.0 ± 0.1 to 6.0 ± 0.1 cm towards the core inlet.

Upon increasing the total velocity to 4.58 ft/day, the speed of the backward foam front remained low; the foam front did not move beyond 6.0 ± 0.1 cm even after injecting 17.0 PV, as shown by the CT scan images in Fig. 3.11. However, a closer examination of the CT image reveals that foam becomes stronger in the upper part of the core due to an increase in velocity: water saturation diminishes further to 0.14 ± 0.02 while in the rest of the core it remains at almost the same value as for 2.29 ft/day. Finally, the injection velocity was increased to 9.16 ft/day and foam injection continued for 10 PV, until the overall pressure drop became stable. No CT images were made for this velocity. Thereafter, the foam velocity was decreased successively to 4.58, 2.2, and 1.15 ft/day. The CT images showed that by reducing total velocity from 4.58 to 1.15 ft/day, the generated strong foam persists in the upper part of the core. However, for the bottom part of the core there is a progressive darkening and spreading of the blue zone, indicating that a strong foam is generated. Accordingly, the corresponding average water saturation decreases from 0.35 ± 0.02 to 0.17 ± 0.02 .

The CT images for a cycle of increasing-decreasing velocities indicate clearly the existence of hysteresis. Moreover, the hysteresis can be clearly seen in the plot of MRF along with water saturation as a function of total injection velocity (see Fig. 3.12). The MRF values on the decreasing velocity branch are higher than those for the increasing one. At the increasing branch the lowest injection velocity leads to a relatively weak foam state (MRF equal to 43 ± 5) with an overall water saturation of 0.45 ± 0.02 . As the injection velocity increases (from 2.29 to 4.58 ft/day), the foam strength increases (MRF increases from 75 ± 5 to 238 ± 5) while water saturation decreases to 0.31 ± 0.02 . When the injection velocity decreases, the AOS foam remains strong: MRF decreases only slightly to 317 ± 5 and water remains low at 0.19 ± 0.02 .

The increase of MRF (by a factor of 5.5) as the injection velocity increases (by a factor of 4) indicates that the present AOS foam, under the current experimental conditions, is shear-thickening. This shear-thickening behavior was reported earlier by others for high quality foam (Kibodeaux et al., 1994; Martinez, 1996). It has also been argued that shear-thickening behavior is

likely to occur above certain velocities, as a result of increase in the frequency of lamellae division with velocity (Chou, 1991; Nguyen et al., 2000). However, it should be noted that the decrease in liquid saturation leads to a steep increase in MRF above a certain gas saturation, i.e., there is a sharp transition in the foam state from a weak to a strong foam (Simjoo et al., 2011).

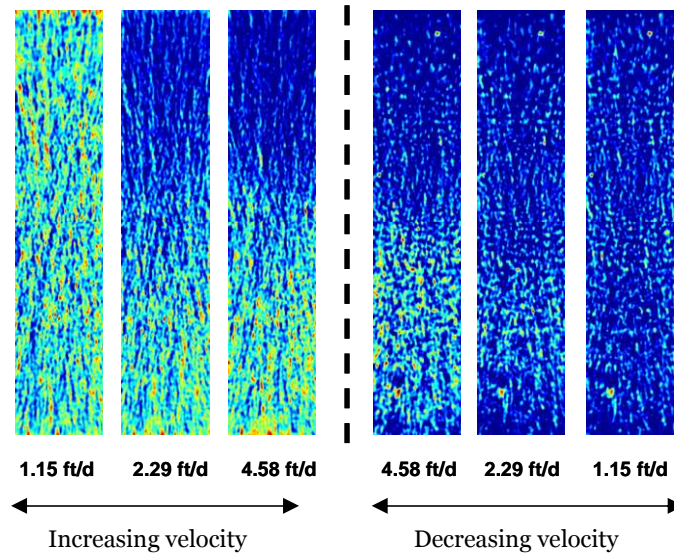


Fig. 3.11: CT images obtained during 0.5 wt% AOS foam (exp. 11 to 17 in Table 3.3). Foam flow was studied in a single core under a cycle of increasing-decreasing velocity. The appearance of the secondary desaturation front coincides with an increase in the total injection velocity from 1.15 to 2.29 ft/day. The resulting strong foam persists even after decreasing velocity to the lowest tested value.

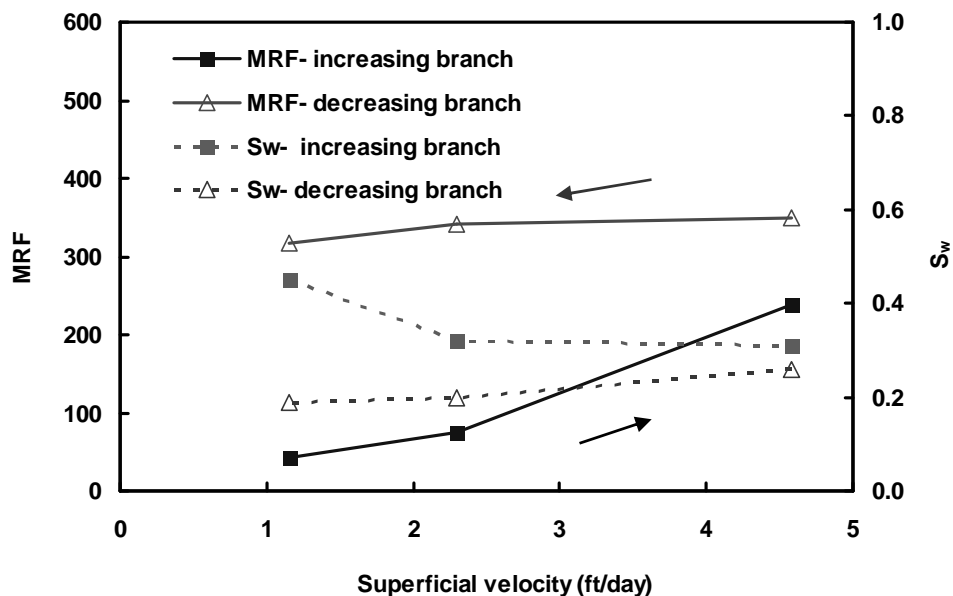


Fig. 3.12: Mobility reduction factor (MRF) and average water saturation (S_w) as a function of total injection velocity for AOS stabilized foam in the single core experiments. A hysteresis is observed during the cycle of increasing-decreasing velocity. The arrows show the direction of the velocity change in the hysteresis plot.

3.4 General discussion

The goal of this study was to investigate foam strength, and in particular its dependence on the surfactant concentration and total injection velocity. The surfactant concentration is the main physical parameter that can be used for adjusting foam strength to the specific field conditions of an EOR application. The total injection velocity, on the other hand, is a key parameter for controlling foam injection and propagation over inter-well distances. One of the critical questions for foam field operations is indeed whether foam can propagate over long distances far away from injection wells, considering the fact that velocity decreases considerably with increasing distance.

To attempt an answer to this question a mechanistic interpretation of the observed effects has been developed relying upon the stochastic bubble population (SBP) foam ideas (Zitha, 2006; Zitha and Du, 2010). The SBP model is simpler than the classical foam population balance model (Kovscek and Radke, 1994; Bertin et al., 1998), but retains the key features of foam flow in porous media. The essence of the SBP foam model is that foam results from a net positive balance of bubble generation and destruction at the propagation front. Bubble generation, i.e. the break-up of gas into bubbles, is essentially a mechanical process. At first approximation, it can thus be assumed that bubble generation is independent of surfactant concentration. This agrees well with the bulk foam studies reported in the previous chapter. The bubble destruction instead depends strongly on the surfactant concentration. For surfactant concentrations below the c.m.c., the bubble coalescence rates can be expected to be rather high leading to low bubble densities or 'poor foaming'. In excellent agreement with available work in the literature, our results have shown clearly that a necessary condition for foam stability in porous media is thus that the surfactant concentration is higher than the c.m.c., which ensures that bubble destruction rates are very small.

The measured saturation maps and profiles shown in Figs. 3.2 and 3.3 are in good qualitative agreement with the prediction of the SBP foam model up to the foam breakthrough (for more details see Chapter 5). Foam flow is reminiscent of a percolation process in a random media (Heiba et al., 1992). In this frame, the foamed gas (non-wetting phase) occupies the largest pores while the liquid (wetting phase) occupies the smallest ones. As already mentioned, when the surfactant concentration increases beyond the c.m.c., the surface tension remains practically constant, but the disjoining pressure curve for the foam films increases considerably (the films are able to withstand greater imposed external forces such as capillary suction pressure). This favors formation of stronger foams, i.e. foam with a higher apparent viscosity, and thus the observed decrease in water saturation. The combined effects of the increase in bubble density and decrease in water saturation lead to an increase of MRF. This self-reinforcing process could in principle

lead to extremely large values of MRF. However, the capillary pressure also increases as water saturation diminishes until equilibrium is established between viscous and capillary forces.

We now turn to the effect of injection velocity. As we have argued above bubble generation is roughly independent of velocity, provided that gas is not moving at an infinitesimally small velocity. This is reasonable approximation for the relatively narrow range of field velocities 1 to 10 ft/day that we considered in this study. Hence, it can be assumed that foam texture (bubble density) is nearly the same for this range of velocities examined. The effect of injection velocity on the mobility of foam can mainly be ascribed to foam rheology. We found that mobility reduction factor increases with injection velocity, which could prompt the assertion that AOS foam is shear thickening. However, MRF includes the effects of viscosity and relative permeability. If we could discount the effects of the relative permeability, it will probably exhibit a shear-thinning behavior: but it is not easy to separate the viscosity and relative permeability effects.

One of the important findings of this study is the formation of a secondary desaturation front propagating into the direction opposite of the foam propagation, thus denoting the backward desaturation front. A similar backward front at different experimental conditions was also observed in previous studies (Apaydin and Kovscek, 2001; Nguyen et al., 2003), but its generation mechanism was not discussed in detail. The occurrence of the backward secondary foam front possibly results from an increase in lamellae generation by capillary snap-off at the outlet boundary. Several studies have indeed shown that when fluids approach a sudden permeability increase, capillary pressure in the low permeable region may diminish sufficiently to cause higher capillary snap-off rates in the low permeable region (Yortsos and Chang, 1990; Chaouche et al., 1993; van Duijn et al., 1995; van Lingen, 1998). This idea is supported by several studies of foam flow in porous media having a permeability contrast larger than four (Falls et al., 1988; Ransohoff and Radke, 1988; Rossen, 1999; Tanzil et al., 2000). In the present study, the outlet boundary of the porous medium is an extreme case of sudden permeability increase from a finite value to practically infinity. This is highly favorable for snap-off, since capillary pressure is nearly zero near the outlet boundary, and thus it is much smaller than the critical capillary pressure for snap-off P_c^{sn} . The presence of foam-forming surfactant (i.e., AOS) ensures formation of stable foam bubbles. Such foam bubbles can invade into smaller liquid-filled pores, which were not contacted by gas during forward foam propagation.

This study leads to a few general remarks about foam propagation over typical inter-well distances. It should be stressed that foam bubbles hardly propagate in porous media like individual fluid particles, but instead they are created and destroyed as the gas moves through the porous medium. This study has established that the desired foam strength can be achieved by

ensuring that bubble density is sufficiently large, by using an adequate surfactant at the appropriate concentration. Therefore, a way to ensure foam propagation in a homogeneous sandstone reservoir is to maintain enough surfactant by pre-flushing the reservoir with a surfactant slug ahead of the foam front. The optimum surfactant slug size should be determined using numerical modeling (e.g. using the SBP model including surfactant transport) according to reservoir characteristics, rock-fluid properties, presence of oil and economic factors. This is supported by several laboratory studies (Svorstøl et al., 1996; Vassenden et al., 1999), field trials (Friedman et al., 1994; Skauge et al., 2002; Blaker et al., 1999) and commercial projects (Martin et al., 1992) that showed foam propagation over distance between 10 and 100s of meters.

3.5 Conclusions

A series of CT scanned foam flow experiments was conducted in the oil-free Bentheimer sandstones to investigate the dependence of foam mobility on the surfactant concentration and total injection velocity. AOS surfactant was used to stabilize foam. Either a fresh core sample for each concentration was used (multiple cores experiments) or foam flow was performed in a single core for a cycle of increasing-decreasing concentration and velocity (single core experiments). Below are the main conclusions of this study:

- From the measured CT scan data it was found that, in the first injected pore volume, foam flows in a front-like manner, characteristic of the displacement of a less viscous fluid by a more viscous one. Shortly after the foam breakthrough, a secondary backward desaturation front emerges for a sufficiently high surfactant concentration.
- Foam mobility is reduced by an order of magnitude during the first injected pore volume. During a longer injection time foam mobility decreases further with increasing surfactant concentration. The steady-state foam mobility diminishes by two to three orders of magnitude.
- The secondary desaturation front appears earlier for higher surfactant concentration and injection velocity. This front is characterized by a large foam mobility reduction and further liquid desaturation in the foam-filled porous medium.
- A hysteresis is observed for the cycles of increasing-decreasing surfactant concentration, ranging from 0.1 to 1.5 wt%. Hysteresis is related to the adsorption-desorption kinetics of the surfactant. A separate study is required to investigate these mechanisms in detail.
- Foam mobility exhibits a hysteresis for a velocity cycle ranging from 1 to 10 ft/day. This indicates that foam trapping occurs during the increase of velocity and that the trapping persists when velocity decreases.

Chapter 4

FOAM MOBILITY TRANSITION IN POROUS MEDIA*

Abstract

Flow of nitrogen foam stabilized by alpha olefin sulfonate (C_{14-16} AOS) was studied in a natural sandstone porous media using X-ray Computed Tomography. Foam was generated by a simultaneous injection of gas and surfactant solution into a porous medium initially saturated with the surfactant solution. It was found that the foam undergoes a transition from a weak to a strong state at a characteristic gas saturation of $S_{gc} = 0.75 \pm 0.02$. This transition coincided with a substantial reduction in foam mobility by a two-order of magnitude and also with a large reduction in overall water saturation to as low as 0.10 ± 0.02 . Foam mobility transition was interpreted by the surge of yield stress as gas saturation exceeded the S_{gc} . We proposed a simple power-law functional relationship between yield stress and gas saturation. The proposed rheological model captured successfully the mobility transition of foams stabilized by different surfactant concentrations and for different core lengths.

* Adapted from Simjoo et al. 'Rheological transition during foam flow in porous media', *J. Industrial & Engineering Chemistry Research*, 51 (30), 10225-10231, 2012.

4.1 Introduction

Foam is a dispersion of gas in a continuum liquid phase stabilized by a surfactant (Exerowa and Kruglyakov, 1998). Foaming leads to gas mobility decreases significantly (Patzek, 1988; Schramm and Wassmuth, 1994; Rossen, 1996). This has numerous applications in oil and gas recovery operations, including acid diversion during matrix stimulation (Kibodeaux et al., 1994; Behenna, 1995; Rossen, 1996), water and gas shutoff (Hanssen and Dalland, 1994; Zhdanov et al., 1996) and mobility control for enhanced oil recovery (EOR) (Patzek, 1996; Turta and Singhal, 1998).

In the previous chapter, we investigated in detail foam propagation in porous media. An anomalous transition in foam mobility was observed due to the presence of a backward secondary foam front. A similar behavior of foam mobility was also reported earlier (Apaydin and Kovscek, 2001; Nguyen et al., 2003), but was not discussed in detail. The mobility transition is crucial since it determines the mobility reduction factor used as input in modeling and numerical simulations of foam applications. This study attempts to demonstrate that foam mobility transition is a real physical effect and to provide an explanation for this. The premise of this study is that foam in porous media is a non-Newtonian fluid (Falls et al., 1988; Zitha and Du, 2010), which is characterized by a yield stress: when external forces are smaller than yield stress, foam does not shear, but when external forces are larger than yield stress, then foam shears with a power-law behavior. Since we expect yield stress to increase during foam flow, this rheological model could account for gas trapping and for the observed mobility transition.

In previous studies (Rossen, 1988; Falls et al., 1989; Kovscek and Radke, 1994; Robert and Mack, 1997; Chen et al., 2005) the existence of yield stress during foam flow was described by a threshold pressure gradient. It was found that when the pressure gradient exceeds a certain value, foam generation is triggered due to the mobilization of stationary lamellae, leading to a further reduction in foam mobility (Falls et al., 1989; Rossen and Gauglitz, 1990; Tanzil et al., 2002; Kam and Rossen, 2003). The threshold pressure gradient may vary from several psi/ft to as low as 1 psi/ft depending on the type of gas, petrophysical properties of porous media, and surfactant type and concentration (Ranshoff and Radke, 1988; Yang and Reed, 1989; Rossen and Gauglitz, 1990; Friedmann et al., 1994; Tanzil et al., 2002; Gauglitz et al., 2002). To describe the yield behavior of stationary lamellae on the pore scale level several studies (Falls et al., 1989; Rossen, 1990; Cohen et al., 1997; Nguyen et al., 2004) employed the Young-Laplace relation as a balance between the imposed pressure gradient and the equilibrium lamella tension. Others (Rossen and Wang, 1999; Balan et al., 2011) described yield stress as a fixed parameter defined by a ratio of surface tension to pore-throat radius, by approximating the porous medium as a bundle of capillary tubes. However, for modeling foam in porous media most of the previous studies (Friedmann et al.,

1991; Kovscek et al., 1997; Bertin et al., 1998; Myers and Radke, 2000; Kam, 2008; Chen et al., 2010, Ashoori et al., 2012) described foam as a simple power-law fluid, thus ignoring the contribution of yield stress. Neglect of yield stress may not always be satisfied during foam flow and using this simplification without caution may lead to miscalculation of foam mobility.

To check this hypothesis we conducted experiments where nitrogen and a surfactant solution (1.0 wt% AOS in 0.5 M NaCl brine) were co-injected in the Bentheimer core with a diameter of 3.8 ± 0.1 cm and a length of 38.4 ± 0.1 cm. CT scan images were taken during foam flow and sectional pressure drops were measured at eleven points through the core length. We also revisited the results of the foam flow experiment reported in Chapter 3. In this chapter we will provide the experimental description, followed by a presentation and discussion of the results. Finally, main conclusions of the study are drawn.

4.2 Experimental description

4.2.1 Materials

The surfactant used to perform the experiments was C₁₄₋₁₆ alpha olefin sulfonate (AOS, Stepan). It was provided as an aqueous solution containing 40.0 wt% of active material and was used as received without further treatment. The surfactant solution was prepared using 0.5 M sodium chloride (NaCl, Merck) and its critical micelle concentration (c.m.c) was 4.0×10^{-3} wt%. Nitrogen gas with a purity of 99.98% was used to perform the experiments.

The porous medium used was Bentheimer sandstone. This is a quartzitic, quasi-homogeneous and isotropic natural porous media. The core samples with a diameter of 3.8 ± 0.1 cm and length of 38.4 ± 0.1 cm were used in the experiments. The absolute permeability to brine was 2.5 ± 0.1 Darcy. The average porosity estimated from the CT images was $21.0\% \pm 0.1$. The core samples were encapsulated in a thin layer of low X-ray attenuation Araldite self-hardening glue to avoid possible bypassing along the side of the core. After hardening, the glued core was machined to ensure that the core fits precisely into the core-holder. Several holes were also drilled through the glue layer into the core surface along the core length for pressure measurements.

4.2.2 Set-up and CT imaging settings

The set-up used to perform core-flooding experiments is shown in Fig. 4.1. It consists of a core-holder in line with a double effect piston displacement pump (Pharmacia Biotech P-500) parallel with a gas mass flow controller (Bronkhorst) and on the other end a back pressure regulator and a fraction-collector for the produced fluids. The pump was used to inject brine and surfactant solution. Nitrogen gas was supplied by a 200 bar cylinder equipped with a pressure regulator (KHP Series, Swagelok) and connected to the core inlet through a mass flow controller. A data

acquisition system (National Instruments) was used to record pressure, liquid production and gas and liquid injection rates. The core-holder was placed horizontally on the couch of the scanner. Eleven differential pressure transducers were used to monitor local pressure drops along the core length. The pressure ports divided the core length into twelve equal sections with a length of 3.2 cm. The pressure drop was measured between the core sections. Another differential pressure transducer was also used to record the overall pressure drop.

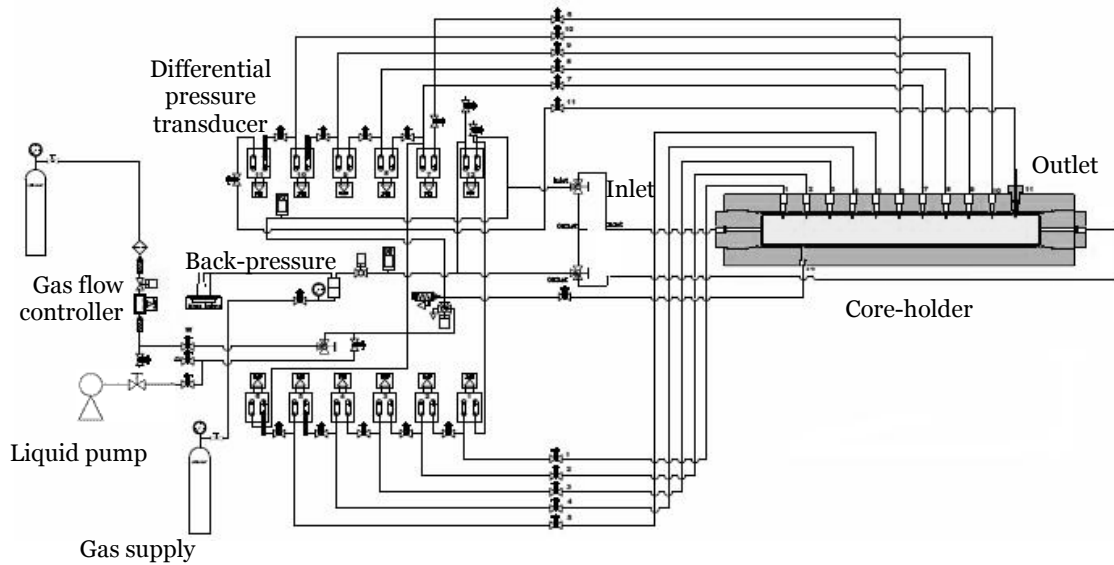


Fig. 4.1: Schematic of the experimental set-up used to perform foam flow experiment. The core-holder was placed horizontally on the couch of the CT scanner.

The CT imaging settings used in the experiments are listed in Table 4.1. The CT scans were obtained using a third generation SAMATOM Volume Zoom Quad slice scanner. The X-ray tube of the CT scanner operated at a voltage of 140 kV and a current of 250 mA. The thickness of each CT slice was 3 mm and one series of scan included 128 slices. The spiral scan mode was used for image acquisition. This allowed fast and continuous acquisition of the CT scan data from a complete volume and generated images using a standard reconstruction kernel after the data interpolation (Mees et al., 2003). The B40 medium filter was used for the reconstruction of the images. A typical slice image consists of 512×512 pixels with the pixel size of $0.3 \text{ mm} \times 0.3 \text{ mm}$. Since noise for CT images typically ranges from 3 to 20 Hounsfield units, accuracy of measured fluid saturations was within $\pm 2\%$. Image analysis was performed using a series of numerical codes developed by the authors in Matlab (The MathWorks) and visualization of the 3D CT images was done with Avizo (Visualization Sciences Group).

Table 4.1: Settings of CT scan measurements.

Specification	Quantity
Tube voltage (kV)	140
Tube current (mA)	250
Slice thickness (mm)	3
Pixel size (mm×mm)	0.3×0.3
Image reconstruction kernel	B40 medium
Scan mode	Spiral

To compute water saturation S_w , from the measured attenuation coefficients in Hounsfield units (HU), the following equation was used:

$$S_w = \frac{HU_{foam} - HU_{dry}}{HU_{wet} - HU_{dry}} \quad (4.1)$$

where subscripts *dry*, *wet*, and *foam* stand for the dry core, surfactant-saturated core, and foam flow, respectively.

4.2.3 Experimental procedure

The basic sequence used to conduct core-flooding experiments is given in Table 4.2. After flushing the core with CO₂, it was saturated by injecting brine for at least 10 pore volumes (PV) while maintaining a back-pressure of 25 bar. This was done to dissolve any CO₂ present in the core and thus to ensure complete core saturation with brine. Then three pore volumes of the surfactant solution were injected into the core to satisfy its adsorption capacity. Next, N₂ and surfactant solution were co-injected to generate foam in the porous medium at a fixed superficial velocity of 4.58 ft/day and with foam quality of 91% at a back-pressure of 20 bar and ambient temperature (21±1 °C).

Table 4.2: Basic sequence used to perform core-flooding experiments.

Step	Description	Back pressure (bar)	Surfactant concentration (wt%)	Flow rate (cm ³ /min)
1	CO ₂ flushing	-	-	5.0
2	Core saturation	25	-	1.0
3	Surfactant pre-flush	20	1.0	1.0
4	Co-injection of N ₂ and surfactant	20	1.0	1.0 (gas) + 0.1 (surfactant)

The foam flow experiments were analyzed in terms of CT images, water saturation profiles obtained from these images and reduction of foam mobility. In this study, the foam mobility reduction factor (MRF) was defined as a ratio of measured pressure drop for foam flow to the corresponding pressure drop for the flow of water at the same superficial velocity:

$$MRF = \frac{\Delta P_{foam}}{\Delta P_{water}} \Big|_u \quad (4.2)$$

4.3 Results and discussion

In the following section we will first elucidate the dynamics of foam flow for 1.0 wt% AOS foam in a core with the length of 38.4 cm (long core). A detail description of AOS foam flow using a shorter core length (17.0 cm) at different surfactant concentrations was described in Chapter 3. Then we will examine the relation between foam mobility and gas saturation for different AOS concentrations and core lengths.

4.3.1 Long core foam flow

Fig. 4.2 shows a series of 3D CT images taken at different injected pore volumes during 1.0 wt% AOS foam in the long core. As foam generation proceeds, first a blue front appears in the left side (inlet) of the core after 0.09 PV. This gives a first qualitative impression about the change in water saturation. The frontal region is sharp, indicating that foam displaces the surfactant solution in a characteristic front-like manner. The foam front breaks through the core at around 0.67 PV. Slightly after breakthrough time, a secondary foam front emerges at the outlet region, which propagates backward. The presence of a secondary front is evident by a progressive darkening and spreading of the green zone into the core (see the image at 2.0 PV). The change in color from blue to green means that the secondary front is stronger leading to more liquid desaturation from the previously foam-filled porous medium.

For further analysis of foam flow, water saturation (S_w) profiles at different injected pore volumes are shown in Fig. 4.3. For each profile, before foam breakthrough, S_w increases from 0.35 ± 0.02 to unity through a sharp transition zone. This behavior of the S_w profile supports the stable displacement of the surfactant solution by foam as shown in the CT images. After foam breakthrough the remaining S_w is distributed uniformly through the core length and exhibits an average value of 0.35 ± 0.02 (see the S_w profile at 1.5 PV). Thereafter, similarly to section 3.3.1 a secondary desaturation front emerges in the outlet region, leading to a substantial reduction in S_w to as low as 0.10 ± 0.02 . The secondary foam front propagates with a slower rate compared to the initial forward foam front. Let us consider the S_w profile at 18.7 PV. As the secondary front crosses the downstream core sections, the average S_w diminishes from 0.35 ± 0.02 to 0.10 ± 0.02 . This part

is followed by a long transition zone extending from 23.0 ± 0.1 to 10.0 ± 0.1 cm toward the core inlet. Through this length S_w increases gradually from 0.10 ± 0.02 to 0.35 ± 0.02 .

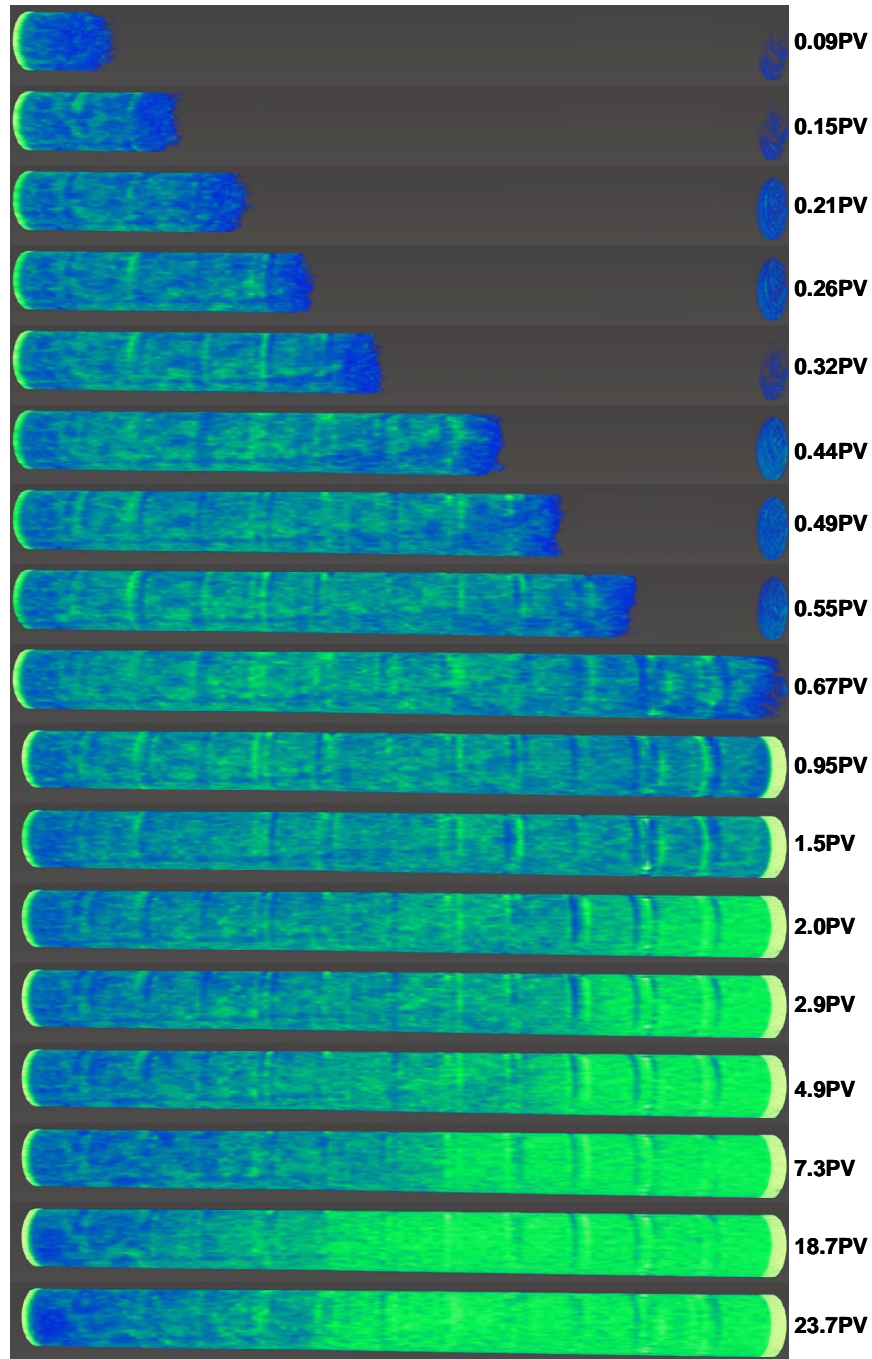


Fig. 4.2: 3D CT images obtained during 1.0 wt% AOS foam in the Bentheimer sandstone core with the length of 38.4 cm. First, a forward foam front (blue colored zone) propagates throughout the core and breaks through at around 0.67 ± 0.02 PV. Slightly after breakthrough time, a secondary foam front (green color) emerges at the outlet region and propagates backward. This leads to further liquid desaturation from the previously foam-filled porous medium.

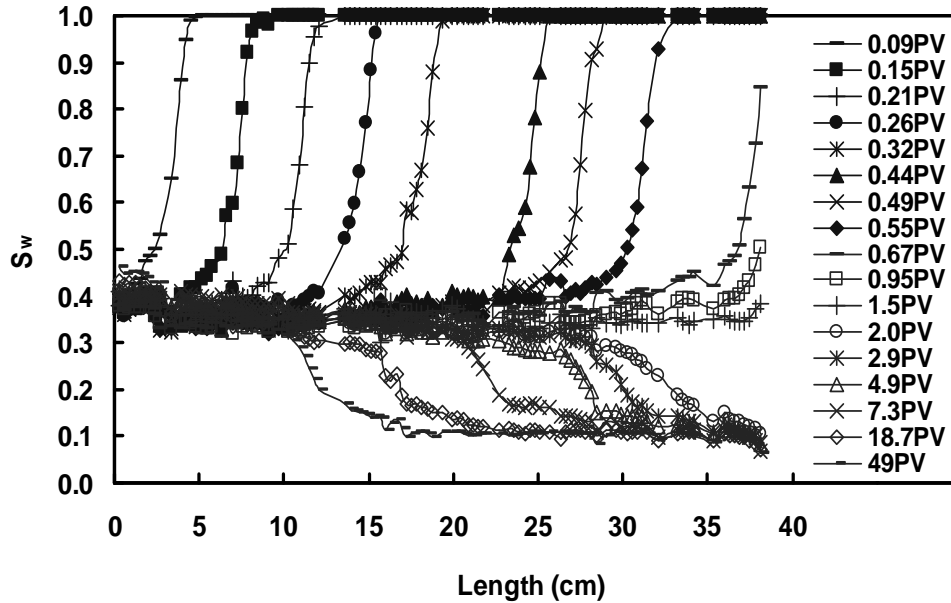


Fig. 4.3: Water saturation profiles obtained from the CT images shown in Fig. 4.2. The closed symbols stand for the forward foam front until breakthrough time. The open symbols indicate foam flow after breakthrough time. The presence of secondary foam front is more evident after 1.5 PV: it leads to a significant reduction in the average S_w from 0.35 ± 0.2 to 0.10 ± 0.02 .

The description of foam propagation can be elaborated further by plotting the sectional MRF for different injected pore volumes as shown in Fig. 4.4. The inset shows the MRF profiles until slightly after foam breakthrough. It shows that when the foam front reaches each section, the corresponding MRF first increases steeply and then remains practically constant as the foam front passes through the section. The behavior of the sectional MRF correlates well with the S_w profile. Let us consider the MRF profile at 0.22 PV injected. Over the first 10.0 cm the sectional MRF increases from unity to 25 ± 5 and S_w diminishes to about 0.35 ± 0.02 as a result of foam propagation. Then MRF decreases steeply and reaches unity for the downstream sections subject to single-phase flow, i.e., $S_w = 1.0$. After foam breakthrough a constant MRF of about 28 ± 5 is established in all core sections, see for instance the MRF profile at 0.71 PV in Fig. 4.4. This MRF leads to an average water saturation $S_w = 0.35 \pm 0.02$ over the core length (Fig. 4.3), except near the outlet region where S_w is slightly higher due to the capillary end effect. As foam flow continues further, MRF increases significantly starting from the last section near the core outlet proceeding through consecutive core sections toward the core inlet. For instance the sectional MRF over the last section of the core increases substantially from 28 ± 5 to 500 ± 5 after 3.0 PV of foam injection. This means that foam with a higher strength was developed near the core outlet. The steep increase observed above in the sectional MRF coincides with the development of a backward secondary foam front noted in the CT images. The MRF profile also confirms that the secondary

foam front travels at a slower rate compared to the initial forward foam front. For instance, after 3.0 PV the secondary front travels up to 27.2 ± 0.1 cm from the core inlet.

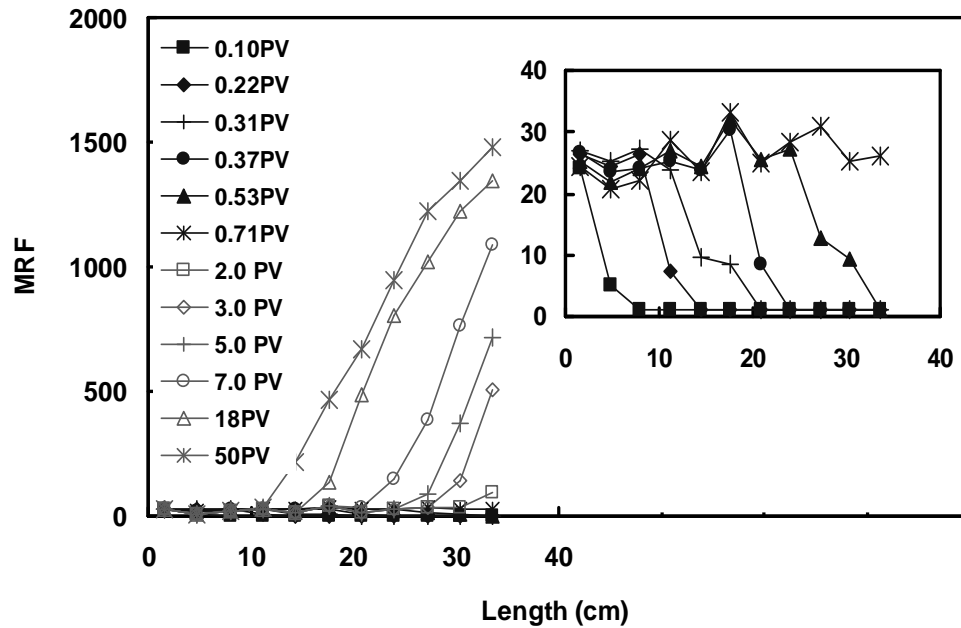


Fig. 4.4: Sectional mobility reduction factor (MRF) obtained during 1.0 wt% AOS foam. MRF was defined as a ratio of pressure drop for foam flow to that for single-phase water flow. In the inset figure sharp increase in the sectional MRF corresponds to reach foam front to that section. The presence of secondary foam front leads to a substantial increase in MRF (open symbols) compared to the forward foam front (inset figure).

Fig. 4.4 shows that MRF due to the backward secondary foam front is much higher than that due to the forward foam front. A substantial increase in MRF leads to a steep decrease of remaining water saturation: its average value after the forward foam front was 0.35 ± 0.02 , whereas it diminished further to 0.10 ± 0.02 in the region swept by the secondary foam front. From the above observations it follows that during the forward foam flow a weak foam state is established over the entire core length. Then, when the secondary foam front emerges, the foam undergoes a transition to a strong state: through this transition MRF increases by two orders of magnitude.

4.3.2 Foam mobility transition

To inspect the relation between gas saturation (S_g) and foam mobility in porous media, we examine the behavior of MRF as a function of S_g for different AOS concentrations and core lengths, as shown in Figs. 4.5 through 4.7. Gas saturation was obtained by averaging the CT data over each core section. Let us first consider foam flow in the short core for 0.5 wt% AOS (Fig. 4.5). For the first section, MRF remains at a low value slightly higher than 150 ± 5 with the S_g of 0.73 ± 0.02 . For the second section, MRF is initially very low, but when S_g exceeds a certain critical value, MRF increases steeply, reaching a final value of 988 ± 5 at $S_g = 0.86 \pm 0.02$. MRF behavior is

even more striking in the third and fourth sections. MRF remains very low as long as S_g is below 0.70 ± 0.02 . However, slightly above this value MRF increases significantly and finally reaches a value nearly equal to 2000 ± 5 at $S_g = 0.88 \pm 0.02$.

Qualitatively, similar MRF behavior was observed for 1.0 wt% AOS foam in the short core as shown in Fig. 4.6. For the S_g below 0.70 ± 0.02 , MRF in all sections exhibits values that are lower than 100 ± 5 . However, above a critical gas saturation MRF increases steeply, reaching a final value of 2500 ± 5 at the $S_g = 0.90 \pm 0.02$.

In order to examine the effect of core length on the foam mobility transition, Fig. 4.7 shows MRF as a function of S_g for 1.0 wt% AOS foam in the long core. The general behavior of mobility transition is similar to that observed in the short cores. The first and second sections are characterized by a very low value of MRF only slightly higher than 20 ± 5 and with the S_g of 0.65 ± 0.02 . For the third section, MRF increases slightly to 50 ± 5 as S_g approaches 0.70 ± 0.02 . By further increase in S_g , MRF exhibits a modest increase as can be seen for the fourth section. As S_g goes beyond a certain value, MRF increases more steeply and reaches a maximum value nearly equal to 1400 ± 5 at the $S_g = 0.90 \pm 0.02$. From the above results it is inferred that as gas saturation exceeds a critical value, MRF rises sharply indicating again a transition from a weak to a strong foam state. This mobility transition occurs at a characteristic gas saturation of $S_{gc} = 0.75 \pm 0.02$.

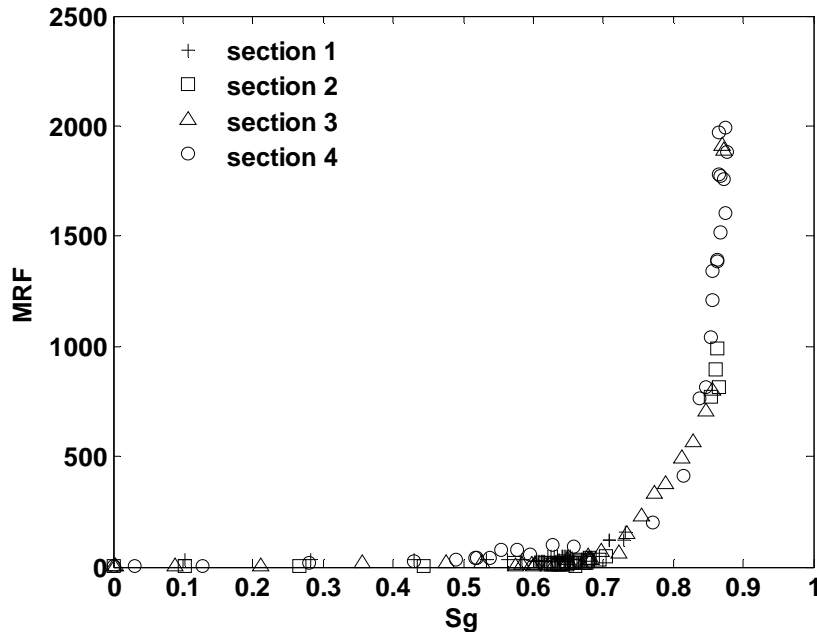


Fig. 4.5: Foam mobility reduction factor versus gas saturation during 0.5 wt% AOS foam in the Bentheimer sandstone core with the length of 17.0 ± 0.1 cm. The length of each section is 4.25 cm. Foam mobility transition occurs at a characteristic gas saturation of $S_{gc} = 0.75 \pm 0.02$.

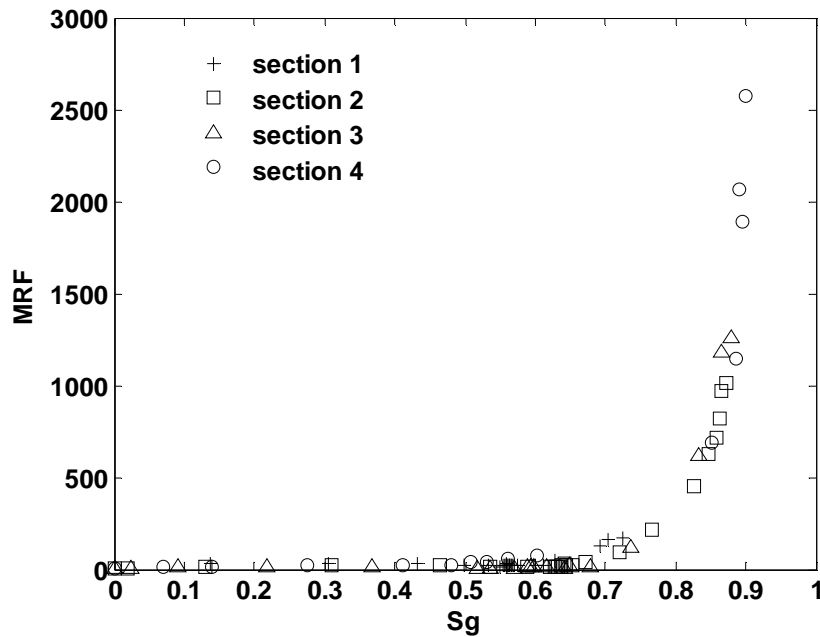


Fig. 4.6: Foam mobility reduction factor versus gas saturation during 1.0 wt% AOS foam in the Bentheimer sandstone core with the length of 17.0 ± 0.1 cm. The length of each section is 4.25 cm.

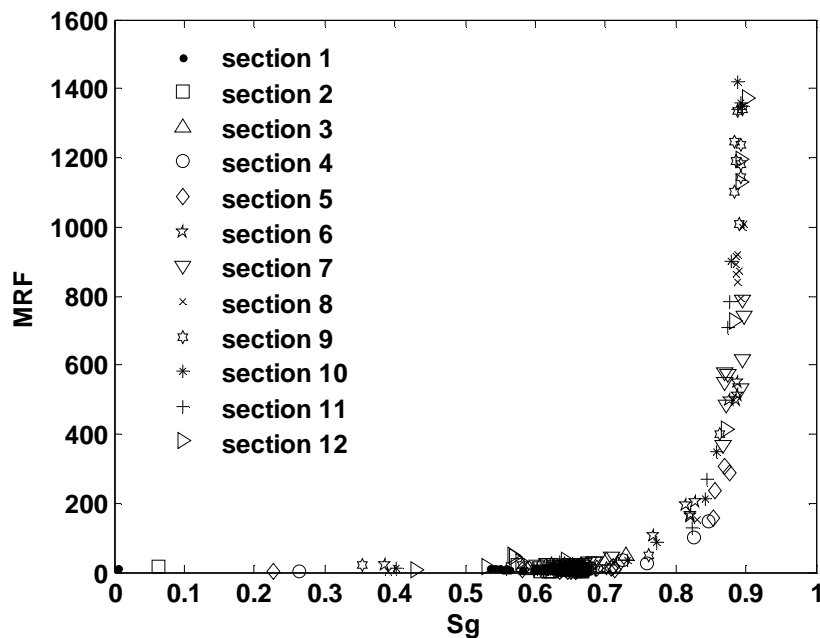


Fig. 4.7: Foam mobility reduction factor versus gas saturation during 1.0 wt% AOS foam flow in the Bentheimer sandstone core with the length of 38.4 ± 0.1 cm. The length of each section is 3.2 cm.

4.3.3 Mechanistic description of foam mobility transition

To interpret foam mobility transition, we provide a mechanistic description of foam rheological behavior within a wide range of gas saturation. To this end, we rely upon the stochastic bubble population model (Zitha, 2006; Zitha and Du, 2010) where the basic postulate is that bubble

generation is a stochastic process. In this model foam flow in porous media is described as a yield stress fluid obeying a Herschel-Bulkley rheological model, which can be expressed as follows:

$$\begin{cases} \dot{\gamma} = 0 & \tau \leq \tau_y \\ \tau = \tau_y + \mu_p |\dot{\gamma}| & \tau > \tau_y \end{cases} \quad (4.3)$$

where $\dot{\gamma}$ and μ_p are shear rate and plastic viscosity, respectively. The plastic viscosity μ_p is defined as follows:

$$\mu_p = \mu_g + K_0 |\dot{\gamma}|^{m-1} \quad (4.4)$$

where K_0 and m are plasticity coefficient and power-law exponent. Foam viscosity can be described by dividing Eq. (4.3) by shear rate and then we will have:

$$\mu_f = \frac{\tau}{|\dot{\gamma}|} = \frac{\tau_y}{|\dot{\gamma}|} + \mu_p \quad (4.5)$$

Eq. (4.5) shows that foam rheology exhibits different behaviors depending on shear rate. Foam behaves like a solid material if the shear rate approaches zero, while a gas-like behavior is expected when the shear rate becomes very large. To describe the shear rate we approximate porous medium as a bundle of capillary tubes, thus we have:

$$|\dot{\gamma}| = c_0 v_f / r \quad (4.6)$$

where $r = c_1 (k / \phi)^{1/2}$ is pore radius, k is absolute permeability, ϕ is porosity, and c_0 and c_1 are geometric constants. Substituting in Eq. (4.3) using Eqs. (4.4), (4.5) and (4.6) we obtain:

$$\begin{cases} v_f = 0 & \tau \leq \tau_y \\ \mu_f = \mu_g + K_1 v_f^{m-1} + K_2 \frac{\tau_y}{v_f} & \tau > \tau_y \end{cases} \quad (4.7)$$

where K_1 and K_2 read as follows:

$$K_1 = K_0 \left(\frac{c_0}{c_1} \right)^{m-1} \left(\frac{\phi}{k} \right)^{\frac{1}{2}(m-1)} ; \quad K_2 = \frac{c_1}{c_0} \left(\frac{k}{\phi} \right)^{\frac{1}{2}} \quad (4.8)$$

If yield stress is left out from Eq. (4.7), the resulting expression will be similar to the common form of foam viscosity equation, which is as follows:

$$\mu_f = \mu_g + \frac{\alpha n}{v_f^{1/3}} \quad (4.9)$$

where α is a constant parameter, and n is bubble density. By comparing Eq. (4.9) with Eq. (4.7) while leaving yield stress out we will have:

$$m = 2/3 \quad (4.10)$$

$$K_1 = \alpha n \quad (4.11)$$

Since in the porous medium bubbles are as large as the pores, bubble density could be described as a number of pores occupied by gas bubbles per unit volume. From the Kozeny-Carman relationship the number of pores per unit volume is obtained as follows:

$$n_{pores} = \kappa \left[\frac{150(1-\phi)^2}{\phi^3} k \right]^{-3/2} \quad (4.12)$$

where κ is a coefficient depending on the packing system. This coefficient was assumed to be one. Therefore, bubble density reads:

$$n = S_g \left[\frac{150(1-\phi)^2}{\phi^3} k \right]^{-3/2} \quad (4.13)$$

by substituting in Eq. (4.7) using Eqs. (4.10), (4.11) and (4.13) we will have the following expression to describe foam viscosity:

$$\begin{cases} v_f = 0 & \tau \leq \tau_y \\ \mu_f = \mu_g + \alpha S_g \left[\frac{150(1-\phi)^2}{\phi^3} k \right]^{-3/2} v_f^{-1/3} + K_2 \frac{\tau_y}{v_f} & \tau > \tau_y \end{cases} \quad (4.14)$$

For using Eq. (4.14) we need to find a way to directly quantify yield stress during foam flow. Moreover, the relevant data to describe the behavior of yield stress are scarce in the literature of foam in porous media. In order to examine how yield stress evolves during foam flow, we used Eq. (4.14) to calculate yield stress by substituting foam viscosity from Darcy's equation and using the experimental pressure drop and saturation data. For water and gas relative permeability functions we used the following Corey-type correlations:

$$k_{rw}(S_w) = \begin{cases} 0 & 0 \leq S_w \leq S_{wc} \\ k_{rw}^0 \left(\frac{S_w - S_{wc}}{1 - S_{wc} - S_{gr}} \right)^{n_w} & S_{wc} \leq S_w \leq 1 - S_{gr} \\ k_{rw}^0 + (1 - k_{rw}^0) \frac{S_w + S_{gr} - 1}{S_{gr}} & 1 - S_{gr} \leq S_w \leq 1 \end{cases} \quad (4.15)$$

where S_{wc} , k_{rw}^0 and n_w are connate water saturation, end-point water relative permeability and the relative permeability exponent for water. Similarly $k_{rg}^f(S_w)$ is expressed as:

$$k_{rg}^f(S_w) = \begin{cases} 1 - \left(1 - k_{rg}^{f,0}\right) \frac{S_w}{S_{gr}} & 0 \leq S_w \leq S_{wc} \\ k_{rg}^{f,0} \left(\frac{1 - S_w - S_{gr}}{1 - S_{wc} - S_{gr}} \right)^{n_f} & S_{wc} \leq S_w \leq 1 - S_{gr} \\ 0 & 1 - S_{gr} \leq S_w \leq 1 \end{cases} \quad (4.16)$$

where $k_{rg}^{f,0}$ is the end-point foamed-gas relative permeability, and n_f is the corresponding Corey exponent. As Eq. (4.16) shows, no trapped gas term was used in the gas relative permeability function. The absence of gas trapping indicates that during foam development flow occurs at a finite velocity. This is consistent with the CT images (Fig. 4.2) and water saturation profiles (Fig. 4.3), reflecting the fact that both forward and backward foam fronts propagate with finite velocity: 58.0 ± 0.1 cm/PV for forward foam and 0.8 ± 0.1 cm/PV for backward foam. Thus as a first approximation we can discount the trapping effect and use the gas relative permeability function without modification. Now by using the measured pressure drops and saturation data along with other required parameters, Table 4.3, yield stress can be calculated during the course of foam flow by using Eq. (4.14).

Table 4.3: Parameters used in the numerical computations.

Parameter	Value
k (m ²)	2.5×10^{-12}
ϕ	0.21
S_{wc}	0.10
S_{gr}	0
k_{rw}^0	0.75
$k_{rg}^{f,0}$	1.0
n_w	5
n_f	3.4
c_1/c_0	0.71
α (Pa s ^{2/3} m ^{10/3})	5.8×10^{-16}
σ_{gw} (N/m)	30.0×10^{-3}
u_w (m/s)	1.47×10^{-6}
u_g (m/s)	1.47×10^{-5}
μ_g (Pa s)	1.8×10^{-5}

Fig. 4.8 shows the calculated yield stress τ_y as a function of gas saturation S_g for 1.0 wt% AOS foam in the long core. It shows that τ_y is small for low S_g , but it rises sharply above a certain gas saturation, $S_{gc} = 0.75 \pm 0.020$. For the S_g smaller than 0.75 ± 0.02 , τ_y hardly exceeds 1.0 ± 0.1 Pa. However, when S_g is larger than 0.75 ± 0.02 , τ_y rises sharply and finally reaches a maximum value of 43.0 ± 0.1 Pa at $S_g = 0.90 \pm 0.02$.

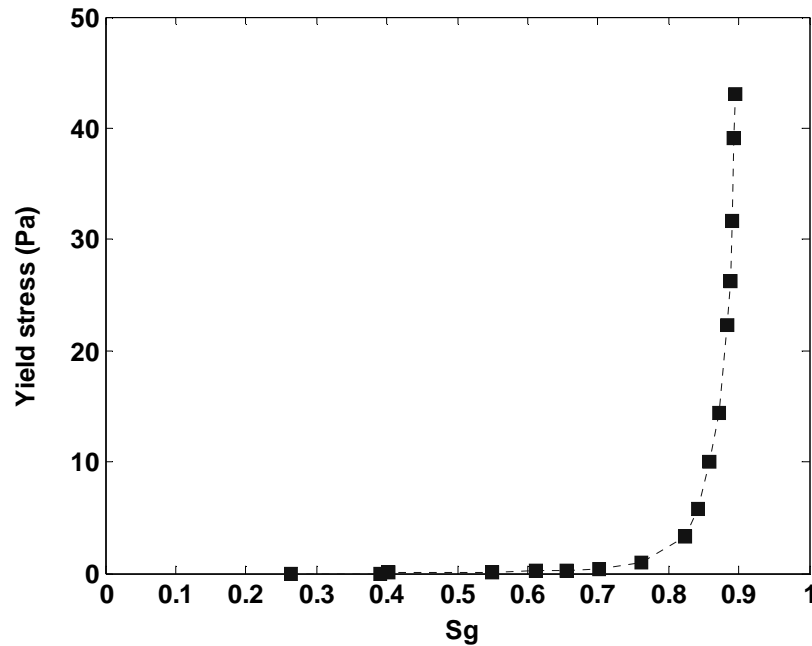


Fig. 4.8: Yield stress versus gas saturation for 1.0 wt% AOS foam flow in the Bentheimer sandstone core with the length of 38.4 ± 0.1 cm. A sharp rise of the yield stress occurs above a characteristic gas saturation of $S_{gc} = 0.75 \pm 0.02$.

The dependence of τ_y on S_g reflects itself in the behavior of MRF as a function of S_g (Figs. 4.5 to 4.7). When the forward foam front breaks through the core, the average gas saturation along the core is about 0.65 ± 0.02 , which is below the S_{gc} . This results in a very small yield stress according to Fig. 4.8. Therefore, foam viscosity remains low, leading to a low MRF observed during forward foam flow (see inset in Fig. 4.4). After foam breakthrough, however, more liquid desaturation occurs in the core due to the presence of the secondary foam front. This leads to a large increase in the average gas saturation, and also, so does yield stress. Thus, a higher foam viscosity is obtained during the secondary foam flow, leading to a large reduction in foam mobility. From the above discussion it can be inferred that the change in MRF from a low to a high value is essentially due to the build-up of yield stress during foam flow.

4.3.4 Dependence of yield stress on saturation

The dependence of foam mobility transition on gas saturation has not been discussed in the literature. In order to develop a mechanistic model, we inspired ourselves to bulk foam studies, recognizing that foam in porous media is fundamentally different from bulk foam. The dependence of yield stress on gas volume fraction is a commonly observed feature of bulk foams and concentrated emulsions (Khan et al., 1988; Princen and Kiss, 1989; Gardiner et al, 1998; Pal, 1999; Quintero et al., 2008): the yield stress rises sharply when the gas or oil volume fraction is higher than a critical value. Several authors (Mason et al., 1996; Saint-Jalmes and Durian, 1999; Rouyer et al., 2005) proposed the following power-law relationship to describe the yield stress of bulk foams:

$$\tau_y = a \frac{\sigma}{r} (S_g - S_{gc})^b \quad (4.17)$$

where σ is surface tension, r is bubble radius, S_{gc} is critical gas volume fraction, a and b are model parameters. The behavior of yield stress described by Eq. (4.17) is qualitatively consistent with our observation for the relation between yield stress and gas saturation shown in Fig. 4.8. Thus, as a first approximation we adopt this power-law relationship to describe yield stress during foam flow in porous media. We note that the origin of yield stress in bulk foam is from the dissipation among the gas bubbles, while in porous media the dissipation mainly results from the interaction of bubbles with the pore walls. To find the model parameters (a and b) we fitted the yields stress data obtained from the experiments to Eq. (4.17). The results are given in Table 4.4 for foam with different surfactant concentrations and core lengths. The yield stress data are well fitted by the power-law model, in which the coefficient a ranges from 17 to 52, and the exponent b ranges from 3.78 to 3.91.

Table 4.4: Model parameters obtained by fitting Eq. (4.17) to the yields stress data. The S_{gc} is equal to 0.75 ± 0.02 for all the foam flow experiments.

Sample	a	b	R^2
0.5 wt% AOS foam, short core	52	3.91	0.96
1.0 wt% AOS foam, short core	26	3.84	0.95
1.0 wt% AOS foam, long core	17	3.78	0.96

For the sake of simplicity we set the exponent b at four, and thus yield stress as a function of gas saturation reads as follows:

$$\tau_y = a \frac{\sigma}{r} (S_g - S_{gc})^4 \quad (4.18)$$

Thus, when gas saturation is below the S_{gc} , yield stress is zero and above that it is described by a power-law behavior. The proposed rheological model, with the coefficient a as the only fitting parameter, was used to calculate foam mobility. This is shown by the solid blue line in Fig. 4.9 to 4.11. We also provided the model results (solid red line) for the case where yield stress was left out of the foam viscosity equation, see Eq. (4.9). The figures show that the ‘model without yield stress’ does not capture the observed MRF behavior during mobility transition above the S_{gc} . However, by including yield stress into the foam viscosity equation, Eq. (4.14), the model results successfully captured the foam mobility transition. The good match of the model and the measured MRF supports the above idea that yield stress grows during the secondary foam front.

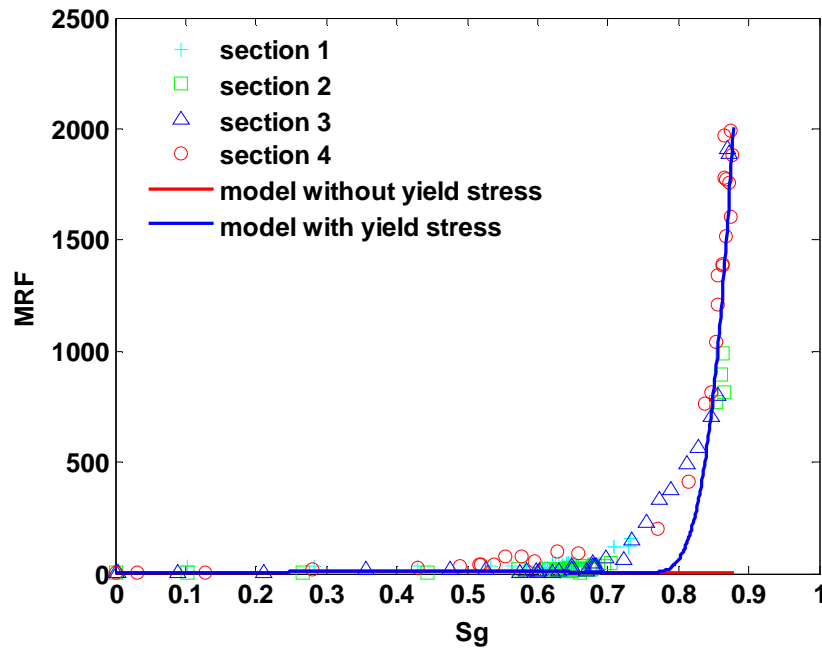


Fig. 4.9: Foam mobility reduction factor (MRF) versus gas saturation during 0.5 wt% AOS foam in the Bentheimer sandstone core with the length of 17.0 ± 0.1 cm. The solid lines represent the model results and the open symbols are experimental data.

We showed that the anomalous transition in foam mobility is a real physical effect and could be interpreted by the surge of the yield stress. We proposed a power-law model to describe the yield stress of foam as a function of gas saturation. In the frame of this model, foam flow in porous media is a yield stress fluid obeying a Herschel-Bulkley rheological model. It is based on the premise that the generated bubbles are as large as the pores and thus bubble density could be described as a number of pores occupied by gas bubbles per unit volume. This model also discounted the effect of gas trapping, reflecting that foam moves with a finite velocity consisting with the CT images and water saturation profiles (Figs. 4.2 and 4.3). We found that the proposed model is a valid heuristic representation of the foam mobility transition. However, further work is

still needed to refine the model for foams at different experimental conditions. Also, understating of the secondary desaturation effect and its connection to the mobility transition need to be elucidated further by the future studies.

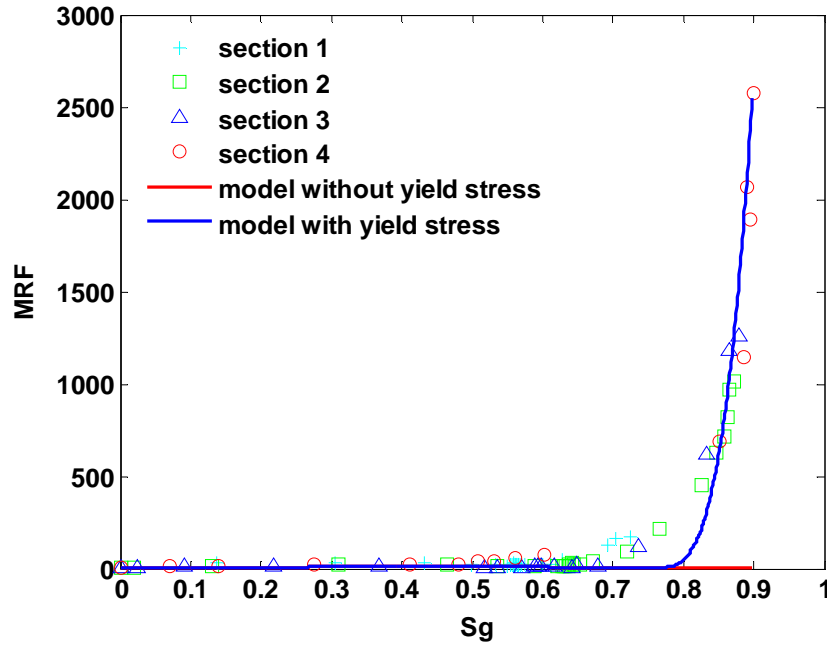


Fig. 4.10: Foam mobility reduction factor (MRF) versus gas saturation during 1.0 wt% AOS foam in the Bentheimer sandstone core with the length of 17.0 ± 0.1 cm.

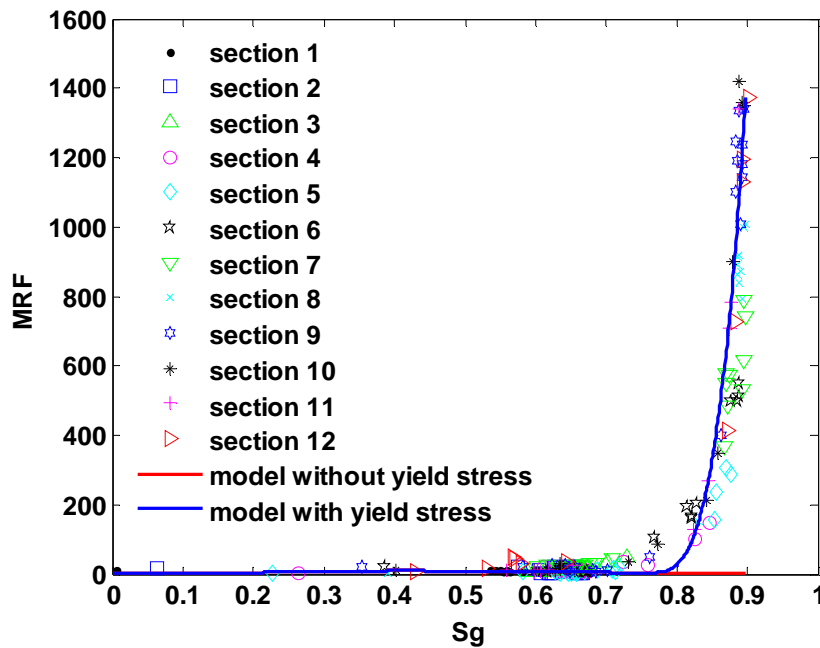


Fig. 4.11: Foam mobility reduction factor (MRF) versus gas saturation during 1.0 wt% AOS foam in the Bentheimer sandstone core with the length of 38.4 ± 0.1 cm.

4.4 Conclusions

Foam propagation in Bentheimer sandstone cores generated by the co-injection of nitrogen and alpha olefin sulfonate (C₁₄₋₁₆ AOS) surfactant in 0.5 M NaCl brine was studied. The displacement of the foam front was visualized with the aid of a CT scanner. The CT data were examined to map fluid saturations at different times. The sectional pressure drops were measured to determine the foam mobility reduction factor (MRF). The following conclusions can be drawn from this study:

- The 3D CT images revealed two foam propagation fronts: (a) the forward primary foam front, characterized by $MRF = 28 \pm 5$ and an overall water saturation of 0.35 ± 0.02 and (b) the backward secondary foam front which appears after foam breakthrough, characterized by $MRF = 1500 \pm 5$, and an overall water saturation of 0.10 ± 0.02 .
- The transition of foam mobility from a weak (low MRF) to a strong (high MRF) state occurs at a characteristic gas saturation of $S_{gc} = 0.75 \pm 0.02$.
- Foam mobility transition was successfully interpreted in terms of the surge of yield stress during foam flow. It was found that when gas saturation is below the S_{gc} , yield stress is nearly equal to zero coinciding with a weak foam. However, when gas saturation is larger than the S_{gc} , yield stress increases significantly leading to the observed strong foam.
- A functional relationship between yield stress and gas saturation was proposed to describe foam mobility transition, which is $\tau_y = a(\sigma/r)(S_g - S_{gc})^4$. When gas saturation is below the S_{gc} , yield stress falls to zero, and above that it is described by a power-law behavior.
- Foam mobility transition was successfully described by the stochastic bubble population model where foam rheology was modeled as a power-law fluid with a yield stress term. This combined rheological model was capable to capture foam mobility transition for different surfactant concentrations (0.5 and 1.0 wt%) and core lengths (17.0 ± 0.1 and 38.4 ± 0.1 cm).

Chapter 5

MODELING OF TRANSIENT FOAM FLOW USING STOCHASTIC BUBBLE POPULATION MODEL*

Abstract

A numerical analysis of the transient foam flow in an oil-free porous medium was presented using the stochastic bubble population (SBP) model. The premise of this model is that foam flow in porous media is a complex fluid and bubble generation is a stochastic process. The model is simple as it describes the net bubble generation using three parameters: maximum bubble density, bubble generation and bubble destruction coefficients. The SBP foam model was described in a series of non-linear partial differential equations in saturation, pressure and bubble density. We solved these equations using the IMPES method and performed a sensitivity analysis. Finally, we compared the saturation and pressure profiles obtained numerically with those obtained from the foam flow experiment in Bentheimer sandstone previously saturated by a surfactant solution. The good match between the numerical results and the experiments confirms that the SBP foam model is robust and reproduces the main features of the transient behavior of foam flow in porous media.

** Submitted to Transport in Porous Media (2012).*

5.1 Introduction

Foam has numerous applications in oil and gas recovery operations including acid diversion during matrix stimulation (Behenna, 1995), water and gas shutoff (Zhdanov et al., 1996) and mobility control for enhanced oil recovery (Patzek, 1996). Foam is generated when gas is injected in a porous medium containing a surfactant solution leading to large reduction of gas mobility (Kovscek and Radke, 1994; Rossen, 1996).

Besides the experimental studies, the description and prediction of foam behaviour in porous media rely on the proper modelling. Several foam models have been proposed to describe foam development, but among them fractional flow and population balance models have been more popular. Foam fractional flow modelling was advocated by Rossen et al. (Zhou and Rossen, 1994; Rossen, 1996; Rossen and Wang, 1999). They identified foam states using the so-called time-distance diagrams computed from the core flow studies. The authors argued that the computation is simplified when done near the critical capillary pressure (Khatib et al., 1988). This model assumes implicitly that foam is incompressible. The population balance approach introduced by Patzek (1988) and further developed by Falls et al. (1988) and Kovscek et al. (1994, 1995 and 1997) is based on the premise that foam mobility depends on bubble density. This model splits foam flowing in porous media in mobile and immobile fractions, which is in good qualitative agreement with the early experiments of Bernard et al. (1965) and Holm (1968). In spite of being comprehensive, the population balance theory did not gain full acceptance thus far, because this model involves many parameters that are difficult to determine experimentally.

Recently Zitha et al. (Zitha, 2006; Zitha and Du, 2010; Du et al., 2011) proposed an alternative population balance theory for foam flow in porous media. This theory (stochastic bubble population, SBP) is built upon the following basic postulates: (a) foam is a complex fluid and its rheology is described by the Herschel-Bulkley model, (b) foam rheology is mainly controlled by bubble density and (c) bubble generation is a simple stochastic process and the kinetics of foam generation obeys a simple exponential growth function. When applied to transient foam flow (forward movement of foam flow until breakthrough time), the SBP foam model does not require taking into account foam trapping, because the yield stress of foam is negligible and then foam trapping is unlikely to occur (for more detailed analyses see Chapter 4). This is in good agreement with studies of tracer transport during foam flow in porous media using X-ray computed tomography, which showed that foam could be trapped in parts of the domain during steady-state flow, but no trapped foam was discernible during transient flow (Nguyen et al., 2003 and 2007; Zitha et al., 2006). The new stochastic bubble population model lies therefore upon a more realistic picture of foam physics. Previous numerical studies showed that the SBP foam model is

physically and mathematically robust (Zitha, 2006; Zitha and Du, 2010). Kam and Rossen (Kam and Rossen, 2003; Kam et al., 2007; Kam, 2008) proposed a simplified population balance foam model where local equilibrium bubble density is a function of pressure gradient. In addition to covering the same features as the SBP, this model predicts multiple steady states observed in certain foam flow experiments (Gauglitz et al., 2002; Kam and Rossen, 2003). Ashoori et al. (2011-b) showed that the local equilibrium population balance model is a good approximation to describe large scale foam displacement, in a good agreement with the work of Chen et al. (2010).

In this chapter, we present a numerical analysis of foam flow in porous media by using the stochastic bubble population model and validate the analysis using experiments reported in Chapter 4. We use IMPES method (Carretero-Carralero et al., 2007; Zinati et al., 2008; Du et al., 2011) to solve the set of equations provided hereinafter and obtain water saturation, bubble density and water pressure profiles. We restrict our study to the injection of gas and surfactant solution until breakthrough time. This choice was made because the new population balance model reproduces the main features of the transient foam flow very well, but further work is needed to clarify foam behaviour after breakthrough.

5.2 Model formulation

Let us consider a porous medium with porosity ϕ and permeability k in a domain Ω with a bounding $\partial\Omega = \partial\Omega_I \cup \partial\Omega_B \cup \partial\Omega_O$, where $\partial\Omega_I$, $\partial\Omega_O$ and $\partial\Omega_B$ are the inlet, outlet and no-flow boundaries, respectively. The porous medium is initially saturated with the surfactant solution. The surfactant solution and gas are co-injected through the porous medium causing gas to break into stable foam bubbles. Denoting U_g and U_w Darcy velocity for gas and water, the total velocity for the mixture can be written as $U = U_g + U_w$. Ignoring gravity, the stochastic bubble population model amounts to the following system of partial differential equations:

$$\begin{cases} \phi \frac{\partial(\rho_i S_i)}{\partial t} + \nabla \cdot (\rho_i \mathbf{u}_i) = 0 \\ \mathbf{u}_i = -\lambda_i \nabla p_i \\ \phi \frac{\partial(n S_f)}{\partial t} + \nabla \cdot (n \mathbf{u}_f) = \phi S_f [K_g (n_\infty - n) - K_d n] \end{cases} \quad (5.1)$$

where ρ_i , S_i , \mathbf{u}_i , λ_i , p_i are density, saturation, Darcy velocity, mobility and total pressure of the i -th fluid, with $i \in \{w, f\}$ (the subscript w and f denote water and foam). K_g and K_d are bubble generation and bubble destruction coefficients and n_∞ is maximum bubble density. K_g and K_d can be obtained by fitting the numerical solutions with the experimental data during transient foam propagation in a porous medium. For strong foam, K_d is negligible compared to K_g . Maximum bubble density can be determined by assuming that bubble and pore volume are approximately equal near the steady-state foam flow, so a rough estimate of n_∞ is obtained by equating it to the

number of pores occupied by gas, i.e., $n_\infty = S_f \phi / r^3$, where r is the mean pore radius. The closure relations for volume conservation and capillary pressure are as follows:

$$S_w + S_g = 1, \quad p_c = p_f - p_w \quad (5.2)$$

where S_w and S_g are saturation of water and gas, p_w and p_f are pressure of water and foam. The mobility λ_i of the i -th fluid is defined as the ratio of fluid permeability $k_i = k k_{ri}$ (k_{ri} = relative permeability) to fluid viscosity μ_i , that is:

$$\lambda_i = \frac{k_i}{\mu_i} = \frac{k k_{ri}}{\mu_i} \quad (5.3)$$

5.3 Constitutive relations

In order to determine the dependence of the parameters $\{\rho_i, k_{ri}, \mu_i, p_c\}$ on the physical variables $\{S_i, \mathbf{u}_i, p_i\}$, the following constitutive relations were used. Under isothermal conditions, the density ρ_i is related to pressure p_i through the following thermodynamic expression:

$$c_i = \frac{1}{\rho_i} \frac{\partial \rho_i}{\partial p_i} \quad (5.4)$$

where c_i is the isothermal compressibility of the i -th fluid. The expression of water relative permeability relies on the principle that the function of $k_{rw} = k_{rw}(S_w)$ is not modified when gas is replaced by foam (Bernard et al., 1965). This principle can be extended to foam relative permeability so that the function of $k_{rf} = k_{rf}(S_w)$ is the same as for the free gas during transient foam flow. Accordingly, foam and water relative permeabilities can be defined as a function of water saturation using Brooks-Corey correlations:

$$k_{rw}(S_w) = k_{rw}^0 \left(\frac{S_w - S_{wc}}{1 - S_{wc}} \right)^\lambda; \quad k_{rf}(S_w) = k_{rf}^0 \left(1 - \frac{S_w - S_{wc}}{1 - S_{wc}} \right)^{\frac{3\lambda+2}{\lambda}} \quad (5.5)$$

where k_{rw}^0 and k_{rf}^0 are the end-point relative permeabilities, S_{wc} is connate water saturation and λ is a constant. The absence of trapped gas saturation in Eq. (5.5) reflects the idea that during transient foam development, flow occurs at a finite velocity in the whole flow domain, i.e., there is no trapped gas (Zitha, 2006; Simjoo et al., 2011; section 4.3.3 in Chapter 4). The capillary pressure p_c at a first approximation can be expressed as a function of water saturation as follows:

$$p_c = p_{c,0} \gamma \left(\frac{0.5 - S_{wc}}{1 - S_{wc}} \right)^{\frac{1}{\lambda}} \left(\frac{S_w - S_{wc}}{1 - S_{wc}} \right)^{-\frac{1}{\lambda}} \quad (5.6)$$

where $p_{c,0} = 2(\sigma_{gw}/r) \cos \theta$ is the entry capillary pressure, γ is a fitting parameter which is used when experimental data are not available, σ_{gw} is surface tension between water and gas and r is

effective pore radius. The main modification in Eq. (5.6) for foam flow with respect to free gas-water mixture is in the lowering of surface tension due to the adsorption of surfactant at the water-gas interface.

Foam development does not modify water viscosity μ_w , so the water mobility λ_w will be described by Eq. (5.3). As to the foam flow, we describe it as a yield stress fluid obeying a Herschel-Bulkley rheological model:

$$\begin{cases} u_f = 0 & \text{for } \tau \leq \tau_y \\ \mu_f = \mu_g + K_1 u_f^{m-1} + K_2 \frac{\tau_y}{u_f} & \text{for } \tau > \tau_y \end{cases} \quad (5.7)$$

where τ_y is yield stress, μ_g is gas viscosity, u_f is foam velocity, and K_1 and K_2 are model parameters defined as follows:

$$K_1 = K_0 \left(\frac{c_0}{c_1} \right)^{m-1} \left(\frac{\phi}{k} \right)^{\frac{1}{2}(m-1)} ; K_2 = \frac{c_1}{c_0} \left(\frac{k}{\phi} \right)^{\frac{1}{2}} \quad (5.8)$$

where K_0 is the plasticity coefficient, m is the power-law exponent, k is absolute permeability, ϕ is porosity, and c_0 and c_1 are geometric constants. As discussed in Chapter 4, yield stress is negligible during transient foam flow. Therefore, Eq. (5.7) will be reduced to the Hirasaki and Lawson equation (1985):

$$\mu_f = \mu_g + \alpha \frac{n}{u_f^d} \quad (5.9)$$

where α and d are constants and n is bubble density.

5.4 Numerical simulation

In this section we present a numerical method based on a finite difference scheme as described by Aziz and Settari (1979). First, Darcy velocity is substituted into the material balance equations (Eq. 5.1) for both phases:

$$\begin{cases} \phi \frac{\partial(\rho_w S_w)}{\partial t} = \nabla \cdot (\rho_w \lambda_w \nabla p_w) \\ \phi \frac{\partial(\rho_f S_f)}{\partial t} = \nabla \cdot (\rho_f \lambda_f \nabla p_f) \\ \phi \frac{\partial(n S_f)}{\partial t} - \nabla \cdot (n \lambda_f \nabla p_f) = \phi S_f [K_g (n_\infty - n) - K_d n] \end{cases} \quad (5.10)$$

Next, S_f and p_f are eliminated by using the following identity derived from Eq. (5.4):

$$\frac{1}{\rho_i} \frac{\partial \rho_i}{\partial t} = c_i \frac{\partial p_i}{\partial t} \quad (5.11)$$

This identity is substituted in the second expression of the Eq. (5.10). Then, using the closure condition, Eq. (5.2), we obtain the following set of equations:

$$\begin{cases} \phi \frac{\partial(\rho_w S_w)}{\partial t} = \nabla \cdot (\rho_w \lambda_w \nabla p_w) \\ C_{wf} \frac{\partial p_w}{\partial t} + C_{ff} \frac{\partial p_c}{\partial t} = \frac{1}{\rho_w} \nabla \cdot (\rho_w \lambda_w \nabla p_w) + \frac{1}{\rho_f} \nabla \cdot (\rho_f \lambda_f \nabla p_w) + \frac{1}{\rho_c} \nabla \cdot (\rho_c \lambda_c \nabla p_c) \\ \phi \frac{\partial[n(1-S_w)]}{\partial t} - \nabla \cdot (n \lambda_f \nabla p_w) - \nabla \cdot (n \lambda_c \nabla p_c) = \phi(1-S_w) [K_g(n_\infty - n) - K_d n] \end{cases} \quad (5.12)$$

with

$$\begin{cases} C_{ww} = \phi S_w c_w \\ C_{ff} = \phi(1-S_w) c_f \\ C_{wf} = \phi [S_w c_w + (1-S_w) c_f] = C_{ww} + C_{ff} \end{cases} \quad (5.13)$$

These three equations are valid in the domain Ω and involve three dependent variables, water saturation S_w , water pressure p_w and bubble density n . The set of equations in (5.12) will be solved with the following initial conditions:

$$\begin{cases} S_w(\mathbf{r}, t) = 1 \\ p_w(\mathbf{r}, t) = p_0(\mathbf{r}), \mathbf{r} \in \Omega, t = 0 \\ n(\mathbf{r}, t) = 0 \end{cases} \quad (5.14)$$

and the following boundary conditions at the inlet:

$$\begin{cases} n(\mathbf{r}, t) = 0 \\ \rho_w \lambda_w \nabla p_w = -\mathbf{q}_w, \mathbf{r} \in \partial\Omega_I, \text{ and } t > 0 \\ \rho_f \lambda_f \nabla p_f = -\mathbf{q}_f \end{cases} \quad (5.15)$$

and at the outlet:

$$p(\mathbf{r}, t) = p_0(\mathbf{r}), \mathbf{r} \in \partial\Omega_O, t > 0 \quad (5.16)$$

The pressure field $p_0(\mathbf{r})$ at $t = 0$ is found by solving the appropriate steady-state flow problem for the surfactant solution.

5.5 Method of solution

We apply the set of equations in (5.12) for one-dimensional case, i.e. for foam flow in a porous medium with the length of l . The system of equations for one dimension case becomes then:

$$\begin{cases} \phi \frac{\partial}{\partial t} (S_w \rho_w) = \frac{\partial}{\partial x} \left(\lambda_w \rho_w \frac{\partial p_w}{\partial x} \right) \\ C_{wf} \frac{\partial p_w}{\partial t} + C_{ff} \frac{\partial p_c}{\partial t} = \frac{1}{\rho_w} \frac{\partial}{\partial x} \left(\lambda_w \rho_w \frac{\partial p_w}{\partial x} \right) + \frac{1}{\rho_f} \frac{\partial}{\partial x} \left(\lambda_f \rho_f \frac{\partial p_w}{\partial x} \right) + \frac{1}{\rho_f} \frac{\partial}{\partial x} \left(\lambda_f \rho_f \frac{\partial p_c}{\partial x} \right) \\ \phi \frac{\partial [n(1-S_w)]}{\partial t} - \frac{\partial}{\partial x} \left(n \lambda_f \frac{\partial p_w}{\partial x} \right) - \frac{\partial}{\partial x} \left(n \lambda_f \frac{\partial p_c}{\partial x} \right) = \phi (1-S_w) [K_g (n_\infty - n) - K_d n] \end{cases} \quad (5.17)$$

By using finite difference approximation the above equations will be discretized with upstream mobility weighting and forward in time. Then, following Aziz and Settari scheme (1979) the equations will be solved with the IMPES method, implicit pressure-explicit saturation. This method consists basically of obtaining a single pressure equation by a combination of the flow equations. After pressure has been advanced in time, saturation and bubble density are updated explicitly. The flow domain is a line segment of length l , which is segmented in N identical grid blocks ($i = 1, 2, \dots, i-1, i, i+1, \dots, N$). The value of each variable (S_w , p_w and n) is calculated at the centre of the grid block. Therefore, the following vector is obtained:

$$\underline{p}_w = \begin{bmatrix} p_{w,1} \\ p_{w,2} \\ \vdots \\ p_{w,i} \\ \vdots \\ p_{w,N} \end{bmatrix}, \quad \underline{S}_w = \begin{bmatrix} S_{w,1} \\ S_{w,2} \\ \vdots \\ S_{w,i} \\ \vdots \\ S_{w,N} \end{bmatrix} \quad \text{and} \quad \underline{n} = \begin{bmatrix} n_1 \\ n_2 \\ \vdots \\ n_i \\ \vdots \\ n_N \end{bmatrix} \quad (5.18)$$

Thus following the IMPES scheme by discretizing of the set of equations in (5.17) we have the following compact form:

$$\underline{S}_w^{k+1} = \underline{M}_1 \underline{S}_w^k + \underline{M}_2 \underline{P}_w^{k+1} \quad (5.19-a)$$

$$\underline{M}_3 \underline{P}_w^{k+1} = \underline{M}_4 \underline{P}_w^k + \underline{M}_5 \underline{P}_c^k \quad (5.19-b)$$

$$\underline{n}^{k+1} = \underline{M}_6 \underline{n}^k + \underline{M}_7 \quad (5.19-c)$$

where \underline{M} are $N \times N$ matrices. The sequence of calculations will be as follows: for each time step from $t = 0$ to a determined time, first the new pressure \underline{P}_w^{k+1} is computed using Eq. (5.19-a) from the old pressure \underline{P}_w^k , water saturation \underline{S}_w^k and bubble density \underline{n}^k . Then, the new water saturation \underline{S}_w^{k+1} is computed from the old \underline{S}_w^k with the new water pressure \underline{P}_w^{k+1} using Eq. (5.19-b). The last step is to compute the new bubble density from Eq. (5.19-c) by using the new water pressure \underline{P}_w^{k+1} and new water saturation \underline{S}_w^{k+1} , which are included in \underline{M}_6 , and the old bubble density \underline{n}^k .

Table 5.1 and 5.2 list a series of parameter used in numerical computations. The parameters of two-phase flow and SBP model are obtained from the foam flow experiment reported in Chapter 4. The length of the core and the number of grid block were $l = 38.4$ cm and $N = 250$, respectively. The time span for the simulation of the experiment was 3120 s with each time increment of 0.01 s. This time span was used to simulate the transient foam flow until foam breakthrough at the core outlet. We further assumed that the bubble destruction coefficient (K_d) is zero.

Table 5.1: Model parameters used in the numerical simulation.

Two phase flow parameters		Stochastic bubble population parameters	
Parameter	Value	Parameter	Value
k (m^2)	2.5×10^{-12}	α ($Pa\ s^{2/3}\ m^{10/3}$)	5.8×10^{-16}
ϕ	0.21	d	1/3
S_{wc}	0.10	n_{∞} (mm^{-3})	250-1000
k_{rw}^o	0.75	K_d (s^{-1})	0
k_{rf}^o	1.0	K_g (s^{-1})	0.001-0.1
σ_{gw} (N/m)	30.0×10^{-3}		
γ	0.5		
λ	5.0		
μ_g ($Pa\ s$)	1.8×10^{-5}		
μ_w ($Pa\ s$)	1.0×10^{-3}		

Table 5.2: Parameters used for numerical simulation in the base case.

Computational domain		Two phase flow conditions	
l (cm)	38.4	u_g (m/s)	1.47×10^{-5}
t (s)	3120	u_w (m/s)	1.47×10^{-6}
N	250	$p_{w,out}$ (Pa)	2026500
Δl (cm)	1.536×10^{-1}	n_{∞} (mm^{-3})	500
Δt (s)	0.01	K_g (s^{-1})	0.1

5.6 Results and discussion

5.6.1 Sensitivity to the grid size and time step

A series of numerical simulations was performed at the base condition (Table 5.2) varying the number of grids (N) and time step (Δt), which are as follows: 1) $N=150$, $\Delta t=0.1$, 2) $N=250$,

$\Delta t = 0.01$, and 3) $N=300$, $\Delta t = 0.001$. The numerical results on water saturation and bubble density are shown in Figs. 5.1 and 5.2, respectively. It can be seen that at $N \geq 250$ and $\Delta t \leq 0.01$ s numerical results does not show any dependence on the grid number and time step, which validate the employed grid number and time step in the numerical computations.

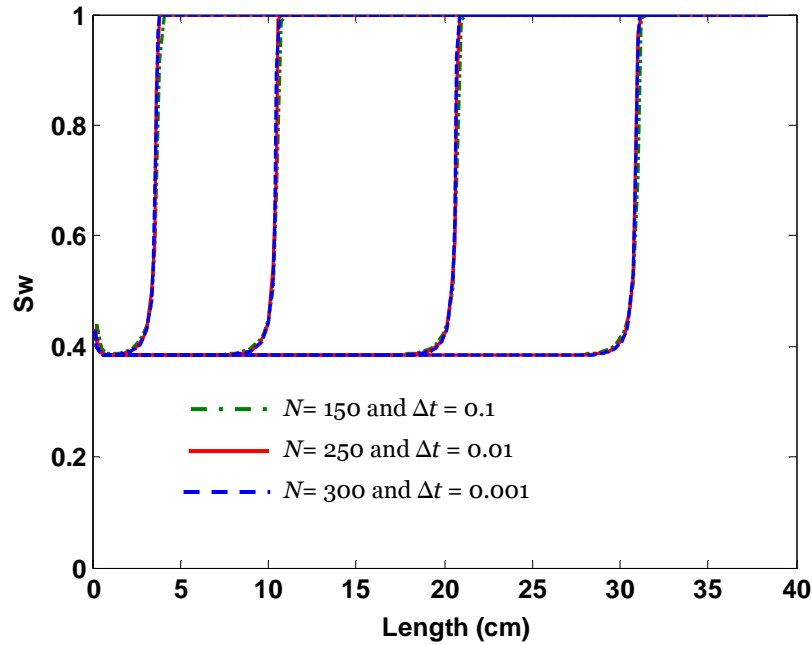


Fig. 5.1: Water saturation profiles at different combinations of grid number (N) and time step (Δt).

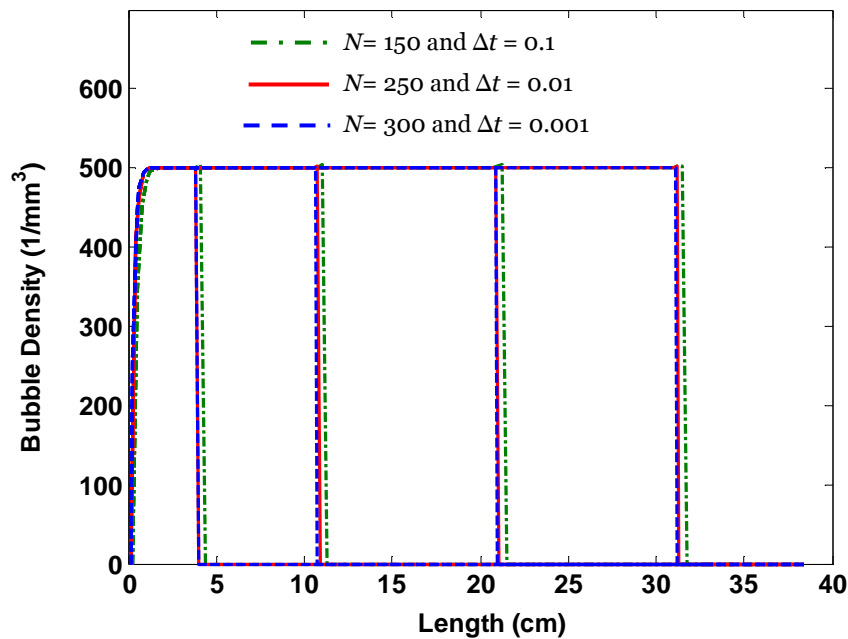


Fig. 5.2: Bubble density profiles at different combinations of grid number (N) and time step (Δt).

5.6.2 Transient foam flow: base case

Figs. 5.3 to 5.5 show a set of numerical results for water saturation, bubble density and water pressure profiles obtained for the base case foam flow. The SBP model parameters, K_g and n_∞ , were set to be 0.1 s^{-1} and 500 mm^{-3} (see Table 5.2). The numerical results were plotted for four injected pore volumes (PV) to show the transient behaviour of foam propagation.

Data in Fig. 5.3 show that foam propagation exhibits a characteristic front-like behaviour. The model also predicts that water saturation is slightly higher near the core inlet with $S_w = 0.43$ at $x = 0$, but it decreases further to 0.38 at the distance of 1.0 cm from the core inlet face. This can be attributed to the rapid increase of bubble density from zero at the inlet face to its maximum value (n_∞) at $x = 1.0 \text{ cm}$ as shown in Fig. 5.4. Bubble density remains at the maximum value within the flowing foam until it drops sharply to zero at the liquid-filled region. The transient foam flow can be examined further by water pressure profile, Fig. 5.5. The pressure gradient is gentle at the inlet region due to the lower bubble density. This corresponds to a weak foam state, and thus higher water saturation. However, the pressure gradient is much steeper at downstream of the inlet region, indicating that a stronger foam was developed in the core. Ahead of the advancing foam front the pressure gradient exhibits a much lower value. This corresponds to the single-phase water flow with a much higher mobility compared to the foam flow.

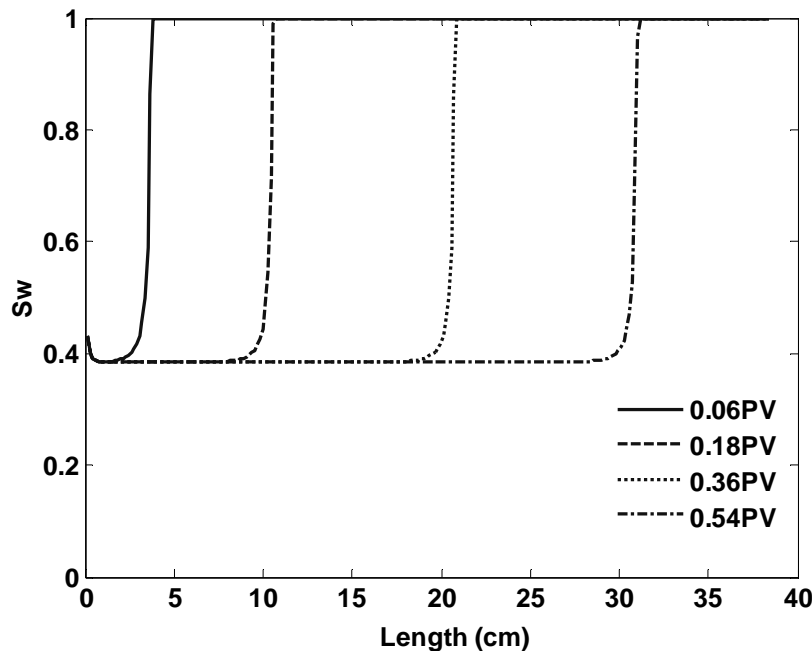


Fig. 5.3: Water saturation profiles for the transient foam flow. Foam flow propagates in a front-like manner.

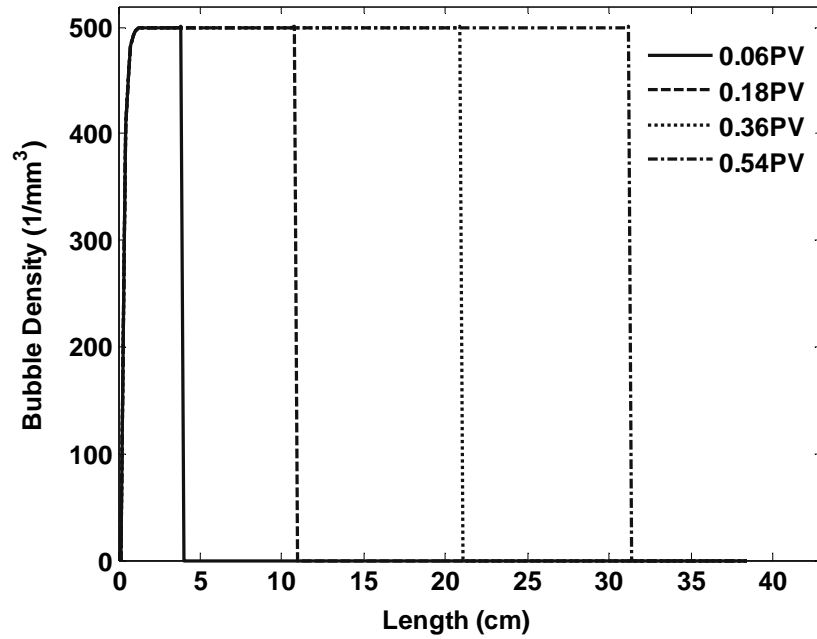


Fig. 5.4: Bubble density profiles for the transient foam flow. Bubble density profiles exhibit a characteristic exponential form.

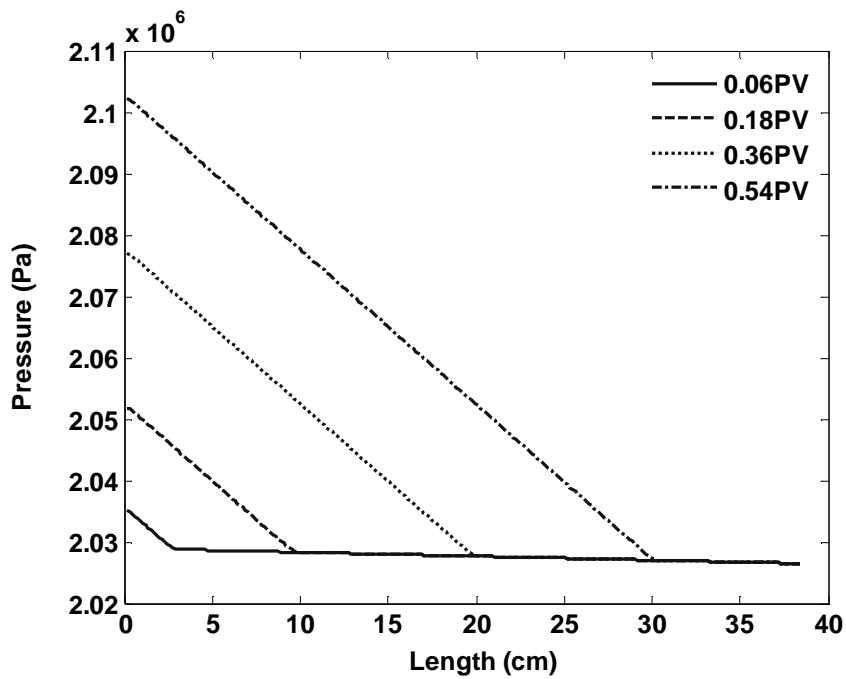


Fig. 5.5: Water pressure profiles for the transient foam flow. Water pressure is high in the foam-filled region, indicating the presence of low foam mobility.

5.6.3 Influence of the physical parameters

5.6.3.1 Effect of maximum bubble density

Figs. 5.6 to 5.8 show a set of numerical results for water saturation, bubble density and water pressure profiles at three maximum bubble densities, namely $n_{\infty} = 250, 500, \text{ and } 1000 \text{ mm}^{-3}$. The foam generation coefficient was fixed at 0.1 s^{-1} . It is seen from the figures that although foam flow in porous media maintains its front-like behaviour, foam propagation rate, water saturation and water pressure profile differ considerably. Foam flow with lower n_{∞} propagates faster, with higher water saturation at the foam upstream and consequently exhibits a lower pressure drop. It is observed from the bubble density profiles that although the values of n_{∞} are much different, the foam generation rate in the inlet part maintains similar values: they all approach the maximum bubble density within the distance of 1.0 cm from the inlet face. Therefore, we can conclude that the value of n_{∞} mainly affects the intensity of foam mobility. Higher n_{∞} stands for stronger foam, thus leads to a slower foam propagation rate, lower water saturation and higher pressure drop.

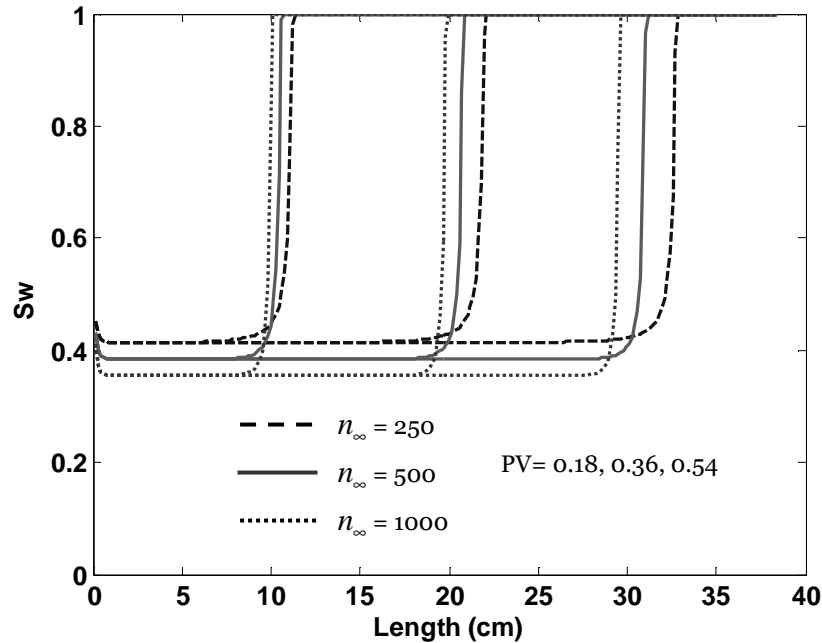


Fig. 5.6: Effect of maximum bubble density on the water saturation profiles during transient foam flow.

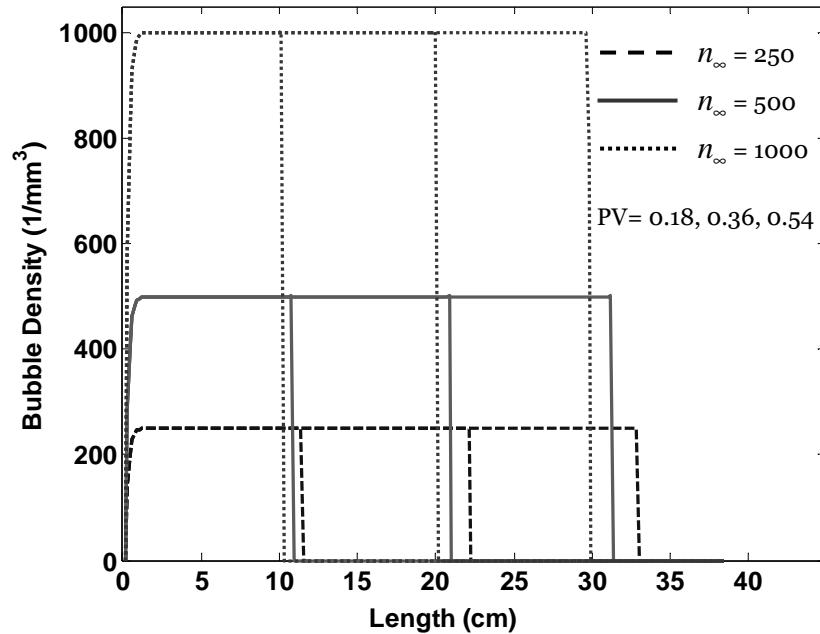


Fig. 5.7: Effect of maximum bubble density on the bubble density profiles during transient foam flow.

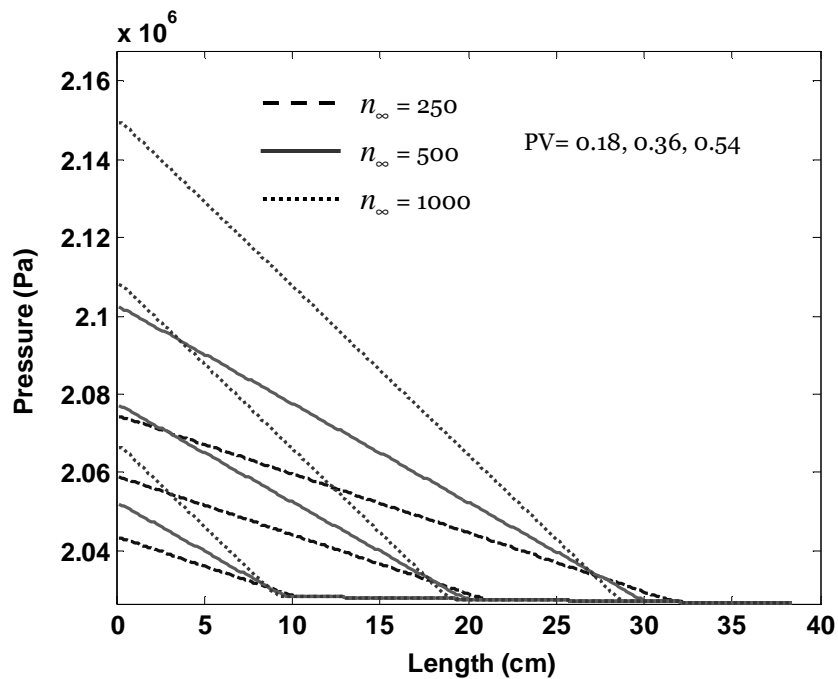


Fig. 5.8: Effect of maximum bubble density on the water pressure profiles during transient foam flow.

5.6.3.2 Effect of bubble generation coefficient

Figs. 5.9 to 5.11 show a set of numerical results for water saturation, bubble density and water pressure profiles at three foam generation coefficients, namely $K_g = 0.001, 0.01, \text{ and } 0.1 \text{ s}^{-1}$. The maximum bubble density was fixed at 250 mm^{-3} . Water saturation profiles shows that the value of

K_g exhibits a significant effect on the foam propagation rate and the inlet water saturation, Foam flow with $K_g = 0.001 \text{ s}^{-1}$ propagates faster and decreases the inlet water saturation only up to 0.57 compared to 0.45 for foam flow with $K_g = 0.1 \text{ s}^{-1}$. Also, a longer entrance region is obtained with a smaller foam generation coefficient such that for $K_g = 0.001 \text{ s}^{-1}$ the entrance region is extended as long as 15 cm from the core inlet compared to 0.4 cm for $K_g = 0.1 \text{ s}^{-1}$. This is consistent with the previous studies (Friedmann and Jensen, 1986; Kovscek et al., 1995; Myers and Radke, 2000; Ashoori et al., 2011-a) reporting that the length of entrance region depends on the foam generation parameter. Fig. 5.10 shows that bubble density increases more rapidly at higher values of K_g . Increasing K_g to as much as 0.1 s^{-1} results in steeper increment of bubble density to the maximum value in a distance of 1.0 cm from the inlet face. This indicates quicker foam development at higher K_g . However, for the K_g as low as 0.001 s^{-1} , bubble generation is too slow to reach the maximum bubble density even after 0.54 PV of foam injection. As to the water pressure profile, foam with higher K_g exhibits a higher and steeper pressure gradient. From the above results, we can conclude that the value of K_g mainly controls the foam generation rate, with higher K_g corresponding to a quicker foam development.

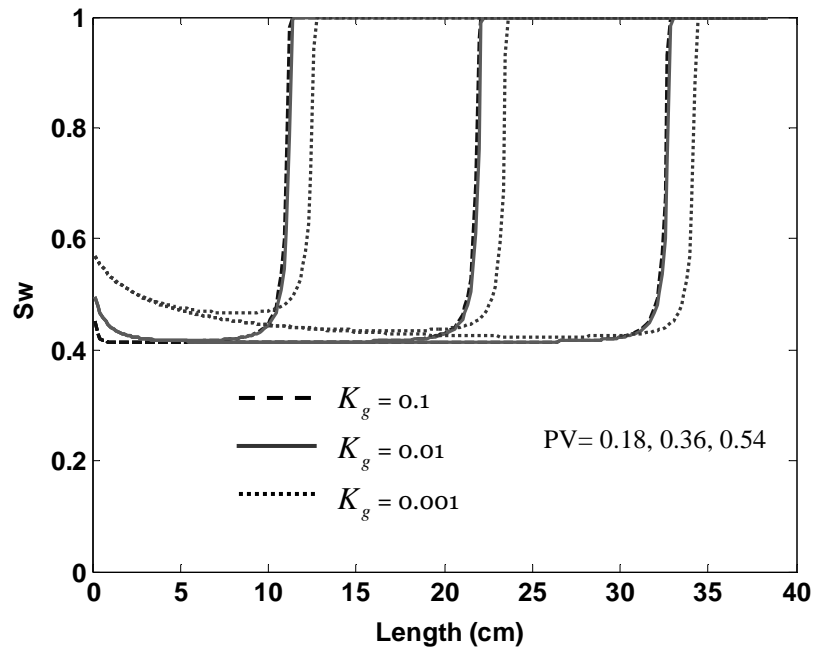


Fig. 5.9: Effect of bubble generation coefficient on the water saturation profiles during transient foam flow.

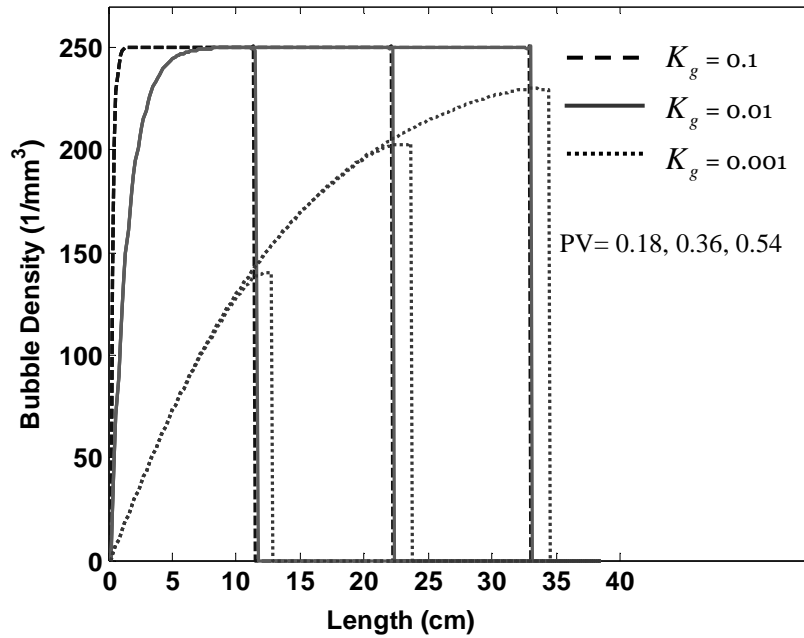


Fig. 5.10: Effect of bubble generation coefficient on the bubble density profiles during transient foam flow.

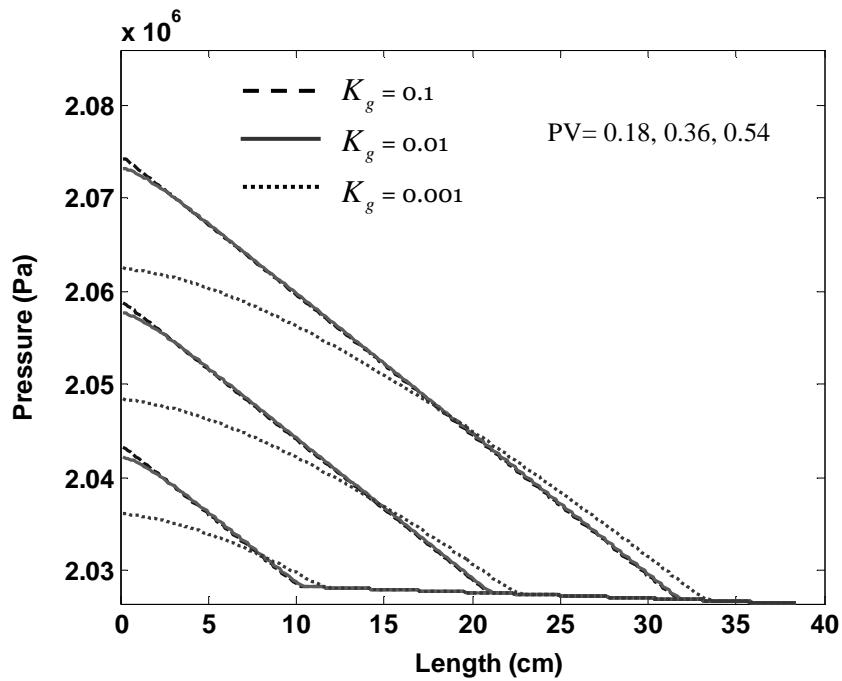


Fig. 5.11: Effect of bubble generation coefficient on the water pressure profiles during transient foam flow.

5.6.4 Comparison of SBP model and experiments

In this section we provide a comparison between the experimental results and the numerical calculations. The experimental results were obtained for 1.0 wt% AOS foam flow in a Bentheimer sandstone core with the diameter of 3.8 ± 0.1 cm and length of 38.4 ± 0.1 cm. More detailed

description of the experimental conditions was provided in Chapter 4. Fig. 5.12 shows water saturation profiles obtained from the experiment (solid lines) and from the SBP model (dashed lines) at different PV injected during transient foam flow. The corresponding water pressure profiles are presented in Fig. 5.13 where the model results are shown by solid lines and the experimental data are represented by the circles. To track the experimental transient foam behaviour, the model results were obtained at $K_g = 0.1 \text{ s}^{-1}$ and $n_\infty = 250 \text{ mm}^{-3}$. The other parameters used in the numerical computation are given in Table 5.1 and 5.2.

As to the water saturation profiles, the results of SBP model show that foam displaces the liquid phase in a characteristic front-like manner in good agreement with the experimental results. The SBP model successfully captured the experimental fronts and provided a good match for the foam propagation rate. However, water saturations predicted by the model are slightly higher than those obtained experimentally.

The predicted pressure profiles are in good agreement with the ones obtained from the experiments. Similar to the experiments, the numerical water pressure profiles are divided into two branches: (a) an upstream branch with a higher pressure gradient corresponding to foam flow with a lower mobility and (b) a downstream branch with a much lower pressure gradient corresponding to single-phase water flow with a much higher mobility. The model shows that as the foam front propagates downstream, water pressure increases sequentially along the core length. This corresponds to the arrival of foam front in a specific core section, which is consistent with the experiments. From the above comparisons, it can be concluded that the SBP foam model reproduces the main features of the transient foam flow in a homogenous porous medium containing a surfactant solution.

5.6.5 Comparison of SBP model with other foam models

In this section we compare the capability of the SBP foam model to describe the behaviour of transient foam flow (the flow of foam until breakthrough time) with the results predicted by the population balance model (PBM) (Kovscek et al., 1995) and by the fractional flow method (Rossen et al., 1999). Kovscek et al. (1995) applied the PBM model with ten parameters to their foam-coreflood data and produced a front-like displacement. They predicted well the pressure drop profiles, except in the inlet region where the model prediction overestimates the experiments. The predicted water saturation profiles tracked qualitatively well the experimental results, although the model fronts were somewhat steeper and sharper than the experiments. Rossen et al. (1999) applied the fractional flow method with only one fitting parameter (water saturation at limiting capillary pressure, S_w^*) and without using a bubble population balance to the data of Kovscek et al. (1995). Similar to the results of the PBM model, the fractional flow method did not capture the

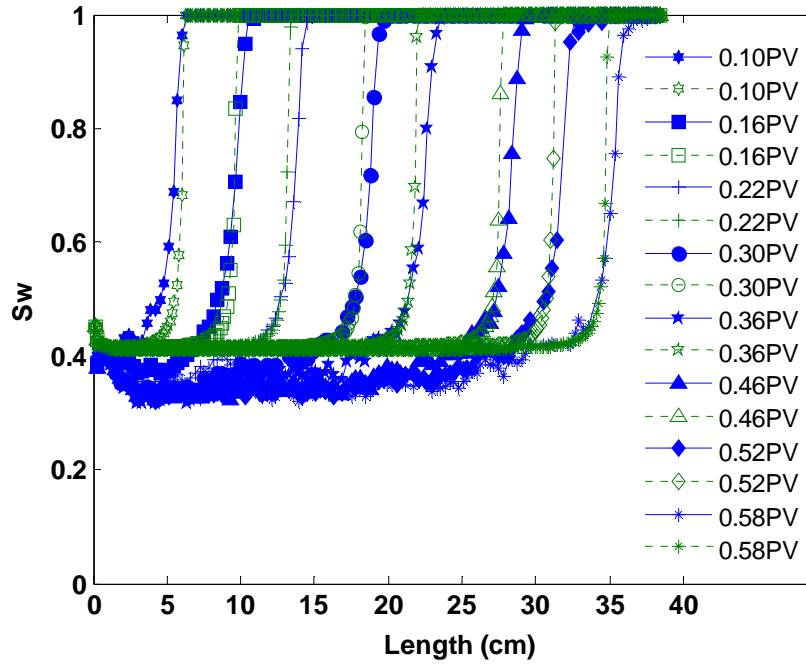


Fig. 5.12: Experimental and numerical water saturation profiles during transient foam flow in a surfactant-saturated Bentheimer sandstone core. The solid lines stand for the experimental results and the dashed line are the model results.

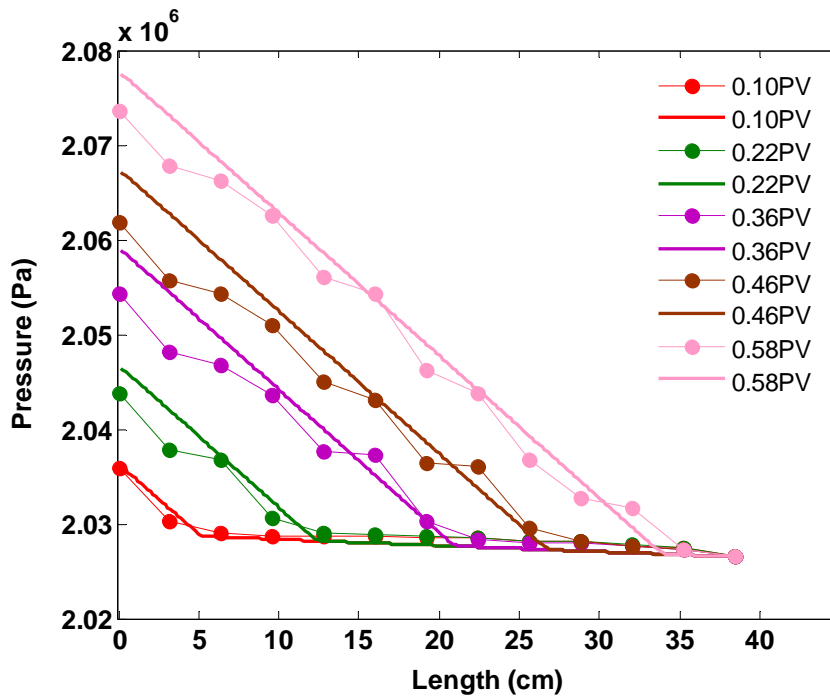


Fig. 5.13: Experimental and numerical water pressure profiles during transient foam flow in a surfactant-saturated Bentheimer sandstone core. The experimental data are marked by the circle symbols and the model results are shown by solid lines.

experimental pressure drop in the inlet region, while beyond that it was virtually identical to the results predicted by the PBM model. No match for the water saturation profiles was reported. Our SBP foam model described by one fitting parameter (foam generation coefficient, K_g) also produced a front-like displacement similar to the one produced by the PBM model and the fractional flow method. The pressure drop and saturation profiles obtained by the SBP model track well the experimental profiles. This good match of the model and experiment shows that the SBP foam model reproduces the main features of transient foam flow in a core saturated with a surfactant solution. However, the description of the foam flow behavior after breakthrough time, in which a secondary backward desaturation front appears in the core (see Fig. 4.2 in Chapter 4), requires further studies.

5.7 Conclusion

- We have conducted a numerical analysis using a foam model honouring the complex macroscopic foam rheology and stochastic bubble population ideas. This foam model is described by two parameters: maximum bubble density (n_{∞}) and bubble generation coefficient (K_g). n_{∞} can be obtained from the number of pores occupied by gas ($n_{\infty} \approx S_f \phi / r^3$). K_g , as only fitting parameter, is determined by matching the numerical solutions with the experimental data.
- Numerical results show that the transient foam flow, forward movement of foam flow until breakthrough, propagates in a front-like manner. Water saturation profiles exhibit a low value upstream and a high value downstream. Bubble density profiles show a characteristic exponential form, increases to a maximum as a function of distance from the core inlet. In the foam filled region, the pressure gradient is high, indicating the presence of foam with a lower mobility.
- The increase of maximum bubble density mainly affects the intensity of foam mobility. Higher n_{∞} leads to stronger foam characterized by a slower foam propagation rate, lower water saturation and a higher pressure drop.
- The increase of bubble generation coefficient mainly controls the foam generation rate. Higher K_g leads to bubble density increases more rapidly.
- The stochastic bubble population foam model reproduces the main features of the transient foam flow in a homogeneous porous medium containing a surfactant solution. This was supported by a good match between water saturation and pressure profiles obtained numerically with those obtained from the foam flow experiment in Bentheimer sandstone.

Chapter 6

EFFECTS OF OIL ON FOAM GENERATION AND PROPAGATION IN POROUS MEDIA

Abstract

Foaming of nitrogen stabilized by C₁₄₋₁₆ alpha olefin sulfonate (AOS) in natural sandstone porous media, previously subject to water flooding, was studied. Foam was generated in-situ by co-injection of gas and surfactant solution at a fixed foam quality of 91%. Effect of surfactant concentration on foam strength and foam propagation was examined. X-ray CT scans were obtained to visualize the foam displacement process and to determine fluid saturations at different times. Foam was generated in the presence of water-flood residual oil, even at a surfactant concentration as low as 0.1 wt%. CT images revealed that foaming of the injected gas provides a better mobility control as the surfactant concentration increases from 0.1 to 1.0 wt%. This was reflected by a delay in the gas breakthrough time and a substantial reduction in foam mobility, leading to more oil production. Incremental oil due to foam flow was obtained first by a formation of an oil bank and then by a long tail production due to transport of dispersed oil within the flowing foam. The size of the oil bank was found to increase with surfactant concentration. Foam flooding provided an incremental oil recovery ranging from 13±0.5% of the oil initially in place for 0.1 wt% foam to 29±2% for 1.0 wt% foam.

6.1 Introduction

Gas flooding is a widely applied enhanced oil recovery (EOR) method. The main underlying mechanism for this EOR method is that the residual oil saturation for gas flooding is lower than that for water flooding (Lake, 1989; Green and Willhite, 1998). However, the full potential of gas flooding is often not realized in real oil reservoirs due to poor vertical and areal sweep efficiency of the injected gas. Gas injection suffers from gravity segregation and viscous instabilities, leading to uneven oil displacement, early gas breakthrough and low oil recovery factor.

Foaming of the injected gas can potentially improve gas flooding performance by a considerable increase of gas viscosity and also by trapping a part of the gas inside the porous medium (Bernard et al., 1965; Hirasaki and Lawson, 1985; Kovscek and Radke, 1994; Rossen, 1996; Zitha, 2006). Hereby gas mobility substantially decreases and instead volumetric sweep efficiency increases during gas flooding into oil reservoirs. Thus this has obvious potential benefits for enhancing oil recovery.

Bond and Holbrook (1958) were the first to propose that foam could be generated in oil reservoirs to obtain a favorable mobility ratio. This idea has been supported by several laboratory studies (Fried, 1961; Chiang et al., 1980; Wellington and Vinegar, 1988), field trials and commercial projects (Patzek and Koinis, 1990; Friedmann et al., 1994; Turta and Singhal, 1998; Skauge et al., 2002). Although foam has been widely applied during various stages of oil production to control fluid mobility, there are still some important questions about the effects of oil on foam stability and foam propagation in reservoirs containing residual oil. Available experimental evidence resulted from bulk and porous media studies presents varied results for foam-oil interaction. While several studies argued that the presence of oil could be detrimental on foam stability (Minssieux, 1974; Jensen and Friedmann, 1987; Schramm and Novosad, 1992; Svorstøl et al., 1996; Arnaudov et al., 2001; Hadjiiski et al., 2001; Denkov, 2004; Farajzadeh et al., 2012), others supported that stable foam could be effectively generated in the presence of oil by selecting appropriate foaming agents (Nikolov et al., 1986; Suffridge et al., 1989; Schramm et al., 1993; Mannhardt et al., 1998; Aarra et al., 2002; Vikingstad and Aarra, 2009; Emadi et al., 2011; Andrianov et al., 2012). The latter idea has been discussed in several studies where development of sufficiently stable foam leads to incremental oil recovery on top of water and gas flooding (Ali et al., 1985; Mannhardt et al., 1998; Yin et al., 2009; Andrianov et al., 2012). However, it was argued that before foam could propagate in porous media, oil saturation must be below a critical value (Jensen and Friedmann, 1987; Svorstøl et al., 1996; Mannhardt and Svorstøl, 1999). This was not supported by other studies in which foam was generated at relatively high oil saturation (Ali et al., 1985; Farajzadeh et al., 2010; Andrianov et al., 2012). From the previous studies one

can infer that the topic of foam-oil indication is still a matter of debate and more systematic studies are needed to elucidate the corresponding mechanisms.

The goal of this chapter is to gain better insight into the effects of oil on foam stability and foam propagation in natural sandstone cores containing water-flood residual oil. More specifically, this chapter is concerned with the question of whether immiscible foam can be a tertiary oil recovery method. We also investigate the effect of surfactant concentration because it is one of main physical parameters that directly affects the stability of foam films in the presence of oil (see section 2.3.2.2 in Chapter 2). The use of a CT scanner enables us to provide new insight into foam-oil interaction in porous media. We provide a detailed analysis of the incremental oil recovery by foam that has not been elaborated in the previous studies. This chapter proceeds with a description of experimental part; presentation and discussion of the results and then the main conclusions are drawn.

6.2 Experimental description

6.2.1 Materials

Brine was prepared by dissolving sodium chloride (NaCl, Merck) at a fixed concentration of 0.5 M in de-ionized water (pH=6.8±0.1). Density and viscosity of the brine at 21°C were 1.02±0.01 g/cm³ and 1.18±0.01 cP, respectively. The surfactant used to perform experiments was C₁₄₋₁₆ alpha olefin sulfonate (AOS, Stepan) with the molecular weight of 315 g/mole. It was provided as an aqueous solution containing 40.0 wt% active content and used as received without further treatment. The critical micelle concentration of AOS solution in the presence of 0.5 M NaCl was 4.0×10⁻³ wt%. Normal hexadecane (n-C₁₆, Sigma-Aldrich) with a purity of 99.99% was used as model oil. Density and viscosity of the oil at 21°C were 0.77±0.01 g/cm³ and 3.28±0.01 cP, respectively. Nitrogen gas with a purity of 99.98% was used to conduct the experiments.

6.2.2 Core sample and core-holder

Bentheimer sandstone cores were used to perform the experiments. This sandstone contains up to 97% quartz and is consolidated and nearly homogeneous. The core samples were drilled from a cubical block and then sawn to the desired dimensions using a water-cooled diamond saw. Next, the cores were dried in an oven at 60 °C for 48 hours. Then they were encapsulated in a thin layer of low X-ray attenuation Araldite self-hardening glue to avoid possible bypassing along the side of the core. From the CT scans of the dry core it was estimated that the glue penetrates about 1.0 mm of the core sample. The effective diameter was used for the calculation of the total pore volumes of the cores. After hardening, the glued core was machined to ensure that the core fits precisely into the core-holder. The physical properties of the core samples are presented in Table 6.1.

The core-holder was made of polyether-ether-ketone (PEEK), a synthetic material that combines good mechanical properties with a low X-ray attenuation. It transmits X-ray within a narrow energy window (refiltering the polyenergetic source X-rays), which significantly minimizes the beam hardening artifact due to the polychromaticity of the X-ray beam. Several holes were drilled through the glue layer into the core surface along the core length for pressure measurements. The pressure connectors were also made of PEEK to prevent interference of the pressure lines with the CT scanning.

Table 6.1: Physical properties of the core samples used for core-flooding experiment.

Core sample	Bentheimer sandstone
Length (cm)	17.0±0.1
Diameter (cm)	3.8 ±0.1
Porosity (%)	21.0 ±0.1
Pore volume (cm ³)	40.5 ±0.5
Absolute permeability to brine (Darcy)	2.5 ±0.1

6.2.3 Experimental set-up

The set-up used to conduct the core-flooding experiments is shown in Fig. 6.1. It consists of a core-holder in line with a double effect piston displacement pump (Pharmacia Biotech P-500) in parallel with a gas mass flow controller (Bronkhorst) and on the other end a back pressure regulator and a collector for the produced fluids. The pump was used to inject brine, oil and surfactant solution. Nitrogen gas was supplied by a 200 bar cylinder equipped with a pressure regulator (KHP Series, Swagelok) and connected to the core inlet through a mass flow controller. Three differential pressure transducers were used to record sectional pressure drop over the core segments with increasing length from the core inlet (section 1: 4.25 cm, section 2: 8.5 cm, section 3: 12.75 cm). A fourth differential pressure transducer was used to record the overall pressure drop along the core length. A data acquisition system (National Instruments) was used to record pressure, liquid production and gas and liquid injection rates.

6.2.4 CT scanner

The CT scans were obtained using a third generation SAMATOM Volume Zoom Quad slice scanner. The core flow set-up was placed on the couch of the CT scanner and core-holder was fixed vertically to the edge of the couch using polymethyl methacrylate (PMMA) stand, which is equally transparent to X-rays. The imaging settings used in the experiments are listed in Table 6.2. The X-ray tube of the CT scanner operated at a voltage of 140 kV and a current of 250 mA. The sequential scan mode was used for image acquisition. The thickness of each CT slice was 1 mm and one series of scans included 8 slices. The B40 medium filter was used for the

reconstruction of the images. A typical slice image consists of 512×512 pixels with the pixel size of $0.3 \text{ mm} \times 0.3 \text{ mm}$. Since the noise for CT images typically ranges from 3 to 20 Hounsfield units, the accuracy in the measured fluid saturation is within $\pm 2\%$.

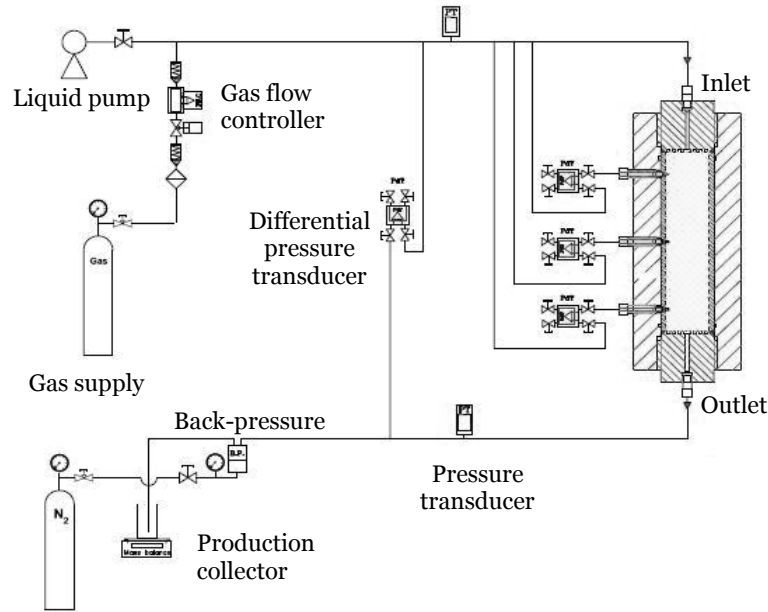


Fig. 6.1: Schematic of the experimental set-up used to perform core-flooding experiments. The core-holder was placed vertically on the couch of CT scanner. Local pressures were monitored based on the inlet pressure. There were additional lines, not shown in the schematic, that allowed the injection of fluids from the bottom of the core.

Table 6.2: Setting of CT scan measurements.

Specification	Quantity
Tube voltage (kV)	140
Tube current (mA)	250
Slice thickness (mm)	3
Pixel size (mm \times mm)	0.3×0.3
Image reconstruction kernel	B40 medium
Scan mode	Sequence

The following equation was used to obtain oil saturation from the measured attenuation coefficients in Hounsfield units (HU), eliminating the contribution of rock by the subtraction:

$$S_o = \frac{1}{\phi} \left(\frac{HU - HU_{wet}}{HU_o - HU_w} \right) \quad (6.1)$$

where ϕ is porosity of the core. Subscripts wet , o , and w stand for brine saturated core, oil and water phases, respectively.

To describe the distribution of fluids during foam (or gas) flooding, the CT images were converted into the total liquid saturation ($S_{liq}=S_o+S_w$) profiles. The reason to obtain total liquid saturation rather than oil and water saturations is that for the latter case one needs to CT scan the core using a true dual energy method. This option was available in the CT scanner, but the contrast of the images resulting from the pair of energies was not good enough to discriminate fluids at three-phase conditions. Therefore, total liquid saturation was reported in terms of the summation of oil and water saturations using the following equation:

$$S_{liq} = \frac{HU_{foam} - HU_{dry}}{HU_{pre-flush} - HU_{dry}} \quad (6.2)$$

where subscripts *foam*, *pre-flush*, and *dry* stand for core with foam, core at the end of surfactant pre-flush and dry core, respectively.

6.2.5 Experimental procedure

The basic sequence used to conduct core-flooding experiments is shown in Table 6.3. First air was removed by flushing the core with CO₂ at 5 bar injection pressure. Then the dry core was saturated by injecting at least 10 pore volumes (PV) of brine while maintaining a back-pressure of 25 bar. This was done to dissolve any CO₂ present in the core and thus to ensure a complete saturation of the core with brine. Next, primary drainage was performed by injecting model oil at 0.5 cm³/min under gravity stable conditions (from top of the core). Subsequently, imbibition was done by injecting brine from the bottom of the core and continued until no more oil was produced and the pressure drop over the core became constant. Then 2.0 PV of the surfactant solution were injected into the core to satisfy its adsorption capacity. Next, N₂ gas and surfactant solution were co-injected downward to generate foam at different surfactant concentrations (0.1, 0.5, 1.0 wt%). Foam flooding was performed at a fixed superficial velocity of 4.58 ft/day and with foam quality of 91% at a back-pressure of 20 bar and ambient temperature (21±1 °C). One baseline gas flooding experiment was performed at a superficial velocity of 4.2 ft/day at the same experimental conditions.

At each stage of the experiment, CT scans of the core were made to determine the distribution of fluid saturations in the porous medium and to reveal the propagation of the foam front. The results of core-flooding experiments were examined in terms of CT scan images, total liquid saturation, mobility reduction factor (as a ratio of foam to single-phase water flow pressure drops at the same superficial velocity), incremental oil recovery (oil recovered during gas or foam flooding divided by oil initially in place, OIIP, after primary drainage) and dynamic capillary desaturation curve.

Table 6.3: Basic sequence used to conduct core-flooding experiments.

Step	Description	Back pressure (bar)	Flow rate (cm ³ /min)	Injection direction
1	CO ₂ flushing	-	5.0	Down
2	Core saturation	25	1.0	Up
3	Oil injection	-	0.5	Down
4	Water flooding	-	0.5 - 1.0	Up
5	Surfactant pre-flush	-	1.0	Up
6	Foam flooding	20	1.1	Down

6.3 Results and discussion

6.3.1 Primary drainage and imbibition

Since the results of primary drainage and imbibition were similar for all core-flooding experiments, only one prototypical experiment will be discussed in detail.

6.3.1.1 CT scan images

Fig. 6.2 shows a series of CT images taken at different injected pore volumes during the primary drainage and imbibition. The image at zero PV represents a core fully saturated with brine, which is characterized by a dark red color. As oil is injected from top of the core, the color of images changes from red to yellow, indicating that oil drains water from the porous medium. Oil breakthrough occurred at 0.74 ± 0.02 PV and thereafter the color in the image changes only slightly. After the breakthrough a relatively high intensity of red color is evident near the outlet face. This is due to the capillary end effect: the wetting phase saturation must satisfy the zero capillary pressure conditions prevailing at outlet boundary. Further injection of oil partially eliminates the capillary end effect. Subsequently, imbibition was done by injection brine upward. Change in the color of the images from yellow to orange indicates the displacement of oil by the brine. Water breakthrough occurred before 0.36 ± 0.02 PV and thereafter the color of the images remained practically unchanged. The last image represents the end of the surfactant pre-flush, where 2.0 PV of the AOS solution was injected at the same rate as brine during water flooding. Only a small amount of oil of about $2.0 \pm 0.5\%$ of the OIIP was produced during surfactant pre-flush. We recall that the main purpose of surfactant pre-flush is to quench the adsorption capacities of the rock sample to reduce surfactant loss as much as possible during foam flooding.

6.3.1.2 Saturation profiles

For further quantitative analysis we plotted oil saturation during primary drainage and imbibition for different injected pore volumes as shown in Figs. 6.3 and 6.4. The general behavior of the oil saturation profiles, Fig. 6.3, during the primary drainage is reminiscent of a Buckley-Leverett

displacement: a sharp shock region followed by a rarefaction wave. As mentioned before, at the outlet face after breakthrough time oil saturation remained low due to the capillary end effect, but it increased gradually by injecting more oil. The average oil saturation along the core at the end of the primary drainage was 0.85 ± 0.02 , equal to connate water saturation $S_{wc} = 0.15 \pm 0.02$. This is consistent with the value obtained from the measured SCAL data for Bentheimer sandstone, where S_{wc} varied from 0.14 to 0.18 (Andrianov et al., 2012).

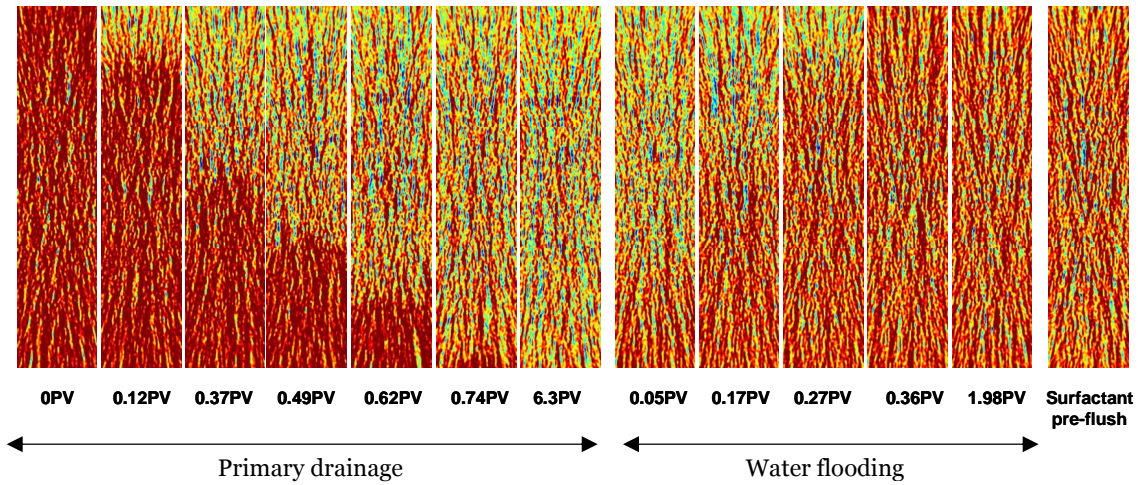


Fig. 6.2: Displacement profile during primary drainage (left), water flooding (middle) and surfactant pre-flush (right). Image at zero PV corresponds to the core fully saturated with brine. During primary drainage water (dark red) is displaced by oil (yellow). Oil production by water flooding is evident by a change in the color from yellow to orange.

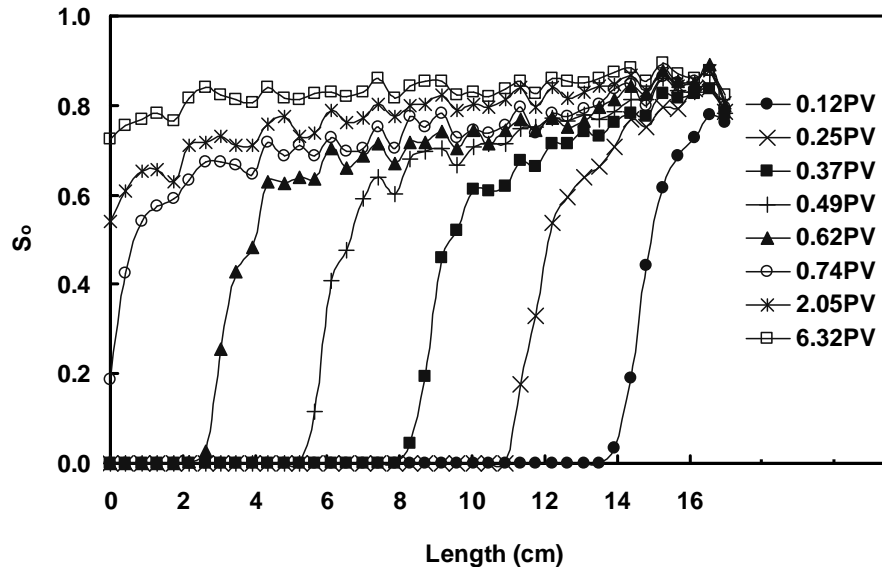


Fig. 6.3: Oil saturation profile for primary drainage, obtained from the corresponding CT images shown in Fig. 6.2. Oil was injected from the top of the core, which is located in the right side of the figure. The average oil saturation at the end of drainage was 0.85 ± 0.02 .

Fig. 6.4 shows oil saturation profile during water flooding. The general behavior of the advancing front is similar to that for primary drainage, although the broadening of the frontal region due to capillary pressure is more pronounced. Most of the oil was produced before water breakthrough and thereafter only a tiny amount of extra oil was recovered. The remaining oil was distributed uniformly through the core length and had an average value of 0.46 ± 0.02 . This value is higher than values obtained from SCAL measurements, which is about 0.28 ± 0.05 (Andrianov et al., 2012). However, several pore volumes of brine were injected after water breakthrough, but very little oil was produced. Instead, water cut (i.e., fraction of water in total produced liquid) increased considerably and reached nearly unity. Therefore, we concluded that the measured oil saturation at the end of the imbibition is water-flood residual oil saturation.

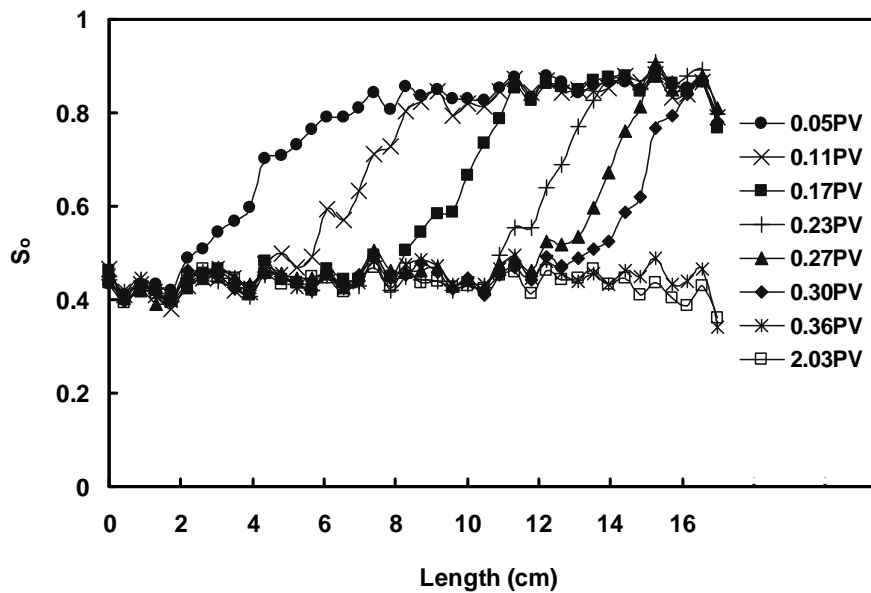


Fig. 6.4: Oil saturation profile for water flooding, obtained from the corresponding CT images shown in Fig. 6.2. Water was injected from the bottom of the core, which is located in the left side of the figure. The average oil saturation at the end of water flooding was 0.46 ± 0.02 .

6.3.1.3 Pressure drop profiles

Fig. 6.5 shows pressure drop profiles during primary drainage at $0.5 \text{ cm}^3/\text{min}$ for the first two pore volumes injected. When oil reaches the core inlet face, pressure drop increases sharply. The rise in pressure drop is about $45 \pm 5 \text{ mbar}$, which is consistent with the calculation of entry capillary pressure using the Young-Laplace equation ($P_c = 2\sigma \cos\theta/r$). Taking $\sigma_{ow} = 35 \text{ mN/m}$, $\theta = 0^\circ$ (totally water-wet system) and $r = 15 \text{ }\mu\text{m}$ (average pore radius obtained from mercury intrusion porosimetry), we obtain $P_{entry} = 47 \text{ mbar}$. After this steep rise, pressure drop in the first section increases gradually, indicating movement of oil front through this section. Ahead of the oil front, pressure drop is rather low, consistent with a Buckley-Leverett type displacement. When oil front reaches the first pressure port located at $1/4$ of the core length, a local oil breakthrough

occurs at 0.16 PV, which coincides with an abrupt reduction in the first pressure drop profile. The magnitude of the pressure drop reduction could be an indication of capillary pressure at the oil front. After the oil front passes through the first section, the corresponding pressure drop remains constant, consistent with the flow of oil in the presence of connate water. The observed trend of the pressure drop profile (i.e., a gradual increase followed by a sharp reduction to a plateau) repeats itself over the core length as the oil front moves toward other subsequent sections, located at 1/2 and 3/4 of the core inlet. The overall pressure drop along the core also increases gradually until reaching a maximum of 88 ± 5 mbar followed by a small reduction and then levels off to a plateau value of 73 ± 5 mbar, which is equal to a pressure gradient of 0.43 bar/m. Visual inspection of the effluents revealed that the maximum pressure drop coincides with the oil breakthrough at the core outlet.

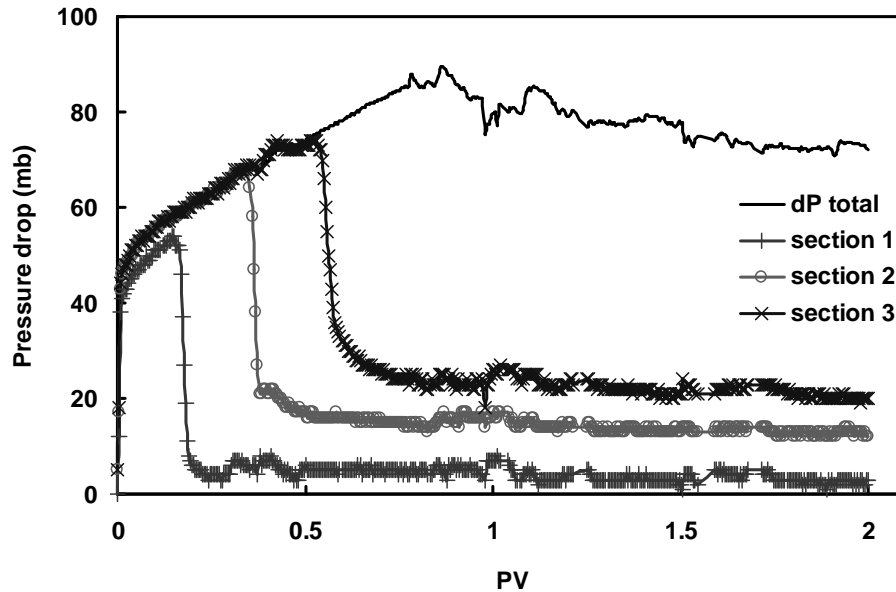


Fig. 6.5: Pressure drop profile during primary drainage over the core sections with increasing length from the inlet (section 1: 4.25 cm, section 2: 8.5 and section 3: 12.75 cm). Oil was injected at $0.5 \text{ cm}^3/\text{min}$ under gravity stable conditions. The initial jump in the pressure drop profiles corresponds to the entry capillary pressure.

Fig.6.6 shows the total pressure drop over the core during water flooding at $0.5 \text{ cm}^3/\text{min}$ for the first two injected pore volumes. The sectional pressure drops were low and fell below the accuracy of the pressure difference transducers. As brine is injected into the oil-saturated core, the total pressure drop increases revealing movement of the water front through the core. During this period only oil moving ahead of the water front is produced. The total pressure drop increases further until the water front breaks through the core outlet. Thereafter, it declines slightly and then levels off to a plateau value of 32 ± 5 mbar (equal to a pressure gradient of 0.19 bar/m), indicating that only water is produced from the core.

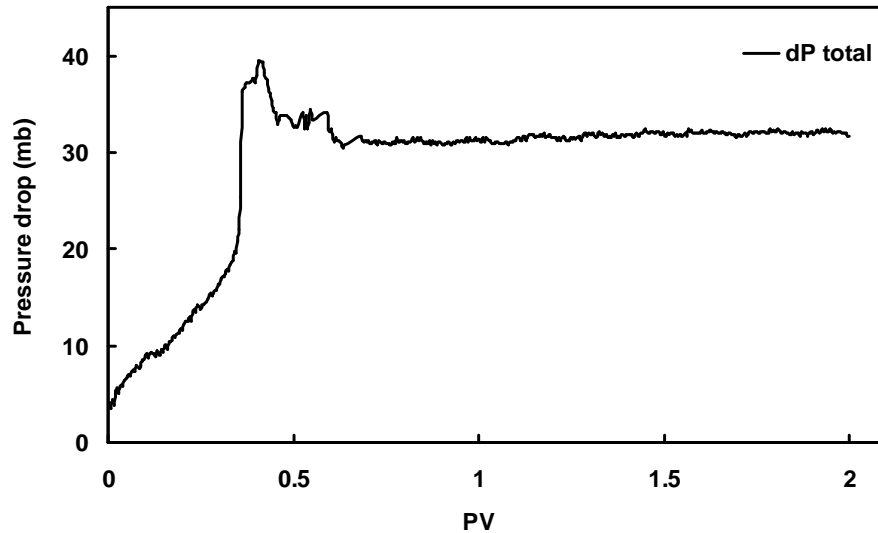


Fig. 6.6: Total pressure drop profile during water flooding at $0.5 \text{ cm}^3/\text{min}$ during the first two pore volumes injected. Water breakthrough coincides with the time at which pressure drop obtains a maximum value.

6.3.2 Gas flooding

Before performing foam-flooding experiments, a baseline gas flooding was done by injecting nitrogen directly after water flooding from the top of the core. The gas injection was done under gravity stable conditions according to the Dietz stability analysis (Dietz, 1953) by which the critical injection velocity was 4.2 ft/day , which is the same as the injected velocity. Fig. 6.7 shows the CT scan images taken during gas flooding. As gas is injected downward, there is a change in the image color from red to yellowish-green, indicating that a part of liquid is displaced by gas. During this period only water moving ahead of the gas front is produced. Gas breakthrough was observed early after the beginning of gas injection at $0.25 \pm 0.02 \text{ PV}$. This time coincided with the start of oil production at the core outlet. Visual inspection of the effluents revealed that after gas breakthrough a small amount of oil was recovered in a highly dispersed form (tiny droplets).

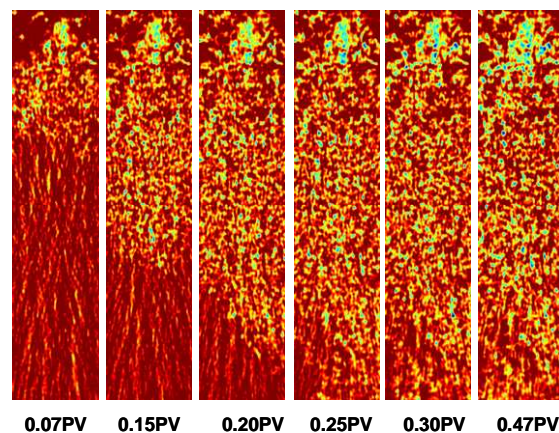


Fig. 6.7: CT images obtained during gravity stable gas flooding at $1.0 \text{ cm}^3/\text{min}$ in a water-flooded core. Gas breakthrough occurred at the early time only after $0.25 \pm 0.02 \text{ PV}$ of gas injection.

For further analysis of gas flooding, total liquid saturation ($S_{liq}=S_o+S_w$) profiles was obtained using Eq. (6.2) at different injected pore volumes. As shown in Fig. 6.8, only a very small fraction of total liquid (and thereby a very small fraction of water-flood residual oil) was produced by gas. After gas breakthrough the average liquid saturation along the core is 0.86 ± 0.02 . This shows that the performance of gas flooding, even under gravity stable conditions, is not satisfactory due to the high mobility of the injected gas and thus most of the initial liquid including water-flood residual oil is left in the porous medium. This high amount of remaining oil is a potential target for foam EOR as will be discussed in the next section.

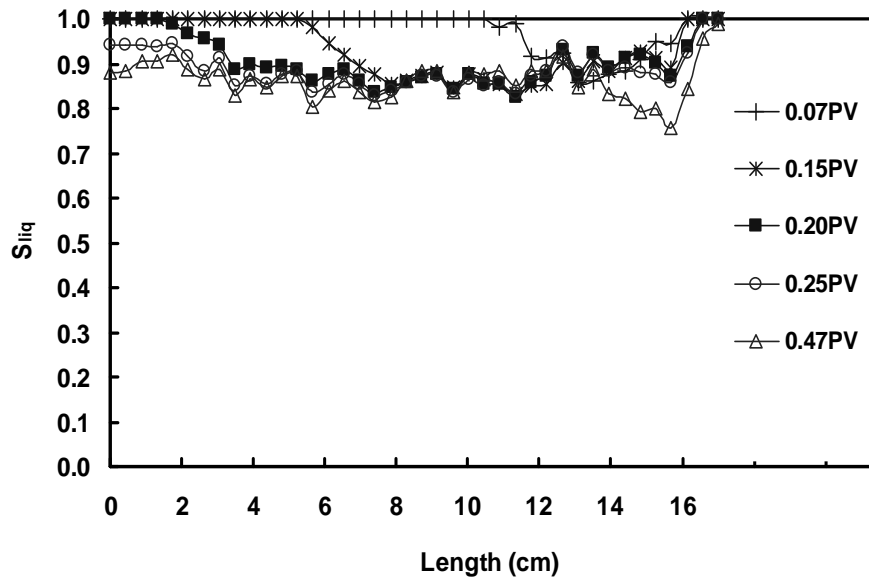


Fig. 6.8: Liquid saturation profiles during gas flooding, obtained from the CT images shown in Fig. 6.7. Gas was injected from the top of the core, which is located in the right side of the figure.

6.3.3 Foam flooding

6.3.3.1 CT scan images

Figs. 6.9 to 6.11 present a series of CT scan images obtained during foam flooding for different AOS concentrations (0.1, 0.5 and 1.0 wt%). In the CT images, the region with orange color corresponds to the liquid phase consisting of residual oil plus surfactant solution, two-phase flow region. As gas and surfactant solution are co-injected from the top of the core, the intensity of orange color diminishes progressively in favor of more blue/green, representing the three-phase region. This gives a first qualitative impression about the change in fluid saturations in the core.

Four main regions can be distinguished from the CT images before foam breakthrough time. The first one is located over the first 2.0 ± 0.2 cm from the core inlet. In this region orange color persists for a large number of injected pore volumes. This indicates a presence of high liquid saturation in the inlet region. It can be explained by the fact that the injected gas needs to travel a

certain distance into the core before foam is fully developed. As a result gas mobility remains high, resulting in a weak liquid displacement. Moreover, if the oil phase is present in the pore spaces, it might slow down the net rate of foam development and thus leading to even higher gas mobility. The second region is the upstream of the advancing front, characterized by a clear change in the image color from orange to blue/green. This region grows over the core length as the foam front moves toward the core outlet. The third region is a transition zone between swept and un-swept parts of the core. This transition zone is not as sharp as the one for foam flow in the absence of oil (see Fig. 3.2). This is most likely due to the fact that oil mobilized by foam forms a diffuse oil bank with high oil saturation ahead of the advancing foam front, which could partially destabilize foam. The fourth region is downstream of the advancing front, shown by orange color indicating liquid saturation equal to unity.

Closer examination of the CT images, however, reveals that the intensity of the orange color in the region displaced by foam decreases with increasing surfactant concentration. Let us consider the CT image at 0.30 PV for different surfactant concentrations. For 0.1 wt% AOS foam orange color is more visible in the flow domain. However, for 0.5 and 1.0 wt% AOS foams the number of orange spots diminishes and instead a progressive appearance and spreading of blue color are evident. Recall that the higher intensity of blue color in the CT image indicates the presence of a stronger foam and thus more liquid desaturation from the liquid-filled pores. Therefore, we can conclude that foam development improves considerably when surfactant concentration increases.

Foam breakthrough time is another indicator of foam performance: breakthrough time for 0.1 wt% foam was 0.28 ± 0.02 PV, which is longer than the breakthrough time for baseline gas flooding (about 0.25 ± 0.02 PV). Foam breakthrough time increases with surfactant concentration: 0.41 ± 0.02 PV for 0.5 wt% foam and 0.57 ± 0.02 PV for 1.0 wt% foam. The above results reveal that the foam propagation rate decreases with increasing surfactant concentration, which indicates a better macroscopic sweep of the core. For a longer time of foam injection, the CT images of 1.0 wt% AOS foam reveal that a new secondary foam front emerges at the downstream of the core and propagates upward against the main flow direction (see the image at 16.62 PV in Fig. 6.11). The appearance of this new front was visualized by a higher intensity of the blue colored zone, indicating that strong foam was generated in the downstream of the core. The general feature of this new secondary front is qualitatively similar to that observed for 1.0 wt% AOS foam in the absence of oil (see Fig. 3.2). However, the secondary foam front in absence of oil was developed earlier: after 1.5 PV compared to 16 PV for foam in the presence of oil.

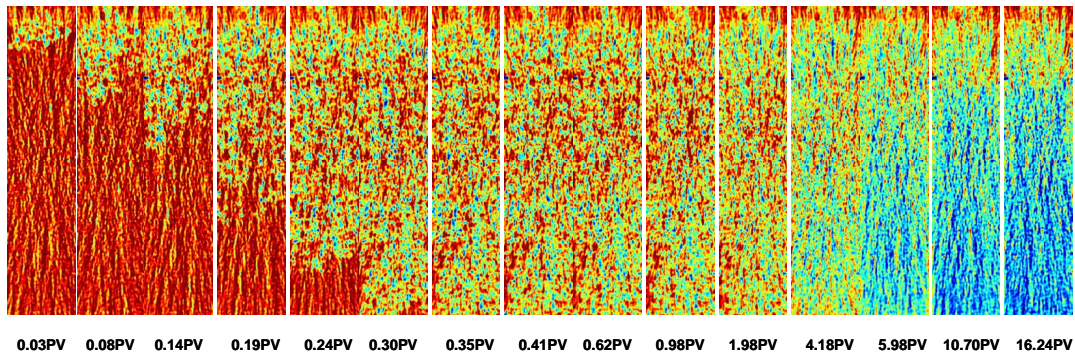


Fig. 6.9: CT images obtained during 0.1 wt% AOS foam flooding. Co-injection of gas and surfactant solution was done under gravity stable conditions, $q_g=1.0$ cm³/min and $q_{liq}=0.1$ cm³/min. Orange colour stands for residual oil plus surfactant solution. Green/blue colour indicates three-phase region. Foam breakthrough occurred at 0.28 ± 0.02 PV.

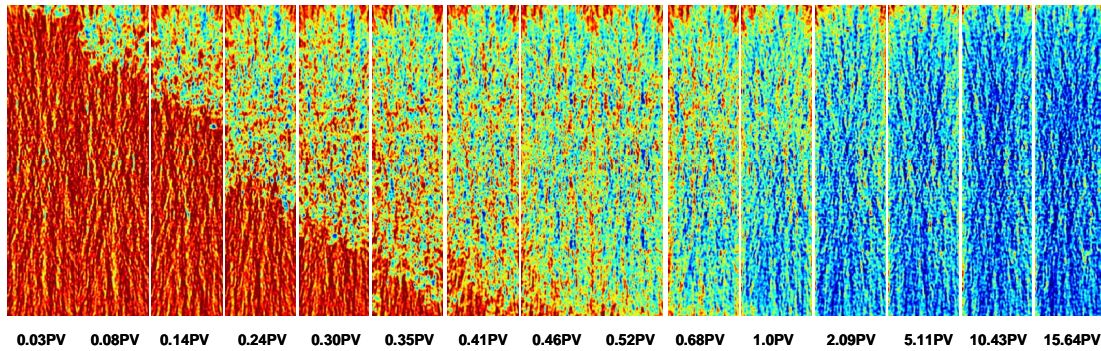


Fig. 6.10: CT images obtained during 0.5 wt% AOS foam flooding. Foam breakthrough occurred at 0.41 ± 0.02 PV.

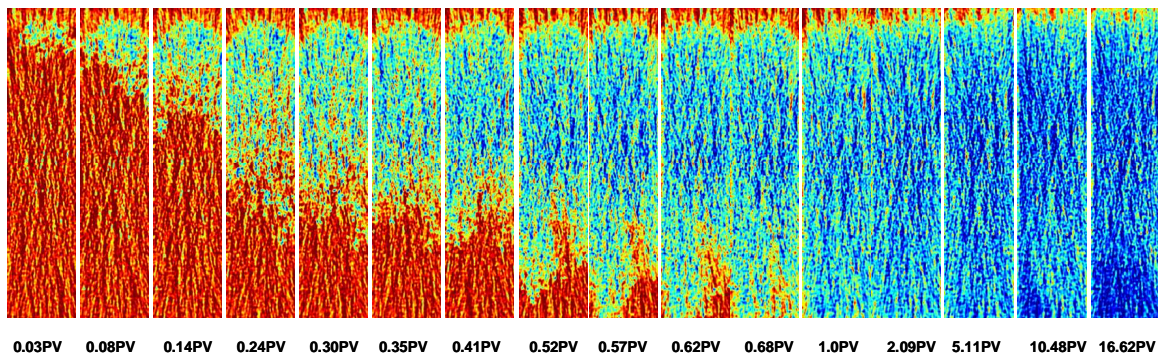


Fig. 6.11: CT images obtained during 1.0 wt% AOS foam flooding. Foam breakthrough occurred at 0.57 ± 0.02 PV.

6.3.3.2 Saturation profiles

For further quantitative analysis of foam propagation in the presence of oil we examine total liquid saturation ($S_{liq}=S_o+S_w$) at different injected pore volumes. Figs. 6.12 to 6.14 show S_{liq}

profiles obtained for three surfactant concentrations investigated. Let us first consider 0.1 wt% foam flow (Fig. 6.12). The four regions observed before foam breakthrough can be characterized further as follows: in the inlet region S_{liq} decreases from 0.90 ± 0.02 to 0.80 ± 0.02 at a distance of 2.0 ± 0.2 cm from the core inlet. In the upstream region displaced by foam, average S_{liq} is about 0.80 ± 0.02 . This region is followed by a transition zone at which S_{liq} increases from 0.80 ± 0.02 to unity. After foam breakthrough at 0.28 ± 0.02 PV, the remaining liquid saturation is distributed uniformly through the core and exhibits an average value of 0.78 ± 0.02 , except the inlet region (see the S_{liq} profile at 0.98 PV in Fig. 6.12). As more foam is injected, liquid saturation decreases continuously through the core: average S_{liq} decreases further from 0.78 ± 0.02 to 0.55 ± 0.02 after injecting 5.98 PV of foam. Beyond this pore volume, liquid saturation continues to decrease but at a slower rate: S_{liq} obtains an average value of 0.43 ± 0.02 after 16 PV injected. Note that even after injecting 16 PV, S_{liq} in the inlet region remains high. This reflects the fact that the injected gas needs some distance, which is 2.0 ± 0.2 cm for the conditions investigated, before it is developed into foam.

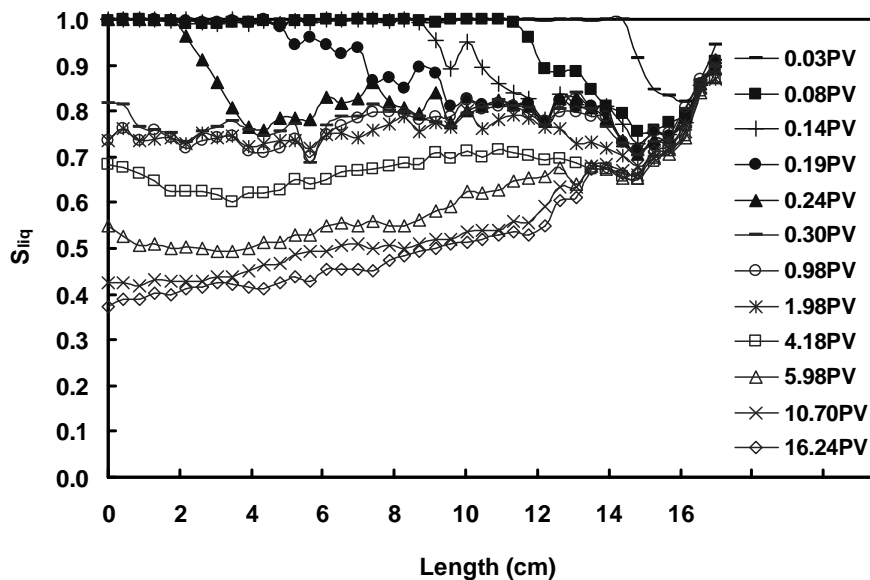


Fig. 6.12: Liquid saturation profiles for 0.1 wt% foam obtained from the CT scan images shown in Fig. 6.9. Gas and surfactant solution were co-injected from the top of the core, which is located in the right side of the figure. Closed and open curves indicate liquid saturation profiles before and after foam breakthrough.

Now let us consider the S_{liq} profiles for foam at higher surfactant concentrations (Figs. 6.13 and 6.14). The overall trend of the S_{liq} profiles for 0.5 and 1.0 wt% foams is qualitatively similar to that for 0.1 wt% foam: a high amount of S_{liq} in the inlet region, followed by a reduction in S_{liq} in the upstream region, and then a transition zone through which S_{liq} increases to unity. However, when the surfactant concentration increases from 0.1 to 1.0 wt%, more liquid desaturation occurs by foam and thus a smaller S_{liq} is obtained in the upstream region. Let us compare the average S_{liq}

before foam breakthrough for different surfactant concentrations. For 0.1 wt% foam average S_{liq} is 0.80 ± 0.02 while for 0.5 and 1.0 wt% foams it decreases further to 0.70 ± 0.02 and 0.50 ± 0.02 , respectively. Note that the corresponding average S_{liq} for the baseline gas flooding was 0.88 ± 0.02 .

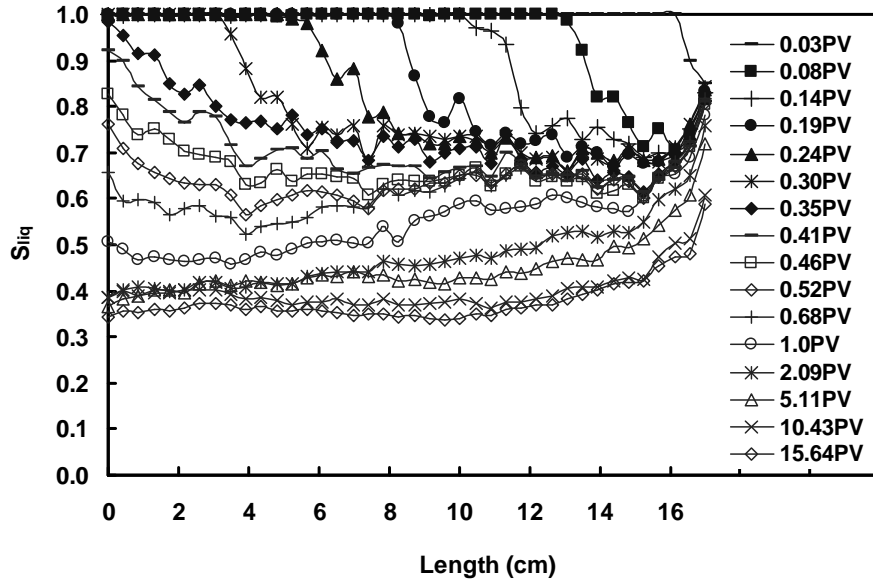


Fig. 6.13: Liquid saturation profiles for 0.5 wt% foam obtained from the CT scan images shown in Fig. 6.10.

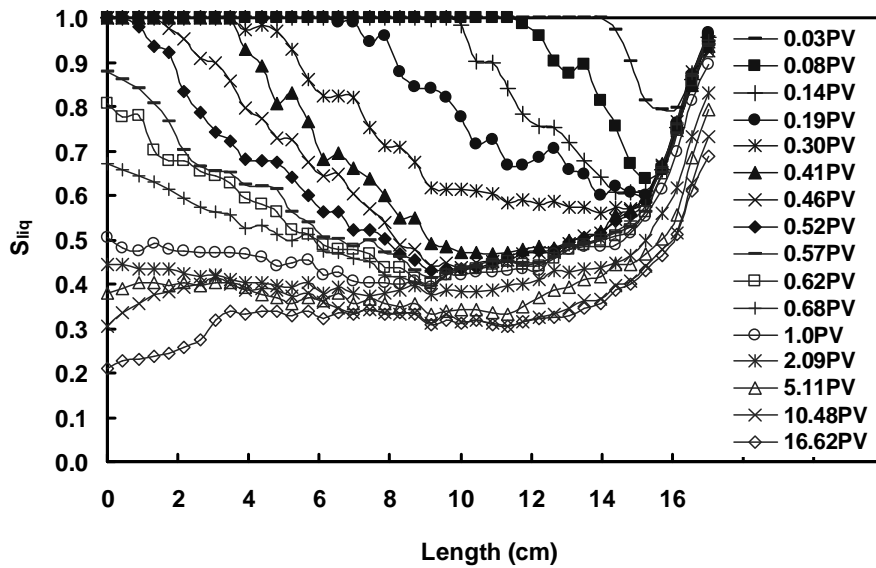


Fig. 6.14: Liquid saturation profiles for 1.0 wt% foam obtained from the CT scan images shown in Fig. 6.11.

The effect of the surfactant concentration on the S_{liq} profiles is also evident after foam breakthrough. Let us compare S_{liq} after 1.0 PV of foam injection. While the average S_{liq} for 0.1 wt% foam is 0.78 ± 0.02 , it decreases further to 0.55 ± 0.02 for 0.5 wt% foam and 0.47 ± 0.02 for 1.0 wt% foam. The results above prove that foaming of the injected gas, even at surfactant concentration as low as 0.1 wt%, provides a better mobility control compared to gas flooding and,

correspondingly, diminishes liquid saturation more. Also, as the surfactant concentration increases from 0.1 to 1.0 wt%, foam flow exhibits better macroscopic sweep efficiency due to the development of a stronger foam.

Table 6.4 gives a summary of the effect of the surfactant concentration on foam propagation rate and foam breakthrough time in the absence and presence of oil. The data show that for all concentrations investigated the foam propagation rate is higher in the presence of oil due to the partial destabilization of foam. This leads to foam breakthrough time occurring earlier. For instance for 1.0 wt% concentration when oil is present in the porous medium, foam propagation rate increases from 0.22 ± 0.01 to 0.30 ± 0.01 m/PV, corresponding with a reduction in foam breakthrough time from 0.76 ± 0.2 to 0.57 ± 0.2 PV. Remarkably, although the generated foam becomes partially destabilized by oil, the foam front is still strong enough to induce a reduction in liquid saturation as noted in the CT images and saturation profiles (Figs. 6.11 and 6.14). Comparing the magnitude of the foam propagation rate in the absence and presence oil shows that the increasing effect of the surfactant concentration is more pronounced when oil is present in the porous medium: foam propagation rate in the presence of oil decreases twice as the surfactant concentration increases from 0.1 to 1.0 wt%. These results once again show that surfactant concentration is a key physical parameter to adjust the properties of the advancing foam front for a given EOR application.

Table 6.4: Effect of surfactant concentration on foam propagation rate and foam breakthrough time in the absence and presence of oil.

Concentration (wt%)	In the absence of oil		In the presence of oil	
	Propagation rate	Breakthrough	Propagation rate	Breakthrough
	(m/PV, ± 0.01)	time (PV, ± 0.02)	(m/PV, ± 0.01)	time (PV, ± 0.02)
0.1	0.29	0.58	0.61	0.28
0.5	0.24	0.71	0.42	0.41
1.0	0.22	0.76	0.30	0.57

6.3.3.3 Foam mobility reduction factor

Fig. 6.15 shows mobility reduction factor (MRF) obtained for three surfactant concentrations investigated. Recall that MRF was defined as a ratio of foam to single-phase water pressure drops. MRF for 0.1 wt% foam remains low over the first 4.0 PV injected: it increases very slowly from 18 ± 5 to 40 ± 5 , corresponding to a pressure gradient of 1.9 bar/m. This slow increase is consistent with liquid saturation remaining high (about 0.68 ± 0.02) in the porous medium. Beyond 4.0 PV, MRF rises progressively, and then levels off to 335 ± 5 . As the surfactant concentration increases, MRF grows rapidly in the first injected pore volume, reaching 300 ± 5 for 0.5 wt% foam and 470 ± 5

for 1.0 wt% foam. These correspond to a pressure gradient of 14 bar/m for 0.5 wt% foam and of 21 bar/m for 1.0 wt% foam. The sharp increase of MRF is consistent with the substantial reduction in liquid saturation within the first injected pore volume (Figs. 6.13 and 6.14). The rate of increase of MRF is faster (about two times) for 1.0 wt% foam compared to 0.5 wt% foam. It seems that MRF for 0.5 wt% foam continues to increase very slowly such that, after the initial rise, it reaches 630 ± 5 . MRF for 1.0 wt% foam, however, tends to decrease slowly after peaking at 700 ± 5 . The above results combined with the liquid saturation profiles show that increasing the surfactant concentration enhances foam stability in the presence of oil, giving a large MRF. This improves the sweep efficiency and displaces more liquid (including part of residual oil) from the core.

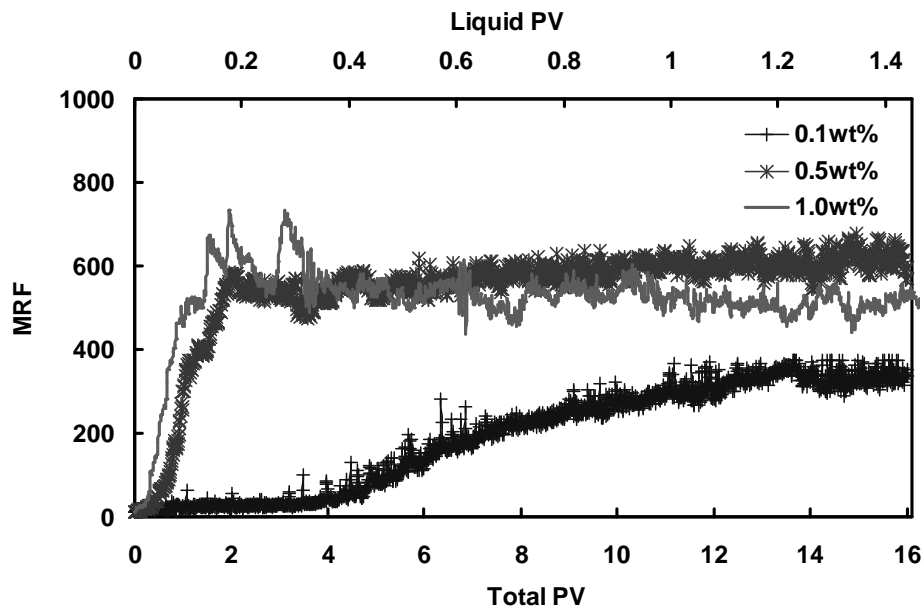


Fig. 6.15: Mobility reduction factor during foam flooding for different surfactant concentrations. A higher surfactant concentration leads to a larger MRF in the presence of oil.

6.3.3.4 Incremental oil recovery by foam

Figs. 6.16 and 6.17 show oil cut profiles and incremental oil recovery due to foam flooding for the three-surfactant concentrations investigated. The amount of produced oil was obtained from the material balance on the core and the analysis of the effluents. Oil cut was defined as the fraction of oil in the produced liquid. The incremental oil recovery was a ratio of the produced oil to the oil initially in place. Let us first consider 0.1 wt% foam. In the first 0.3 PV, oil is produced at a high rate and presents a jump in the oil cut profile, which is consistent with the formation of an oil bank. Then the oil cut profile decreases significantly to as low as 3.0% up to 2.0 PV. Thereafter, no more oil is produced until 4.0 PV. Beyond that oil production resumes with a modest increase in the oil cut profile to 8.0% until 10 PV and then it continues with an almost constant oil cut for the rest of the experiment. We note that increase in oil production after 4.0 PV coincides with a

progressive rise of MRF from 40 ± 5 to 300 ± 5 and also with a reduction in average liquid saturation from 0.68 ± 0.02 to 0.50 ± 0.02 (see Figs. 6.12 and 6.15). Beyond 10.0 PV, when the oil production rate becomes constant, the MRF profile also levels off to a plateau value of 335 ± 5 .

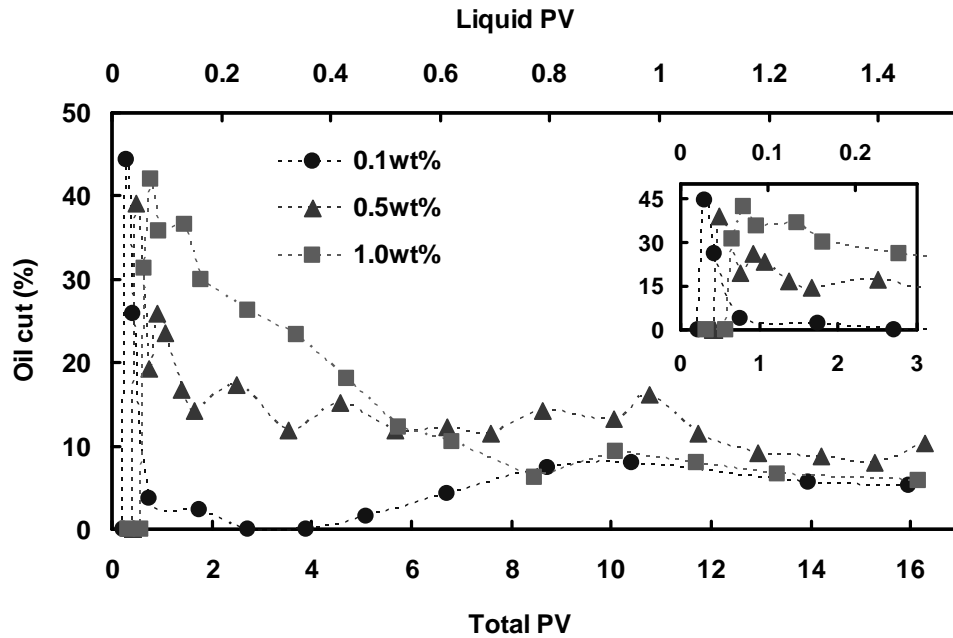


Fig. 6.16: Oil cut profile during foam flooding for different surfactant concentrations. The first peak corresponds to the production of the generated oil bank. The size of oil bank is extended for a longer PV as surfactant concentration increases.

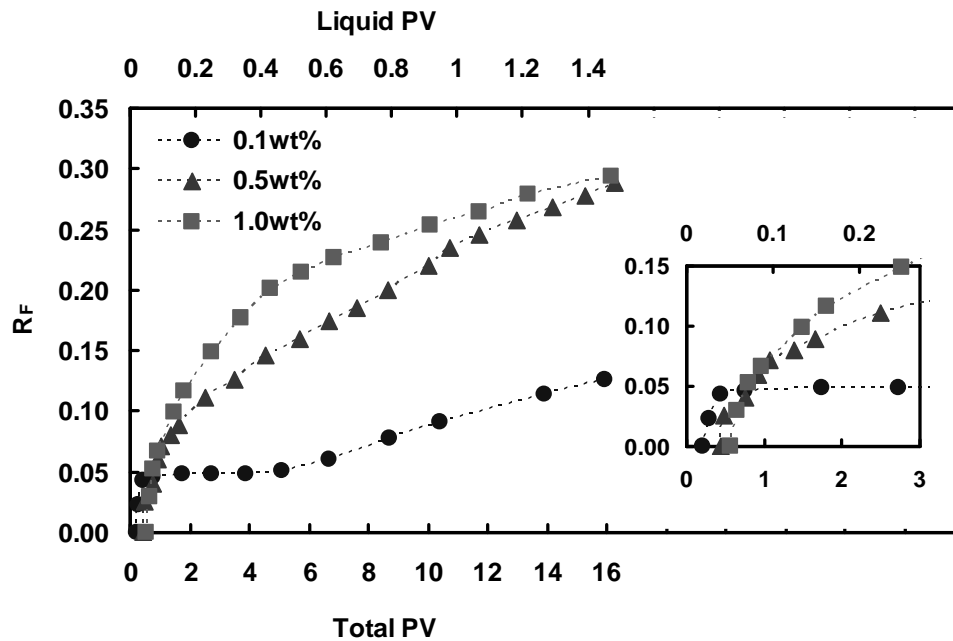


Fig. 6.17: Incremental oil recovery during foam flooding for different surfactant concentrations.

When the surfactant concentration increases to 0.5 and 1.0 wt%, a qualitatively different oil recovery is observed. First of all for both concentrations oil breakthrough is delayed due to a good mobility control provided by foam. At short times (within the first 1.5 PV) the oil production rate tends to increase as can be judged from the oil cut profiles, while during long times it decreases progressively. Therefore, oil is produced first by the formation of an oil bank followed by a long tail production. The size of the oil bank increases with surfactant concentration: after 3.0 PV the oil cut for 0.5 wt% foam is $15\pm 1\%$ compared to $25\pm 1\%$ for 1.0 wt% foam. The tailing oil production is, however, less sensitive to the surfactant concentration: the oil cut for 0.5 and 1.0 wt% foams is $7\pm 1\%$ and $9\pm 1\%$ respectively. For both 0.5 and 1.0 wt% foams the oil bank production coincides with a sharp increase in MRF, while the tailing production occurs without drastic changes in MRF and also in liquid saturation profiles.

Table 6.5 gives a summary of the incremental oil recovery by foam for the three surfactant concentrations investigated at two different pore volumes, namely 3.0 and 16.0 PV (respectively equal to the injection of 0.27 and 1.46 PV of surfactant solution) representing the short and long time of foam injection. The results show that an increase in the surfactant concentration leads to a substantially higher oil recovery consisting with a larger MRF (see Fig. 6.15). After 3.0 PV the incremental oil recoveries by 0.1, 0.5 and 1.0 wt% foams were respectively $5.0\pm 0.5\%$, $12\pm 2\%$, and $16\pm 2\%$ of the OIIP. The corresponding oil recovery by gas flooding was $4.0\pm 0.5\%$ of the OIIP. At a long time of foam injection oil recovery continues to increase, but at a slower rate. For example for 1.0 wt% foam beyond the first $16\pm 2\%$ oil recovery obtained after 3.0 PV, an additional oil production of $13\pm 2\%$ was recovered for the next 13 PV. Table 6.5 also shows that oil recovery by 0.1 wt% foam after 16 PV is about half of the 0.5 and 1.0 wt% foams. The lower oil recovery ($13.0\pm 0.5\%$ of the OIIP) by 0.1 wt% AOS foam is consistent with its lower stabilized MRF.

Table 6.5: Incremental oil recovery by foam at different surfactant concentrations.

Concentration (wt%)	Incremental oil recovery (% of OIIP)	
	After 3.0 PV of foam injection	After 16 PV of foam injection
0.1	5.0 ± 0.5	13.0 ± 0.5
0.5	12 ± 2	28 ± 2
1.0	16 ± 2	29 ± 2

6.3.4 Foam EOR mechanism

In the previous sections we provided tangible evidence that stable foam can be obtained by co-injection of surfactant (AOS in brine) and nitrogen in sandstone cores pre-flushed by surfactant solution. This was established by a careful analysis of the CT scan images and the liquid saturation profiles in Figs. 6.9 to 6.14 and the mobility reduction factor in Fig. 6.15. We

demonstrated that foam is generated at a surfactant concentration as low as 0.1 wt%, but its mobility reduction factor remained low and correspondingly the incremental oil recovery was slightly higher than that of gas flooding. We also found that the foam mobility reduction factor increases considerably upon increasing the surfactant concentration to 0.5 and 1.0 wt%. The increase of surfactant concentration also resulted in higher oil recovery by foam as shown in Fig. 6.17. We identified that the incremental oil by foam is obtained first by a formation of an oil bank followed by a long tail production.

In order to explore further the foam flooding mechanisms, we have plotted oil saturation as a function of the capillary number N_c , as shown in Fig. 6.18. This curve can be viewed as a dynamic picture of the evolution of oil saturation with respect to N_c during foam flow. The capillary number N_c was defined as follows:

$$N_c = \frac{kk_{rf}\Delta P}{\sigma_{ow}L} \quad (6.3)$$

where k is absolute permeability of the core sample, k_{rf} is foam relative permeability, ΔP is pressure drop over the core, σ_{ow} is the interfacial tension between oil and water, and L is the core length. For simplicity, it was assumed that foam is a single-phase fluid such that k_{rf} is equal to one. Each N_c profile in Fig. 6.18 starts with water flooding at two injection velocities of 2.1 and 4.2 ft/day. The corresponding N_c changes in the order of 10^{-7} to 10^{-6} , at which capillary forces are dominant to trap the oil phase. The oil recovery factor due to water flooding was about $44 \pm 2\%$ of the OIIP. The third point stands for the surfactant pre-flush by which IFT between oil and water decreases to 1.9 ± 0.1 mN/m under the experimental conditions. Although N_c increases by one order of magnitude when we switch from water to surfactant, capillary forces are still dominant and keep most of the water-flood residual oil trapped. During the surfactant pre-flush, only a small amount of oil of about $2.0 \pm 0.5\%$ of the OIIP was recovered. The next point at each N_c profile corresponds to the beginning of foam flooding, which shows that N_c increases during foam flooding. This can be explained by a larger magnitude of viscous forces as a result of pressure build-up due to the foam development. An increase in viscous forces along with a modest reduction in IFT, due to the presence of surfactant, ensures partial mobilization of the trapped oil. Our results also show that N_c increases with the surfactant concentration. For 0.1 wt% foam N_c remains low at the early time hardly exceeding 1.0×10^{-4} . Thereafter, N_c increases progressively reaching 2.0×10^{-3} after 16.0 PV of foam injection. For 0.5 and 1.0 wt% foams N_c instead increases from 5.0×10^{-5} at the end of the surfactant pre-flush to 3.3×10^{-3} after 3.0 PV of foam injection and then remains fairly constant at this value for the rest of the injection time. The last point of the dynamic capillary desaturation curve for 1.0 wt% foam shows that $43 \pm 2\%$ of the water-flood

oil and then incremental oil recovery by the foam. However, for 0.1 wt% concentration it appears that foam strength increases as oil saturation decreases.

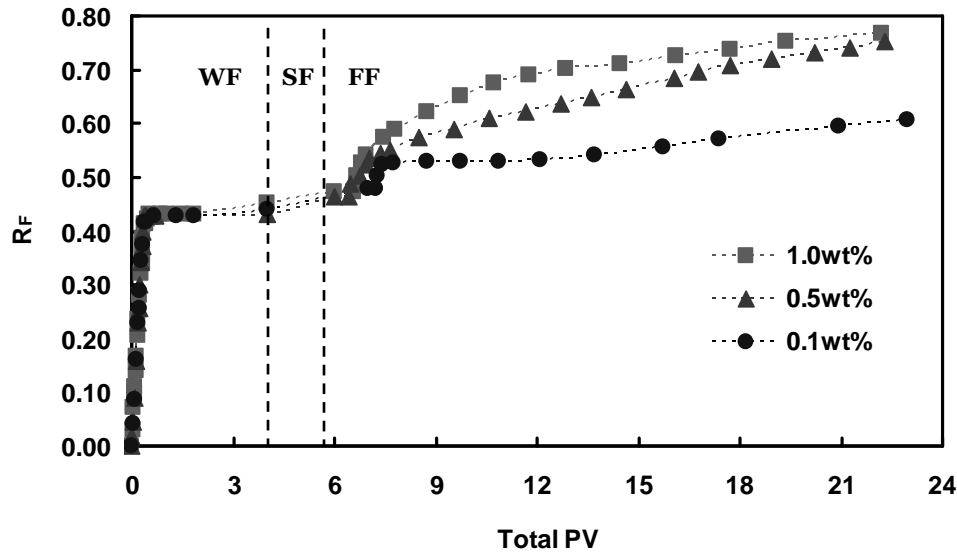


Fig. 6.19: Oil recovery factor profile for core-flooding experiments performed in this study. Each profile starts with water flooding (WF) followed by surfactant pre-flush (SF) and then foam flooding (FF) at different surfactant concentrations. Oil recover factor by water flooding was about $44 \pm 2\%$ of the OIIP. A small amount of oil of about $2.0 \pm 0.5\%$ of the OIIP was produced during surfactant pre-flush. Additional oil was produced during foam flooding.

Fig. 6.19 summarizes the incremental oil recovery for the three-surfactant concentrations investigated. As can be seen during foam flooding, incremental oil is first produced at high rates and then the oil production rate decreases slowly. Visual inspection of the effluents together with the CT scan images and foam mobility data have already indicated that early incremental oil is obtained by a generated oil bank while the later oil is due to the transport of tiny oil droplets within the flowing foam. This is consistent with the fact that at a long time of foam injection, oil saturation decreases further under a fairly constant N_c . Previous studies (Nikolov et al. 1986; Jensen and Friedmann, 1987; Raterman, 1989; Mannhardt et al., 1998; Schramm and Novosad, 1990; Yin et al., 2009) demonstrated only final oil recoveries without mentioning in detail how such produced oil was obtained over the time of foam injection. Mannhardt et al. (1998) reported additional oil production by foam over several tens of injected pore volumes, with a mechanism by which emulsified oil droplets are carried inside the foam structure. This proposed mechanism agrees qualitatively with other micro-models and bulk studies of foam-oil interaction (Nikolov et al. 1986; Manlowe and Radke, 1990; Koczo et al., 1992). The physical picture emerging from our core-flood analyses at a long time of foam injection and also bulk foam stability in the presence of oil (see Fig. 6.20 and section 2.3.3 in Chapter 2) are in agreement with the work of Mannhardt et

al. (1998). As shown in Fig. 6.20 for AOS bulk foam in the presence of normal hexadecane, in which the model oil was colored red, the oil phase is mostly accumulated in the Plateau borders. Such oil transporting property might work for carrying oil droplets by foam in the porous medium. However, we emphasize that the oil recovery mechanism by foam transport becomes important only at a later time of foam injection, namely after producing the oil bank.



Fig. 6.20: Distribution of oil droplets inside 0.5 wt% AOS bulk foam. The model oil was n-hexadecane, which was colored red for the visualization purposes. The image shows the accumulation of oil droplets in the Plateau borders.

Based on the above discussion the question arises whether the standard definition of the capillary number as a ratio of viscous to capillary forces is an appropriate representation of the active mechanism(s) in the decrease of oil saturation during foam flooding at a constant N_c . In fact more precisely, the question arises whether foam flow is just water or surfactant flooding at a high gas saturation. To answer these questions, more detailed studies focusing on the microscopic mechanisms of foam flooding are required. The first step could be to perform foam-flooding experiment with the aid of an appropriate dual source CT scanner to provide three-phase saturation maps. In this way we would be able to track the local distribution of the oil phase to validate the proposed oil mechanisms (formation of oil bank and long tail production) and also to determine precisely at which period during foam injection these mechanisms play a main role. In addition, micro-model studies could be performed while ensuring that pore structures are as close as possible to those of granular porous media. These results could provide more insight into the microscopic aspects of the transport of oil droplets inside the foam structure.

This study demonstrated that stable foam is obtained in natural sandstone cores containing water-flood residual oil. Foam flooding provided an incremental oil recovery ranging from $13 \pm 0.5\%$ to $29 \pm 2\%$ of the OIIP as the surfactant concentration increases from 0.1 to 1.0 wt% (Fig. 6.19). This provides the first-hand experimental results showing that immiscible foam can

increase oil recovery, thus supports the concept that foam could be potentially employed for EOR application. However, to implement foam EOR process in the field further studies are required to address more realistic situations such as the effects of crude oil and temperature on foam stability and also the way to generate foam to obtain an appropriate foam strength. It seems that existing foam models need only slight modifications to capture early oil recovery, but for the later oil recovery, i.e. transport of dispersed oil, one requires a novel phenomenological framework.

6.4 Conclusions

Flow of nitrogen foam stabilized by C₁₄₋₁₆ alpha olefin sulfonate (AOS) in natural sandstone cores containing water-flood residual oil was studied. Foam flooding was performed under gravity stable conditions at a fixed superficial velocity of 4.58 ft/day and foam quality 91% at a back-pressure of 20 bar and ambient temperature (21±1 °C). Effect of surfactant concentration (0.1, 0.5 and 1.0 wt%) on the foam strength and foam propagation was examined. The main conclusions from this study are as follows:

- CT scan saturation maps, foam mobility profile and effluent measurements confirm that stable foam can be obtained in the presence of water-flood residual oil.
- By increasing the surfactant concentration from 0.1 to 1.0 wt%, foam exhibited a better front-like displacement, characterized by a longer breakthrough time and a further reduction in liquid saturation as well as in oil saturation.
- Incremental oil production by foam was obtained at two distinct regimes in line with CT scan images and visual inspection of the effluents. The first one was due to the generation of an oil bank and occurred in the first few pore volumes injected. The second one was a tailing regime where the incremental production was obtained due to the transport of dispersed oil within the flowing foam, which could be consistent with a picture of tiny oil droplets carried in the Plateau borders. The size of the oil bank increased with the surfactant concentration, but the second regime was found to be less sensitive to the surfactant concentration.
- The two oil recovery regimes observed during foam flooding were described by a dynamic capillary desaturation curve. In the oil bank regime, reduction of oil saturation was accompanied by an increase in the capillary number indicating that viscous forces are high enough to mobilize a part of trapped oil. In the tailing regime, the capillary number remains fairly constant despite the continuous decrease of oil saturation. This could be due to the displacement of oil in a dispersed form.
- Under the experimental conditions of this study AOS foam flooding provided an incremental oil recovery ranging from 5±0.5% of the OIIP for 0.1 wt% foam to 12±2% of the OIIP for 1.0 wt% foam after injection of 3.0 PV (equal to the injection of 0.27 PV of

surfactant solution). At the same injection time gas flooding recovered only $4.0 \pm 0.5\%$ of the OIIP. For a long time of foam injection, after 16.0 PV, oil recovery factors ranged from $13 \pm 0.5\%$ for 0.1 wt% foam to $29 \pm 2\%$ for 1.0 wt% foam.

Chapter 7

FURTHER INVESTIGATION OF OIL RECOVERY BY IMMISCIBLE FOAM*

Abstract

In the previous chapter we investigated foam propagation in the presence of water-flood residual oil and found that foam can improve oil recovery from sandstone porous media previously subject to water flooding. This chapter is aimed to gain further insight into the performance of foam EOR by studying the effects of the following parameters: surfactant pre-flush, injection direction (gravity stable/unstable condition) and core length. To this end, foam was generated in water-flooded sandstone cores by co-injecting nitrogen and surfactant solution at a fixed foam quality of 91%. Foam was stabilized using two surfactants, namely C₁₄₋₁₆ alpha olefin sulfonate (AOS) and mixtures of AOS and a polymeric fluorocarbon (FC) ester. Stable foams were obtained in the presence of water-flood residual oil. It was found that foam strength (mobility reduction factor) increases with surfactant concentration. Foam development and, correspondingly, oil recovery without surfactant pre-flush were delayed compared to the case with pre-flush. Gravity stable foam injection caused a quick increase of foam strength and an incremental oil recovery almost twice that for unstable flow conditions. Core floods revealed that incremental oil recovery by foam was as much as 23±2% of the oil initially in place after injection of 4.0 PV of foam (equal to the injection of 0.36 PV of surfactant solution). Incremental oil recovery was only 5.0±0.5% for gas flooding at the same injection conditions. It appears that oil production by foam flooding occurs due to the following main mechanisms: (1) residual oil saturation to gas flooding is lower than to water flooding, (2) formation of an oil bank in the first few injected pore volumes, coinciding with a large increase of the capillary number and (3) a long tail production due to the transport of tiny oil droplets within the flowing foam at a fairly constant capillary number. Observations of this study support the concept that foam is potentially an efficient EOR method.

* Adapted from Simjoo et al. 'A CT scan study of immiscible foam flow in porous media for enhancing oil recovery', revision submitted to journal of Industrial & Engineering Chemistry Research (2012).

7.1 Introduction

It is now well established that foam can improve sweep efficiency of gas flooding by reducing gravity override, viscous fingering and channeling (Kovscek and Radke, 1994; Rossen, 1996). Reduction of gas mobility due to foaming proved useful for steam flooding conformance control (Hirasaki, 1989; Patzek and Koinis, 1990), water or gas shutoff (Hanssen and Dalland, 1994; Zhdanov et al., 1996) and acid diversion (Behenna, 1995). Successful field trials of hydrocarbon gas and CO₂ foams have also been reported (Hanssen et al., 1994; Hoefner et al., 1995; Skauge et al., 2002). Foam was also used for contaminated soil remediation (Hirasaki et al., 1997; Zhong et al., 2010).

Much research was done on foam in the past, but most of the experimental studies were restricted to foam in the absence of oil. Current interest to study foam behavior in the presence of oil arose mainly from the potential application of foam for enhanced oil recovery (EOR). For a long time the topic of the effect of oil on foam has been a subject of debate. Several authors (Minssieux, 1974; Jensen and Friedmann, 1987; Low et al., 1992; Svorstøl et al., 1996) argued that it is hard to develop 'strong' foam if oil saturation is above a certain critical value while others (Schramm et al., 1993; Arra et al., 2002; Vikingstad and Arra, 2009) supported the possibility of generating strong foam even at 'relatively high' oil saturation. This would lead to an increase of oil recovery compared to gas flooding (Ali et al., 1985; Mannhardt et al., 1998). Available evidence suggests that foam generation and propagation in porous media in the presence of oil depends on the surfactant type (Jensen and Friedmann, 1987) or on a combination of surfactant and oil types (Nikolov et al., 1986; Raterman, 1989). It was also found that co-injection of gas and surfactant generates stronger foam and provides better sweep efficiency than surfactant-alternating-gas (SAG). This can be attributed to better gas-liquid mixing and a continuous surfactant supply (Huh et al.; 1988; Raterman, 1989).

Recent studies of gas-surfactant co-injection and SAG in natural sandstone cores showed that sufficiently stable foams can be developed in the presence of water-flood residual oil, leading to substantial incremental oil recovery (Yin et al., 2009; Farajzadeh et al., 2010; Andrianov et al., 2012). Other studies have demonstrated that the use of foam together with alkaline-surfactant greatly enhances oil recovery similarly to alkaline-surfactant-polymer (ASP) flooding (Li et al., 2008; Srivastava et al., 2009; Guo et al., 2011). While these studies have shown that stable foams can be formed in the presence of water-flood residual oil giving rise to additional oil recovery, more work is needed to elucidate the underlying mechanisms.

The purpose of this study is to conduct a systematic investigation of the flow of immiscible foams, stabilized either by a mixture of surfactants or by a single surfactant in the presence of a model

oil. Effects of surfactant concentration, surfactant pre-flush, injection direction (gravity stable or unstable) and core length on foam strength and on additional oil recovery were carefully examined. This chapter proceeds with experimental materials and methods. Next, the results of core-flooding experiments are presented and discussed. Then the main conclusions are drawn.

7.2 Experimental description

7.2.1 Materials

Brine containing 0.5 M sodium chloride (NaCl, Merck) in de-ionized water (pH=6.8±0.1) was used to prepare surfactant solutions. Density and viscosity of the brine at 21°C were 1.02±0.01 g/cm³ and 1.18±0.01 cP, respectively. Two surfactants were used to perform foam experiments: (a) C₁₄₋₁₆ alpha olefin sulfonate (AOS, Stepan) and (b) a mixture of AOS and polymeric fluorocarbon ester surfactant (FC-4434, 3M). AOS is an anionic surfactant while FC is a neutral polymeric surfactant. AOS and FC were provided in a solution containing 40.0 wt% and 25.0 wt% active material, respectively. Both surfactants were used as received without further treatment. Their critical micelle concentration (c.m.c.) in the presence of 0.5 M NaCl was determined from the surface tension measurements and found to be 4.0×10⁻³ wt% for AOS surfactant and 1.6×10⁻³ wt% for the surfactant mixture. The model oil used in the experiments was normal hexadecane (n-C₁₆, Sigma-Aldrich) with purity equal to 99.99%. Density and viscosity of this oil at 21°C are 0.77±0.01 g/cm³ and 3.28±0.01 cP, respectively. Nitrogen gas with a purity of 99.98% was used to conduct the experiments.

7.2.2 Core sample and core-holder

Bentheimer sandstone cores were used to perform the experiments. This sandstone contains up to 97% quartz and is consolidated and nearly homogeneous. Cores having a diameter of 3.8±0.1 cm and lengths of either 17.0±0.1 cm (short core) or 38.4±0.1 cm (long core) were used in the experiments to investigate the effect of core length. Physical properties of the core samples are presented in Table 7.1. The core samples were drilled from a cubical block and then sawn to desired dimensions using a water-cooled diamond saw. Next, cores were dried in an oven at 60°C for 48 hours. Then they were encapsulated in a thin layer of low X-ray attenuation Araldite self-hardening glue to avoid possible bypassing along the side of the core. From the CT scans of the dry core it was estimated that the glue penetrates about 1.0 mm of the core sample. Effective diameter was used for the calculation of the total pore volumes of the cores. After hardening, the glued core was machined to ensure that the core fits precisely into the core-holder.

The core-holder was made of polyether-ether-ketone (PEEK), a synthetic material that combines good mechanical properties with a low X-ray attenuation. The core-holder is especially designed for CT scanning. It transmits X-ray within a narrow energy window (refiltering the polyenergetic

source X-rays), which significantly minimizes the beam hardening artifact due to the polychromaticity of the X-ray beam. Several holes were drilled through the glue layer into the core surface along the core length for pressure measurements. The pressure connectors were also made of PEEK. This helps to prevent interference of the pressure lines with the CT scanning.

Table 7.1: Physical properties of the core samples used for core flooding.

Parameter	Value	
	Short core	Long core
Diameter (cm)	3.8±0.1	3.8±0.1
Length (cm)	17.0±0.1	38.4±0.1
Porosity (%)	21.0±0.1	21.0±0.1
Pore volume (cm ³)	40.5±0.5	91.5±0.5

7.2.3 Experimental set-up

The set-ups used to conduct the core-flooding experiments, for both short and long cores, are shown schematically in Fig. 7.1. Each set-up consists mainly of a core-holder in line with a double effect piston displacement pump (Pharmacia Biotech P-500) in parallel with a gas mass flow controller (Bronkhorst) and on the other end a back-pressure regulator and a fraction collector for the produced fluids. The pump was used to inject brine, oil and surfactant solution. Nitrogen gas was supplied by a 200 bar cylinder equipped with a pressure regulator (KHP Series, Swagelok) and connected to the core inlet through a mass flow controller. A data acquisition system (National Instruments) was used to record pressure, liquid production and gas and liquid injection rates.

For the short core experiments, the core-holder was fixed vertically and pressure drop over the core length was recorded using a differential pressure transducer. For the long core experiments, the core-holder was placed horizontally. Eleven differential pressure transducers were used to monitor the local pressure drops along the core length. The pressure ports divided the core length into twelve equal sections with a length of 3.2 cm. The pressure drop was measured between the core sections. The overall pressure drop was also recorded by another differential pressure transducer.

7.2.4 CT scanner

CT scans were obtained using a third generation SAMATOM Volume Zoom Quad slice scanner. In this study the long core experiments were CT scanned. The core-holder was placed horizontally on the couch of the CT scanner. This was done because it was not possible to accommodate such a long core-holder in a vertical position in the gantry of the CT scanner. The imaging settings used

during scanning the core are listed in Table 7.2. The X-ray tube of the CT scanner operated at a voltage of 140 kV and a current of 250 mA.

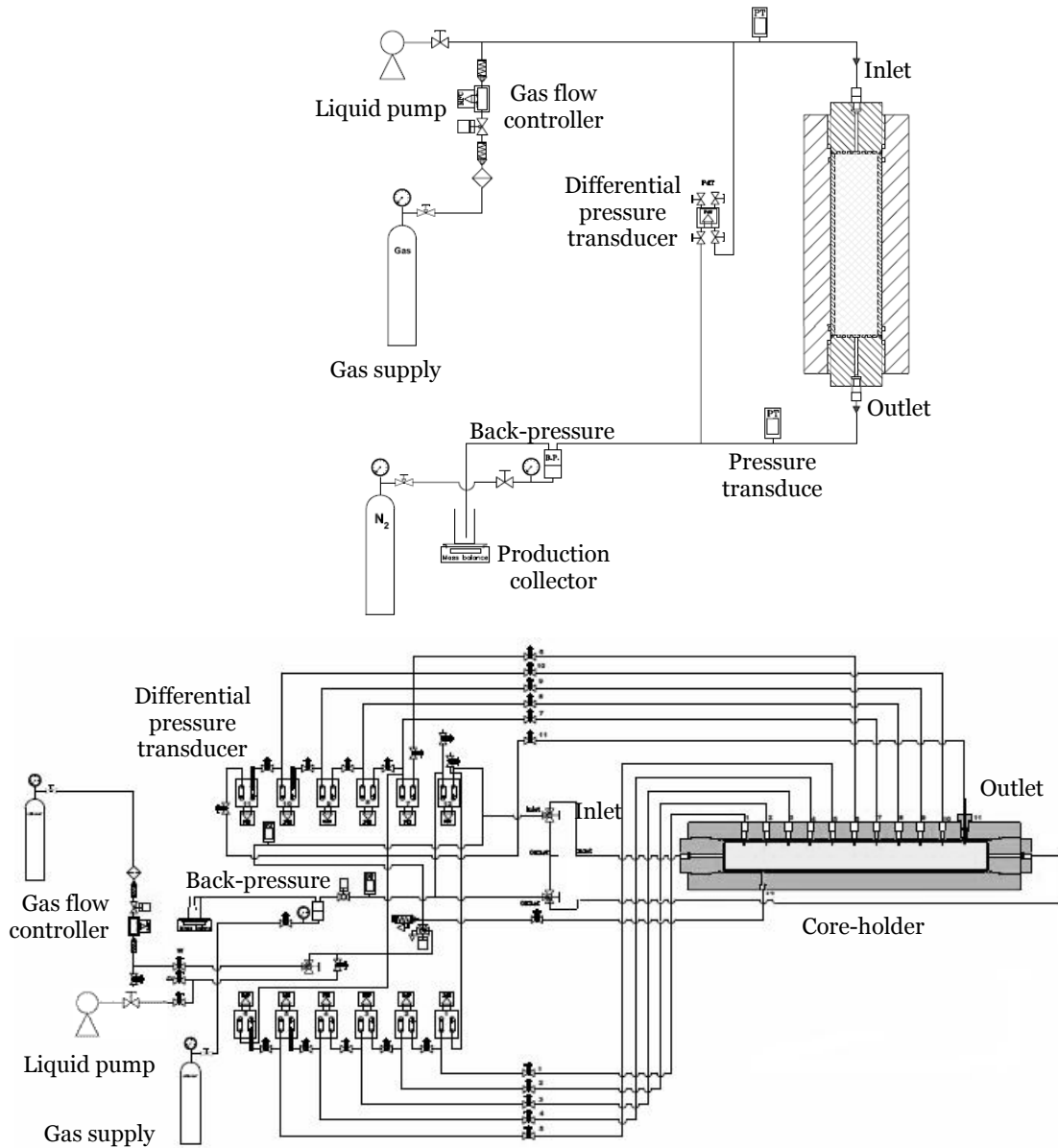


Fig. 7.1: Schematic of the experimental set-up used to perform core-flooding experiments: (top) for short core and (bottom) for long core. The short core-holder was fixed vertically and the long core-holder was placed horizontally. For the short core set-up, there were additional lines, not shown in the schematic, that allowed the injection of fluids from the bottom of the core.

The thickness of each CT slice was 3 mm and one series of scans included 128 slices. The spiral scan mode was used for image acquisition. This allowed fast and continuous acquisition of the CT scan data from a complete sample volume and generated images using standard reconstruction kernel after the data interpolation (Mees et al., 2003). The B40 medium filter was used for the

reconstruction of the images. A typical slice image consists of 512×512 pixels with the pixel size of $0.3 \text{ mm} \times 0.3 \text{ mm}$. Since noise for CT images typically ranges from 3 to 20 Hounsfield units, the accuracy of the measured fluid saturations was within $\pm 2\%$. Image analysis was performed using a series of numerical codes developed by the authors in Matlab (The MathWorks) and visualization of the 3D CT images was done with Avizo (Visualization Sciences Group).

Table 7.2: Setting of CT scan measurements.

Specification	Quantity
Tube voltage (kV)	140
Tube current (mA)	250
Pixel size (mm \times mm)	0.3×0.3
Image reconstruction kernel	B40 medium
Scan mode	Spiral

7.2.5 Experimental procedure

Experiments using short or long cores were done following the basic sequence shown in Table 7.3. First air was removed by flushing the core with CO_2 at 5 bar injection pressure. Then the dry core was saturated by injecting at least 10 pore volumes (PV) of brine while maintaining a back-pressure of 25 bar: this was done to dissolve any CO_2 present in the core and thus to ensure complete core saturation with brine. Next, primary drainage was done by injecting oil at $0.5 \text{ cm}^3/\text{min}$. Such a low flow rate was chosen to avoid instable flow and to ensure even distribution of injected oil in the core. For the short cores, drainage was performed under gravity stable conditions from the top of the core. Subsequently, imbibition was done by injecting brine that continued until no more oil was produced and the pressure drop over the core became constant. Next, 2.0 PV of surfactant solution were injected into the core to satisfy its adsorption capacity. Then N_2 gas and surfactant solution were co-injected to generate foam at a back-pressure of 20 bar and ambient temperature ($21 \pm 1 \text{ }^\circ\text{C}$). Gas and liquid flow rates were set at 1.0 and $0.1 \text{ cm}^3/\text{min}$, respectively. This corresponds to a total superficial velocity of 4.58 ft/d and foam quality, i.e. a ratio of gas to total flow rates, of 91% at the indicated back pressure.

The first part of this study was devoted to the effects of surfactant (AOS+FC) concentration, the presence of surfactant pre-flush and injection direction on the foam flooding performance. The use of short cores enabled us to continue foam injection for a long time and also to gain further insight about steady-state foam behavior in the presence of oil under the above-mentioned conditions. The effect of surfactant concentration was evaluated at two levels of 0.5 and 1.0 wt%. The weight ratio of the surfactant mixture AOS+FC was 1:1. One gas flooding experiment was also performed at a superficial velocity of 4.2 ft/day at 20 bar back-pressure and ambient temperature

to serve as a baseline. The rest of the foam floods were performed at 1.0 wt% concentration under the following conditions: (a) downward co-injection directly after water flooding (no surfactant pre-flush) and (b) upward co-injection in a surfactant pre-flushed core to represent a gravity unstable displacement. The second part of the study was devoted to the effect of core length. For these experiments, foam was generated using 1.0 wt% AOS solution. Table 7.4 gives an overview of the core-flooding experiments performed in this study.

Table 7.3: Basic sequence used to conduct core-flooding experiments.

Step	Description	Back pressure (bar)	Flow rate (cm ³ /min)	Injection direction
1	CO ₂ flushing	-	5.0	Down
2	Core saturation	25	1.0	Up
3	Oil injection	-	0.5	Down
4	Water flooding	-	0.5 - 1.0	Up
5	Surfactant pre-flush	-	1.0	Up
6	Foam or gas flooding	20	See overview in Table 7.4	

Table 7.4: Overview of the EOR experiments done in this study. Foam quality was fixed at 91%.

Exp.	Core size	Brine Permeability (Darcy)	Surfactant	Concentration (wt%)	Surfactant pre-flush	Injection direction
1	Short	1.4±0.1	-	0	-	Down
2	Short	1.0±0.1	AOS+FC (1:1 by weight)	0.5	Yes	Down
3	Short	1.5±0.1		1.0	Yes	Down
4	Short	1.1±0.1		1.0	No	Down
5	Short	1.4±0.1		1.0	Yes	Up
6	Short	2.5±0.1	AOS	1.0	Yes	Down
7	Long	2.4±0.1		1.0	Yes	Horizontal

The results of core-flooding experiments were examined in terms of CT scan images (for the long core experiment), mobility reduction factor (MRF), incremental oil recovery (oil recovered during gas or foam flooding divided by oil initially in place, OIIP, after primary drainage) and a dynamic capillary desaturation curve constructed for each foam flooding experiment. MRF was defined as a ratio of pressure drop during foam flooding to a corresponding baseline pressure drop, which was for a water-saturated core, at the same superficial velocity:

$$MRF = \frac{\Delta P_{foam}}{\Delta P_{water}} \Big|_u \quad (7.1)$$

Other authors (Mannhardt et al., 1998; Mannhardt and Svorstøl, 2001; Farajzadeh et al., 2010; Aarra et al., 2011) used the mobility of gas/brine injection as a reference, but that might lead to confusion because fluid saturations in the core might not be uniform after gas/brine flooding.

CT scans of the long core were made at each stage of the experiment to determine the distribution of fluid saturations and also reveal the propagation of the advancing front. The following equation was used to obtain oil saturation during drainage and water flooding from the measured attenuation coefficients in Hounsfield units (HU), eliminating the contribution of rock by the subtraction:

$$S_o = \frac{1}{\phi} \left(\frac{HU - HU_{wet}}{HU_o - HU_w} \right) \quad (7.2)$$

where ϕ is porosity of the core. Subscripts wet , o , and w stands for brine saturated core, oil and water phases, respectively. To describe the distribution of fluids during foam flooding, the CT images were converted into the total liquid saturation ($S_{liq}=S_o+S_w$) profiles using Eq. (7.3). The reason to calculate S_{liq} was that the contrast of the CT images was not good enough to discriminate fluids at three-phase conditions.

$$S_{liq} = \frac{HU_{foam} - HU_{dry}}{HU_{pre-flush} - HU_{dry}} \quad (7.3)$$

where subscripts $foam$, $pre-flush$, and dry stand for core with foam, core at the end of surfactant pre-flush and dry core, respectively.

7.3 Results and discussion

7.3.1 Primary drainage and imbibition

Since the results of primary drainage and imbibition were similar for all core-flooding experiments, only one prototypical experiment will be discussed in detail. Below we will present the results obtained in the experiment with the long core, which was CT scanned at different times.

7.3.1.1 CT scan images

Fig. 7.2 shows a series of 3D CT images taken at different injected PVs (dimensionless times) during primary drainage and imbibition (exp. 7, Table 7.4). A change in the color of the CT images from dark red to yellow (see Fig. 7.2a) reveals the frontal displacement of water by oil in the porous medium. Oil breakthrough at the core outlet occurs at 0.69 ± 0.02 PV. Thereafter, the color in the image changes only slightly. A change in the color of the CT images from yellow to orange (see Fig. 7.2b) indicates the displacement of oil by brine. Water breakthrough occurs slightly

before 0.35 ± 0.02 PV and thereafter the color of the images remains practically unchanged. The last image represents the end of surfactant pre-flush, where 2.0 PV of surfactant solution was injected at the same rate as brine during water flooding. No measurable oil was produced during surfactant pre-flush. We recall that the main purpose of surfactant pre-flush is to satisfy the adsorption capacities of the rock sample and to reduce surfactant loss as much as possible during foam flooding when it is needed to generate and sustain.

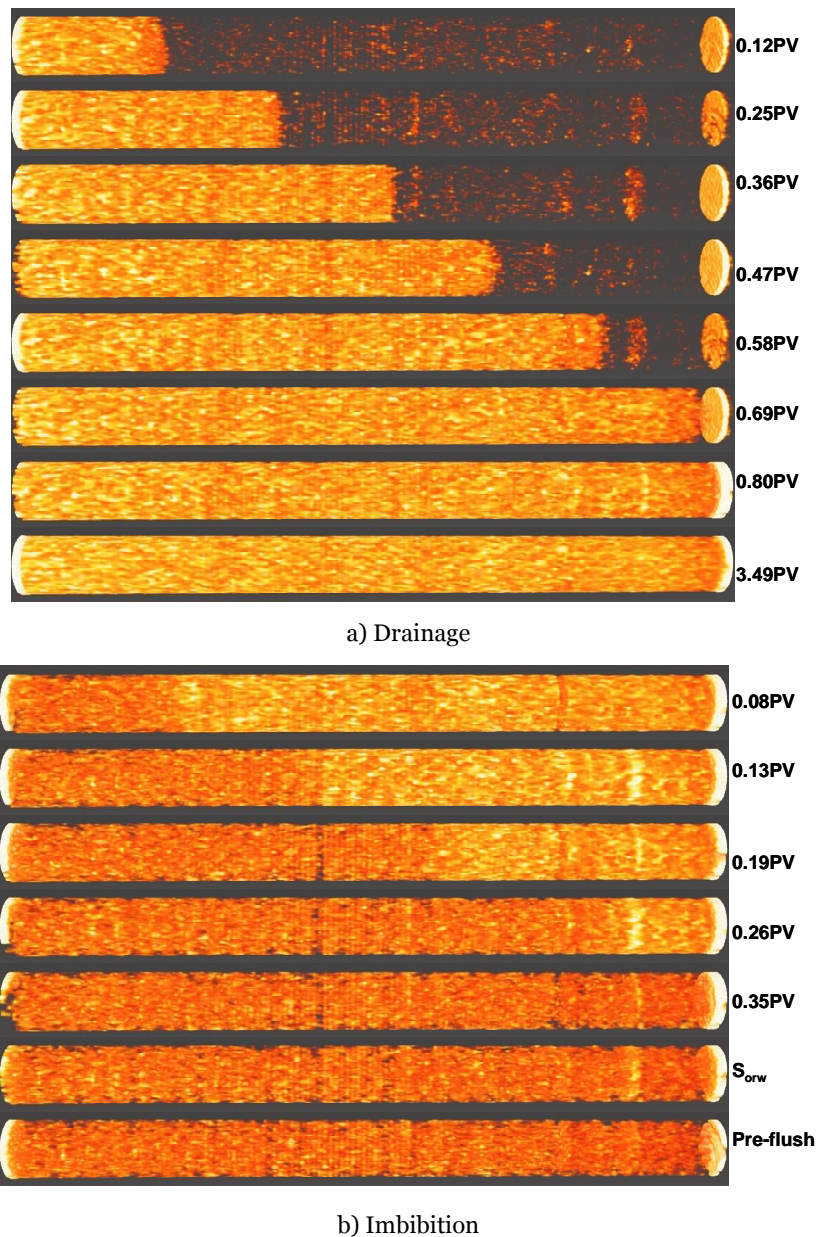


Fig. 7.2: 3D CT images during primary drainage, imbibition and surfactant pre-flush (long core; exp. 7). During primary drainage water (dark red) is displaced by oil (yellow). Oil production by water flooding is evident by a change in the color from yellow to orange. No more oil was produced during surfactant pre-flush.

7.3.1.2 Saturation profiles

For further quantitative analysis we plotted oil saturation during primary drainage and imbibition for different injected pore volumes in Figs. 7.3 and 7.4. The general trend of the oil saturation profiles during primary drainage is reminiscent of a Buckley-Leverett displacement (see Fig. 7.3), characterized by a shock front followed by a rarefaction wave at which oil saturation gradually increases from 0.60 ± 0.02 to about 0.80 ± 0.02 . Near the core outlet region after breakthrough, oil saturation remained low compared to the other sections due to the capillary end effect. The average oil saturation along the core at the end of the primary drainage is 0.83 ± 0.02 and, correspondingly, the connate water saturation is $S_{wc} = 0.17 \pm 0.02$. This is consistent with the values obtained from the measured SCAL data for Bentheimer sandstone where S_{wc} varies from 0.14 to 0.18 (Andrianov et al., 2012). It also agrees with the values obtained in Chapter 6 for shorter cores.

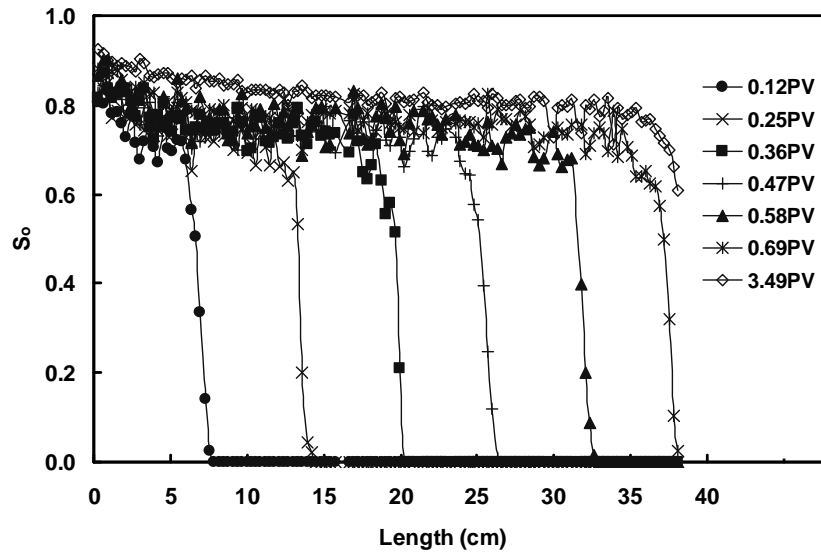


Fig. 7.3: Oil saturation profile for primary drainage, obtained from CT images shown in Fig. 7.2a. The average oil saturation at the end of drainage was 0.83 ± 0.02 .

Fig. 7.4 shows oil saturation profiles during water flooding. The general behavior of the advancing front is similar to that for the primary drainage. Most of the oil was produced before water breakthrough. Thereafter, more than 10 PV of water were injected, but only a tiny amount of oil was produced. The remaining oil saturation was distributed uniformly through the core length and had an average value of 0.45 ± 0.02 . This value is higher than that obtained from the SCAL measurements, which is $S_{or,SCAL} = 0.28 \pm 0.05$ (Andrianov et al., 2012). This difference between the remaining oil in the core flood and the residual oil saturation is due to a higher bond number (a ratio of bouncy to capillary forces) used in the SCAL measurements (King et al., 1986; Al-Omair

and Christiansen, 1998). Fig. 7.4 also shows that the oil saturation profile at the end of surfactant pre-flush remained unchanged.

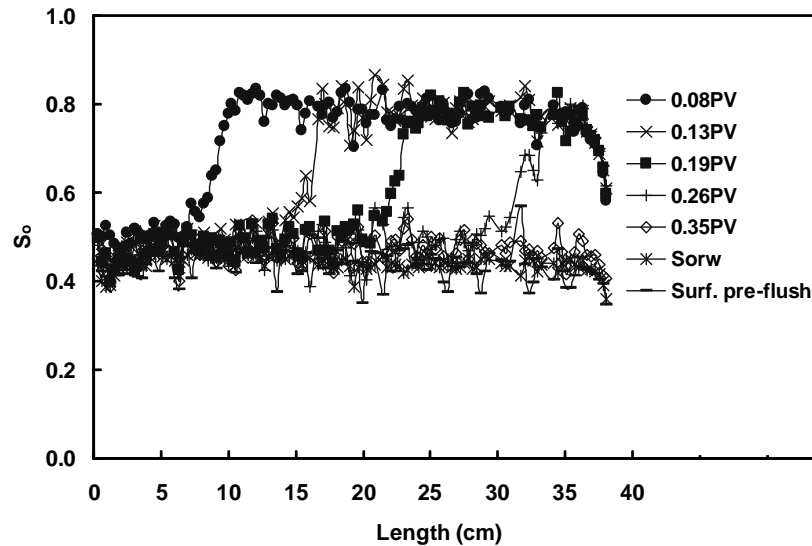


Fig. 7.4: Oil saturation profile for water flooding and surfactant pre-flush, obtained from CT images shown in Fig. 7.2b. The average oil saturation at the end of water flooding was 0.45 ± 0.02 .

7.3.2 Gas flooding

Before performing foam-flooding experiments, a baseline gas flooding (exp. 1, Table 7.4) was conducted by injecting nitrogen at $1.0 \text{ cm}^3/\text{min}$, directly after water flooding under gravity stable conditions. The result of this gas flooding experiment will be used as a reference to evaluate the foam flooding performance.

Fig. 7.5 shows the total pressure drop and corresponding mobility reduction factor, determined after using the pressure drop of water flow as reference. When gas first reaches the core inlet face, the total pressure drop rises from 150 ± 5 to 198 ± 5 mbar. The rise in the pressure drop seems to correspond to a minimum entry capillary pressure for gas (non-wetting phase) into a porous medium containing oil and water (at residual oil saturation). Then the total pressure drop increases more gradually, revealing the movement of gas front through the core. During this period only water moving ahead of gas front is produced. The total pressure drop increases until the gas front breaks through the core outlet at around 0.27 ± 0.02 PV injected. This time coincides with the start of oil production. Once gas breakthrough occurs, the total pressure drop decreases and then gradually levels off to a plateau value of 81 ± 5 mbar.

Visual inspection of the effluents revealed that after gas breakthrough, a small amount of oil was recovered in a highly dispersed form (tiny droplets). Fig. 7.6 shows the evolution of average oil saturation in the core during gas flooding. The initial value of oil saturation corresponds to the

end of water flooding and is equal to 0.49 ± 0.02 . The oil saturation decreased slowly during gas flooding and reached 0.39 ± 0.02 after 25 PV injected. Setting the short time cutoff arbitrarily at 4.0 PV, it was found that oil saturation decreased by $8.0 \pm 0.5\%$, which corresponds to an incremental oil recovery of $5.0 \pm 0.5\%$ of the OIIP. This incremental oil recovery can be interpreted by a relative permeability effect, more precisely by the fact that the residual oil saturation for gas flooding (three-phase flow) is lower than that for water flooding (two-phase flow).

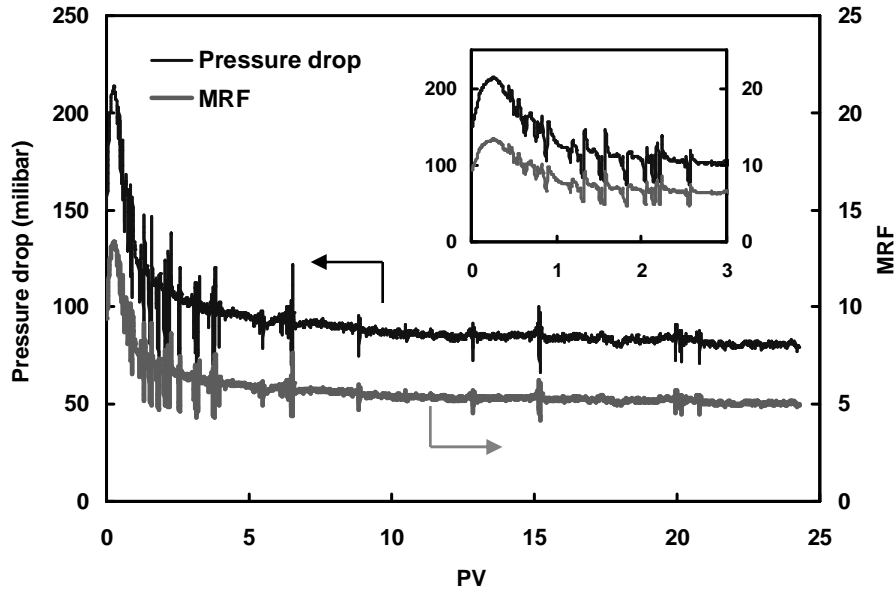


Fig. 7.5: Total pressure drops and mobility reduction factor obtained during gas flooding (short core, downward injection; exp. 1). MRF was defined as a ratio of the total pressure drop of gas-flood to single-phase water flow.

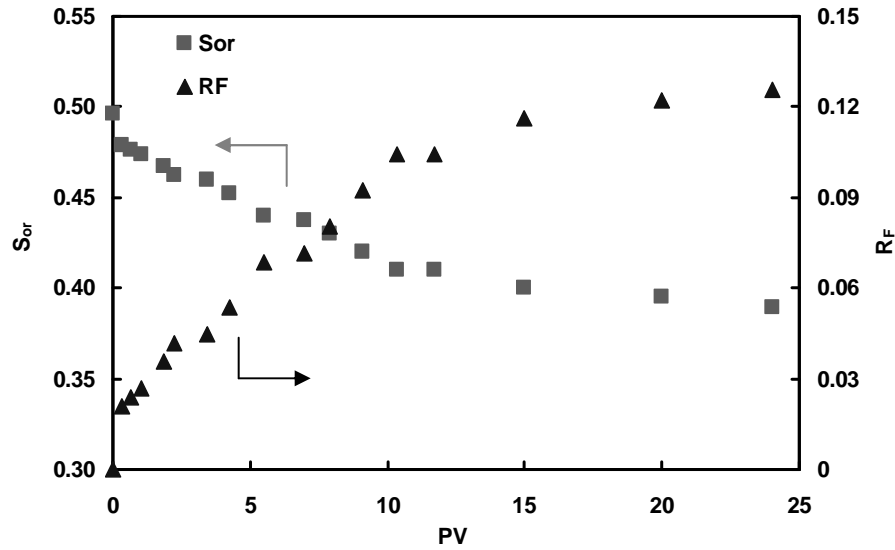


Fig. 7.6: Average oil saturation profile and incremental oil recovery during gas flooding (short core, downward injection; exp. 1). Gas was injected under gravity stable conditions directly after water flooding.

7.3.3 Foam flooding

7.3.3.1 Effect of surfactant concentration

Fig. 7.7 shows MRF vs. injected pore volumes during foam flooding for two surfactant concentrations (exp. 2 and 3, Table 7.4). MRF grows rapidly in the first injected pore volume and reaches 95 ± 5 for 0.5 wt% foam and 164 ± 5 for 1.0 wt% foam, corresponding to a pressure gradient of 11 bar/m and 19 bar/m, respectively. Then MRF levels off to a plateau value for the rest of the foam injection. The maximum value of MRF for 1.0 wt% foam is nearly 200 ± 5 while for 0.5 wt% foam MRF exhibits a peak of about 160 ± 5 . The inset also compares the MRF profiles for gas and foam flooding during the first 4.0 PV. The MRF of 1.0 wt% and 0.5 wt% foams are 35 and 25 times larger than that of gas flooding.

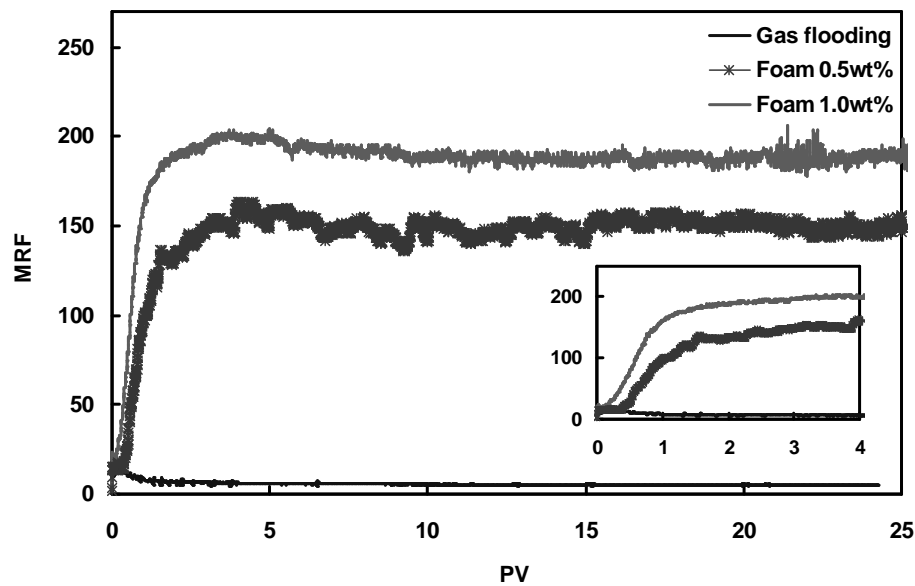


Fig. 7.7: Mobility reduction factor for different surfactant concentrations (AOS+FC foam, short core, downward injection, pre-flush; exp. 2 and 3). The inset shows that higher surfactant concentration results in faster foam generation and also a stronger foam in the presence of oil.

A higher MRF means that the magnitude of viscous forces increases due to foam development in the porous medium. As a consequence, part of the remaining liquid including water-flood residual oil is mobilized from the pores during foam propagation. An increase of viscous forces can be estimated using the macroscopic capillary number, N_c , defined by:

$$N_c = \frac{kk_{rf}\Delta P}{\sigma_{ow}L} \quad (7.3)$$

where k is absolute permeability of the core sample, k_{rf} is foam relative permeability, ΔP is the pressure drop over the core, σ_{ow} is the interfacial tension between oil and water, and L is the core length. For simplicity, it was assumed that foam is a single-phase fluid such that k_{rf} is equal to

one. Fig. 7.8 shows N_c as a function of injected PV for the surfactant concentrations investigated. The capillary number increases over time for both concentrations. For 1.0 wt% foam N_c increases rapidly reaching a maximum of 2.4×10^{-3} over the first 4.0 injected PV, while for 0.5 wt% foam N_c does not exceed 1.3×10^{-3} . For long periods of time the stabilized capillary number of 1.0 wt% foam is nearly twice that of 0.5 wt% foam. However, the corresponding N_c for gas flooding is three-order of magnitude smaller than that of the foam flooding. An increase in N_c coincides with more oil production as can be inferred by comparing the average oil saturation profile for gas and foam flooding (see Fig. 7.9).

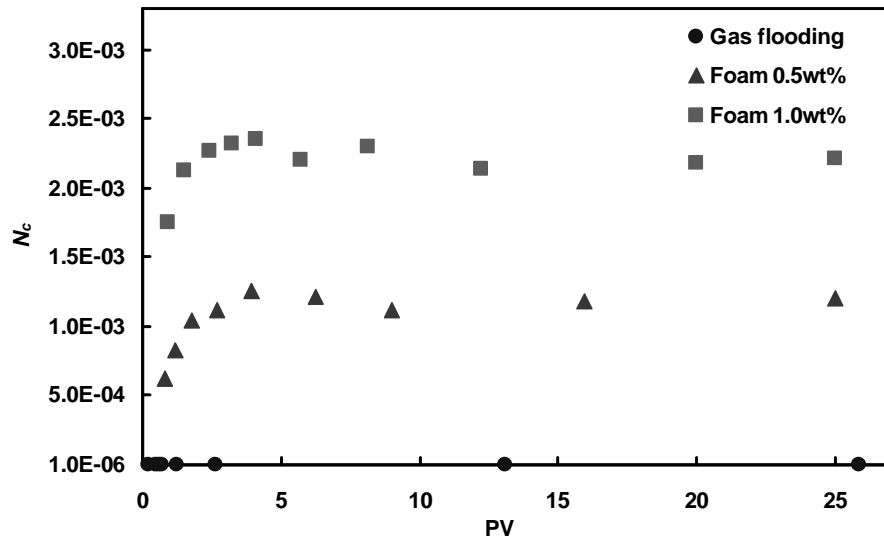


Fig. 7.8: Capillary number profile during foam flooding for different surfactant concentrations (AOS+FC foam, short core, downward injection, pre-flush; exp. 2 and 3).

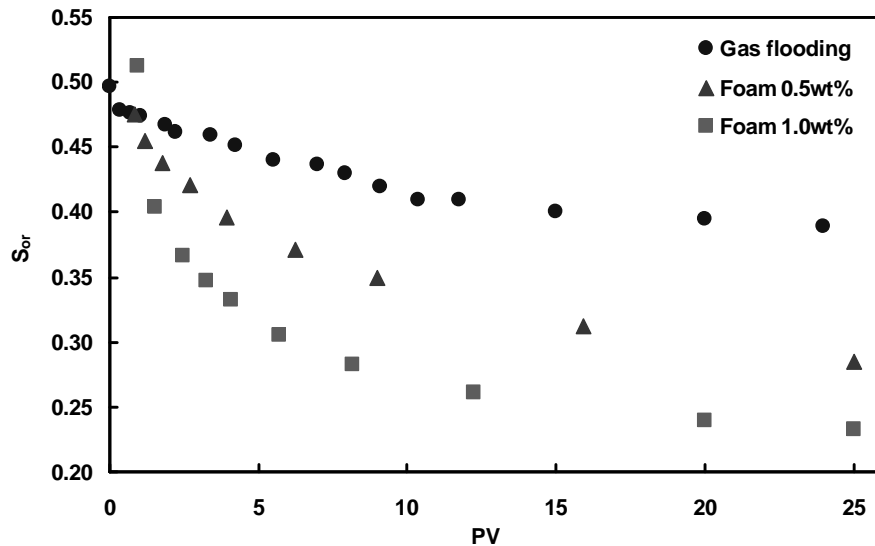


Fig. 7.9: Average oil saturation profile during foam flooding (AOS+FC foam, short core, downward injection, pre-flush; exp. 2 and 3). For foam at higher surfactant concentration, oil saturation decreases more rapidly during the first few PVs injected. It also exhibits a lower stabilized oil saturation at later times.

Let us compare oil saturation after 4.0 PV of foam injection. For 1.0 wt% foam, it decreases steeply to 0.33 ± 0.02 . For 0.5 wt% foam it diminishes, but at a slower rate and reaches 0.39 ± 0.02 . For gas flooding, however, oil saturation remains high at about 0.45 ± 0.02 after 4.0 PV injected. As foam flooding continues for longer time, N_c becomes fairly constant while oil saturation continues to decrease, though at a slower rate. Surfactant concentration also affects the magnitude of the stabilized oil saturation. At later times of foam injection, oil saturation reaches 0.23 ± 0.02 for 1.0 wt% foam compared to 0.29 ± 0.02 for 0.5 wt% foam.

7.3.3.2 Effect of surfactant pre-flush

Fig. 7.10 compares MRF for foam experiments at 1.0 wt% surfactant concentration with and without pre-flush (exp. 3 and 4, Table 7.4). The MRF profile of gas flooding was added as a reference. MRF profile without surfactant pre-flush exhibits the following characteristic trend: in the first 7.0 PV it increases only modestly to nearly 10, which is similar to that of gas flooding. Beyond 7.0 PV, MRF increases steeply from 10 to 120 in about two pore volumes, similarly to the pre-flushed experiment. However, the sharp rise in MRF for the foam without pre-flush is almost half that for the foam with pre-flush. Subsequently, MRF increases further at a slower rate until it reaches a maximum of 215 ± 5 after 22 PV. Then, it remains fairly constant for the rest of the injection period. Delay in the foam development for the case of no pre-flush can be explained by the adsorption of surfactant from the flowing surfactant solution. Indeed, the amount of surfactant required to satisfy the adsorption capacity of the rock surface is 181.0 mg as estimated from adsorption measurements (adsorption level: 0.45 mg surfactant/g rock (Du, 2007)). This amount corresponds to 0.50 PV of surfactant solution injected. Accounting for retardation of the surfactant front, the core sample should be pre-flushed with at least twice this volume. According to the MRF profiles in Fig. 7.10, the surfactant volume required to initiate foam development (after 7.0 PV) corresponds to 0.64 PV of surfactant solution given a foam quality of 91%: this surfactant volume is 28% larger than the value of 0.50 PV estimated from the adsorption measurements. This is most likely due to small differences in the properties of the cores used for the surfactant adsorption and for the foam flooding. Also, the presence of oil could create a large surface area for surfactant adsorption. The stabilized MRF for foam without pre-flush is slightly larger than that with pre-flush, i.e., 215 ± 5 and 190 ± 5 , respectively.

The N_c profile as a function of injected PV is shown in Fig. 7.11. For foam without surfactant pre-flush over the first 7.0 PV injected, N_c is in the order of 10^{-5} , showing that a gas-like flow occurs in the porous medium. Then N_c increases by two orders of magnitude and reaches 1.1×10^{-3} , followed by a gradual increase to 1.9×10^{-3} . However, for foam with surfactant pre-flush N_c exhibits a faster response and stabilizes much sooner. The stabilized N_c for foam without pre-flush is slightly lower

than that with pre-flush. This seems to contradict the MRF trends observed in Fig. 7.10. The discrepancy could be due to the slight difference in the permeability of the core samples used in the two experiments, i.e. 1.5 ± 0.1 Darcy for the pre-flushed experiment and 1.1 ± 0.1 Darcy for the no pre-flushed one.

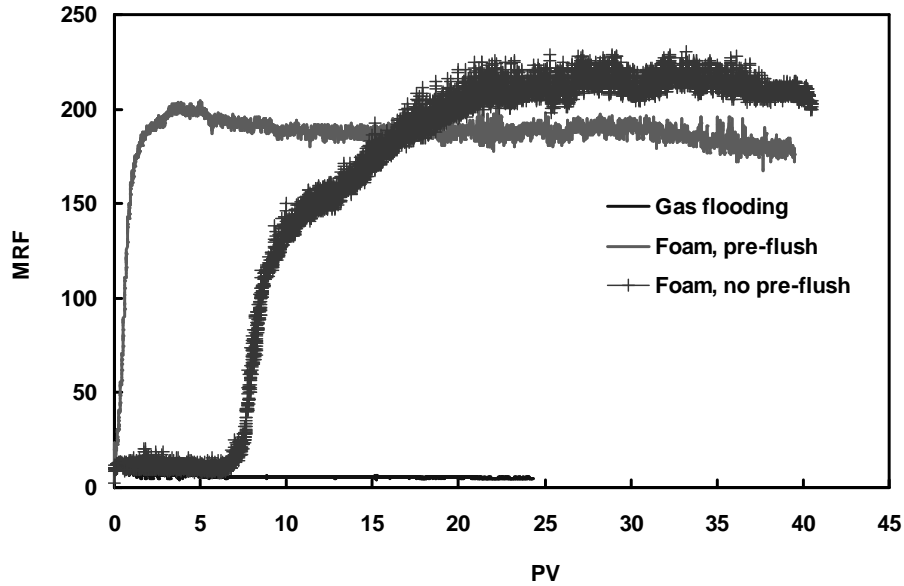


Fig. 7.10: Effect of surfactant pre-flush on foam mobility reduction factor (AOS+FC foam, short core, downward injection; exp. 3 and 4).

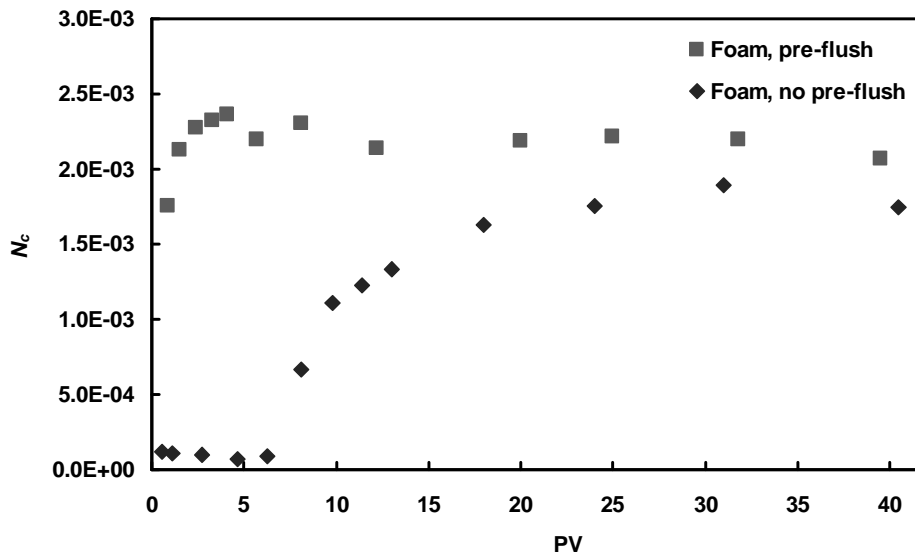


Fig. 7.11: Effect of surfactant pre-flush on the capillary number (AOS+FC foam, short core, downward injection; exp. 3 and 4). The N_c for foam without pre-flush lags behind that with pre-flush.

Fig. 7.12 demonstrates how the presence of surfactant pre-flush affects oil recovery by foam. For the case of no pre-flush, the reduction of oil saturation seemingly takes place in two steps: first it

reduced from 0.51 ± 0.02 to 0.38 ± 0.02 resulting from the gas-like flow, and then it reduced further to 0.31 ± 0.02 due to the foam development. Focusing on the first 4.0 PV injected, it is observed that foam with pre-flush recovers $35 \pm 2\%$ of the water-flood residual oil compared to $16 \pm 2\%$ for foam without pre-flush. The effect of surfactant pre-flush is also evident at later times when foam approaches a steady-state condition. For foam with pre-flush oil saturation decreases smoothly to 0.23 ± 0.02 while foam without pre-flush it has a higher value, 0.31 ± 0.02 .

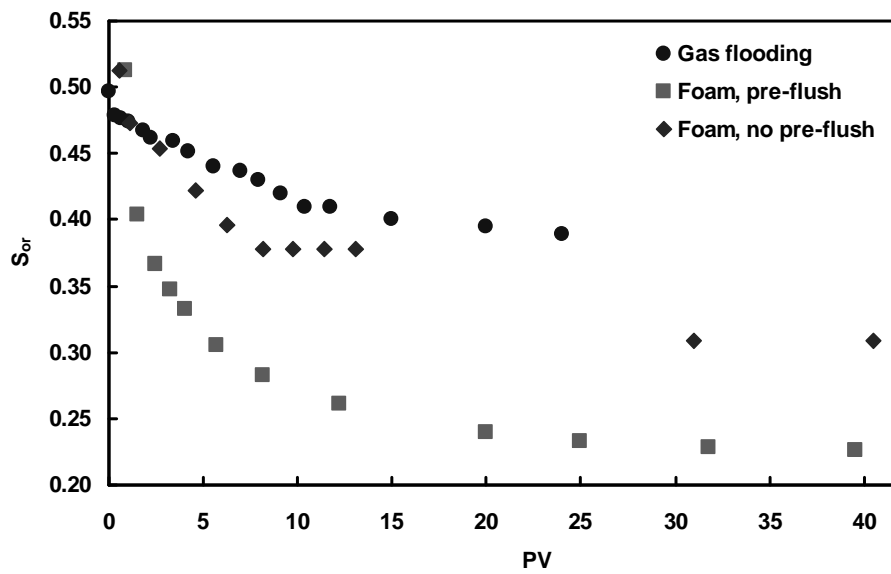


Fig. 7.12: Effect of surfactant pre-flush on the average oil saturation (AOS+FC foam, short core, downward injection; exp. 3 and 4). For foam with pre-flush oil saturation decrease more rapidly over the first few PVs injected and finally obtains a much lower stabilized value.

7.3.3.3 Effect of injection direction

We will now compare the behavior of foam injected either under gravity stable (downward) or gravity unstable (upward) conditions. Experiments were done using 1.0 wt% of surfactant mixture in a core previously pre-flushed with the surfactant solution (exp. 3 and 5, Table 7.4). The MRF profiles are shown in Fig. 7.13, where the inset represents the first 4.0 PV injected. The overall trend of the MRF profiles is qualitatively similar for both foams, but the quantitative differences are significant. MRF for the downward injection rises steeply to a maximum, decreases slightly and then levels off to a plateau of 190 ± 5 . MRF for the upward injection also rises in the first 2.0 PV, but to a lower value of 120. Thereafter, MRF increases further with a slower rate to about 135 ± 5 . We note that under gravity unstable conditions MRF first remains low at about 13, which is similar to that of gas flooding, and then increases after 0.30 PV.

The N_c profiles shown in Fig. 7.14 reveal more clearly the advantage of injecting foam under gravity stable conditions: indeed it leads to quicker increase in N_c leading to a larger steady-state

value. In the first 4.0 PV injected, N_c for foam under gravity stable conditions is two times larger compared to the gravity unstable conditions. The effect of injection direction is also reflected in the evolution of average oil saturation as shown in Fig. 7.15. For the gravity stable conditions, oil saturation decreases more rapidly. Setting the short time cutoff at 4.0 PV injected (recall that this corresponds to 0.36 PV injected of surfactant solution) shows that incremental oil recovery under gravity stable conditions is nearly twice that under gravity unstable conditions.

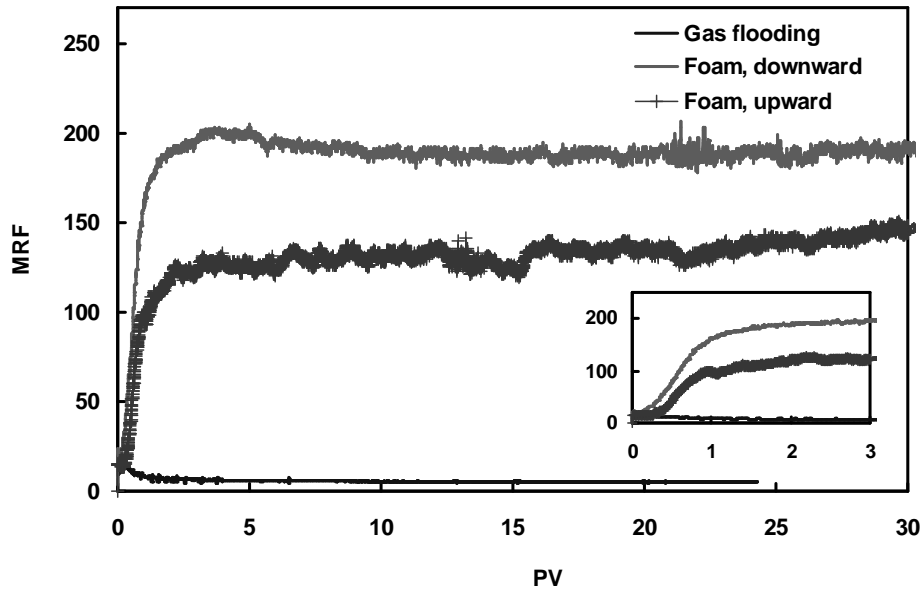


Fig. 7.13: Effect of injection direction on foam mobility reduction factor (AOS+FC foam, short core, pre-flush; exp. 3 and 5). Foam propagation under upward injection lags behind that under downward injection.

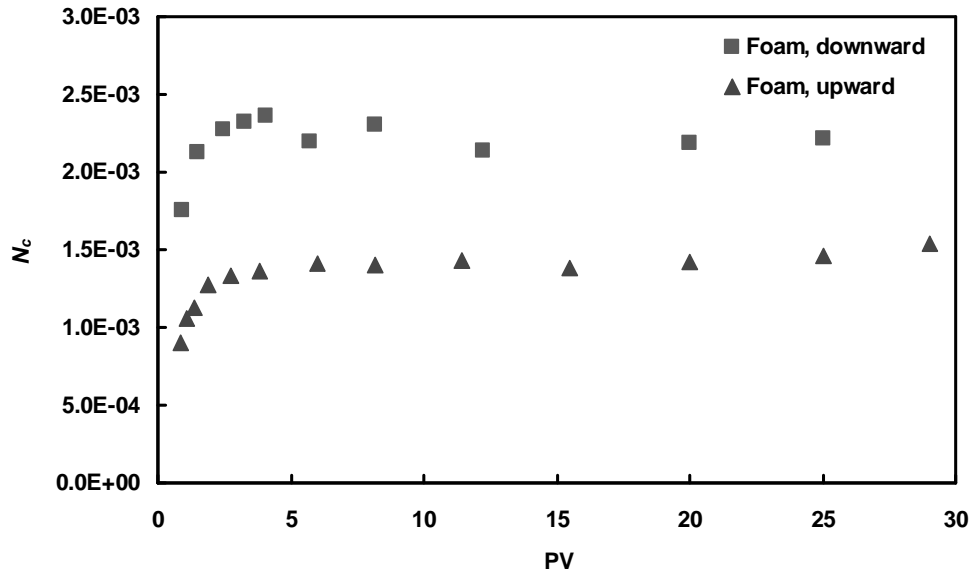


Fig. 7.14: Effect of injection direction on the capillary number (AOS+FC foam, short core, pre-flush; exp. 3 and 5). The N_c for downward injection is twice that for upward injection.

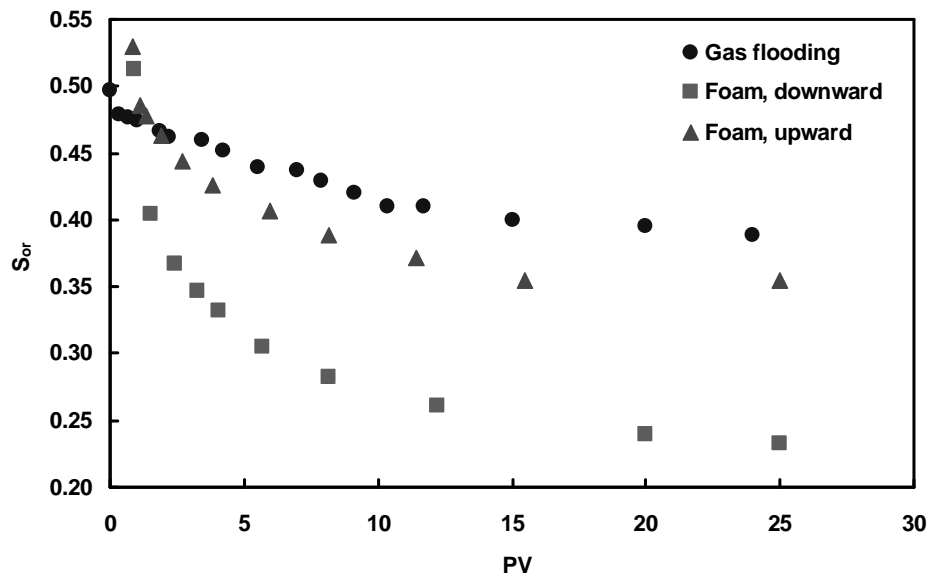


Fig. 7.15: Effect of injection direction on the average oil saturation (AOS+FC foam, short core, pre-flush; exp. 3 and 5). Gravity stable foam injection (downward) results in a lower value of oil saturation both at the beginning and later stage of foam flooding.

7.3.3.4 Effect of core length

In the previous sections we have provided tangible proof for foam development in the presence of oil and incremental oil recovery compared to gas flooding using short cores (length of 17.0 ± 0.1 cm). This supports the idea that immiscible foam is potentially an efficient EOR method, which can significantly improve the performance of gas or WAG (water-alternating-gas) flooding. Here we present a series of experiments performed using longer core (length of 38.4 ± 0.1 cm) to investigate whether increasing the core length has an impact on foam performance. The core was pre-flushed with 1.0 wt% AOS solution (exp. 7, Table 7.4) after performing primary drainage and water flooding as described (Figs. 7.2 to 7.4). Then gas and surfactant solution were co-injected at a fixed quality of 91% into the horizontally placed core. Fig. 7.16 shows the corresponding series of 3D CT images taken at different times during foam flooding. The initial liquid (including water and water-flood residual oil) was visualized by the semi-transparent blue dots in the flow domain. As foam generation proceeds, first a blue/green front appears in the left side (inlet) of the core after 0.06 PV. As the foam front advances, the intensity of the green color increases, which means that the generated foam becomes stronger and, consequently, more liquid desaturation occurs. The frontal region is not sharp and is characterized by a modest overriding pattern (see for instance the image at 0.13 PV). This is most likely because the oil mobilized by foam forms an oil bank with a high oil saturation ahead of the advancing foam front, which partially destabilizes foam. Therefore, foam apparent viscosity diminishes slightly and gas mobility increases. The

latter effect along with gravity segregation eventually causes a small gas override in the frontal region.

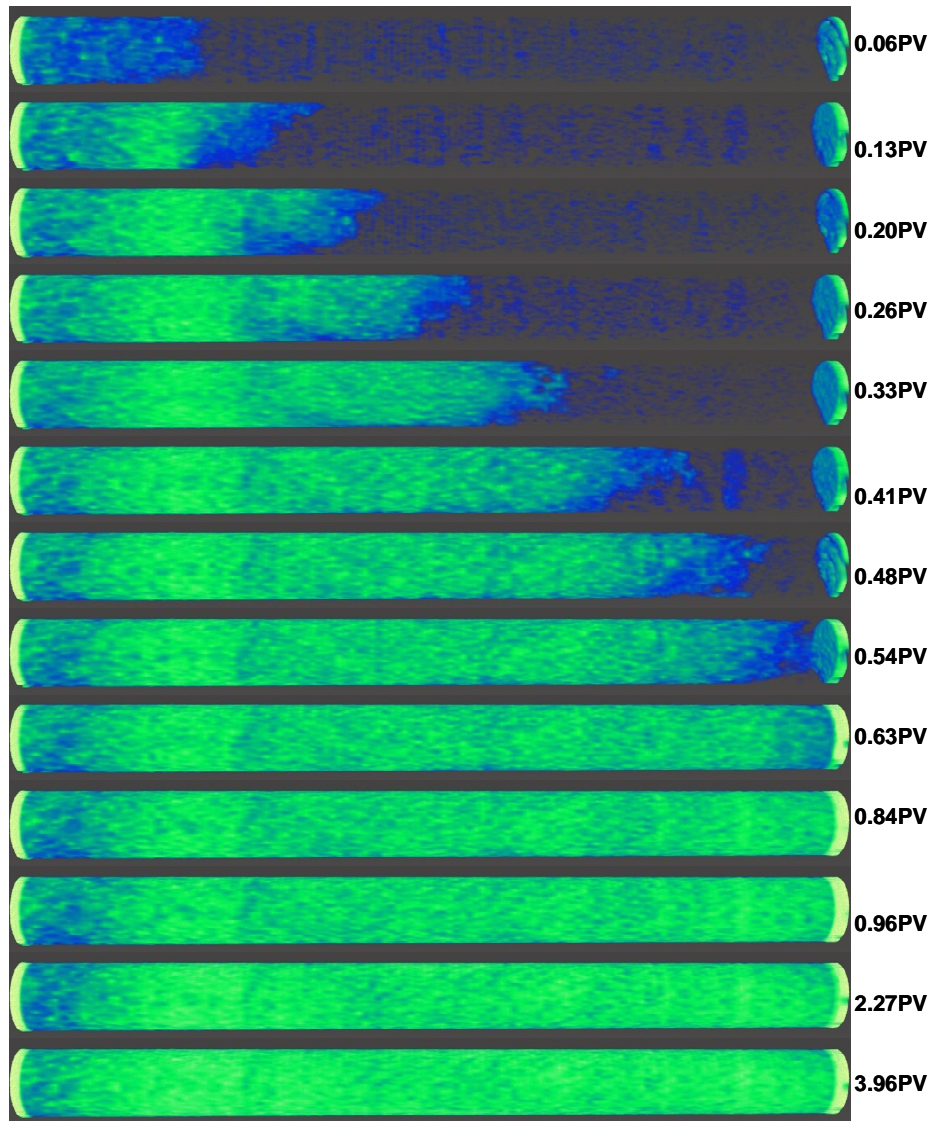


Fig. 7.16: Displacement profile during foam flooding in the long core (AOS foam, pre-flush; exp. 7). Initial liquid (water and water-flood residual oil) was visualized by the semi-transparent blue dots. The presence of foam is evident by a blue/green front emerging from the left side (inlet) of the core. A higher intensity of the green color corresponds to a stronger foam and thus higher liquid desaturation.

Fig. 7.17 shows total liquid saturation ($S_{liq} = S_w + S_o$) profiles through the core length at different injected pore volumes. Before foam breakthrough, which occurs at 0.54 ± 0.02 PV, each S_{liq} profile increases from 0.40 ± 0.02 to unity. This behavior of liquid saturation supports the discussion above concerning the CT scan images, i.e., it is reminiscent of a stable displacement of a less viscous fluid by a more viscous one. This proves that a good mobility control was achieved due to

foaming of the injected gas. Note that relatively high liquid saturation ($S_{liq} = 0.65$) near the core inlet face occurs because gas travels a certain distance into the core before foam development (entrance effect). The above discussion can be elaborated further by plotting the sectional MRF during foam flooding as shown in Fig. 7.18. Before foam breakthrough the MRF profiles exhibit a characteristic bell-shape: a monotonic increase until reaching a maximum followed by a decreasing trend.

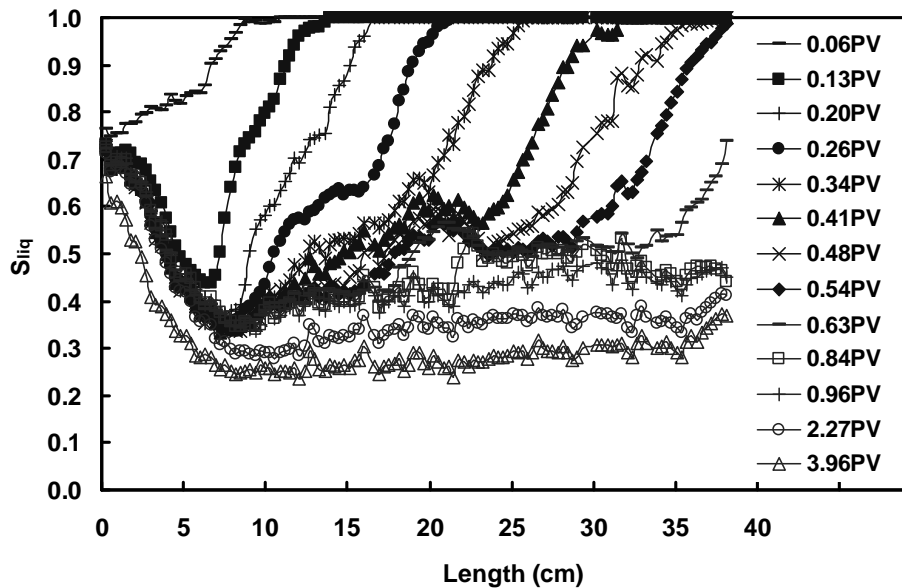


Fig. 7.17: Liquid saturation ($S_w + S_o$) during foam flooding obtained from the CT images shown in Fig. 7.16.

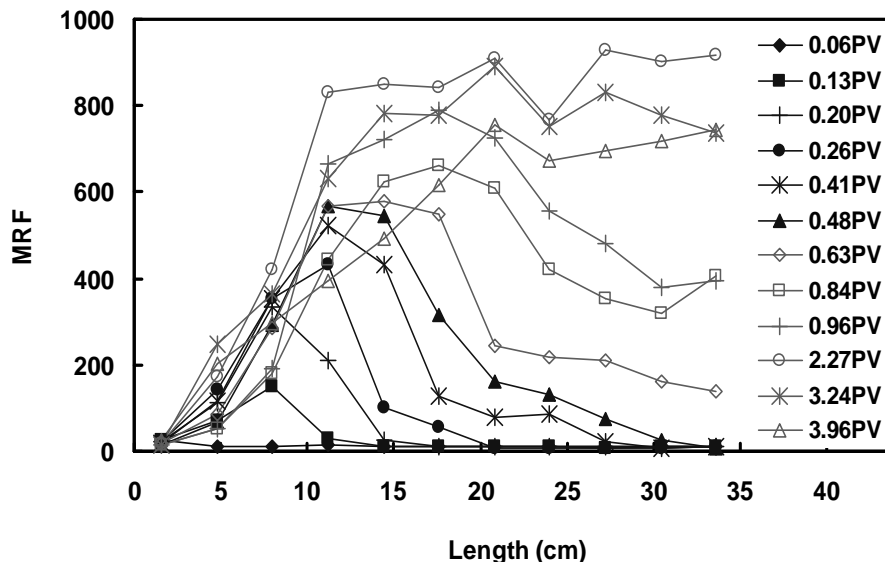


Fig. 7.18: Sectional MRF profiles during foam flooding in the long core (AOS foam, pre-flush; exp. 7).

Let us, for instance, consider the MRF profile at 0.26 PV. In the first section, MRF exhibits a rather small value corresponding to weak foaming, which is consistent with high liquid saturation

as is discussed above. Then MRF increases monotonically to a maximum value, indicating good foaming, by which liquid saturation diminishes to about 0.40 ± 0.02 . Finally, MRF decreases to a small value of 10 over the distance of 8.0 cm downstream. The behavior of MRF reveals once again that foam front is diffused and it is in excellent agreement with the CT images and the corresponding S_{liq} profiles. Looking at fixed core sections, MRF continues to increase as the foam front advances through the core. However, the increase of MRF is not very significant for the first two sections near the inlet. This indicates that foam remains weak in these sections, which is consistent with the presence of a high liquid saturation (see Fig. 7.17). The MRF profiles reveal that foam has to travel over 10.0 ± 0.5 cm to be fully developed.

In order to inspect the effect of the core length on the incremental oil recovery by foam, we examine now the evolution of average oil saturation at different injected PVs for both short and long cores (exp. 6 and 7, Table 7.4) as shown in Fig. 7.19. For both curves the initial value corresponds to the water-flood residual oil saturation. In both cases oil saturation remains constant up to 0.55 ± 0.02 PV and then it decreases. The delay in the decrease of oil saturation can be explained by the frontal propagation of foam (good mobility control). The average oil saturation of the short and long cores diminishes to 0.29 ± 0.02 and 0.26 ± 0.02 , respectively, after about 4.0 PV injected, which corresponds to the injection of 0.36 PV of surfactant solution. Hence, it can be concluded that MRF and oil recovery increase slightly with core length for the duration of the injection. We expect that this relative increase reaches a plateau as core length increases, but more experiments are needed to confirm this point.

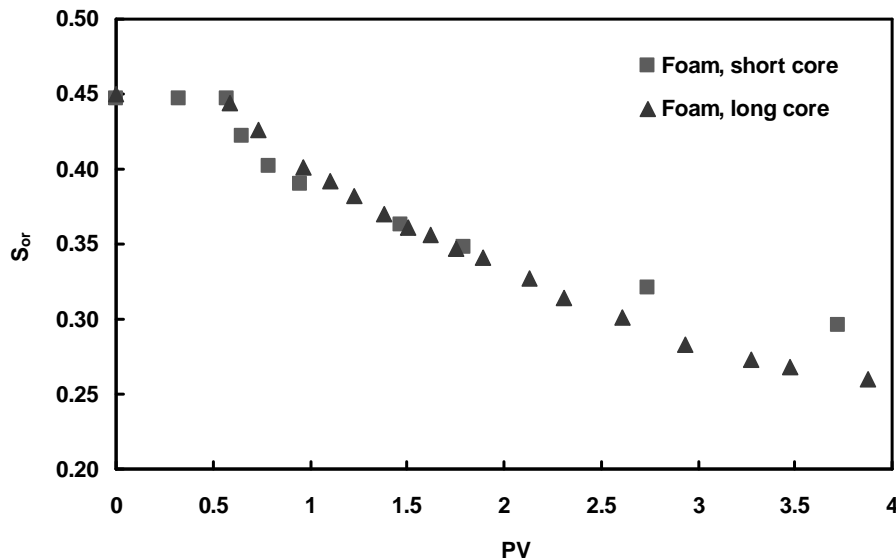


Fig. 7.19: Average oil saturation profile during 1.0 wt% AOS foam flooding for different core lengths: short core with 17.0 ± 0.1 cm and long core with 38.4 ± 0.1 cm (exp. 6 and 7).

7.4 General discussion

The goal of this study was to gain better insight into the foam behavior in the presence of oil and, more specifically, to investigate further the effects of oil on foam stability and oil recovery by foam. Until recently, the most accepted view was that the presence of oil is detrimental to foam stability, which left little hope that foam could become an efficient EOR process when oil saturation is high. Previous studies (Farajzadeh et al., 2010; Andrianov et al., 2012) provided tangible evidence that foam could be adequately stable in the presence of oil, leading to the recovery of a significant fraction of oil remaining in the core after water flooding. This was performed by using a method where sandstone cores were only partially saturated with oil, leaving the other part free of oil so that it could serve as a ‘foam generation chamber’. It was clearly demonstrated that foam that was generated in that ‘chamber’ did not completely decay upon coming in contact with oil. However, it also raised the question of whether stable foam could be developed similarly in porous media containing oil over its entire length. This question is important, because this case reflects more realistically the situation occurring in the field, where oil is also present in near-wellbore area. The systematic laboratory study reported here provides some elements to answer this question.

The gas flooding under gravity stable conditions (i.e., slow downward injection) proved to be fairly efficient to recover incremental oil on top of water flooding. It revealed that suppression of gravity segregation ensures acceptable macroscopic sweep of the core and measurable incremental oil recovery compared to water flooding. This is in good agreement with other studies (Schulte et al., 1990). The corresponding incremental oil recovery (see Fig. 7.6) can be explained by the fact that residual oil for gas flooding is lower than that for water flooding. The associated mobility reduction factor, mainly due to the relative permeability effects, remained low and oil production was slow, continuing for a fairly long time after gas mobility had reached a stable value. It appears that after the initial oil production by the formation of a diffused oil bank, oil continued to be recovered from the core by a mechanism involving oil spreading over gas-water interfaces (Oren et al., 1992; Grattoni and Dawe, 2003). Despite gravity stable conditions of the displacement, high frontal gas velocity and early gas breakthrough could not be avoided due to high gas-to-liquid mobility ratio.

Foaming of gas using 0.5 and 1.0 wt% AOS+FC (or AOS) surfactant gave rise to large MRF (see Fig. 7.7) and a substantial increase in the macroscopic sweep efficiency of the core demonstrated by the CT scan images. AOS+FC surfactant also reduced the oil-water interfacial tension (IFT), i.e. decreased the capillary forces, leading to better microscopic oil displacement (oil mobilization). A

combined increase of foam apparent viscosity and a lowering of IFT are clearly manifested in a dynamic capillary desaturation curves (see Fig. 7.20).

The data suggest that the existence of two main oil displacement regimes. The first arises from the formation of an oil bank already noted for gas flooding, but which is much clearer for foam. The oil bank regime continues until oil saturation reaches a certain value, below which oil cannot be displaced by viscous forces alone anymore. The second oil recovery regime corresponds to oil displacement as a dispersed phase that is transported by the flowing foam. Remarkably, in this regime the capillary number remains practically constant.

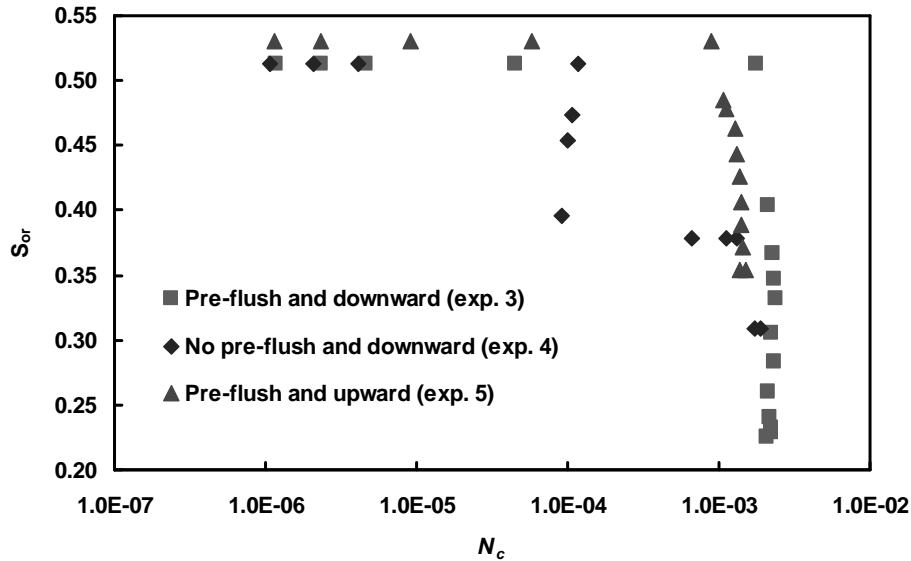


Fig. 7.20: Dynamic capillary desaturation curve for core-flooding experiments with foam generated by 1.0 wt% AOS+FC surfactant at different conditions: with surfactant pre-flush and downward injection (■, exp. 3), no surfactant pre-flush and downward injection (◆, exp. 4), with surfactant pre-flush and upward injection (▲, exp. 5). At each curve the first three points stand for water flooding. The fourth point is for the surfactant pre-flush, except for exp. 4. The rest data points correspond to foam flooding.

In spite of clear increase of MRF and improvement of oil displacement by foam, gravity effects could not be suppressed completely and differences between gravity stable or unstable conditions, respectively down- and up-ward flow, could not be neglected. Higher mobility reduction factors and a longer breakthrough time were obtained for foam injected under gravity stable conditions. These effects are reflected in a higher incremental oil recovery obtained under gravity stable conditions (Fig. 7.21).

Our study has also demonstrated that a stronger foam was developed with the increase of the core length. The mobility reduction factor increases steeply as foam crosses consecutive core segments,

consistent with the 3D CT images showing sharp foam fronts propagating in the presence of water-flood residual oil. The oil bank emerging after foam breakthrough recovers $23\pm 2\%$ of the OIIP after 4.0 PV compared to water flooding. Under similar conditions, foam in the short core recovers $18\pm 2\%$ of the OIIP (Fig. 7.22). Note that at the same PV injected, the incremental oil recovery by gas flooding was only $5.0\pm 0.5\%$.

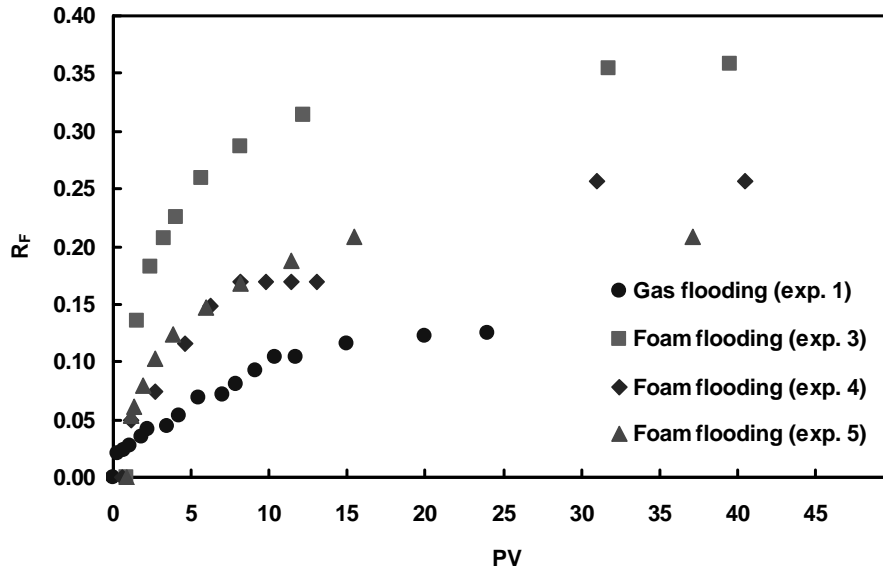


Fig. 7.21: Incremental oil recovery by 1.0 wt% AOS+FC foam at different conditions: with surfactant pre-flush and downward injection (\blacksquare , exp. 3); no surfactant pre-flush and downward injection (\blacklozenge , exp. 4); with surfactant pre-flush and upward injection (\blacktriangle , exp. 5). Oil recovery due to gas flooding (\bullet , exp. 1) was shown as a baseline. Recovery factor was defined as a ratio of the recovered oil by gas or foam to the OIIP.

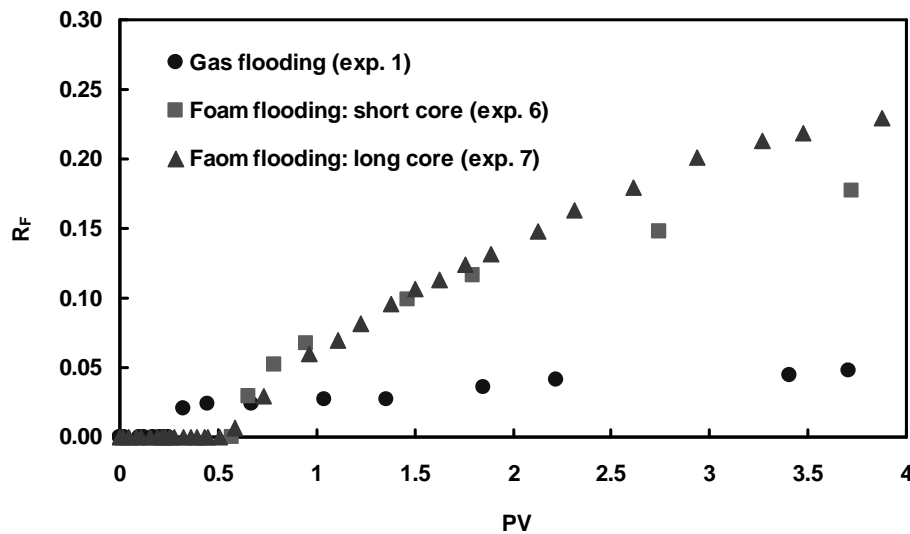


Fig. 7.22: Incremental oil recovery by 1.0 wt% AOS foam using different core lengths: short core with 17.0 cm (\blacksquare , exp. 6); long core with 38.4 cm (\blacktriangle , exp. 7). Gas flooding (\bullet , exp. 1) was used as a baseline.

The above results support the observations of the previous studies (Farajzadeh et al., 2010; Andrianov et al., 2012) and confirm that foam is potentially an efficient EOR method improving gas or WAG flooding. However, more work is still needed to develop a practical immiscible foam EOR process. The first step towards this goal is to develop a new improved foam model accounting for the effects of oil on foam stability. This could be done for instance by modifying the population balance model. Next, the effects of temperature, salt concentration and rock characteristics, as representative of real reservoir conditions should be studied. Then results of the feasibility of the foam EOR concept should be tested under field pilot conditions to check whether foam can propagate over long distances and, correspondingly, whether foam can be used as a recovery (and not only blocking) agent.

7.5 Conclusions

Immiscible foam flooding for enhancing oil recovery was studied systematically with the aid of X-ray Computed Tomography. Foam was generated by co-injecting nitrogen and either AOS or AOS+FC surfactant solution at a fixed foam quality of 91% into the previously water-flooded Bentheimer sandstone cores. Effects of surfactant concentration, injection direction, surfactant pre-flush and core length (17.0 ± 0.1 and 38.4 ± 0.1 cm) were examined in detail. The main conclusions are:

- Stable foams were obtained under the experimental conditions in the presence of water-flood residual oil, ranging from 0.45 ± 0.02 to 0.52 ± 0.02 , for both AOS and AOS+FC surfactants.
- Foam strength was confirmed to increase with surfactant concentration. The mobility reduction factor for foam stabilized by 0.5 and 1.0 wt% of the surfactant mixture was 25 and 35 times larger than that of gas flooding.
- Without surfactant pre-flush foam development and, correspondingly, incremental oil recovery were delayed. It appears that for the case of no pre-flush, foam propagation was impacted by surfactant adsorption while for the foam with pre-flush, gas controls the foam propagation rate. Surfactant pre-flushing is a better foam injection strategy.
- Foam injection under gravity stable conditions was favorable to foam generation and oil recovery. It caused a quick increase of foam strength and a longer foam breakthrough time along with a higher steady-state mobility reduction factor. Incremental oil recovery under gravity stable conditions was almost two times larger compared to the gravity unstable conditions.

- Injection of foam into a previously surfactant pre-flushed core under gravity stable conditions considerably improved the efficiency of gas utilization by reducing the volume of gas required per unit volume of oil produced.
- From the 3D CT scan visualization it was found that foam exhibited a good mobility control with the increase in the core length. The incremental oil recovery by foam in the long core was $23\pm 2\%$ of the oil initially in place after 4.0 PV injected (equal to 0.36 PV injected of surfactant solution), compared to $18\pm 2\%$ for the foam in the short core. Gas flooding at the same injected PV increased oil recovery only by $5.0\pm 0.5\%$.
- Three factors contribute to an increase in oil production by foam: (1) lower residual oil saturation for gas flooding than for water flooding, (2) formation of an oil bank in the first few injected pore volumes, coinciding with a substantial increase of the capillary number and (3) long tail oil production due to the transport of tiny oil droplets within the flowing foam at a fairly constant capillary number.

Chapter 8

SUMMARY AND CONCLUSIONS

This thesis presents novel results concerning the behavior of immiscible gas and foam in natural sandstone samples previously subject to water flooding. It provides insight into processes that could be highly relevant for the application of enhanced oil recovery (EOR) in clastic reservoirs. Firstly, a systematic study of foaming in bulk was conducted to investigate the effects of oil phase on the foamability and foam stability. A foaming agent, the AOS surfactant, which forms stable foam in the presence of alkane-type oils, was thus identified. Secondly, the flow of that surfactant foam in natural porous media was studied in the absence of oil. Effects of surfactant concentration and injection velocity on foam mobility and foam propagation were examined in detail. Mechanisms involved in the foam mobility reduction were also explored. Knowledge obtained from the above part formed the basis for further study of the behavior of foam in porous media in the presence of oil. Thirdly, foam flow in water-flooded porous media was studied in detail, enabling us to provide evidence that foam is potentially a viable EOR process. Below we will give a summary of the main findings obtained from this thesis.

Investigation of foaming behavior of selected commercial surfactants (Dowfax 8390, C₁₂₋₁₅ Enordet, Petrostep SB, and C₁₄₋₁₆ AOS) in the absence and in the presence of model oils (i.e., pure alkanes) revealed that AOS forms the most oil-tolerant foam. Further scrutiny of the foaming behavior of the AOS surfactant by varying surfactant concentrations (0.1, 0.5 and 1.0 wt%) and oil types (n-C₆, n-C₁₀, and n-C₁₆) showed that AOS had excellent foamability despite the variation of the carbon chain length of the alkanes. This was asserted by the build-up of foam volume and also by a monotonic increase in the amount of liquid fraction in the foam. Decay of AOS foam in the presence of oil was characterized by two main stages: 1) a rather small and rapid reduction in foam volume at the early time, followed by a stabilized value, 2) a second reduction by which foam either reached a finite volume (in the presence of n-C₁₆) or was completely broken down (in the presence of n-C₆). From the evolution of liquid fraction in the foam we found that gravity drainage

was dominant in the first reduction of foam volume, while bubble coalescence was dominant during the second stage of the foam volume decay. The effect of oil type was also more pronounced during this second foam decay. AOS foam in the presence of alkane with a shorter carbon chain entered the second decay earlier and exhibited the least foam stability. Increase of surfactant concentration enhanced foam stability in the presence of oil. The effect was more pronounced for the lowest concentrations investigated, namely 0.1 and 0.5 wt%. The results for foam stability in the presence of oil were discussed in terms of the classical entering/spreading coefficient, oil solubilization effect and stability of pseudoemulsion film. Lower foam stability in the presence of short chain alkane was described by larger spreading and bridging coefficients. Higher foam stability in the presence of long chain alkane was attributed to the accumulation of oil droplets in the Plateau borders, which is expected to slow down the rate of thinning of the foam films.

Nitrogen foam stabilized by AOS surfactant in oil-free natural sandstone porous media was generated according to two distinct processes: 1) a primary forward foam front occurred in the first injected pore volume, displacing the liquid phase in a front-like manner and 2) after foam breakthrough a secondary liquid desaturation front emerged at the core outlet and propagated backward toward the core inlet. The speed of the secondary desaturation front was much slower than the primary foam front. We observed that the secondary foam front appeared earlier for a higher surfactant concentration and injection velocity. Accordingly, the foam mobility decreased in two steps: during primary forward foam propagation, foam mobility decreases by one order of magnitude compared to water mobility, and during secondary backward foam propagation, it decreased further by one to two orders of magnitude. We also examined the behavior of foam mobility when surfactant concentration and injection velocity varied through an increasing-decreasing cycle. Foam mobility exhibited a hysteresis for the concentration cycle. This was explained by the adsorption-desorption kinetics of the surfactant. A similar hysteresis was found for the velocity cycle. This indicates that the strong foam, generated through the increasing velocity branch, persists even after decreasing velocity to the lowest tested value (1 ft/day).

Expressing the mobility reduction factor MRF as a function of gas saturation S_g , it was found that foam undergoes a transition from a weak (low MRF) to a strong (high MRF) state at a characteristic gas saturation of $S_{gc} = 0.75 \pm 0.02$. The transition coincided with a substantial reduction in foam mobility by two orders of magnitude and also with a large reduction in overall water saturation to as low as 0.10 ± 0.02 . The foam mobility transition could be interpreted by the surge of yield stress during foam flow: when gas saturation is below the S_{gc} , yield stress is nearly

equal to zero, coinciding with a weak foam, whereas when gas saturation is larger than the S_{gc} , yield stress increases significantly, leading to the observed strong foam. A functional relationship between yield stress and gas saturation was proposed: $\tau_y = a(\sigma/r)(S_g - S_{gc})^4$. When gas saturation is below the S_{gc} , yield stress falls to zero and above that it is described by a power-law behavior. The proposed rheological model successfully captured the mobility transition of foams stabilized by different surfactant concentrations (0.5 and 1.0 wt%) and for different core lengths (17.0 and 38.4 cm). This supports the idea that yield stress grows during the secondary foam flow.

Transient foam flow, forward movement of foam until breakthrough time, in an oil-free porous medium was analyzed using the stochastic bubble population (SBP) model. The premise of this model is that foam flow in porous media is a complex fluid and bubble generation is a stochastic process. We performed a sensitivity analysis to investigate the effects of grid number, time step, maximum bubble density and bubble generation coefficient. We found that numerical results do not show any dependence on grid number (N) and time step (Δt) for $N \geq 250$ and $\Delta t \leq 0.01$ s. An increase of the maximum bubble density led to generation of a stronger foam, characterized by a slower foam propagation rate and a larger foam mobility reduction. The bubble generation coefficient (K_g) mainly controlled the foam generation rate such that a higher K_g led to a more rapidly increasing bubble density. We also provided a comparison between the numerically obtained saturation and pressure data with those obtained from the experiment. The good match between the numerical results and the experiment confirmed that the SBP foam model is robust and captures the main features of the transient foam flow in porous media.

Building upon the above results of AOS foam behavior in bulk and porous media enabled us to conduct very well-controlled core flood experiments in the presence of oil. The experiments have clearly demonstrated that stable foam could be obtained in the presence of water-flood residual oil. More significantly, they proved that immiscible foam displaced additional oil from water-flooded sandstone cores, supporting the idea that foam is potentially an effective EOR method. CT scan images, fluid saturation profiles and mobility reduction factors demonstrated that foam exhibited a good mobility control in the presence of water-flood residual oil. This was further confirmed by a delay in the gas breakthrough. Foam strength and incremental oil recovery increased with the surfactant concentration (ranging from 0.1 to 1.0 wt%). For surfactant concentration equal to 1.0 wt%, incremental oil recovery by foam was as much as $23 \pm 2\%$ of the oil initially in place after injection of 4.0 PV of foam (equal to 0.36 PV injected of surfactant solution). Incremental oil recovery was only $5.0 \pm 0.5\%$ for gas flooding at the same injection time. We found that incremental oil production by foam flooding occurs due to the following main

mechanisms: (1) a lower residual oil saturation to gas flooding compared to water flooding, (2) formation of an oil bank in the first few injected pore volumes, which coincides with a large increase of the capillary number and (3) a long tail oil production due to the transport of dispersed oil within the flowing foam at a fairly constant capillary number. We observed that the oil bank size increased with surfactant concentration, but the dispersed oil regime was less sensitive to the surfactant concentration. We also found that surfactant pre-flushing is a better foam injection strategy. Foam development and, correspondingly, oil recovery without surfactant pre-flush were significantly delayed compared to the case with pre-flush. Foam injection under gravity stable conditions was favorable to foam generation and oil recovery. It caused a quick increase of foam strength and a longer foam breakthrough time along with a higher steady-state mobility reduction factor. Incremental oil recovery under gravity stable conditions was almost two times larger compared to the gravity unstable conditions.

The contribution of this thesis to foam knowledge has been in demonstrating that foam is potentially an efficient EOR method. However, many questions remain, underscoring the need for further scientific study and research to fully develop a practical immiscible foam EOR process. The first step towards this latter goal is to develop a new and improved foam model accounting for the effects of oil on foam stability. Next, the effects of temperature, salt concentration and rock characteristics, as representative of real reservoir conditions, should be studied. Then the results of the feasibility of the foam EOR concept should be tested under field pilot conditions to check whether foam can propagate over long distances and, correspondingly, whether foam can be used as a recovery agent.

References

- Aarra, M. G., Skauge, A., Søgne sand, S., and Stenhaug, M., A foam pilot test aimed at reducing gas inflow in a production well at the Oseberg Field, *Petroleum Geoscience*, 2, 125-132 (1996).
- Aarra, M.G., Skauge A., and Martinsen, H.A., FAWAG: A breakthrough for EOR in the North sea, SPE 77695, *SPE Annual Technical Conference and Exhibition*, San Antonio, Texas, 29 September-2 October (2002).
- Aarra, M.G., Ormehaug, P.A., Skauge, A., and Masalmeh, S.K., Experimental study of CO₂- and methane-foam using carbonate core material at reservoir conditions, SPE 141614, *SPE Middle East Oil and Gas Show and Conference*, Manama, Bahrain, 25-28 September (2011).
- Ali, J., Burley, R.W., and Nutt, C.W., Foam enhanced oil recovery from sand packs, *Chemical Engineering Research and Design*, 63 (2), 101-111 (1985).
- Al-Mutairi, S.M., Kokal, S.L., EOR potential in the Middle East: current and future trends, SPE 143287, *SPE EUROPEC/EAGE Annual Conference and Exhibition*, Vienna, Austria, 23-26 May (2011).
- Al-Omair, O.A., Christiansen, R.L., Measurement of capillary pressure by direct visualization of a centrifuge experiment, *International symposium of the society of core analysts*, Abu Dhabi, UAE (1998).
- Alvarado, V., and Manrique, E., Enhanced oil recovery: An update review, *Energies*, 3, 1529-1575 (2010).
- Alvarez, J.M., and Rossen, W.R., Unified model for steady-state foam behavior at high and low foam qualities, *SPE J.*, 6 (3), 325-333 (2001).
- Andrianov, A., Liu, M.K., Rossen, W.R., Sweep efficiency in CO₂ foam simulations with oil, SPE 142999, *SPE EUROPEC/EAGE Annual Conference and Exhibition*, Vienna, Austria, 23-26 May (2011).
- Andrianov, A., Farajzadeh, R., Mahmoodi Nick, M., Talanana, M., and Zitha, P.L.J., Immiscible foam for enhancing oil recovery: bulk and porous media experiments, *Ind. Eng. Chem. Res.*, 51 (5), 2214-2226 (2012).
- Apaydin, O.G., Kovscek, A.R., Transient foam flow in homogeneous porous media: surfactant concentration and capillary end effects, *Transport in Porous Media*, 43 (3), 511-536 (2001).
- Aronson, A.S., Bergeron, V., Fagan, M.E., and Radke, C.J., The influence of disjoining pressure on foam stability and flow in porous media, *Colloids and Surfaces A: Physicochemical Eng. Aspects*, 83 (2), 109-120 (1994).
- Arnaudov, L., Denkov, N.D., Surcheva, I., Durbut, P., Effect of oily additives on foamability and foam stability. 1. Role of interfacial properties, *Langmuir*, 17 (22), 6999-7010 (2001).
- Ashoori, E., Marchesin, D., and Rossen, W.R., Dynamic foam behavior in the entrance region of a porous medium, *Colloids and Surfaces A: Physicochemical and Engineering Aspects*, 377 (1-3), 217-227 (2011 a).
- Ashoori, E., Marchesin, D., Rossen, W.R., Roles of transient and local equilibrium foam behavior in porous media: traveling wave, *Colloids and Surfaces A: Physicochemical and Engineering Aspects*, 377 (1-3), 228-242 (2011 b).
- Ashoori, E., Marchesin, D., and Rossen, W.R., Multiple foam states and long-distance foam propagation in EOR displacements, SPE 154024, *SPE Improved Oil Recovery Symposium*, Tulsa, Oklahoma, USA, 14-18 April (2012).

- Aveyard, R., Binks, B.P., Fletcher, P.D.I., Peck, T.G., Garrett, P.R., Entry and spreading of alkane drops at the air-surfactant solution interface in relation to foam and soap film stability, *J. Chem. Soc. Faraday Trans.*, 89 (24), 4313-4321 (1993).
- Aveyard, R., Cooper, P., Fletcher, P.D.I., and Rucherford, C.E., Foam breakdown by hydrophobic particles and nonpolar oil, *Langmuir*, 9, 604-613 (1993).
- Aveyard, R., Binks, B.P., Fletcher, P.D.I., Peck, T.G., Rucherford, C.E., Aspects of aqueous foam stability in the presence of hydrocarbons oils and solid particles, *Advances in Colloid and Interface Science*, 48, 93-120 (1994).
- Aveyard, R., and Clint, J.H., Foam and thin film breakdown processes, *Current Opinion in Colloid & Interface Science*, 1(6), 764-770 (1996).
- Aziz, K., Settari, A., *Petroleum Reservoir Simulation*, Elsevier Applied Science Publishers (1979).
- Babadaghi, T., Development of mature oil fields- A review, *Journal of Petroleum Science and Engineering*, 57, 221-246 (2007).
- Balan, H.O., Balhoff, M.T., Nguyen, Q.P., and Rossen, W.R., Network modeling of gas trapping and mobility in foam enhanced oil recovery, *Energy Fuels*, 25 (9), 3974-3987 (2011).
- Behenna, F.R., Acid diversion from an undamaged to a damaged core using multiple foam slugs, SPE 30121, *European Formation Damage Conference*, The Hague, Netherlands, 15-16 May (1995).
- Bernard, G.G., Holm, L.W., Jacob L.W., Effect of foam on trapped gas saturation and on permeability of porous media to water, *SPE J.*, 5(4), 295-300 (1965).
- Bergeron, V., Fagan, M.E., Radke, C.J., Generalized entering coefficients: a criterion for foam stability against oil in porous media, *Langmuir*, 9 (7), 1704-1713 (1993).
- Bergeron, V., Radke, C.J., Disjoining pressure and stratification in asymmetric thin-liquid films, *J. Colloid and Polymer Science*, 273 (2), 165-174 (1995).
- Bertin, H.J., Quintard, M.Y., Castanier, L.M., Development of a bubble-population correlation for foam-flow modeling in porous media, *SPE J.*, 3(4), 356-362 (1998).
- Blaker, T., Celius, H.K., Lie, T., Martinsen, H.A., Rasmussen, L., Vassenden, F., Foam for gas mobility control in the Snorre field: The FAWAG project, SPE 56478, *SPE Annual Technical Conference and Exhibition*, Houston, Texas, 3-6 October (1999).
- Blaskovich, F.T., Historical problems with oil field rejuvenation, SPE 62518, *2000 SPE/AAPG Western Regional Meeting.*, Long Beach, CA, 19- 23 June (2000).
- Blauer, R.E., and Kohlhaas, C.A., Formation fracturing with foam, SPE 5003, *Fall meeting of the Society of Petroleum Engineers of AIME*, Houston, Texas, 6-9 October (1974).
- Bond, D.C., and Holbrook, O.C., Gas drive oil recovery process, *US Patent*, No. 2,866,507 (1958).
- Bonfillon A., Sicoli F., and Langevin D., Dynamic surface tension of ionic surfactant solutions, *J. of Colloid and Interface Science*, 168, 497-504 (1994).
- BP Statistical Review of World Energy June 2011, Available at: www.bp.com/statisticalreview.
- Carretero-Carralero, M.D., Farajzadeh, R., Du, D.X., Zitha, P.L.J, Modeling and CT-scan study of foams for acid diversion, SPE 107795, *European Formation Damage Conference*, Scheveningen, the Netherlands, 30 May -1 Jun (2007).
- Caudle, B.H., Dyes, A.B., Improving miscible displacement by gas-water injection, *Transactions AIME*, 213, 281-284 (1959).
- Ceglie, A., Das, K.P., Lindman, B., Microemulsion structure in four-component systems for different surfactants, *J. Colloids Surf*, 28, 29-40 (1987 a).
- Ceglie, A., Das, K.P., Lindman, B., Effect of oil on the microscopic structure in four-component cosurfactant microemulsions, *J. Colloid and Interface Science*, 115 (1), 115-120 (1987 b).
- Chang, Y.B., Pope, G. A., Sepehrnoori, K., CO₂ Flow patterns under multiphase flow: heterogeneous field-scale conditions, *SPE Reservoir Engineering*, 9 (3), 208-216 (1993).
- Chaouche, M., Rakotomalala, N., Salin, D., Xu, B. and Yortsos, Y.C., Capillary effects in heterogeneous porous media: experiments, pore network simulations, and continuum modeling, SPE 26658, *SPE Annual Technical Conference and Exhibition*, Houston, 3-6 October (1993).

- Chen, M., Yortsos, Y.C., and Rossen, W.R., Insights on foam generation in porous media from pore-network studies, *Colloids Surfaces A: Physicochem Eng. Aspects*, 256 (2-3), 181-189 (2005).
- Chen, Q., Gerritsen, M.G., and Kovscek, A.R., Modeling foam displacement with the local-equilibrium approximation: theory and experimental verification, *SPE J.*, 15 (1), 171-183 (2010).
- Chiang, J. C., Sawyal, S. K., Castanier, L. M., Brigham, W. E., Sufi, A., Foam as a mobility control agent in steam injection processes, SPE 8912, *SPE California Regional Meeting*, 9-11 April, Los Angeles, California (1980).
- Chou, S.I., Conditions for generation foam in porous media, SPE 22628, *SPE Annual Technical Conference and Exhibition*, Dallas, TX, USA, 6-9 October (1991).
- Christensen, J.R., Stenby, E.H. , and Skauge, A., Review of WAG field experience, *SPE Reservoir Evaluation & Engineering*, 4(2), 97-106 (2001).
- Cohen, D.G., Patzek, T.W, and Radke, C.J., Onset of mobilization and the fraction of trapped foam in porous media, *Transport in Porous Media*, 28 (3), 253-284 (1997).
- Davis, H.T., *Statistical mechanics of phases, interfaces and thin films*, VCH, New York (1996).
- Denkov, N.D., Mechanisms of foam destruction by oil-based antifoams, *Langmuir*, 20 (22), 9463-9505 (2004).
- Dietz, D.N., A theoretical approach to the problem of encroaching and by-passing edge water, *Akad. van Wetenschappen, Amsterdam. Proc. V.56-B: 83* (1953).
- Du, D.X., AOS adsorption in Bentheim sandstone, *Internal report* (2007).
- Du, D.X., Zitha, P.L.J., Uijttenhout, M.G.H., Carbon dioxide foam rheology in porous media: a CT scan study, *SPE J.*, 12(2), 245-252 (2007).
- Du, D.X., Zitha, P.L.J., and Vermolen, F.J., Numerical analysis of foam motion in porous media using a new stochastic bubble population model, *Transport in Porous Media*, 86(2), 461-474 (2011).
- Emadi, A., Sohrabi, M., Jamiolahmady, M., Ireland, S., and Robertson, G., Mechanistic study of improved heavy oil recovery by CO₂-foam injection, SPE 143013, *SPE Enhanced Oil Recovery Conference*, Kuala Lumpur, Malaysia, 19-21 July (2011).
- Exerowa, D., and Kruglyakov, P.M., *Foam and Foam Films: Theory, Experiments, Application*, Elsevier (1998).
- Falls, A.H., Hirasaki, G.J., Patzek, T.W., Gauglitz, D.A., Miller, D.D., Ratulowski, T., Development of a mechanistic foam simulator: the population balance and generation by snap-off, *SPE Reservoir Engineering*, 3(3), 884-892 (1988).
- Falls, A., Musters, J.J. and Ratulowski, J., The apparent viscosity of foams in homogeneous bead packs, *SPE Reservoir Engineering*, 4 (2), 155-164 (1989).
- Farajzadeh, R., Krastev, R., Zitha, P.L.J., Properties of foam films stabilized by AOS surfactant, *Colloids and Surfaces A: Engineering Aspects*, 324, 35-40 (2008).
- Farajzadeh, R., Andrianov, A., Bruining, J., Zitha, P.L.J., Comparative study of CO₂ and N₂ foams in porous media at low and high pressure-temperatures, *Ind. Eng. Chem. Res.*, 48 (9), 4542-4552 (2009).
- Farajzadeh, R., Andrianov, A., and Zitha, P.L.J., Investigation of immiscible and miscible foam for enhancing oil recovery, *Ind. Eng. Chem. Res.*, 49 (4), 1910-1919 (2010).
- Farajzadeh, R., Andrianov, A., Hirasaki, G.J., Krastev, R., and Rossen, W.R., Foam-oil interaction in porous media: implications for foam assisted enhanced oil recovery, SPE 154197, *SPE EOR Conference at Oil and Gas West Asia, Muscat*, Oman, 16-18 April (2012).
- Farouq Ali, S.M., and Thomas, S., Enhanced oil recovery- what we have learned, *J. of Canadian Petroleum Technology*, 39, 7-11 (2000).
- Fried, A.N., The foam drive process for increasing the recovery of oil, *Report of investigations 5866*, U.S. Department of the Interior, Bureau of Mines, Washington, D.C. (1961).
- Friedmann, F. and Jensen, J.A., Some parameters influencing the formation and propagation of foams in porous media, SPE 15087, *California Regional Meeting of Society of Petroleum Engineers*, Oakland, California, USA, 2-4 April (1986).

- Friedmann, F. Chen, W.H. and Gauglitz, P.A., Experimental and simulation study of high temperature foam displacement in porous media, *SPE Reservoir Engineering*, 6(1), 37-45 (1991).
- Friedman, F., Smith, M.E., Guice, W.R., Gump, J.M. and Nelson, D.G., Steam-foam mechanistic field trial in the Midway-Sunset field, *SPE Reservoir Engineering*, 9(4), 297-304 (1994).
- Gardiner, B.S., Dlugogorski, B.Z., Jameson, G.J., and Chhabra, R.P., Yield stress measurements of aqueous foams in the dry limit, *J. of Rheology*, 42(6), 1437-1450 (1998).
- Garrett, P.R., Preliminary considerations concerning the stability of a liquid heterogeneity in a plane-parallel liquid film, *J. Colloid Interface Sci.*, 76 (2), 587-590 (1980).
- Garrett, P.R. *The mode of action of antifoams*, In: Defoaming: theory and industrial applications; Garrett, P.R. (ed.), Marcel Dekker, New York (1993).
- Grattoni, C.A., and Dawe, R.A., Gas and oil production from waterflood residual oil: effect of wettability and oil spreading characteristics, *J. of Petroleum Science and Engineering*, 39 (3-4), 297-308 (2003).
- Gauglitz, P.A., Friedmann, F., Kam, S.I., and Rossen, W.R., Foam generation in homogeneous porous media, *Chemical Engineering Science*, 57, 4037-4052 (2002).
- Green, D.W., Willhite, G.P., *Enhanced oil recovery*, SPE Textbook Series, Vol. 6, Richardson, TX (1998).
- Guo, H., Faber, R., Buijse, M., Zitha, P.L.J., A novel Alkaline-Surfactant-Foam EOR process, SPE 145043, *SPE Enhanced Oil Recovery Conference*, Kuala Lumpur, Malaysia, 19-21 July (2011).
- Hadjiiski, A., Tcholakova, S., Denkov, N.D. Durbut, P., Effect of oily additives on foamability and foam stability. 2. Entry barriers, *Langmuir*, 17 (22), 7011-7021 (2001).
- Halibouty, M.T., Giant oil and gas fields of the decade, *64th Annual Meeting of AAPG*, Houston, Texas, (1979).
- Hanssen, J.E., Dalland, M, *Gas blocking foams*. In: Foams: Fundamentals and Applications in the Petroleum Industry, Schramm, L.L. (ed.), American Chemical Society, Washington, DC (1994).
- Hanssen, J.E., Holt, T., and Surguchev, L.M., Foam processes: an assessment of their potential in North sea reservoirs based on a critical evaluation of current field experience, SPE 27768, *SPE/DOE Improved Oil Recovery Symposium*, Tulsa, Oklahoma, 17-20 April (1994).
- Harkins, W.D., A general thermodynamic theory of the spreading of liquids to form duplex films and of liquids or solids to form monolayers, *J. Chemical Physics*, 9 (7), 552-568 (1941).
- Heiba, A. E. H., Sahimi, M., Scriven L. E. and Davis, H. T., Percolation theory for two phase flow relative permeability, *SPE Reservoir Engineering*, 7(1), 123-132 (1992).
- Hirasaki, G. J. and Lawson, J., Mechanisms of foam flow in porous media: apparent viscosity in smooth capillaries, *SPE J.*, 25 (2), 176-190 (1985).
- Hirasaki, G.J., The steam foam process, *J. Petroleum Technology*, 41, 449-456 (1989).
- Hirasaki, G.J., Miller, C.A., Szafranski, R., Tanzil, D., Lawson, J.B., Meinardus, H.W., Jin, M., Londergan, J.T., Jackson, R.E., Pope, G.A., and Wade, W.H., Field demonstration of the surfactant/foam process for aquifer remediation, SPE 39292, *SPE Annual Technical Conference and Exhibition*, San Antonio, Texas, 5-8 October (1997).
- Holm, L.W., The mechanism of gas and liquid flow through porous media in the presence of foam, *SPE J.*, 8(4), 359-369 (1968).
- Holm, L.W., Evolution of the carbon dioxide flooding processes, *J. Petroleum Technology*, 11, 1337-1342 (1987).
- Hoefner, M.L., Evans, E.M., Buckles, J.J., and Jones, T.A., CO₂ foam: results from four developmental field trials, *SPE Reservoir Engineering*, 10 (4), 273-281 (1995).
- Höök, M, Hirsch, R., Aleklett, K., Giant oil field decline rates and their influence on world oil production, *Energy Policy*, 37, 2262-2272 (2009).
- Huang, D.D., and Honarpour, M.M., Capillary end effects in core-flood calculations, *J. of Petroleum Science and Engineering*, 19, 103-117 (1998).
- Huh, D.G., Cochrane, T.S., and Kovarik, F.S., The effect of microscopic heterogeneity on CO₂ foam mobility: Part 1- a mechanistic study, *J. of Petroleum Technology*, 41 (8), 872-879 (1988).
- IEA, Energy technologies at the cutting edge, *OECD and IEA*, Paris (2005).

- Ivanhoe, L.F., Get ready for another oil shock, *The Futurist*, 31, 20-27 (1997).
- Jensen J.A., and Friedmann F., Physical and chemical effects of an oil phase on the propagation of foam in porous media, SPE 16375, *SPE California Regional Meeting*, Ventura, California, 8-10 April (1987).
- Jeong, S.W., Evaluation of the use of capillary numbers for quantifying the removal of DNAPL trapped in a porous medium by surfactant and surfactant foam floods, *J. Colloid Interf. Sci.*, 282, 182-187 (2005).
- Kabalnov, A.S., and Shchukinb, E.D., Ostwald ripening theory: applications to fluorocarbon emulsion stability, *Advances in Colloid and Interface Science*, 38, 69-97 (1992).
- Kam, S.I., and Rossen, W.R., A model for foam generation in homogeneous porous media, *SPE J.*, 8 (4), 417-425 (2003).
- Kam, S.I., Nguyen, Q.P., Li, Q., Rossen, W.R., Dynamic simulations with an improved model for foam generation, *SPE J.*, 12(1), 35-48 (2007).
- Kam, S.I., Improved mechanistic foam simulation with foam catastrophe theory, *Colloids and Surfaces A: Physicochem. Eng. Aspects*, 318 (1-3), 62-77 (2008).
- Khan, S.A., Schnepfer, C.A., and Armstrong, R.C, Foam rheology: III. Measurement of shear flow properties, *J. of Rheology*, 32 (1), 69-92 (1988).
- Khatib, Z.I., Hirasaki, G.J., Falls, A.H., Effects of capillary pressure on coalescence and phase mobilities in foams flowing through porous media, *SPE Reservoir Engineering*, 3 (3), 919-926 (1988).
- Kibodeaux, K.R., Zeilinger, S.C., Rossen, W.R., Sensitivity study of foam diversion processes for matrix acidization, SPE 28550, *Annual Technical Conference and Exhibition*, New Orleans, Louisiana, 25-28 September (1994).
- King, M.J., Flazone, A.J., Cook, W.R., Jennings Jr., J.W., and Mills, W.H., Simultaneous determination of residual saturation and capillary pressure curves utilizing the ultracentrifuge, SPE 15595, *61st Annual Technical Conference and Exhibition*, New Orleans, LA, 5-8 October (1986).
- Koczo K., Lobo L., and Wasan D.T., effete of oil on foam stability: aqueous film stabilized by emulsions, *J. Colloid and Interface Science*, 150 (2), 492-506 (1992).
- Koehler, S.A., Hilgenfeldt, S., Stone, H.A., A generalized view of foam drainage: experiment and theory, *Langmuir*, 16(15), 6327-6341 (2000).
- Koval, E. J., A method for predicting the performance of unstable miscible displacement in heterogeneous media, *SPE J.*, 3(2), 145-154 (1963).
- Kovscek, A.R., and Radke, C.J., *Fundamentals of foam transport in porous media*, In: *Foams: Fundamentals and Applications in the Petroleum Industry*, Schramm, L.L. (ed.), ACS, Washington, DC (1994).
- Kovscek, A.R., Patzek, T.W., Radke, C.J., A mechanistic population balance model for transient and steady-state foam flow in Boise sandstone, *Chemical Engineering Science*, 50, 3783-3799 (1995).
- Kovscek, A.R., Patzet, T.W., and Radke, C.J., Mechanistic foam flow simulation in heterogeneous and multidimensional porous media, *SPE J.*, 2 (4), 511-526 (1997).
- Krause, R.E., Lane, R.H., Kuehne, D.L., Bain, G.F, Foam treatment of producing wells to increase oil production at Prudhoe Bay, SPE 24191, *8th SPE/DOE Symposium on EOR*, Tulsa, OK, 22-24 April (1992).
- Kuhlman, M.I., Visualizing the effect of light oil on CO₂ foams, *Journal of Petroleum Technology*, 42(7), 90-908 (1990).
- Lake, L.W., *Enhanced oil recovery*, Prentice-Hall, Englewood Cliffs, New Jersey (1989).
- Lau, H.C., O'Brien, S.M, Effects of spreading and nonspreading oils on foam propagation through porous media, *SPE Reservoir Engineering*, 3(3), 893-896 (1988).
- Le, V.Q., Nguyen, Q.P., Sanders. A.W., A novel foam concept with CO₂ dissolved surfactants SPE 13370, *SPE/DOE Symposium on Improved Oil Recovery*, Tulsa, Oklahoma, USA, 20-23 April (2008).

- Lee, H.O., and Heller, J.P., *Mobility of CO₂ and Surfactant Adsorption in Porous Rocks*. In: Oil-Field Chemistry, Borchardt, J.K., and Yen, T.F. (ed.), American Chemical Society, Washington, DC (1989).
- Li, B., Hirasaki, G.J., and Miller, C.A., Upscaling of foam mobility control to three dimensions, SPE 99719, *SPE/DOE Symposium on Improved Oil Recovery*, Tulsa, Oklahoma, USA, 22-26 April (2006).
- Li, R.F., Yan, W., Liu, S.H., Hirasaki, G.J. and Miller, C.A., Foam mobility control for surfactant EOR, *SPE J.*, 15(4), 928-942 (2008).
- Low, D.H.-S., Yang, Z.-M., and Stone, T.W., Effect of the presence of oil on foam performance: A field simulation study, *SPE Reservoir Engineering*, 7(2), 228-236 (1992).
- Maldal, T., Gulbrandsen, A.H. and Gilje, E., Correlation of capillary number curves and remaining oil saturations for reservoir and model sandstones, *In Situ*, 21(3), 239-269 (1997).
- Manlowe D.J., and Radke C.J., A pore-level investigation of foam/oil interactions in porous media, *SPE Reservoir Engineering*, 5(4), 495-502 (1990).
- Mannhardt K., Novosad J.J., and Schramm L.L., Foam- oil interactions at reservoir conditions, SPE 39681, *SPE/DOE Improved Oil Recovery Symposium*, Tulsa, OK, 19-22 April (1998).
- Mannhardt, K., Svorstøl, I., Effect of oil saturation on foam propagation in Snorre reservoir core, *J. of Petroleum Science and Engineering*, 23 (3-4), 189-200 (1999).
- Mannhardt, K., Svorstøl, I., Surfactant concentration for foam formation and propagation in Snorre reservoir core, *J. of Petroleum Science and Engineering*, 30, 105-119 (2001).
- Marinova K.G., Basheva E.S., Nenova B., Temelska M., Mirarefi A.Y., Campbell B, Ivanov, I.B., Physico-chemical factors controlling the foamability and foam stability of milk proteins: sodium caseinate and whey protein concentrates, *Food Hydrocolloids*, 23 (7), 1864-1876 (2009).
- Martin, F.D., Heller, J.P., Weiss, W.W., Tsau, Jyun-Syung, Zornes, D.R., Sugg, L.A., Stevens, J.E., and Kim, J.E., CO₂-foam field verification pilot test at EVGSAU injection project phase I: project planning and initial results, SPE 24176, *SPE/DOE Enhanced Oil Recovery Symposium*, Tulsa, Oklahoma, 22-24 April (1992).
- Martinez, J. M. A., *Foam flow behavior in porous media: effects of flow regime and porous medium heterogeneity*, Ph.D. Thesis, The University of Texas at Austin, USA (1996).
- Mason, T.G., Bibette, J., and Weitz, D.A., Yielding and Flow of Monodisperse Emulsions, *J. of Colloid and Interface science*, 179 (2), 439-448 (1996).
- Mees, F., Swennen, R., Van Geet, M., and Jacobs, P., *Application of X-ray computed tomography in the geoscience*, Geological Society, Special Publications 215, London (2003).
- Minssieux, L., Oil displacement by foams in relation to their physical properties in porous media, *J. of Petroleum Technology*, 26(1), 100-108 (1974).
- Montaron, B., Carbonate evolution, *Oil & Gas Middle East*, 26-31(2008).
- Moritis, G., EOR/heavy oil survey, *Oil & Gas Journal*, 108 (36), April 19 (2010).
- Myers, T.J. and Radke, C.J., Transient foam displacement in the presence of residual oil: experiment and simulation using a population-balance model, *Ind. Eng. Chem. Res.*, 39(8), 2725-2741 (2000).
- Namdar Zanganeh, M., Kam, S.I., LaForce, T.C., and Rossen, W.R., The method of characteristics applied to oil displacement by foam, *SPE J.*, 16 (1), 8-23 (2011).
- Neethling, S.J., Morris, G., and Garrett P.R., Modeling oil droplets in plateau borders, *Langmuir*, 27 (16), 9738-9747 (2011).
- Nguyen, Q.P., Alexandrov, A. V., Zitha, P.L.J., Currie, P.K., Experimental and modeling studies on foam in porous media: a review, SPE 58799, *International Symposium on Formation Damage Control*, Lafayette, Louisiana, USA, 23-24 February (2000).
- Nguyen, Q.P., Currie, P.K., Zitha, P.L.J., Determination of foam induced fluid partitioning in porous media using X-ray Computed Tomography, SPE 80245, *SPE International Symposium on Oilfield Chemistry*, Houston, Texas, USA, 5-8 February (2003).
- Nguyen, Q.P., Currie, P.K., and Zitha, P.L.J., Motion of foam film in diverging-converging channel, *J. Colloid Interface Sci.*, 271(2), 473-484 (2004).

- Nguyen, Q.P., Currie, P.K., Buijse M., Zitha P.L.J., Mapping of foam mobility in porous media, *J. Petroleum Science and Engineering*, 58, 119-132 (2007).
- Nikolov, A.D., Wasan, D.T., Huang, D.W., and Edwards, D.A., The effect of oil on foam stability: mechanisms and implications for oil displacement by foam in porous media, SPE 15443, *SPE Annual Technical Conference and Exhibition*, New Orleans, Louisiana 5-8 October (1986).
- Oil and gas EOR survey, *Oil & Gas Journal*, 105 (42), November 12 (2007).
- Oil and gas EOR survey, *Oil & Gas Journal*, 108 (36), April 12 (2010).
- Oren, P.E., Billiotte, J. and Pinczewski, W.V., Mobilization of waterflood residual oil by gas injection for water-wet conditions, *SPE Formation Evaluation*, 7(1), 70-78 (1992).
- Orr, F.M., *Theory of gas injection processes*, Tie-Line Publications, Copenhagen, Denmark (2007).
- Osterloh, W.T., Jante, M.J., Effects of gas and liquid velocity on steady-state foam flow at high temperature, SPE 24179, *SPE/DOE Enhanced Oil Recovery Symposium*, Tulsa, Oklahoma, USA, 22-24 April (1992).
- Pal, R., Yield stress and viscoelastic properties of high internal phase ratio emulsions, *Colloid & Polymer Science*, 277 (6), 583-588 (1999).
- Patzek, T.W., *Description of foam flow in porous media by the population balance method*. In: Surfactant-based mobility control progress in miscible-flood enhanced oil recovery, Smith, D.H. (ed.), American Chemical Society, Washington, DC (1988).
- Patzek, T.W., Field applications of foam for mobility improvement and profile control, *SPE Reservoir Engineering*, 11 (2), 79-86 (1996).
- Patzek, T.W., and Koinis, M.T., Kern River steam-foam pilots, *J. of Petroleum technology*, 42 (4), 496-503 (1990).
- Petroleum Economist Magazine, February 2010.
- Princen, H.M., and Kiss, A.D., Rheology of foams and highly concentrated emulsions: IV. An experimental study of the shear viscosity and yield stress of concentrated emulsions, *Colloid and Interface Science*, 128 (1), 176-187 (1989).
- Quintero, C.G., Noik, C., Dalmazzone, C., and Grossiord, J-L, Modelling and characterisation of diluted and concentrated water-in-crude oil emulsions: comparison with classical behaviour, *Rheologica Acta*, 47(4), 417-424 (2008).
- Ranshoff, T.C., Radke, C.J., Mechanisms of foam generation in glass-bead packs, *SPE Reservoir Engineering*, 3 (2), 573-585 (1988).
- Rao, D., Gas injection EOR- a new meaning in the new millennium, *J. of Canadian Petroleum Technology*, 40 (2), 11-18 (2001).
- Rateman, K.T., An investigation of oil destabilization of nitrogen foams in porous media, SPE 19692, *SPE Annual Technical Conference and Exhibition*, San Antonio, Texas, 8-11 October (1989).
- Righi, E.F., Royo, J., Gentil, P., Castelo, R., Del Monte, A., Bosco, S., Experimental study of tertiary immiscible WAG injection, SPE 89360, *SPE/DOE Symposium on Improved Oil Recovery*, Tulsa, OK, 17-21 April (2004).
- Robert, J.A., and Mack, M.G., Foam diversion modeling and simulation, *SPR Production & Facilities*, 12(2), 123-127 (1997).
- Robinson, J.W. and Woods, W.W., A method of selecting foam inhibitors, *J. Soc. Chem. Ind.*, 67 (9), 361-365 (1948).
- Rosen, M. J. and Solash, J., Factors affecting initial foam height in the Ross-Miles foam test, *J. of the American Oil Chemists' Society*, 46 (8), 399-402 (1969).
- Rossen, W.R., Theories of foam mobilization pressure gradient, SPE 17358, *SPE/DOE Enhanced Oil Recovery Symposium*, Tulsa, OK, 17-20 April (1988).
- Rossen, W.R., Minimum pressure gradient for foam flow in porous media: effect of interactions with stationary lamellae, *Colloid and Interface Science*, 139 (2), 457-468 (1990).
- Rossen, W.R., *Foams in enhanced oil recovery*, In: Foams: Theory, Measurements and Applications, R. K. Prud'homme and S. Khan (eds.). Marcel Dekker, New York (1996).
- Rossen, W.R., Foam generation at layer boundaries in porous media, *SPE J.*, 4(4), 409-412 (1999).

- Rossen, W.R., and Gauglitz, P.A., Percolation theory of creation and mobilization of foam in porous media, *AIChE J.*, 36 (8), 1176-1188 (1990).
- Rossen, W.R., and Shen, C., Gravity segregation in gas-injection IOR, SPE 107262, *EUROPEC/EAGE Conference and Exhibition*, London, U.K, 11-14 June (2007).
- Rossen, W. R., van Duijn, C.J., Nguyen, Q.P. Shen, C., and Vikingstad, A.K., Injection strategies to overcome gravity segregation in simultaneous gas and water injection into homogeneous reservoirs, *SPE J.*, 15 (1), 76-90 (2010).
- Rossen, W.R. and Wang, M.-W., Modeling foams for acid diversion, *SPE J.*, 4(2), 92-100 (1999).
- Rossen, W.R. and Zhou, Z.H., Modeling foam mobility at the limiting capillary pressure, *SPE Advanced Technology*, 3 (1), 146-153 (1995).
- Rossen, W.R., Zeilinger, S.C., Shi, J.-X., Lim, M.T., Simplified mechanistic simulation of foam processes in porous media, *SPE J.*, 4 (3), 279-287 (1999).
- Rouyer, F., Cohen-Addad, S., and Höhler, R., Is the yield stress of aqueous foam a well-defined quantity?, *Colloids and Surfaces A: Physicochem. Eng. Aspects*, 263 (1-3), 111-116 (2005).
- Saint-Jalmes, A., and Durian, D.J., Vanishing elasticity for wet foams: Equivalence with emulsions and role of polydispersity, *J. of Rheology*, 43 (6), 1411-1422 (1999).
- Saint-Jalmes, A., Peugeot, M.-L., Ferraz, H., and Langevin, D., Differences between protein and surfactant foams: microscopic properties, stability and coarsening, *Colloids and Surfaces A: Physicochemical and Engineering Aspects*, 263 (1-3), 219-225 (2005).
- Sanchez, C.C., and Patino, J.M.R., Interfacial, foaming and emulsifying characteristics of sodium caseinate as influenced by protein concentration in solution, *Food Hydrocolloids*, 19 (3), 407-416 (2005).
- Sanchez, J.M., Schechter, R.S., and Monsalve, A., The effect of trace quantities of surfactant on nitrogen/water relative permeabilities, SPE 15446, *SPE Annual Technical Conference and Exhibition*, New Orleans, LA, 5-8 Oct (1986).
- Sandrea, I., Sandrea, R., Global oil reserves- recovery factors leave vast target for EOR technologies, *Oil & Gas Journal*, 105 (42), November 12 (2007).
- Schramm, L.L., *Foam sensitivity to crude oil in porous media*, In: *Foams: Fundamentals & Applications in the Petroleum Industry*, Schramm, L.L. (ed.), American Chemical Society, Washington, DC (1994).
- Schramm, L.L. and Novosad, J.J., Micro-visualization of foam interactions with a crude oil, *Colloids Surfaces*, 46 (1), 21-43 (1990).
- Schramm, L.L., and Novosad, J.J., The destabilization of foams for improved oil recovery by crude oils: effect of the nature of the oil, *J. of Petroleum Science and Engineering*, 7(1), 77-90 (1992).
- Schramm, L.L., Turta, A.T., and Novosad, J.J., Microvisual and coreflood studies of foam interactions with a light crude oil, *SPE Reservoir Engineering*, 8 (3), 201-206 (1993).
- Schramm, L.L., and Wassmuth, F., *Foams: Basic Principles*, In: *Foams: Fundamentals & Applications in the Petroleum Industry*, Schramm, L.L. (ed.), American Chemical Society, Washington, DC (1994).
- Schulte, A.M., Niko, H., and Swinkles, W, Analytical modeling of 2-D flow in gravity stable secondary gas or water drives, SPE 20899, *European Petroleum Conference*, The Hague, Netherlands, 21-24 October (1990).
- Schulze-Schlarman, J, Buchavzovb, N., and Stubenrauch, C., A disjoining pressure study of foam films stabilized by tetradecyl trimethyl ammonium bromide C14TAB, *Soft Matter*, 2, 584-594 (2006).
- Simjoo, M., Nguyen, Q.P., Zitha, P.L.J., Rheological transition during foam flow in porous media, SPE 149070, *SPE/DGS Saudi Arabia Section Technical Symposium and Exhibition*, Al-Khobar, Saudi Arabia, 15-18 May (2011).
- Simjoo, M., Dong, Y., Andrianov, A., Talanana., M., and Zitha, P.L.J., Novel insight into foam mobility control, SPE 15338, *International Petroleum Technology Conference*, Bangkok, Thailand, 7-9 February (2012).

- Simjoo, M., Dong, Y., Andrianov, A., Talanana, M., Zitha, P.L.J., A CT scan study of immiscible foam flow in porous media for EOR, SPE 155633, *SPE EOR Conference at Oil and Gas West Asia*, Muscat, Oman, 16-18 April (2012).
- Skauge, A., Aarra, M.G., Surguchev, L., Martinsen, H.A., and Rasmussen, L., Foam-assisted WAG: experience from the Snorre field, SPE 75157, *SPE/DOE Improved Oil Recovery Symposium*, Tulsa, Oklahoma, 13-17 April (2002).
- Srivastava, M., Zhang, J., Nguyen, Q.P., and Pope, G.A., A systematic study of Alkaline-Surfactant-Gas injection as an EOR, SPE 124752, *SPE Annual Technical Conference and Exhibition*, New Orleans, Louisiana, 4-7 October (2009).
- Suffridge, F.E., Raterman, K.T., Russell, G.C., Foam performance under reservoir conditions, SPE 19691, *SPE Annual Technical Conference and Exhibition*, San Antonio, Texas, 8-11 October (1989).
- Svorstøl, I., Vassenden, F., and Mannhardt, K., Laboratory studies for design of a foam pilot in the Snorre field, SPE 35400, *SPE/DOE Improved Oil Recovery Symposium*, Tulsa, Oklahoma, 21-24 April (1996).
- Tanzil, D., Hirasaki, G.J., and Miller C.A., Mobility of foam in heterogeneous media: flow parallel and perpendicular to stratification, SPE 63228, *SPE Annual Technical Conference and Exhibition*, Dallas, Texas, 1-4 October (2000).
- Tanzil, D., Hirasaki, G. J. and Miller C. A., Conditions for foam generation in homogeneous porous media, SPE 75176, *SPE/DOE Improved Oil Recovery Symposium*, Tulsa, Oklahoma, USA, April 13-17 (2002).
- Tcholakova, S., Mitrinova, Z., Golemanov, K., Denkov, N.D., Vethamuthu, M., and Ananthapadmanabhan, K.P., Control of Ostwald ripening by using surfactants with high surface modulus, *Langmuir*, 27, 14807-14819 (2011).
- Theander, K. and Pugh, R.J., Synergism and foaming properties in mixed nonionic/fatty acid soap surfactant systems, *J. Colloid and Interface Science*, 267 (1), 9-17 (2003).
- Turta, A.T., Singhal, A.K., Field foam applications in enhanced oil Recovery projects: screening and design aspects. SPE 48895, *International Oil and Gas Conference and Exhibition in China*, Beijing, China, 2-6 November (1998).
- van Duijn, C.J., Molenaar, J., and de Neef, M.J., The effect of capillary forces on immiscible two-phase flow in heterogeneous porous media, *Transport in Porous Media*, 21, 71-93 (1995).
- van Lingen, P.P., *Quantification and reduction of capillary entrapment in cross-laminated oil reservoirs*, Ph.D. dissertation, Delft University of Technology, the Netherlands (1998).
- Vassenden, F., Holt T., Ghaderi A, and Solheim, A., Foam propagation on semi-reservoir scale, *SPE Reservoir Evaluation & Engineering*, 2(5), 436-441(1999).
- Vikingstad, A.K., Skauge, A., Hoiland, H., Aarra, M.G., Foam-oil interactions analyzed by static foam tests, *Colloids Surfaces A: Physiochem. Eng. Aspects*, 260 (1-3), 189-198 (2005).
- Vikingstad, A.K., Aarra, M.G., Skauge, A., Effect of surfactant structure on foam-oil interactions comparing fluorinated surfactants and alpha olefin sulfonate in static foam tests, *Colloids Surfaces A: Physiochem. Eng. Aspects*, 279 (1-3), 105-112 (2006).
- Vikingstad, A.K., and Aarra, M.G., Comparing the static and dynamic foam properties of a fluorinated and an alpha olefin sulfonate surfactant, *J. Petroleum Science and Engineering*, 65(1-2), 105-111 (2009).
- Waggoner, J.R., Castillo, J.L., and Lake, L.W., Simulation of EOR processes in stochastically generated permeable media, *SPE Formation Evaluation*, 7(2), 173-180 (1992).
- Wasan, D.T., Koczko, K., Nikolov, A.D., *Mechanism of aqueous foam stability and antifoaming action with and without oil*, In: In: *Foams: Fundamentals & Applications in the Petroleum Industry*, Schramm, L.L. (ed.), American Chemical Society, Washington, DC (1994).
- Wasan, D., Nikolov, A., Huang, D., Edwards, D., *Foam stability: effects of oil and film stratification*, In: *Surfactant-based mobility control progress in miscible-flood enhanced oil recovery*, Smith, D.H. (ed.), American Chemical Society, Washington, DC (1988).
- Wellington, S.L., and Vinegar, H.J., *Surfactant-induced mobility control for carbon dioxide studied with computerized tomography*, In: *Surfactant based mobility control- progress in miscible flood enhanced oil recovery*, Smith, D.H. (Ed.), ACS, Washington, DC (1988).

- Weaire, D. and Hutzler, S., *The physics of foams*, Oxford University Press, Oxford (1999).
- World Oil Outlook 2011, Organization of the Petroleum Exporting Countries (2011).
- Xing, D., Wei, B., Trickett, K., Mohamed, A., Eastoe, J., Soong, Y., Enick, R., CO₂-soluble surfactants for improved mobility control, SPE 129907, *SPE Improved Oil Recovery Symposium*, Tulsa, Oklahoma, USA, 24-28 April (2010).
- Yan, W., Miller, C.A., and Hirasaki, G.J., Foam sweep in fracture for enhanced oil recovery, *Colloid and Surface A*, 282, 348-359 (2006).
- Yang, S.H., and Reed, R.L., Mobility control using CO₂ forms, SPE 19689, *SPE Annual Technical Conference and Exhibition*, San Antonio, TX, 8-11 October (1989).
- Yortsos, Y.C. and Chang, J., Capillary effects in steady-state flow in heterogeneous cores, *Transport in Porous Media*, 5, 399-420 (1990).
- Yin, G., Grigg, R.B., and Yi, S., Oil recovery and surfactant adsorption during CO₂ foam flooding, SPE 19787, *Offshore Technology Conference*, Houston, Texas, 4-7 May (2009).
- Zhdanov, S.A., Amiyani, A.V., Surguchev, L.M., Castanier, L.M. and Hanssen, J.E., Application of foam for gas and water shut-off: review of field experience, SPE 36914, *European Petroleum Conference*, Milan, Italy, 22-24 October (1996).
- Zhong, L., Szecsody, J.E., Zhang, F., and Mattigod, S.V., Foam delivery of amendments for vadose zone remediation: propagation performance in unsaturated sediments, *Vadose Zone J.*, 9 (3), 757-767(2010).
- Zhou, Z.H., Rossen, W.R., Applying fractional-flow theory to foams for diversion in matrix acidizing, *SPE Production & Facilities*, 9(1), 29-35 (1994).
- Zinati, F.F., Farajzadeh, R., Zitha, P.L.J., Foam modeling in heterogeneous reservoirs using stochastic bubble population approach, SPE 113358, *SPE/DOE Symposium on Improved Oil Recovery*, Tulsa, Oklahoma, 20-23 April (2008).
- Zitha, P.L.J., A new stochastic bubble population model for foam in porous media, SPE 98976, *SPE/DOE Symposium on Improved Oil Recovery*, Tulsa, Oklahoma, 22-26 April (2006).
- Zitha, P.L.J., Nguyen, Q.P., Currie, P.K., and Buijse, M.A., Coupling of foam drainage and viscous fingering in porous media revealed by X-ray computed tomography, *Transport in Porous Media*, 64(3), 301-313 (2006).
- Zitha, P.L.J., Du, D.X., A new stochastic bubble population model for foam flow in porous media. *Transport in Porous Media*, 83 (3), 603-621 (2010).

Synopsis van het proefschrift

Dit proefschrift presenteert nieuwe resultaten met betrekking tot het gedrag van niet-mengbaar gas en schuim in monsters van natuurlijk zandsteen, die eerder blootgesteld zijn aan overstromingen. Het geeft inzicht in processen die zeer relevant kunnen zijn voor het toepassen van verbeterde oliewinning (EOR) in klastische reservoirs. Allereerst werd een systematisch onderzoek uitgevoerd naar de schuimvorming in bulk om de effecten te onderzoeken van de oliefase op schuimvermogen en schuimstabiliteit te bepalen. Een schuimmiddel, de AOS surfactant dat stabiel schuim vormt in aanwezigheid van alkaan-type olie, werd aldus geïdentificeerd. Als tweede werd de stroom van dit 'surfactant' schuim in natuurlijke poreuze media onderzocht in afwezigheid van olie. De effecten van surfactant concentratie en injectie snelheid op schuim mobiliteit en schuim propagatie werden in detail onderzocht. Mechanismen betrokken bij een vermindering van schuim mobiliteit werden ook onderzocht. Kennis verkregen uit het bovenstaande deel vormde de basis voor verdere studie naar het gedrag van schuim in poreuze media in de aanwezigheid van olie. Als derde werd deschuim stroom in het met water overgoten poreuze media in detail bestudeerd, zodat het bewijs kon worden geleverd dat schuim een potentieel haalbaar EOR proces is. In onderstaande geven wij een samenvatting van de belangrijkste bevindingen die uit dit proefschrift verkregen zijn.

Onderzoek van schuimgedrag van geselecteerde commerciële surfactants (Dowfax 8390, C₁₂₋₁₅ Enordet, Petrostep SB en C₁₄₋₁₆ AOS), in afwezigheid en in aanwezigheid van model oliën, (bijvoorbeeld zuivere alkanen), toonde aan dat AOS de meeste olie-tolerante schuim vormt. Uit nader onderzoek van het schuimgedrag van de AOS surfactant, met verschillende surfactant concentraties (0.1, 0.5 en 1.0 gew%) en oliesoorten (n-C₆, n-C₁₀ en n-C₁₆), bleek dat het een uitstekend schuimend vermogen heeft, ondanks de variatie in lengte van de koolstofketen van de alkanen. Dit werd bevestigd door de opbouw van schuimvolume en door een monotone toename van de hoeveelheid van de vloeibare fractie in het schuim. Het verval van AOS schuim in de aanwezigheid van olie werd gekenmerkt door twee fasen: 1) een vrij kleine en snelle reductie van schuimvolume in de vroege periode, gevolgd door een gestabiliseerde waarde, 2) een tweede

reductie waarbij schuim een eindig volume bereikte (in aanwezigheid van n-C₁₆) of volledig was afgebroken (in aanwezigheid van n-C₆). Uit de ontwikkeling van de vloeibare fractie in het schuim vonden we dat zwaartekracht- drainage domineerde in de eerste vermindering van schuim volume, terwijl bellencoalescentie dominant was tijdens de tweede fase van het schuimvolume verval. Het effect van het olietype speelt een grotere rol tijdens dit tweede schuim verval. AOS schuim met alkaan met een kortere koolstofketen startte in het tweede verval vroeger en vertoonde de minste schuim stabiliteit. Verhoging van de surfactantconcentratie verbeterde de schuimstabiliteit in de aanwezigheid van olie. Het effect was meer uitgesproken voor de laagste onderzochte concentraties, namelijk 0.1 en 0.5 gew%. De resultaten voor schuimstabiliteit in de aanwezigheid van olie werden besproken in termen van de klassieke invoer/spreidingscoëfficiënt, het olie oplosbaarheids's effect en de stabiliteit van pseudo-emulsie film. Van de klassieke invoer/spreidingscoëfficiënt, olie oplosbaar effect en stabiliteit van pseudoemulsie film. Lagere schuimstabiliteit met een korte keten van alkaan werd beschreven met een grotere spreiding- en overbruggingscoëfficiënten. Hogere schuimstabiliteit met een lange keten van alkaan werd toegeschreven aan de accumulatie van oliedruppels in de Plateau grenzen, die naar verwachting de snelheid van verdunning van het schuimvlies vertragen.

Stikstof schuim gestabiliseerd door AOS surfactant in een poreus media van olievrij zandsteen werd gegenereerd volgens twee afzonderlijke processen: 1) op de eerste plaats, een primaire voorwaarts schuimfront ontstond in het eerst geïnjecteerde poriënvolume, dat de vloeibare fase in een front-achtige manier verplaatste, en 2) in de tweede plaats, na de schuim doorbraak ontstond een secundaire vloeibaar desaturatie front in de kern uitlaat en verspreidde zich naar de toegang van de kern. De snelheid van de secundaire desaturatie was veel langzamer dan van het primaire schuim front. We observeerden dat het secundaire schuim eerder ontstond bij een hogere surfactant concentratie en injectie snelheid. Derhalve, de schuim mobiliteit verminderde in twee stappen: tijdens de vermeerdering van het primaire voorwaartse schuim vermindert de schuimmobiliteit met een ordergrootte in vergelijking met water mobiliteit. Tijdens de secundaire schuim vermeerdering daalde het verder met één tot twee ordergrootte. We onderzochten ook het gedrag van schuim mobiliteit wanneer de surfactant-concentratie en injectie snelheid varieerden in een verhoging- verlaging cyclus. Schuim mobiliteit vertoonde een hysteresis voor de concentratie cyclus. Dit wordt verklaard door de kinetische adsorptie-desorptie van de surfactant. Een soortgelijke hysteresis is gevonden voor de snelheids cyclus. Dit betekent dat het sterke schuim, gegenereerd door een toenemende snelheid, ook doorzet na afnemende snelheid bij de laagst geteste waarde (1 ft/dag).

Bij uitdrukking van de *Mobility Reduction Factor* (MRF) als een functie van gasverzadiging S_g , bleek dat schuim een overgang van zwak (laag MRF) naar sterk (high MRF) ondergaat bij een typische gas verzadiging van $S_{gc} = 0.75 \pm 0.02$. De overgang gaat gepaard met een aanzienlijke vermindering van schuim mobiliteit in twee ordes van grootte en met een grote vermindering van de totale water verzadiging zo laag als 0.10 ± 0.02 . De overgang in schuimmobiliteit kan worden geïnterpreteerd als een sterke stijging van vloeispanning tijdens de schuimstroom: Wanneer gasverzadiging lager is dan de S_{gc} , dan is de vloeispanning nagenoeg gelijk aan nul, samenvallend met zwak schuim, terwijl wanneer gasverzadiging groter is dan de S_{gc} , de vloeispanning significant toeneemt en leidt tot het waargenomen sterke schuim. Een functionele relatie tussen vloeispanning en gasverzadigingsmethode werd voorgesteld: $\tau_y = a(\sigma/r)(S_g - S_{gc})^4$. Wanneer gas verzadiging lager is dan de S_{gc} , daalt de vloeispanning tot nul; daarboven wordt het gedrag beschreven als machtsfunctie. Het voorgestelde rheologische model heeft met succes de mobiliteitstransitie vastgelegd van gestabiliseerd schuim met verschillende surfactant concentraties (0.5 en 1.0 gew%) en voor verschillende kernlengtes (17.0 en 38.4 cm). Dit ondersteunt het idee dat vloeispanning groeit tijdens de secundaire schuim stroom.

De tijdelijke schuimstroom, de voorwaartse beweging van het schuim tot de doorbraak, in een olievrij poreus medium werd geanalyseerd metaan de hand van het stochastische generatie evenwichts (SBP) model. Het uitgangspunt voor dit model is dat schuimstroming in poreuze media een complexe vloeistof is en dat generatie van gasbellen een stochastisch proces is. We hebben een gevoeligheidsanalyse uitgevoerd om de effecten van raster nummer, tijd-stap, maximum (gas) bel-dichtheid en de bel-generatie coëfficiënt te onderzoeken. We vonden dat numerieke resultaten geen enkele afhankelijkheid tonen voor raster nummer (N) en tijd-stap (Δt) voor $N \geq 250$ and $\Delta t \leq 0.01$ s. Een verhoging van de maximale bel- heeft geleid tot de vorming van een sterker schuim, dat gekenmerkt wordt door een langzamere schuimvoortplanting en een grotere schuim mobiliteit reductie. De bel-generatie coëfficiënt (K_g) heeft schuimvorming zodanig beïnvloed dat een hogere K_g heeft geleid tot een sneller toenemende bellen-dichtheid. We hebben ook een vergelijking gemaakt tussen de verkregen numerieke verzadiging en de druk data met de data die we uit het experiment hebben verkregen. De goede overeenkomst tussen de numerieke resultaten en het experiment heeft bevestigd dat het SBP schuim model sterk is en omvat de belangrijkste kenmerken van de tijdelijke schuimstroom in poreuze media.

Voortbouwend op bovenstaande resultaten van AOS schuimgedrag in bulk en poreuze media konden we goed-gecontroleerde overstromingsexperimenten uitvoeren op kern in de

aanwezigheid van olie. De experimenten hebben duidelijk aangetoond dat stabiel schuim kan worden verkregen in de aanwezigheid van met water overstroomde resterende olie. Belangrijker, de experimenten hebben bewezen dat niet-mengbaar schuim de achtergebleven olie uit wateroverstroomde zandsteen kernen verplaatste en ondersteunt het idee dat schuim een potentieel effectieve EOR-methode is. CT scans, vloeistof verzadigingsprofielen en mobiliteits reductiefactoren tonen aan dat schuim een goede mobiliteits controle in aanwezigheid van met water overstroomde resterende olie. Dit werd verder bevestigd door een vertraging in de gas doorbraak. Schuim sterkte en incrementele oliewinning namen toe met de surfactant concentratie (van 0.1 tot 1.0 gew%). Voor een surfactant concentratie gelijk aan 1.0 gew%, de incrementele oliewinning door schuim was zo hoog als $23\pm 2\%$ van de olie die aanvankelijk iaanwezig was na injectie van 4.0 PV schuim (gelijk aan 0.36 PV geïnjecteerde surfactant oplossing). Incrementele oliewinning was slechts $5.0\pm 0.5\%$ voor gas overstromingen bij dezelfde injectietijd. We vonden dat incrementele olieproductie door schuim overstroming plaats vindt door de volgende belangrijkste mechanismen: (1) een lagere resterende olie verzadiging bij gas overstroming in vergelijking met wateroverstroming, (2) vorming van een olie plaat in de eerste paar geïnjecteerd poriënvolumes, wat samenvalt met een grote toename van het capillair getal en (3) een lange staart van olieproductie als gevolg van het transport van de in het stromende schuim verspreidde olie bij een redelijk constant capillair getal. We observeerden dat de grootte van de olie plaat bij surfactant concentratie toenam, maar dat de verspreidde olie minder gevoelig was voor de surfactant concentratie. We vonden ook dat pre-spoeling van de surfactant een betere schuim injectie strategie is. Schuim ontwikkeling en, dienovereenkomstig, olie herstel zonder surfactant pre-spoeling was significant vertraagd in vergelijking met het geval van de pre-spoeling. Schuim injectie onder stabiele zwaartekracht omstandigheden was gunstig voor de schuimvorming en oliewinning. Het veroorzaakte een snelle toename van schuim sterkte en een langere doorbraaktijd van het schuim samen met een hogere stabiele status van de mobiliteit reductiefactor. Incrementele oliewinning onder stabiele zwaartekracht omstandigheden was bijna twee keer zo groot in vergelijking met onstabiele zwaartekracht omstandigheden.

Met de bijdrage van dit werk tot schuim kennis is aangetoond dat schuim potentieel een efficiënte EOR-methode is. Echter, veevragen blijven en benadrukken de noodzaak tot verdere wetenschappelijke studie en onderzoek om een praktisch onmengbaar schuim EOR-proces optimaal te ontwikkelen. De eerste stap in de richting van dit laatste doel is het ontwikkelen van een nieuw en verbeterd schuimmodel, dat de effecten van olie op schuimstabiliteit in acht neemt. Vervolgens zouden de effecten van temperatuur, zoutconcentratie en rots kenmerken,

representatief van reële reservoir omstandigheden, bestudeerd moeten worden. Tenslotte zouden de resultaten van de haalbaarheid van het schuim EOR concept moeten worden getest onder proefveld omstandigheden, om te controleren of schuim zich over lange afstanden kan verspreiden en, overeenkomstig, of schuim kan worden gebruikt als een vorderingsmiddel.

چکیده پایان نامه

این پایان نامه در بردارنده نتایج جدیدی درباره رفتار فوم و گاز امتزاج ناپذیر در مغزه‌هایی ماسه‌سنگی می‌باشد. این نتایج همچنین می‌تواند برای سایر فرآیندهای مرتبط با ازدیاد برداشت نفت (به عنوان مثال انسداد لایه‌های با ضریب تراوایی بالا، کنترل تحرک پذیری در فرایندهای تزریق گاز) نیز مورد استفاده قرار گیرد. در این پایان نامه ابتدا یک مطالعه سیستماتیک درباره رفتار فوم (کف) در حالت بالک (بیرون از محیط متخلخل) به منظور بررسی اثر نفت بر روی قابلیت فوم شوندگی و همچنین پایداری فوم انجام شد. نتایج نشان داد که سورفکتنت آلفا اولفین سولفونات (آ.او.اس) توانایی ایجاد یک فوم پایدار در حضور نفت‌های مختلف از خانواده آلکانها را داراست. در ادامه رفتار فوم آ.او.اس در محیط متخلخل در غیاب نفت مورد مطالعه قرار گرفت. اثر غلظت سورفکتنت و سرعت تزریق بر روی میزان تحرک پذیری فوم و نیز بر روی میزان انتشار فوم در محیط متخلخل مورد بررسی قرار گرفت. سپس مکانیزم‌هایی که باعث کاهش تحرک پذیری فوم می‌شدند، تعیین گردید. در ادامه رفتار فوم در محیط متخلخلی که قبلاً تحت تزریق آب قرار گرفته و به حالت اشباع نفت باقی مانده رسیده بود، مورد مطالعه قرار گرفت. نتایج نشان داد که فوم امتزاج ناپذیر قابلیت تولید بخشی از نفت باقی مانده را داراست و می‌تواند به عنوان یک روش ازدیاد برداشت مورد استفاده قرار گیرد. خلاصه‌ای از مهمترین نتایج حاصله از این پایان نامه به شرح زیر است:

بررسی رفتار فوم در حالت بالک :

رفتار فوم شوندگی مجموعه‌ای از سورفکتنت‌های تجاری که در صنعت نفت مورد استفاده قرار می‌گیرند از طریق آزمایش "ستون فوم" مورد بررسی قرار گرفت. در این آزمایش گاز نیتروژن در محلول سورفکتنت دمیده شد تا ستونی از فوم تشکیل گردد. سپس پایداری فوم از طریق مطالعه ارتفاع ستون تشکیل شده برحسب زمان بررسی گردید. نتایج نشان داد که سورفکتنت آ.او.اس در حضور نفت‌هایی از خانواده آلکان که به عنوان نفت مدل استفاده شدند، پایدارترین فوم را ایجاد نمود. بررسی رفتار پایداری ستون فوم تشکیل شده در حضور نفت نشان داد که ارتفاع فوم آ.او.اس طی دو مرحله کاهش می‌یابد: ۱) کاهش اولیه سریع در ارتفاع ستون فوم در زمانهای ابتدایی که در نهایت باعث شد که ستون فوم به یک ارتفاع ثابتی برسد و ۲) کاهش ثانویه که بواسطه آن ارتفاع ستون فوم باقی مانده به طور پیوسته کاهش یافت (البته با نرخ کاهش کمتری نسبت به حالت اولیه). در نهایت با توجه به نوع نفت مورد استفاده، ستون فوم یا به طور کلی از بین رفت (در حضور نرمال هگزان) یا به ارتفاع محدودی رسید (در حضور نرمال هگزا دکان). از طریق مطالعه میزان مایع موجود در فوم مشخص گردید که کاهش اولیه در ستون فوم تحت تاثیر ریزش ثقلی است؛ ولی کاهش ثانویه تحت تاثیر مکانیزم انعقاد حباب‌ها است که بواسطه آن حباب‌های کوچکتر به حباب‌های بزرگتر می‌پیوندند. نتایج نشان داد که اثر نفت بر روی کاهش ثانویه ستون فوم مهم‌تر است. فوم آ.او.اس در حضور آلکان با زنجیره هیدروکربنی کوتاه‌تر، میزان پایداری کمتری از خود نشان داد و در مدت زمان کوتاه‌تری وارد مرحله کاهش ثانویه شد. افزایش غلظت سورفکتنت (از ۰/۱ الی ۱ درصد وزنی) تاثیر مثبتی بر روی پایداری فوم در حضور نفت داشت. در ادامه، پایداری فوم در حضور نفت

از طریق تنوری های زیر مورد مطالعه قرار گرفت: ضریب ورود و ضریب پخش شوندگی، اثر انحلال نفت و پایداری فیلم شبه امولسیون. پایداری کمتر فوم آ.او.اس در حضور آلکان های با زنجیره هیدروکربنی کوتاه تر از طریق داشتن مقادیر بالاتری برای ضرایب ورود و پخش شوندگی توصیف شد. پایداری بیشتر فوم آ.او.اس در حضور آلکان های با زنجیره هیدروکربنی بلندتر به تجمع قطرات نفت در ساختار فوم نسبت داده شد که در نهایت باعث کاهش نرخ نازک شوندگی در لایه های فیلمی موجود در فوم گردید.

بررسی رفتار فوم در محیط متخلخل بدون حضور نفت:

خواص فوم شوندگی گاز نیتروژن در حضور سورفکتانت آ.او.اس در مغزه های ماسه سنگی با ضریب تراوایی ۱/۵ الی ۲/۵ داری و ضریب تخلخل ۰/۲۲ مورد مطالعه قرار گرفت. برای مشاهده رفتار و نحوه جریان فوم از سی تی اسکن استفاده شد. برای تشکیل فوم، گاز و محلول سورفکتانت به طور همزمان (به ترتیب با نسبت حجمی ۱۰ به ۱) داخل مغزه ای که قبلاً با محلول سورفکتانت اشباع شده بود، تزریق گردید. دو نوع رفتار جریان مختلف از فوم مشاهده شد: (۱) ایجاد جبهه پیش رونده فوم که باعث شد محلول سورفکتانت طی یک جابجایی پیستون مانند حرکت کند و (۲) پس از مشاهده فوم در قسمت خروجی مغزه، یک جبهه برگشتی از فوم در قسمت خروجی مغزه تشکیل شد که به سمت ورودی مغزه انتشار یافت. سرعت انتشار جبهه برگشتی بسیار کمتر از جبهه پیش رونده اولیه بود. همچنین در غلظتهای بالاتر سورفکتانت و سرعت تزریق، جبهه برگشتی فوم زودتر مشاهده شد. بنابراین تحرک پذیری فوم طی دو مرحله کاهش می یابد: ابتدا در طول انتشار اولیه، تحرک پذیری فوم بیش از ۱۰ برابر در مقایسه با تحرک پذیری آب (در سرعت تزریقی یکسان) کاهش یافت و سپس در طول انتشار جبهه برگشتی، تحرک پذیری فوم در حدود ۱۰۰ برابر کاهش یافت. همچنین، رفتار فوم در طی یک چرخه افزایشی-کاهشی از غلظت سورفکتانت و سرعت تزریقی مورد مطالعه قرار گرفت. بر اساس نتایج، یک رفتار هیسترسیس در تحرک پذیری فوم برای سیکل افزایشی-کاهشی غلظت سورفکتانت مشاهده شد. این رفتار بر اساس سینتیک جذب و دفع سورفکتانت مورد بررسی قرار گرفت. یک رفتار هیسترسیس مشابه در مورد سرعت تزریقی نیز مشاهده شد. این رفتار نشان می دهد که فوم قوی (با تحرک پذیری پایین) که به واسطه افزایش تدریجی سرعت تزریقی ایجاد شده است، می تواند با کاهش سرعت تزریقی تا ۱۰ برابر نیز همچنان قوی باقی بماند.

حالت گذار در رفتار رئولوژیکی فوم:

به منظور بررسی دقیق تر رفتار فوم در محیط متخلخل، پارامتر کاهش تحرک پذیری فوم (نسبت اختلاف فشار فوم به اختلاف فشار آب در سرعت تزریق یکسان) بر اساس تابعی از میزان اشباع گاز در مغزه رسم شد. نتایج نشان داد که در یک مقدار مشخص از اشباع گاز، فوم دچار یک تغییر محسوس از حالت یک فوم ضعیف با تحرک پذیری بالا به یک فوم قوی با تحرک پذیری پایین می شود. مقدار بحرانی اشباع گاز برای این تغییر حالت در فوم در حدود 0.75 ± 0.02 بدست آمد. این رفتار ویژه براساس خواص رئولوژیکی فوم قابل تحلیل است. بر این اساس فوم به عنوان یک ماده غیر نیوتونی با یک تنش تسلیم مدل شد. زمانی که درجه اشباع گاز پایین تر از مقدار بحرانی است، تنش تسلیم فوم بسیار کوچک بوده و یک فوم ضعیف بوجود خواهد آمد. با افزایش میزان اشباع گاز به بالاتر از مقدار بحرانی، تنش تسلیم افزایش قابل توجهی می یابد که در نهایت منجر به ایجاد یک فوم قوی می شود. برای توصیف رفتار تنش تسلیم فوم یک رابطه نمایی بر اساس میزان اشباع گاز ارائه شد. همخوانی خوبی بین مدل رئولوژیکی ارائه شده و نتایج آزمایشگاهی مشاهده گردید.

مدلسازی جریان فوم محیط متخلخل:

جهت بررسی رفتار جبهه پیش رونده فوم تا قبل از زمان تولید در خروجی مغزه، از مدل موازنه جمعیت آماری استفاده شد. براساس این مدل، فوم در محیط متخلخل یک سیال غیرنیوتونی با تنش تسلیم است. همچنین در این مدل تولید حبابهای گاز در محیط متخلخل یک فرآیند تصادفی فرض شده است. این مدل بر اساس پارامترهای زیر توصیف می شود: بیشینه مقدار حباب تولیدی، ضریب تولید حباب، ضریب از بین رفتن حباب. برای بررسی رفتار جریان فوم از طریق این مدل ابتدا یک سری معادلات دیفرانسیل جزئی غیر خطی براساس میزان اشباع آب، فشار آب و تعداد حبابها ایجاد شد. سپس این معادلات از طریق روش "حل ضمنی برای فشار- حل صریح برای درجه اشباع" مورد آنالیز قرار گرفت. نتایج مدل نشان داد که پارامتر ضریب تولید حباب به طور خاص بر روی سرعت تولید فوم اثر می گذارد؛ به طوری که هر چقدر این ضریب افزایش یابد، حبابهای تشکیل شده در بازه زمانی کوتاه تری به مقدار بیشینه می رسند. همچنین میزان تحرک پذیری فوم با بیشینه مقدار حباب تولیدی رابطه مستقیمی دارد. در نهایت مدل معرفی شده جهت پیش بینی نتایج حاصل از آزمایش مورد استفاده قرار گرفت. همخوانی خوبی بین داده های فشار و درجه اشباع آب در مدل و آزمایش بدست آمد که بیانگر کارایی مدل فوق الذکر جهت توصیف جبهه پیش رونده فوم (تا قبل از زمان تولید) در یک محیط متخلخل هموزن است.

فوم به عنوان یک روش ازدیاد برداشت:

جهت بررسی عملکرد فوم امتزاج ناپذیر به عنوان یک روش ازدیاد برداشت، رفتار فوم در محیط متخلخل حاوی نفت باقی مانده از فرآیند تزریق آب مورد مطالعه قرار گرفت. گاز نیترژن به همراه سورفکتانت آ.ا.وس جهت تولید فوم در مغزه تزریق شد و رفتار فوم توسط سی تی اسکن مورد بررسی قرار گرفت. بر اساس نتایج بدست آمده، یک فوم پایدار در حضور نفت تشکیل شد و فوم تشکیل شده توانست بخشی از نفت باقی مانده را تولید نماید. این نتایج نشان داد که فوم امتزاج ناپذیر می تواند به عنوان یک عامل ازدیاد برداشت مورد استفاده قرار گیرد. براساس داده های فشار مشخص گردید که فوم میتواند تحرک پذیری گاز نیترژن را کاهش داده و در نتیجه از تولید ناگهانی گاز جلوگیری کند. افزایش غلظت سورفکتانت از ۰/۱ الی ۱ درصد وزنی اثر مثبتی بر روی عملکرد فوم داشت. برای غلظت سورفکتانت ۱ درصد وزنی، میزان تولید نفت توسط فوم در حدود $23 \pm 2\%$ از نفت اولیه موجود در مغزه بوده که در نتیجه تزریقی به مقدار چهار برابر میزان حجم فضای خالی مغزه حاصل شد. در مدت زمان مشابه میزان تولید نفت توسط تزریق گاز نیترژن (بدون حضور سورفکتانت در مغزه) فقط در حدود $5 \pm 0/5\%$ بود. نفت تولیدی توسط فوم طی دو مرحله مختلف حاصل گردید: (۱) ایجاد یک بانک نفتی در جلوی جبهه پیش رونده فوم و (۲) یک دنباله تولید طولانی از قطرات کوچک نفت که در داخل ساختار فوم بودند. مشاهده شد که اندازه بانک نفت تولیدی با افزایش غلظت سورفکتانت از ۰/۱ الی ۱ درصد وزنی زیادتر می شود، در حالیکه حالت دوم تولید نفت، به غلظت سورفکتانت وابستگی خاصی نشان نداد.

نتایج این تحقیق نشان داد که فوم علاوه بر اینکه می تواند به عنوان یک عامل انسدادی جهت بستن لایه های با ضریب تراوایی بالا بکار رود، قابلیت استفاده به عنوان یک عامل ازدیاد برداشت را نیز داراست. با این حال هنوز مطالعات بیشتری جهت طراحی یک فرآیند عملیاتی برای تزریق فوم نیاز است. اولین قدم در این مسیر ایجاد یک مدل مناسب جهت توصیف رفتار فوم در حضور نفت است که بتواند اثرات نفت بر روی پایداری فوم را به خوبی توصیف کند. در ادامه ضروری است که تأثیر پارامترهای مختلفی مانند دما، غلظت نمک و همچنین مشخصات مغزه که بیانگر شرایط واقعی مخزن هستند، مورد مطالعه قرار گیرند. سپس مطالعات امکان سنجی فوم به عنوان عامل ازدیاد برداشت باید در تستهای

پایلوت انجام شود تا مشخص گردد که آیا فوم قابلیت انتشار در شعاع های دورتر از نقطه تزریق را دارا است و همچنین آیا فوم می تواند در شرایط نزدیک به حالت واقعی مخزن نیز باعث تولید نفت گردد؟

Acknowledgments

The praise is due to Allah, most gracious, most merciful, the lord of the worlds; a praise equal to the praise of his close angles, and his prophets.

I would like to express my sincere appreciation to all those who have contributed directly or indirectly in the completion of this study.

I wish to express my sincere gratitude to my supervisor Prof. Pacelli Zitha for his guidance and inspiration throughout my Ph.D. study. His support and advises helped me a lot in my research. My special thanks go to Prof. Bill Rossen, Prof. Hans Bruining, Dr. Susanne Rudolph, Dr. Cas Berentsen and Dr. Rouhi Farajzadeh for their encouraging interest in my project and the knowledge that shared with me. With pleasure, I thank the committee members of my Ph.D. defense for reviewing my thesis and giving valuable comments.

I gratefully acknowledge Iran Ministry of Science, Research, and Technology for awarding me a Ph.D. scholarship. I also thank Shell Global Solutions International for sponsoring part of my Ph.D. research through the Shell GameChanger program on immiscible foam. I am also grateful to Dr. Alexey Andrianov, Rien Faber, Tsuyoshi Matsuura and Dr. Mohand Talanana for their valuable comments in the project meetings in Shell. I would also like to thank Teymour Rezaei, M.D. Carretero-Carralero, Yufei Dong for their help in enriching the contents of this thesis.

I wish to appreciate all the members of the Dietz lab that contributed through good advice and their good spirits to this thesis. Many thanks go to Adri, Dik, Ellen, Frans, Gerard, Henk, Henney, Jan, Joost, Jolanda, Karel, Kees, Marck, Paul and Wim. I also thank Hannie, Lydia, Margot, Marijk, Marlijn and Ralf for their help with the administrative issues. My especial thanks go to Mariette van Tilburg for carefully reading the thesis draft.

I am grateful to all my colleagues in the petroleum group for the good time we had together. Many thanks to Amin Ameri, Elham Ashoori, Chris Boeij, Ehsan Eftekhari, Frazad Farshbaf, Amin Fatemi, Rahul Fonseca, Jiakun Gong, Hua Guo, Yuangnan He, Patrick van Hemert, Mojtaba Hosseini Nasab, Siavash Kahrobaei, Negar Khoshnevis, Roozbeh Khosrokhavar, Christian

Kosack, Tianqi Li, Anna Peksa, Saskia Roles, Hamidreza Salami, Narjes Shojai Kaveh, Samaneh Soroush, Rahul Thorat, Maryam Namder Zanganeh, Ali Vakili, Panneerselvam Ranganathan, Ioannis Xiarchos, Peyman Poor Moghaddam, Araz Mahdad, Ata Abdollahi, Mohsen Kavin and Ahmad Mirhaj. I really appreciate my close friend Mohammad Chahardowli for his strong support; whenever I faced any difficulty, he was kindly available to help me.

I was so fortunate to find a lot of good friends in Delft. Every Friday evening we came together and enjoyed reciting the Holy Quran. I would like to thank Hossein, Azim, Shahab, Hesam, Akbar, Ali, Ali Reza, Amir Ahmad, Amir Reza, Amin, Behzad, Ebrahim, Esmaeil, Hamed, Hamid, Hojjat, Iman, Majid, Masoud, Mohammad, Mohammad Bashir, Mohammad Mahdi, Mohsen, Mehdi, Mojtaba, Nader and Vahid.

I am indebted to my former teachers at Sahand University of Technology and at Petroleum University of Technology for their support and encouragement during my B.Sc. and M.Sc. studies.

I would like to express my deepest thanks to my family. In fact, it is beyond my ability to thank them in a way they deserve. I am extremely thankful to my parents for their love and blessings and for their patience in these years. I am really proud of you. Hope to be able to compensate only a small part of your kindness. I am very grateful to my sisters, my dear Hassan, and my lovely niece Reihaneh who were always my main source of inspiration and motivation.

Mohammad Simjoo

Delft, September 2012

Scientific Contribution

Journal papers:

Simjoo M., Zitha, P.L.J., Foam mobility transition in porous media, submitted to *Industrial & Engineering Chemistry Research* (2012).

Simjoo, M, Zitha, P.L.J., Modeling of transient foam flow using stochastic bubble population model, submitted to *Transport in Porous Media* (2012).

Simjoo, M., Rezaei, T., Zitha, P.L.J., Foam stability in the presence of oil: effect of surfactant concentration and oil type, submitted to *Colloids and Surfaces A: Physicochemical and Engineering Aspects* (2012).

Simjoo, M., Dong, Y., Andrianov, A., Talanana, M., Zitha, P.L.J., A CT scan study of immiscible foam flow in porous media for enhancing oil recovery, revision submitted to *Industrial & Engineering Chemistry Research* (2012).

Simjoo, M., Dong, Y., Andrianov, A., Talanana, M., Zitha, P.L.J., Novel insight into foam mobility control, revision submitted to *SPE Journal* (2012).

Simjoo, M., Nguyen, Q.P., Zitha, P.L.J., Rheological transition during foam flow in porous media, *Industrial & Engineering Chemistry Research*, 51 (30), 10225-10231 (2012).

Conference proceedings:

Simjoo, M., Zitha, P.L.J., Immiscible foam for enhancing oil recovery, *International conference on colloids and complex fluids: challenges and opportunities*, Rueil-Malmaison, France, 17-19 October (2012).

Simjoo, M., Zitha, P.L.J., Foam mobility transition in porous media, *International conference on colloids and complex fluids: challenges and opportunities*, Rueil-Malmaison, France, 17-19 October (2012).

Simjoo, M., Rezaei, T., Zitha, P.L.J., Foam stability in the presence of oil: effect of surfactant concentration and oil type, *9th European Conference on Foams, Emulsions and Applications EUFOAM 2012*, Lisbon, Portugal, 8-11 July (2012).

Simjoo, M., Dong, Y., Andrianov, A., Talanana, M., Zitha, P.L.J., A CT scan study of immiscible foam flow in porous media for EOR, SPE 155633, *SPE EOR Conference at Oil and Gas West Asia*, Muscat, Oman, 16-18 April (2012).

Simjoo, M., Dong, Y., Andrianov, A., Talanana, M., and Zitha, P.L.J., Novel insight into foam mobility control, SPE 15338, *International Petroleum Technology Conference*, Bangkok, Thailand, 7-9 February (2012).

Simjoo, M., Nguyen, Q.P., Zitha, P.L.J., Rheological transition during foam flow in porous media, SPE 149070, *SPE/DGS Saudi Arabia Section Technical Symposium and Exhibition*, Al-Khobar, Saudi Arabia, 15-18 May (2011).

Simjoo, M., Mahamoodi Nick, M., Farajzadeh, R., Mirhaj, S.A., Zitha, P.L.J., A CT scan study of foam flooding in porous media, *EAGE International Petroleum Conference & Exhibition*, Shiraz, Iran, 4-6 May (2009).

Simjoo, M., Mahamoodi Nick, Zitha, P.L.J., Effect of oil saturation on foam for acid diversion, SPE 122152, *8th European Formation Damage Conference*, Scheveningen, The Netherland, 27-29 May (2009).

Simjoo, M., Dadvand Koochi, A., Vafaie Seftie, M., Zitha, P.L.J., Water shut-Off in a fractured system using a robust polymer gel, SPE 122280, *8th European Formation Damage Conference*, Scheveningen, The Netherland, 27-29 May (2009).

About the Author

Mohammad Simjoo was born on February 7, 1982 in Bandar Anzali, Iran. He obtained his B.Sc. degree in 2004 in Chemical Engineering from Sahand University of Technology, Tabriz, Iran and his M.Sc. degree in 2006 in Reservoir Engineering from Petroleum University of Technology, Ahwaz, Iran. In 2008, he was entitled to an overseas Ph.D. scholarship from Iran Ministry of Science, Research, and Technology. He started his Ph.D. research in May 2008 in the Department of Geoscience and Engineering at Delft University of Technology, the Netherlands. His research was focused on the study of immiscible foam for enhancing oil recovery. Currently, he is a member of the Department of Chemical Engineering at Sahand University of Technology.

Contact information:

Chemical Engineering Department
Sahand University of Technology
P.O. Box: 51335-1996
Sahand New Town, Tabriz, Iran

Phone: +98 412 3459152

Fax: +98 412 3444355

Email: simjoo@sut.ac.ir

